UILU–ENG–97–2006

CIVIL ENGINEERING STUDIES

STRUCTURAL RESEARCH SERIES NO. 616

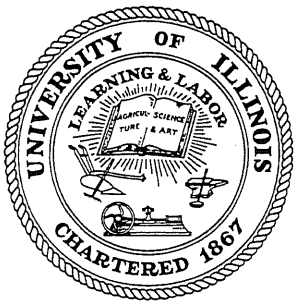

ISSN: 0069–4274

A FIBER REINFORCED PLASTIC JOINT FOR FILAMENT WOUND PIPES: ANALYSIS AND DESIGN

By

HECTOR ESTRADA
University of Illinois

I. DENNIS PARSONS
TransMotive Technologies, Inc.

A Report on a Research Project
Sponsored by the
NATIONAL SCIENCE FOUNDATION
WASHINGTON, D.C.
Under Grant SBC CMS 93-15240

DEPARTMENT OF CIVIL ENGINEERING
University of Illinois at Urbana-Champaign
Urbana, Illinois

July 1997

50272–101

REPORT DOCUMENTATION PAGE	1. REPORT NO. UILU–ENG–97–2006	2.	3. Recipient's Accession No.

4. Title and Subtitle
A Fiber Reinforced Plastic Joint for Filament Wound Pipes: Analysis and Design

5. Report Date
July 1997

6.

7. Author(s)
Hector Estrada and I. Dennis Parsons

8. Performing Organization Report No.
SRS 616

9. Performing Organization Name and Address
University of Illinois at Urbana-Champaign
Department of Civil Engineering
205 N. Mathews Avenue
Urbana, Illinois 61801

10. Project/Task/Work Unit No.

11. Contract(C) or Grant(G) No.
(G) SBC CMS 93-15240

12. Sponsoring Organization Name and Address
National Science Foundation
Washington, D.C.

13. Type of Report & Period Covered

14.

15. Supplementary Notes

16. Abstract (Limit: 200 words)

Fiber reinforced plastic pipe joints are widely used in the piping industry. However, current fiber reinforced plastic joint standards are based on standards written for their metallic counterparts, and the relevant design codes lack reliable design guidelines. We have developed an innovative fiber reinforced plastic joining technique to address these and other problems that have been reported in the literature. The proposed joint can be used with filament wound pipes, the most common fiber reinforced plastic pipe manufacturing technique. This joint can be manufactured using current filament winding equipment with minor alterations. This report emphasizes the design concept and the development of the design calculations for the proposed fiber reinforced plastic joint.Pipe joints are susceptible to two failure mechanisms, failure from the standpoint of strength and leakage. The strength design procedure is derived from first principles taking into account the orthotropy of the fiber reinforced plastic material. The leakage analysis follows the guidelines of the American Society of Mechanical Engineers Boiler and Pressure Vessel code. The analytical design calculations are checked using finite element analysis. The agreement is excellent. We also conducted a detailed finite element analysis of a particular joint, designed using the simplified method, in order to assess the safety of the simple design calculations.

17. Document Analysis a. Descriptors
composites, finite elements, GRP flanged pipe joints, filament winding

b. Identifiers/Open–Ended Terms

c. COSATI Field/Group

18. Availability Statement	19. Security Class (This Report)	21. No. of Pages
Release Unlimited	UNCLASSIFIED	166
	20. Security Class (This Page) UNCLASSIFIED	22. Price

(See ANSI–Z39.18)

OPTIONAL FORM 272 (4–77)
Department of Commerce

A FIBER REINFORCED PLASTIC JOINT FOR FILAMENT WOUND PIPES: ANALYSIS AND DESIGN

By

Hector Estrada
Department of Civil Engineering
University of Illinois

and

I. Dennis Parsons
TransMotive Technologies Inc.

A Report on a Research Project Sponsored by the:
NATIONAL SCIENCE FOUNDATION
WASHINGTON, D.C.

University of Illinois
Urbana, Illinois
July 1997

ABSTRACT

Fiber reinforced plastic pipe joints are widely used in the piping industry. However, current fiber reinforced plastic joint standards are based on standards written for their metallic counterparts, and the relevant design codes lack reliable design guidelines. We have developed an innovative fiber reinforced plastic joining technique to address these and other problems that have been reported in the literature. The proposed joint can be used with filament wound pipes, the most common fiber reinforced plastic pipe manufacturing technique. This joint can be manufactured using current filament winding equipment with minor alterations. This report emphasizes the design concept and the development of the design calculations for the proposed fiber reinforced plastic joint.

Pipe joints are susceptible to two failure mechanisms, failure from the standpoint of strength and leakage. The strength design procedure is derived from first principles taking into account the orthotropy of the fiber reinforced plastic material. The leakage analysis follows the guidelines of the American Society of Mechanical Engineers Boiler and Pressure Vessel code. The analytical design calculations are checked using finite element analysis. The agreement is excellent. We also conducted a detailed finite element analysis of a particular joint, designed using the simplified method, in order to assess the safety of the simple design calculations.

ACKNOWLEDGMENTS

This report is based on the dissertation of Hector Estrada submitted to the Graduate College, University of Illinois at Urbana-Champaign, for the degree of Doctor of Philosophy in Civil Engineering. The thesis was completed under the supervision of Professor I. Dennis Parsons.

This investigation was supported by a grant from the National Science Foundation, grant number SBC CMS 93-15240. The financial support of IMGIP (fellowship) and the department of Civil Engineering at the University of Illinois at Urbana-Champaign (teaching assistantship) for Hector Estrada is appreciated.

The authors acknowledge the help and useful discussions of Professor K. D. Hjelmstad, Professor R. H. Dodds, Professor N. R. Sottos, Wendy Estrada, Dr. Amjad J. Aref, Aliazaro Namazifard, Ertugrul B. Taciroglu and Dr. Rami Haj-Ali.

TABLE OF CONTENTS

Chapter 1

Introduction and Objectives

1.1 Overview

Composite systems are widely used in the pressure vessel and piping industries; their properties make them ideal in the severe oxidizing or reducing atmospheres generally found in these industries. For instance, in the chemical industry, corrosion resistance is the chief advantage composite systems have over their metallic counterparts. In the most severe corrosive environment, the life of steel can be measured in a few days. Only the highest grade chromium-nickel-molybdenum (Cr-Ni-Mo) alloys can satisfactorily survive in these conditions. A more cost effective solution is the use of high molecular weight polymers coupled with suitable reinforcing materials (e.g., fibrous glass). It has been estimated that in the 1980's corrosion cost U. S. industry approximately $8 billion a year and that 60% of the U. S. steel output went into replacement products [37].

Composites also have higher strength and stiffness to weight ratios compared to traditional engineering materials such as steel and concrete. Their low weight can help reduce installation and repair costs. Another important advantage of composites is the designer's ability to tailor the material properties for a specific application. High glass content provides maximum physical strength; high resin content provides maximum corrosion resistance. The designer can combine these two elements to produce a satisfactory design.

Due to these factors, composite piping systems have enjoyed a vast growth over the last three decades [34]; however, the industry suffers from a severe lack of standardization and the relevant design codes lack reliable design guidelines for fiber reinforced plastic (FRP) pipe

joints. As a result of limited research in FRP pipe joining, designers rely on criteria based primarily on well established isotropic designs (typically steel designs) and empirical methods. Due to fundamental differences in the behavior of isotropic and composite materials, the reliability of these design practices is questionable. In this work, we present an innovative joining technique (see figure 1.1) which can be used with filament wound pipes, the most common FRP pipe manufacturing technique. As shown in figure 1.2, the pipe and hub are the only components manufactured by filament winding. We also present a simplified analysis procedure that can be used to proportion the joint.

The FRP joint we are proposing is a modified version of a commonly used FRP joint, the stub flanged joint, which we discuss in the next chapter. Therefore, we refer to our proposed joint as the modified stub flanged joint. We choose this geometry for the joint because of inherent problems with current FRP joints and manufacturing reasons.

Although we have discussed the corrosion problem, it is not the scope of this report to cover piping corrosion resistance design; rather, the FRP pipe joint strength and the stiffness design problems are studied. However, since the strength of the reinforcement can be adversely affected by some chemicals, it is appropriate to comment on the need to protect the reinforcement, typically using a chemical resistant material liner. An important note is that the strength contribution of this liner to the system is negligible and it is not included in calculating the system strength. However, it is important that the integrity of the selected liner is maintained throughout the service life of the piping system. The subject of corrosion and chemical resistant piping is covered by Mallinson [37] in detail. Rolston [46] and Talbot [49] discuss the process of selecting fibrous reinforced plastic materials when corrosion is a problem.

Once a suitable corrosion resistant material has been selected, the joint designer considers two failure mechanisms, failure from the stand point of strength and joint leakage, the latter being more common than the former. These are the only problems dealt with in this report.

1.2 Objectives

Our goal is to investigate current problems faced by the FRP pipe joining industry and propose an innovative joining technique that addresses these problems. The problems have been reported in the literature; therefore, our task is to identify potential pipe joint candidate systems that address these problems and outline a design criterion. The main objectives of the project are:

1. Develop an innovative joining technique for filament wound pipes, which addresses current FRP pipe joining problems.

2. Propose a manufacturing technique using current filament winding equipment with minor alterations.

3. Develop reliable design methods well founded in analytical work that practicing engineers can use to design efficient FRP joints for filament wound pipes.

4. Conduct numerical verification of the design calculations using finite element analysis.

5. Present leakage analysis using state-of-the-art numerical analysis.

The investigation presented here will provide a reliable joining technique for filament wound pipes and a design criterion for this joint that practicing engineers can use to design efficient piping systems. The research will be focused primarily on joints for low pressure and low temperature water main service. But it will not be restricted to low pressure applications; however, since most thermosetting matrix materials undergo a significant reduction in strength at temperatures above $200°C$, high temperature applications will not be considered. Also, this joint can be used with pressure vessels and piping containing medium other than water, provided the structural system is properly protected with a liner.

1.3 Organization

In the following chapter an overview of pipe joining is introduced and the previous relevant research is discussed. In chapter 3 the proposed design and the manufacturing process are presented. The analysis for design of the proposed joint is covered in chapters 4 and 5. Chapter 6 includes a numerical comparison between the simplified analysis and the finite element method. Design examples are presented in chapter 7. In chapter 8 a detailed finite element analysis is conducted for the proposed joint, including leakage analysis using contact finite element analysis. Finally, the conclusions of this study and recommendations for future work are summarized in chapter 9.

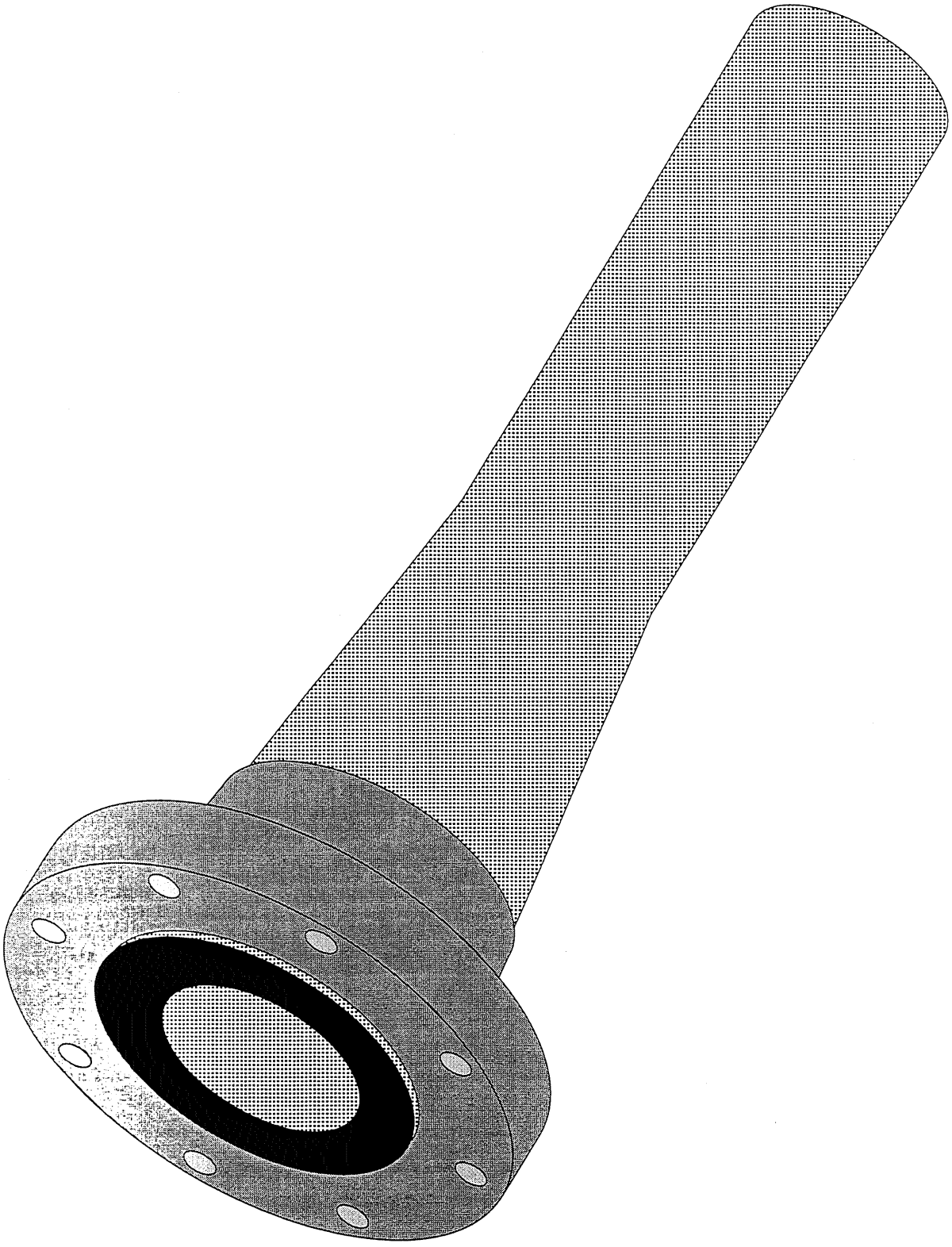

Figure 1.1: Modified Stub Flange.

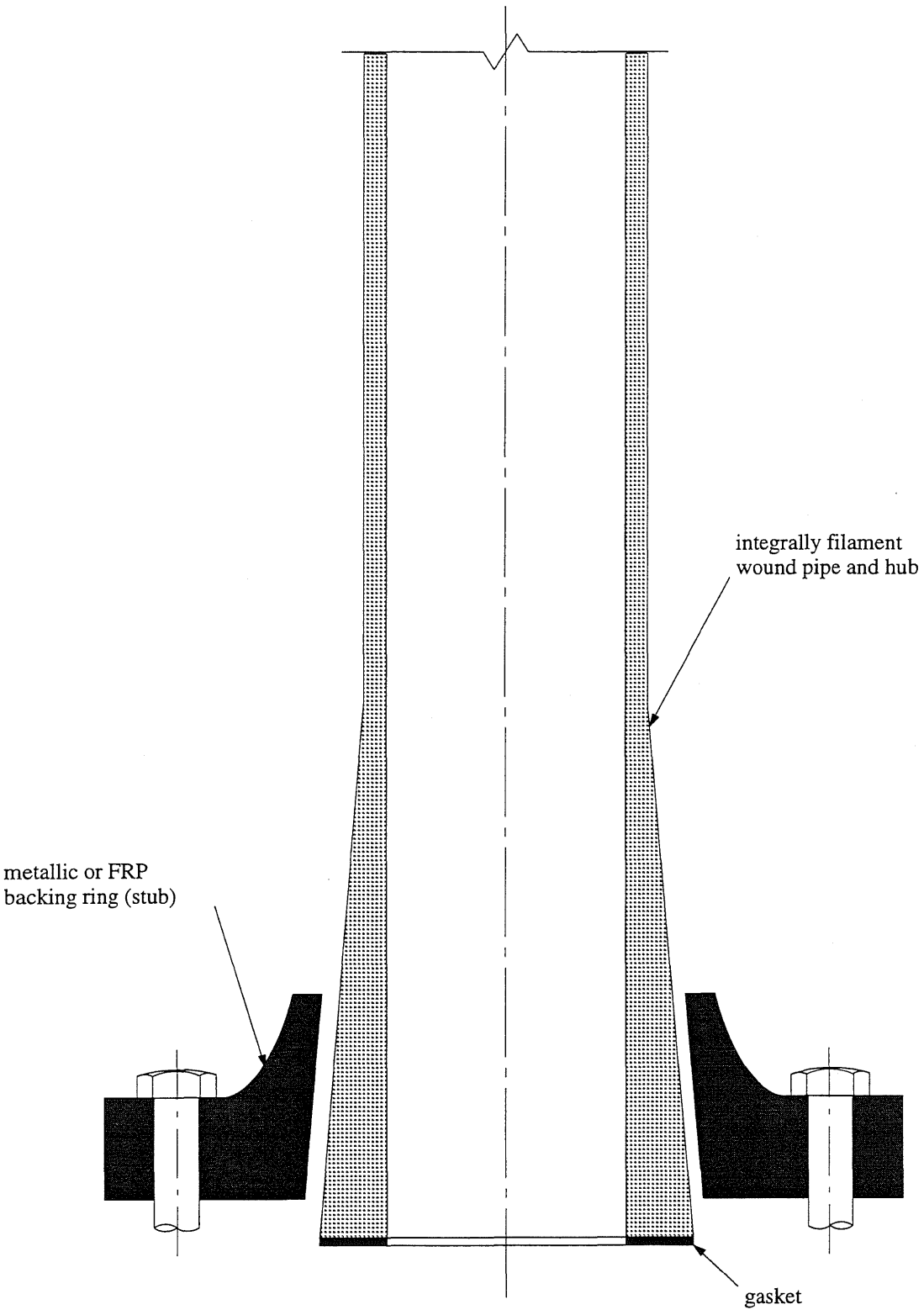

Figure 1.2: Cross-Section of Modified Stub Flange.

Chapter 2

A Survey of Previous Work

In this chapter we give an overview of pipe joining and survey the previous relevant work in both metallic and composite joints. As stated earlier, composite systems are designed using criteria for their metallic counterparts in conjunction with high factors of safety and occasionally experimental testing. For this reason, we will present the previous work done on metallic joints first, followed by previous composite joint work. In the chapters that follow we will point out the relevance of these works to the research presented in this report.

2.1 Problem Definition

Ideally, piping systems would be designed without joints, eliminating a source of added complexity and weakness. However, due to technical or commercial reasons this is seldom possible. Some of these reasons include: size restrictions during manufacturing and transportation, requirements for disassembly for inspection or repair, and the inclusion of valves or pumps, all of which may be called for in the component design. The main purpose of a pipe joint is to convey a liquid or gas from one pipe to another pipe or fitting without leakage. Due to the discontinuity at the joint, there is a complex stress distribution near and in the joining feature. An objective of a given joint geometry will be to minimize stress concentrations arising in order to enhance structural performance. Therefore, an acceptable joint design criteria must (1) ensure stress levels in the joint do not exceed the strength of the joining material and (2) ensure the residual gasket load is sufficient to maintain the joint leak tight.

There are a number of joining methods by which a FRP pipe may be joined. These include butt and strap, adhesive, threaded, bell and spigot and flanged joints. Butt and strap and

adhesive joints are used for permanent joining applications, e.g., in the case where the joints are needed due to transportation or manufacturing limitations. In other cases, a detachable joint is necessary to allow access for repairs and maintenance. Flanged joints are the most commonly used in detachable connections because of the ease and speed of repeated assembly and disassembly. Also, these flanges connect to valves, pumps and any other steel flanges to which the line is joined.

Regardless of the material composition, flanged joint design consists of three fundamental problems, each one separate but related to the others. First, we need to determine the gasket for the service conditions. Second, we determine the bolting required to hold the joint leak tight. Third, we determine the proper flange geometry to transmit the load from the bolts to the gasket without over-stressing the flange material. Although the first two problems seem independent of the joint material composition, certain aspects of the problems depend on the joining material. The last problem is completely different for composite and metallic joints. This depends on the materials from which the joint is manufactured. In chapter 4, we will address all three problems as they relate to our proposed joint.

2.2 Metallic Joints

2.2.1 Joint Types

Although metallic pipe joints have been used for hundreds of years (first lead, then cast iron, and more recently steel), it was not until the first half of this century that most of the work towards a methodical design procedure was conceived. Of the many pipe joint geometries suggested over the years, the one most widely used today is the bolted flanged joint. Metallic bolted flanged joint geometries can be divided into two types, integral and loose flange type, figure 2.1. There are two varieties of the integral flange geometry, raised face and flat face flanges, figure 2.2. The former is typically used for high pressure applications and the later for low pressures. Flat face flanges can be further subdivided into two categories, flanges with and without a hub. The hubless flat face flanges are normally used in conjunction with full face or O-ring gaskets, whereas hubbed flat face flanges are used in conjunction with ring gaskets (gasket outer diameter enclosed by the bolt holes). Flat face flanges with full face gaskets require the greatest bolt load to maintain them sealed. This is due to the greater contact area, which requires more pressure to deform the gasket into the irregularities on the flange face.

With flat face flanges with ring gaskets, as well as raised face flanges, no flange contact occurs outside the bolt circle, which leads to flange rotation when the joint is bolted. This pro-

duces high bending (i.e., axial) stresses in the hub and flange where the two intersect. These axial stresses in the pipe, close to the pipe-flange interface, are much higher for hubless joints than for hubbed ones and reduce down to the same level away from the interface. In hubbed joints these stresses can easily be accommodated, whereas in hubless joints they can reach undesirably high levels. The lower axial stress in the hubbed geometry is because of the additional material in the hub resisting rotation. The same resistance can be accomplished by increasing the thickness of the flange in the hubless joint.

2.2.2 Design Procedures

The relevant American Society of Mechanical Engineers (ASME) Boiler and Pressure Vessel (BPV) code [4] includes design rules for raised face flanged and ring gasketed joints in Appendix 2 and for O-ring gasketed joints in Appendix Y. Full face gasketed joints are proportioned either by Appendix 2 calculations, modified to account for the additional gasket material outside of the bolt circle [1], or by the design method proposed by Blach et al. [13]. Loose type flanges are also proportioned using Appendix 2.

According to the ASME BPV code, there are two acceptable design procedures for bolted flanged joints: standard rated flanges and flange design calculations. The former is the easiest, since the design consists of choosing a flange that has been dimensionally standardized for specific pressure-temperature ratings. There are a number of these standards at the engineer's disposal, mainly company and American National Standards Institute (ANSI) [2] standards. When a flange is selected from one of these standards (taking into account proper factors of safety), no additional calculations are required. The code strongly recommends the use of these standard designs whenever possible. They have proved their safety, and a standard design is usually less expensive than a specialized one.

Given the pipe inside diameter, its thickness and design pressure and temperature, the basic steps in flange design calculations are as follows:

1. Select the gasket (material, type and dimensions) and flange facing type.
2. Calculate loads for both gasket seating (bolt load acting on the flange, figure 2.3) and operating (internal pressure and bolt load acting) conditions from gasket factors.
3. Determine bolting material and number of bolts to be used.
4. Establish flange dimensions, hub proportions, flange width and thickness (usually starting from some standard flange values).

5. Using loads and dimensions, calculate moments for both gasket seating and operating conditions.

6. Find flange stresses and check them against allowable stress for the flange material.

These steps are part of the three aforementioned fundamental joint design problems. The first two steps address the gasket problem, the third step the bolting problem, and the last three steps the flange problem. The solution to this third problem is iterative due to the large number of variables; it entails proportioning a joint geometry (based on experience or one of the many standards), then checking the axial stress at the hub-ring and shell-hub interfaces and the radial and hoop stresses in the ring, so the allowable stress for the material is not exceeded.

The designer chooses a gasket material and type based on the pressure, temperature and chemical resistance to the media being sealed and length of service desired. The purpose of a gasket is to create and maintain a seal between two separable flanges. Gaskets must compensate for nonuniform flange loadings and conform to the flange surface irregularities.

The initial pre-stress in the gasket is provided by the pre-load in the bolts, this is commonly known as the seating condition. In this state, the gasket deforms filling the irregularities on the flange face, insuring full contact over its entire surface. The internal pressure is then applied and the gasket pre-stress decreases; this is commonly known as the operating condition. The code requires the analysis of two distinct load systems, gasket seating and operating loading cases (as defined above). The two load cases are computed using two distinct factors: the yield factor y, which is defined as the minimum gasket stress to cause the gasket material to deform into the flange face irregularities, and the m factor defined as the ratio of minimum gasket stress needed to hold a seal under internal pressure to internal pressure. These factors depend on the gasket material properties and its sealing performance. A list of these factors, which are obtained from a combination of industrial experience and experiments, is given in the ASME code for different gaskets.

Two design bolt loads are computed using these factors and the bolting is proportioned using the greatest of the two loads. Once the bolt load is known, the bolting system can be designed: bolt type, number of bolts, bolt circle and bolt spacing.

The flange can also be proportioned once the bolt load is known using the design calculations found in the code. These calculations are based on work done a half a century ago [51] and were incorporated into the ASME code in 1940. This design procedure, best known as the Taylor Forge method, is based on linear elastic plate and shell theories. As shown in figure 2.4,

the joint is subdivided into three axisymmetric structural components: shell, hub (variable thickness shell) and ring (circular plate). Other major assumptions include the fact that internal pressure and bolt hole effects are not taken into consideration and that the bolt load is applied as a ring load along the outer flange diameter. The relative simplicity of the Taylor Forge method has made it the most widely used calculation method in flange design codes around the world.

2.3 Composite Joints

FRP bolted joints are commonly made with stub flanges and flat face flanges with full face gaskets, which are known as a full faced flanges, figure 2.5. FRP bolted pipe joints are widely used in the piping industry; however, as stated earlier, a lack of standardization and design rules presently exists. Some FRP joint investigation has been done in the past, but no dependable design criteria have been proposed. Instead, metallic joint design calculations in conjunction with high factors of safety are used in their design. Previous investigations have generally focused on FRP joints fabricated by hand lay-up or molding (injection, press or contact) techniques, which are either fabricated directly or bonded onto a previously manufactured pipe, figure 2.6. A fairly long hub is required in either hand lay-up or molded flanges to transfer the shear stresses through the bond.

FRP bolted joints present more difficulties than their metallic counterparts, not only in that the material properties are more complex, but also the bolting technique must be modified. In metallic flanges, the bolt holes present only a minor material discontinuity problem. Whereas in FRP flanges, if bolt holes are drilled the strength of the joint may be compromised, particularly in filament wound joints. One solution to this problem would be to wind the holes, which presents a major manufacturing problem, since current filament winding technology is incompatible with this type of non-axisymmetry. However, for current flange manufacturing techniques (hand lay-up and injection molding), the holes can be incorporated in the flange during the manufacturing process. Another remedy that seems to be very successful in industry is the stub flange, figure 2.5. In this case, metallic backing rings are used to clamp the two flanges together.

2.3.1 Design Codes

The first FRP joint standards appeared on a voluntary product standard in 1969, PS 15-69 [42]. This standard only covers contact molded flanges and advises to keep their use to a minimum with the butt-strap joint recommended as the standard pipe joining technique. This standard recommends that flanges 2 – 24 inches in diameter be proportioned following the

ANSI standard B16.5 [2] for class 150 lb steel flanges, and flanges 30 – 42 inches in diameter following ANSI standard B16.1 for cast iron flanges. It also provides tables with minimum flange thickness values. The flange thickness values are based on a factor of safety of eight for a flexural strength of 20,000 psi. An absolute minimum flange thickness of 3/4 inches, regardless of pipe size or pressure rating, is recommended. The hub length is specified as at least four times the flange thickness and the hub thickness at least one half the flange thickness. Manufacturing tolerances are also specified. The specifications for bolting call for metal washers under all nut and bolt heads. Gaskets, no thinner than 1/8 inches and durometer Shore A or Shore A2 hardness of 40 to 70 degrees are recommended. Durometer reading is a measure of rubber hardness, the magnitude of which is derived from the depth of penetration of a specific indentor into a specimen under specified conditions. It is measure on arbitrary scales (Shore A, Shore A2, etc.) and covers a range of 10 to 100 degrees; 10° represents a material showing no measurable resistance to indentation, and 100° represents a material showing no measurable indentation. This procedure of hardness testing can be found in ASTM D2240 [8].

More recently, ASTM has added standard specifications for machine made [7] and contact molded [6] fiberglass (glass fiber reinforced thermosetting resin) flanges. For these standards, ANSI standard flange sizes are also specified as in the case of PS 15-69 [42]. Basically, the ASTM standard is an updated version of the PS 15-69 standard, the main difference being proof testing. ASTM standards make it clear that the specifications are based on flange performance and do not cover design. The performance requirements are: test pressure of at least 1.5 times the design pressure without leakage for sealing and test pressure of at least four times the design pressure over a period of 60 seconds for rupture strength. Also, the flange material should be able to resist a bolt torque two times that recommended by the manufacturer without visible signs of damage for contact molded flanges, and 1.5 times for any other flange construction. There are no gasket or bolting specifications given, rather it refers the designer to the flange manufacturer's recommendation. In these standards, it is noted that flanges with identical classification from different manufacturers may not be interchangeable due to nonstandardization of piping systems.

ASME design rules for FRP pressure vessels conform to ASME code section X [5]. This section qualifies vessel design by two methods: (1) *Class I* design – the design is qualified through the destructive test of a prototype, and (2) *Class II* design – mandatory design rules and acceptance testing by nondestructive methods.

For *Class I* joint design, one or more full-scale prototype joints should burst at a pressure at least six times the design pressure after having been submitted to 100,000 cycles of pressure

ranging from atmospheric to design pressure at a fluid temperature no less than 150 °*C* throughout the entire test. Only for critical and very large projects can a designer justify the cost of these stringent requirements.

The mandatory design rules for *Class II* flange design are based on the same procedures as their metallic counterparts: standard rated flanges and flange design calculations. Standard rated flange design is based on the same ANSI flanges as PS 15-69 [42] standards. For FRP flange design calculations, not only are the ASME section X code calculations totally based on those for metallic joints (Taylor Forge method), but even the material properties used in the calculations are those used for steel. The only point in the design where the material properties of the FRP joint come into play is in the allowable stresses. According to the code, the flange thickness shall be large enough so the allowable stress does not exceed 0.001 times the lower of the longitudinal or transverse design modulus. This is a maximum strain based design, which limits the absolute value of membrane strain in any direction at each point of the vessel to no more than 0.001. In the design of FRP flanges using these calculations there is an additional stress check, namely the radial stress at the bolt circle. A further restriction on *Class II* design is that the vessels shall be limited to a maximum pressure of 75 psi and maximum inside diameter of 96 inches.

2.3.2 Composite Pipe Joint Research

Of the many flanged joining techniques currently used in FRP piping, we found only one that is integrally manufactured with the pipe in the literature [39]. The manufacturing process is covered in great detail in the paper, but no design calculations are included. The author does state that some finite element analysis was carried out but no details on the results are mentioned. However, this joint apparently did not progress beyond the planning stage.

Press moulded flanges are also machine made [26]. This makes them attractive in pipe joining because of the speed and ease of being duplicated with consistency. However, since the flanges are bonded to the pipe, the joints have a much lower strength than the pipes. A number of tests were conducted to destruction, in most cases failure was observed in the hub section. These tests were conducted on flanges manufactured to the dimensions outlined in PS 15-69 [42] for pipe diameters of two and eight inches. To improve the performance of the joint, the authors increased the flange thickness by a fourth and ran more tests to destruction. However, they found it "impossible to retain" the full face gaskets at higher pressures, which lead to the trial of O-ring gaskets. Also, the authors found that flanges with drilled bolt holes performed better, in terms of strength, than those with molded holes. This might be as a result of potential

resin rich pockets near the holes. The authors also recommend the use of filament wound pipes over contact molded pipes. They also conducted a survey of approximately 30,000 flanges designed following their guidelines and found "remarkably" few failures. Most of these failures were as a result of faulty techniques in the application of the flange or the installation of the system. Some of these faulty techniques include: insufficient surface preparation of the pipe or flange, uneven or insufficient application of adhesive, use of incorrect adhesive systems, contamination of surface to be bonded, incorrect mixing of adhesive, and joints carried out in unsuitable temperatures and environmental conditions. Also, other common failures included overstressing of joints during installation due to: poor alignment, use of partial face gaskets, improper selections and/or position of expansion joints, and bolt over-torquing.

Paliwal et al. [43] conducted an analytical analysis of stub flanges, figure 2.5, for the case when the stub (backing ring) is made from a composite material. They used Lekhnitskii anisotropic circular plate theory for the analysis of an annular plate, using boundary and loading conditions similar to the RING portion in figure 2.4. They did not analyze the flange, however.

Bustillos and Craigie [19] present finite element analysis of three different stub FRP flange designs. They give the finite element mesh, the deformed shape and stress contours for all three designs. The results conform to a factor of safety of ten.

Muscati and Blomfield [40] conducted burst test on FRP pipes with flanged joints. They carried out these tests to check the integrity of a pipeline after higher failure rates than anticipated were observed. The flanges are of the stub type with aluminum backing rings and sealed by rubber gaskets. The construction of the flange is similar to the top left flange in figure 2.6. In two out of seven test, it was not possible to burst the specimen due to the development of a large leak. The results of the test show that the flanges have much lower strength than the pipes, and in all cases, the burst pressure was lower than the six times the design pressure specified by the design standard used. They attributed this lower strength in the flanges to the difficulties in construction resulting in inadequate reinforcement placement.

Muscati and Blomfield [41] later conducted additional burst tests on flanges extracted from the pipeline and attempted to correlate these test results to two theoretical stress models. These models entail a simple analytical solution for the pipe based on membrane shell theory and finite element stress analysis. The results of the simple analytical analysis over predicted the failure pressure for all but four cases out of fourteen test specimens. In some cases the over prediction was by as much as 200%, but in two cases the results of the analytical model were within 10% of the burst pressure. It is interesting to note that in these two cases the failure oc-

curred in the pipe away from the joint, which explains the agreement between the test and analytical model. For the finite element analysis, their investigation fell rather short; one reason is that at the time of their investigation the finite element analysis package they used did not support anisotropic analysis. However, they attempted the analysis by decoupling "axial" degrees of freedom between material layers in an effort to mimic anisotropy. The authors do not provide comparisons of the finite element analysis results and the burst test. They only state that finite element analysis results validate the results of the analytical model when compared to the two specimens that fail in the pipe section. Their major conclusion from this study is that both the analytical and finite element analysis models tend to over predict the strength of the joint. They attributed this, again, to lower strength in the flanges due to the difficulties in construction resulting in inadequate reinforcement placement.

Blach and Hoa [14], in the first of a series of publications on the subject of full-face FRP flanged joints (see figure 2.5), propose the use of steel flange design methods for the design of full-face FRP flanges. They claim that two design methods can be used safely with full-face FRP flanges provided certain safeguards concerning over-bolting are observed. The two methods are the Taylor Forge method [1] and the method of Blach et al. [13]. They also attempted to correlate data from strain gage measurements on full-face FRP flanges with results of a three-dimensional orthotropic finite element analysis. The authors claim that the results from the finite element analysis and both of the metallic design methods appear to agree well with the experimental results. The authors also discuss some problems inherent to FRP flanges. Uneven curing of the resin in hand lay-up flanges can cause a certain amount of convex distortion (pull-back), figure 2.7. Pull-back must be straightened to ensure contact over the entire gasket face. If the pull-back is straightened by bolt load alone, there will be over stress at the pipe-flange interface. Further details on the effects of pull-back for flanges in operation and remedies during and after fabrications were later published [15]. Blach continued the discussion of their stress analysis and experimental work in a later publication [16].

Blach and Sun [17] conducted an experimental investigation into the effect of flange width on the strength performance of a full-face FRP flanged joint system. Several tests were conducted on a single specimen. After each bolt-up and pressure test, the flange of the specimen was machined down on the outside diameter to obtain a smaller flange width. The authors also comment on the use of finite element analysis and two metallic flange analysis methods (Taylor Forge method [1] and the method of Blach et al. [13]). However, no quantitative comparisons were made, since results of the experimental or finite element analysis are not included in the paper; only the results of the two metallic flange analysis methods are provided. Blach continued the discussion of his stress analysis method (Blach et al. [13]) and the experimental work

in a later publication [18]. Again, he only made qualitative comparisons between experiment and analysis.

In his dissertation [48], Sun proposed two analytical methods for the stress analysis of full-face FRP flanges. The two analytical methods are based on classical and shear deformation laminated theories. The analytical methods follow the approach that Waters [51] used in the derivation of the Taylor Forge method, accounting for the FRP material properties. The approach consists in analyzing the flange as two separate components (PIPE and RING in figure 2.4) and obtaining the total solution by applying the appropriate boundary and continuity conditions. One method is based on classical laminated theory, transverse shear deformation is neglected; in the second method the RING is modeled using a formulation that accounts for transverse shear deformation, while the classical formulation is used for the shell. His comparisons with finite element analysis are not in good agreement because of the poor finite element mesh used in the analysis. The author conducted quantitative comparisons between his classical laminated results and the experimental results from [17]. He presents no calculations for the transverse shear deformation formulation.

Leon [34] discusses the development of the Pressure Vessel Research Council (PVRC) program on non-metallic piping and fittings. One of the items is the requirement of industry standards for flanged FRP joints. Leon et al. [35] discuss the progress of the PVRC committee and compare international standards for composite piping design, including FRP flanges. Further details are included in a later paper [36]. Other international designs are essentially the same as those found in the United States of America. In this last paper, Leon et al. also include results on the comparison of finite element analysis with some of the design standards, namely the ASME BPV code Sections X [5] design formulas; the ASME code stress predictions were conservative compared to the finite element analysis results.

Matthews et al. [38] conducted a series of experiments on stub and full-face FRP flanges subjected to an internal pressure. The internal pressure was increased until either leakage or fracture of the pipe or flange occured. For the case of stub FRP flanges, a type of failure due to over-bolting (bearing failure, see figure 2.8) was reported. They also studied the strength of the flanges using finite element analysis. In their finite element analysis results, the axial stresses show large peaks at the pipe hub juncture; the authors concluded that the use of a tapered rather than a stepped hub would reduce these peak stresses. For the case with no hub at all, they found that axial stresses were three times higher than those for the hubbed case. The comparison showed that the experimental and finite element analysis results agreed well. They also conducted leakage finite element analysis for two cases: gasket and no gasket between the mating

flanges. Their results show that with a gasket in place a more uniform stress distribution can be achieved.

Godwin et al. [28] investigated the relationship between clamping force and joint sealing for stub and full-face FRP flanged joints. The details of flange construction for the test specimens are those shown on figure 2.6. The authors also report the pull-back effect, figure 2.7, on the hand lay-up flanges. The experiments showed that the bolt load remained constant with increasing pressure up to a point; it then increased until the point when leakage was observed. The normal stress on the gasket was found to be the principle factor affecting the ability of a flanged joint to seal. Leakage behavior can be improved by reducing the width of the gasket; however, for a full-face FRP flange this causes increased bending in the flange which leads to cracking at the flange radius, greatly degrading the strength of the joint. Therefore, the most desirable flange geometry is the stub flange. In addition to the experimental work, axisymmetric finite element analysis was conducted to predict the internal pressure and pressure distribution on the gasket at which leakage occurs. Although tensile normal stresses developed over part of the gasket face, no flange gasket separation was allowed because their finite element analysis code did not support contact formulations.

Graham [27] discusses the manufacture, design and application of contact molded flanges. The author also includes case histories of several installation failures. He also discusses stress analysis based on the Taylor Forge method [1] following the FRP flange requirements of PS 15-69 [42]. He makes recommendations for design and presents a set of very useful tables of flange dimension for pipes 2 – 42 inches in diameter and pressure ratings of 25 to 150 *psi.* He provides guidelines for torquing the bolts in FRP flanges, and includes bolt torque calculations tabulated in tables.

Current state-of-the-art FRP pipe joint design is basically empirical. The majority of the reported research on FRP pipe joining has been focused on transferring the knowledge from metallic designs to FRP design, with the exception of Dr. Sun's research [48], who has pointed FRP joint design in the right direction. The work presented in this report will hopefully advance our understanding of FRP pipe joining in general.

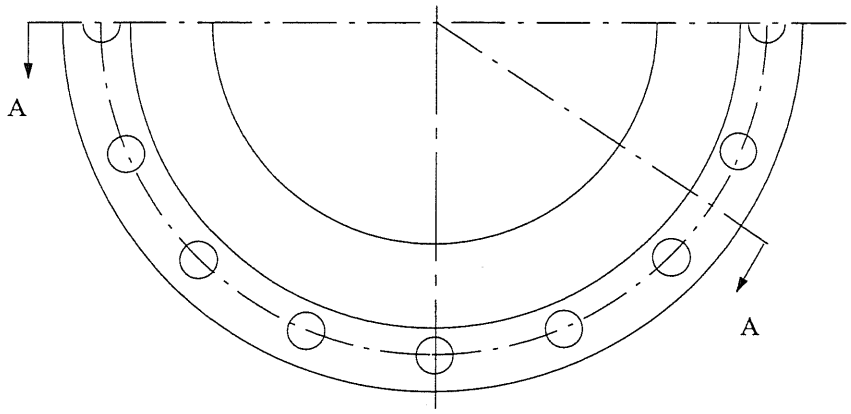

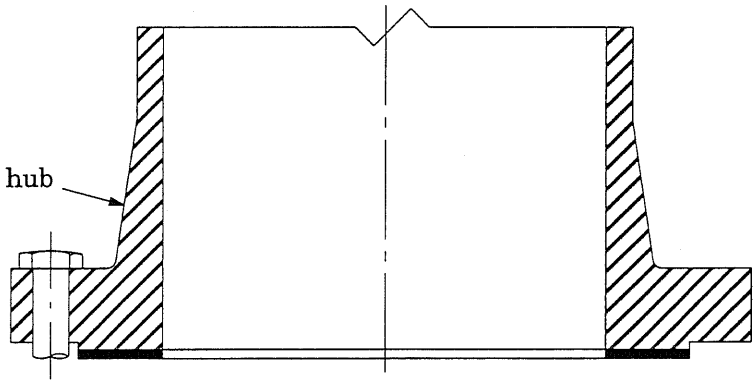

A–A

integral type flange

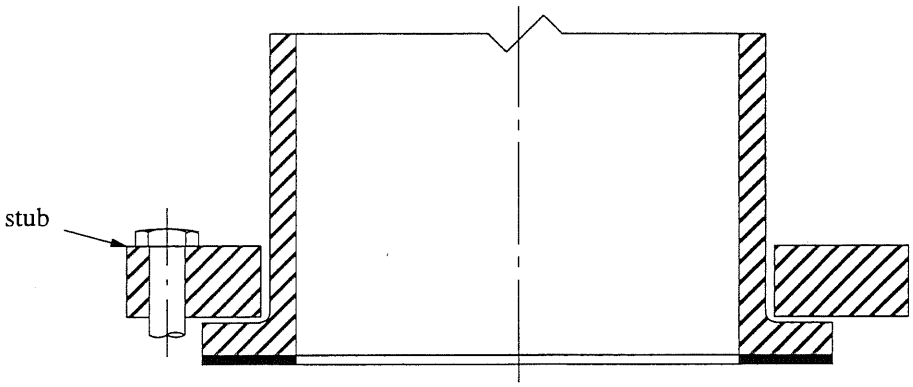

A–A

loose type flange

Figure 2.1: Typical Metallic Flanged Joints.

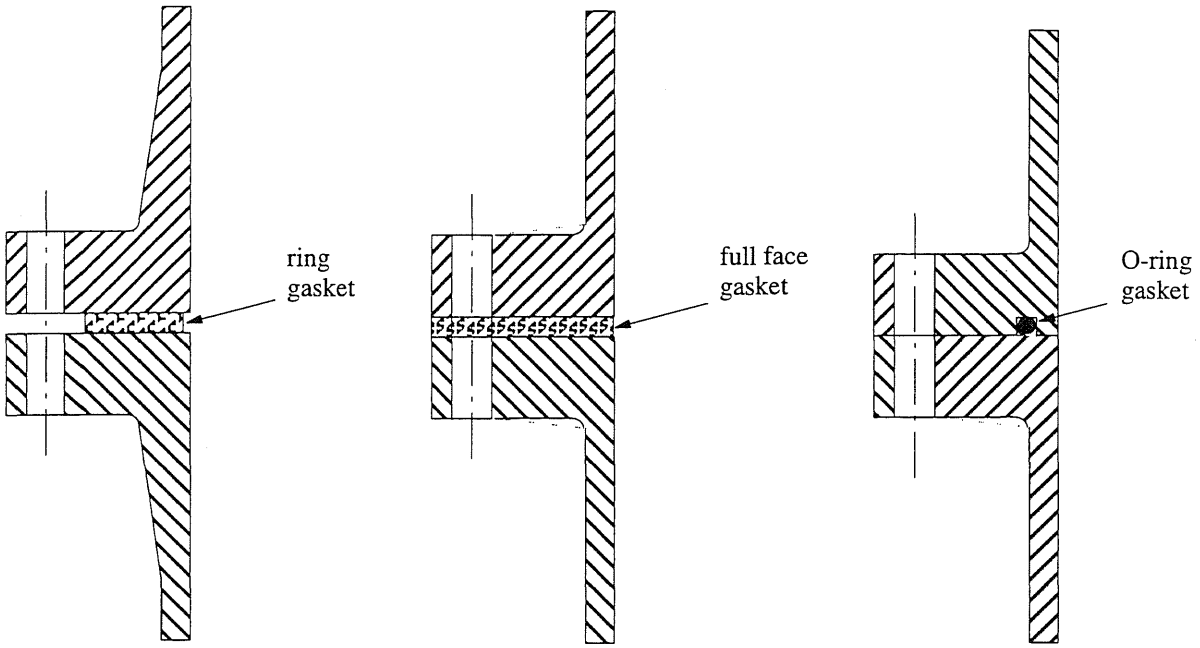

flat faced flanges

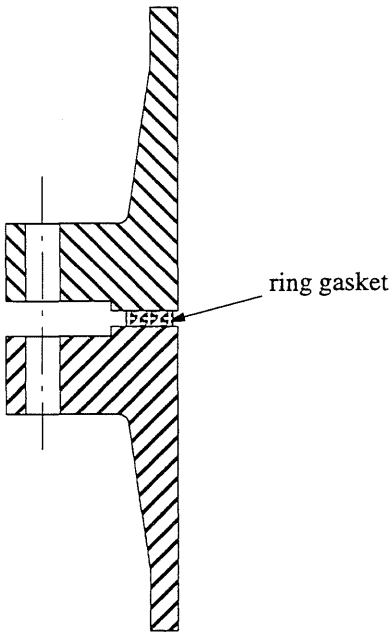

raised faced flange

Figure 2.2: Conventional Metallic Flanged Joints.

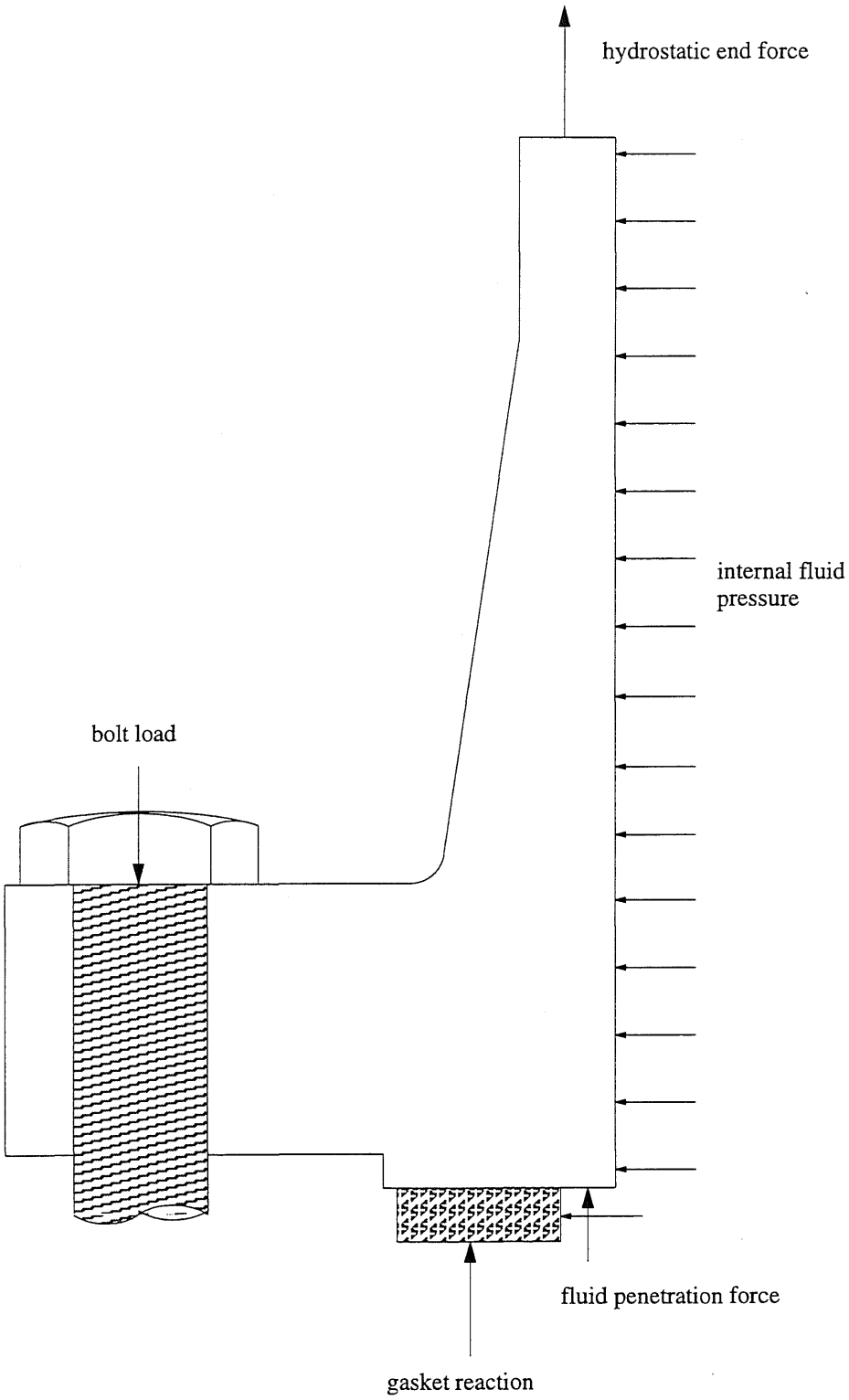

Figure 2.3: Flange Loads.

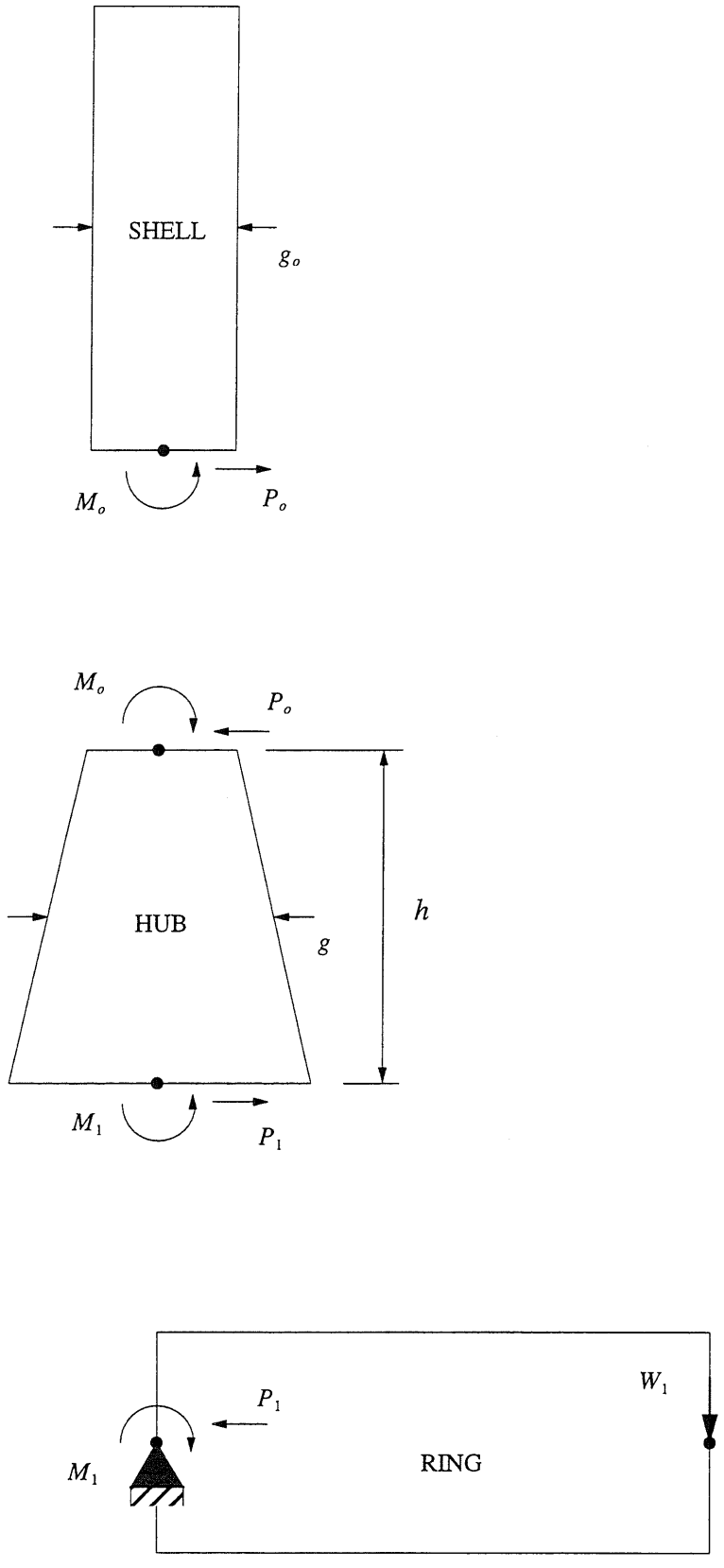

Figure 2.4: Analysis of Forces and Moments in a Joint.

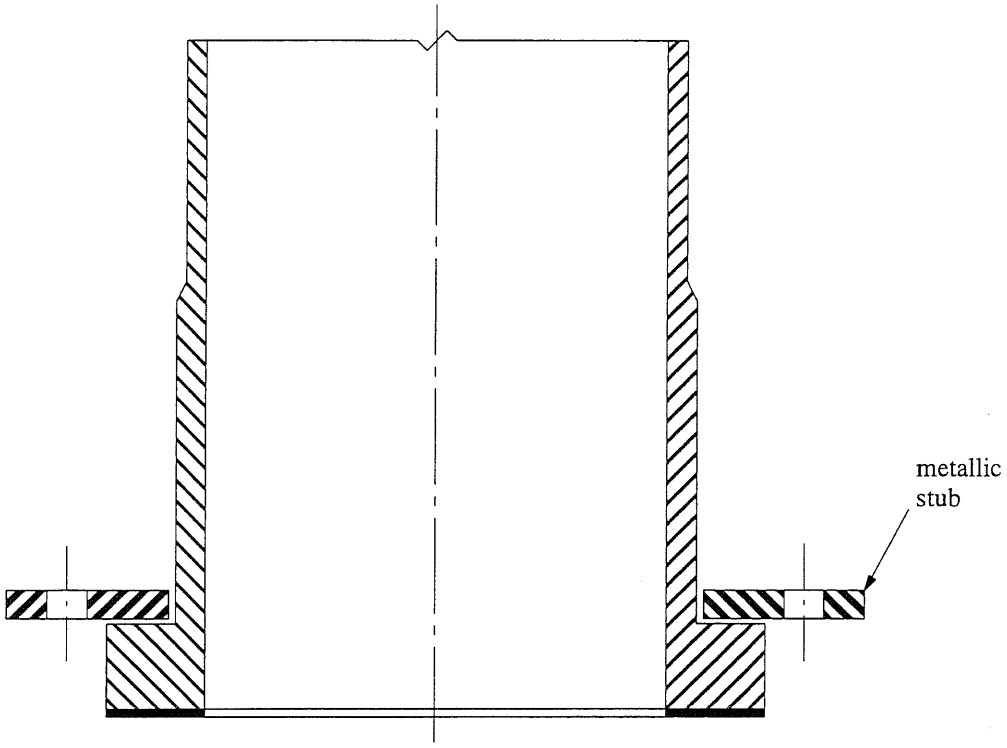

stub flange

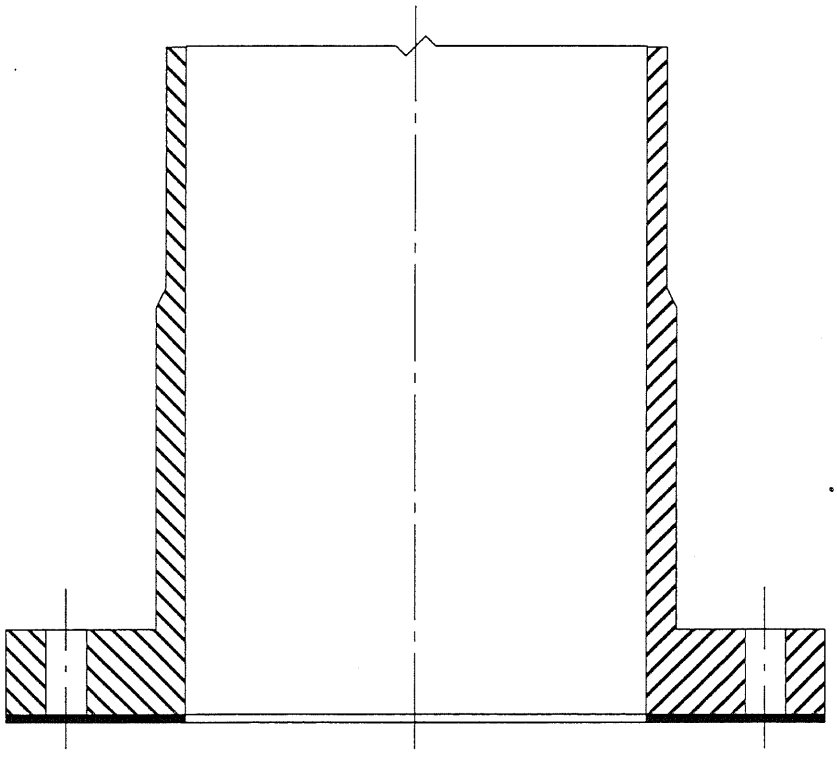

full-faced flange

Figure 2.5: Conventional FRP Flanged Joints.

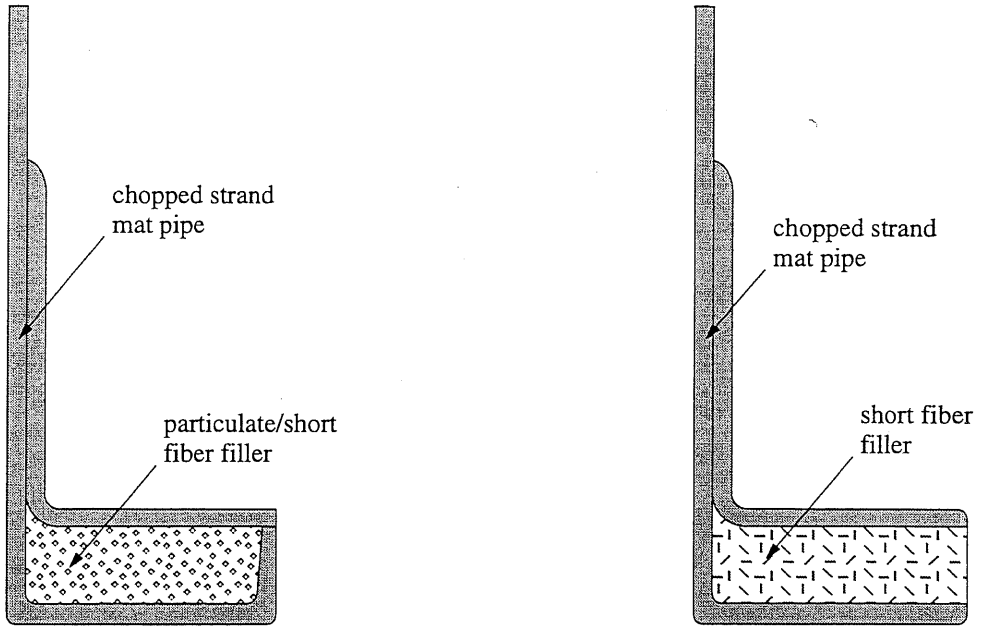

hand lay-up

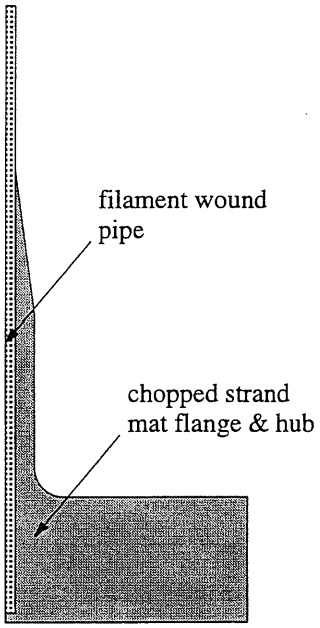

hand lay-up or molded

Figure 2.6: Details of Flange Construction.

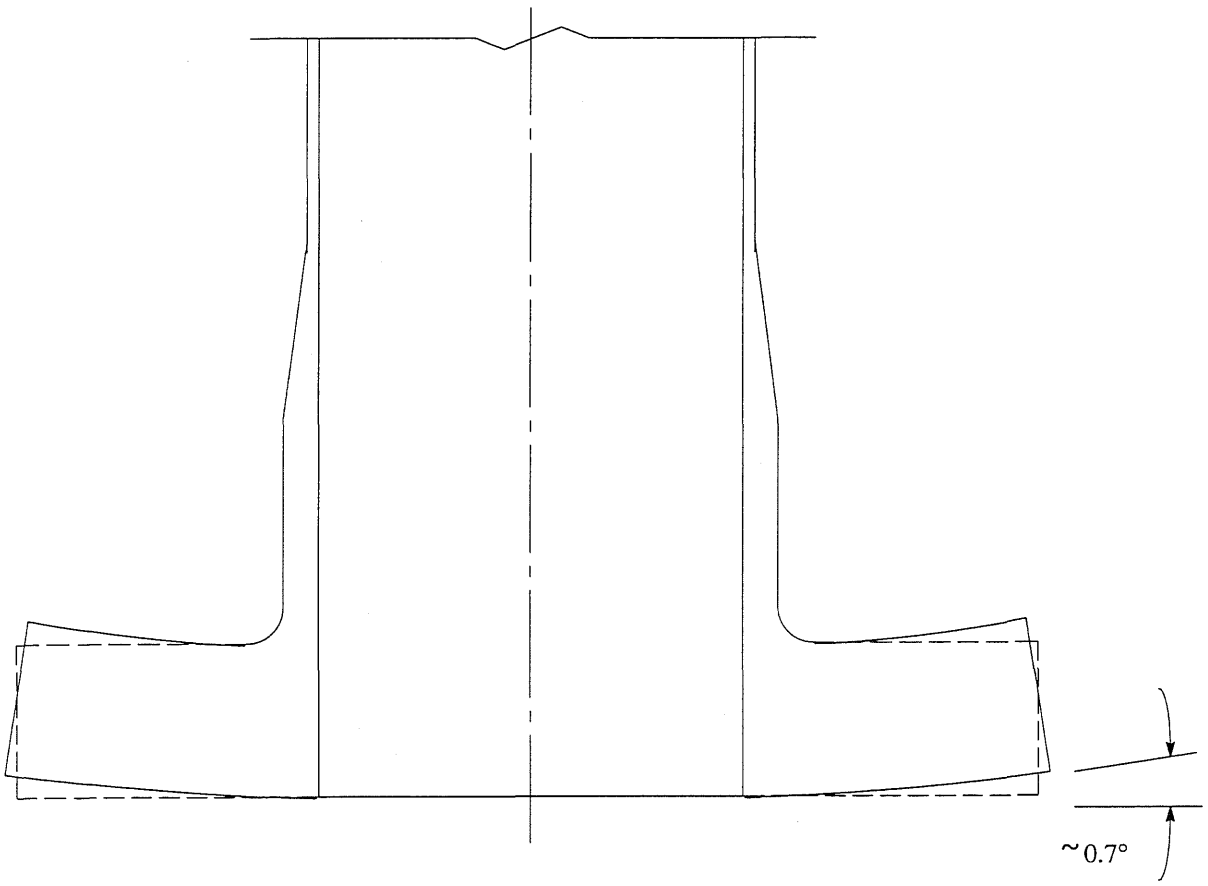

Figure 2.7: Flange Pull-Back

Figure 2.8: Flange Bearing Failure (Matthews et al. [38]).

Chapter 3

Proposed Joint

3.1 Introduction

FRP piping can be produced in any size, free of joints except those required as a result of manufacturing or transportation constraints. The joints will generally be made on site by secondary laminating operations. Therefore, it might seem unnecessary to use such crude and structurally inefficient components as flanges. However, piping includes components such as valves and pumps made of other materials, which are likely to need periodic removal from the system for maintenance. The most common joining technique for these systems is by flanges. In fact, at any point in a FRP system where a demountable joint is needed for service access, a flanged joint is usually employed. FRP flanges are similar to their metallic counterparts because FRP pipes have to be connected to already existing metallic joining systems, typically flanges in valves and pumps.

The primary objective of our study is to develop a new demountable FRP joining technique, hence the focus on flanges. Our focus is on filament winding because this is the most common FRP pipe manufacturing technique. A schematic of the proposed joint components is shown in figure 3.1. Figure 3.2 depicts the filament winding process.

3.2 The Modified Stub Flanged Joint

The proposed FRP joint, which we call the *modified stub flanged joint*, is similar to the current FRP stub flanged joint. The main differences in the modified stub flange joint are the tapered hub, which engages the stub to transfer the bolt load to the gasket, and the manufacturing process.

We chose a stub flange because of the absence of bolt holes in the FRP part of the system and the leakage investigation of Godwin et al. [28]. They concluded that the stub flange performs better than the full-face flange in terms of leakage, the most common joint failure. The latter is a result of the smaller gasket contact area in the stub flange and a more uniform load transfer from the bolts to the gasket via the stiffer metallic stub.

We also used the investigation by Matthews et al. [38] to decide on the tapered hub. Their investigation shows that a tapered rather than a stepped hub is more structurally efficient because of the higher stress concentration in the stepped hub at the pipe-hub juncture.

The current research project addresses other reported problems with the current FRP joining techniques. Some of these problems, which we reviewed in chapter 2, are as follows:

1. Due to the discontinuity at the joint as a result of the current manufacturing process, the joints have much lower strength than the pipes.
2. Uneven curing of the resin causes convex dishing of the flange (pull-back). Pull-back must be straightened to ensure contact over the entire gasket face. If the pull-back is straightened by bolt load alone, there will be over stress at the pipe-flange interface.
3. Faulty construction can be a result of the skill and integrity of the workers. Large voids have been found to be responsible for joint failures in hand-lay up flanges.
4. The bearing stresses from the stub on the flange can crush the material due to bolt over-torquing.

Our joint addresses all four problems: an integral system is employed, since the pipe and hub are filament wound simultaneously, the taper minimizes pull-back, the manufacturing process is machine controlled, and a longer stub length can be specified to spread the bearing stresses more evenly over the hub.

To assemble the joint, the stub is slipped over the end with no hub. In cases where the design calls for a double flanged pipe (flanges on both ends), two pipe-hub sections can be manufactured separately, assembled following the procedure above and then connected by a secondary lamination, such as a butt-and-strap joint. Another possible assembly method for the double flanged pipe is to manufacture the pipe and hubs in one piece and use a split ring which can be bolted together, similar to the end of a piston connecting rod which is attached to the crankshaft in an internal combustion engine.

3.3 The Manufacturing Process

The filament winding process entails passing fibers through a resin bath and then winding them onto a mandrel, see figure 3.2. The dispenser passes backwards and forwards, parallel to the axis of the mandrel as the mandrel spins, thus winding a helical pattern. The speed of the spinning mandrel and the speed of the traveling dispenser determine the winding angle, both speeds are machine controlled. The thickness of each wrap is controlled by varying the winding tension, which leads to variations in resin content since a constant number of fibers are going through the dispenser. In each pass, the fibers are wrapped in adjacent bands so that eventually the entire cylindrical surface is covered. This process is repeated until the desired pipe thickness is obtained. This particular winding process is commonly known as helical.

Even though the filament winding process is a well-established manufacturing technique [47], the proposed joint contains a variable thickness section which may be incompatible with current filament winding machines. We propose a possible alteration to current machines to be able to manufacture this joint. This entails mounting the dispenser on a pivot mechanism, which would be allowed to rotate in a plane parallel to the axis of the mandrel. As shown in figure 3.3, the dispenser rotates, controlling the width of the band. The width is reduced by rotating the dispenser from the horizontal. Since the number of fibers going through the dispenser is not changed, the thickness of the wrap must increase. Therefore, to create the taper hub in the modified stub flanged joint, the dispenser should start to rotate linearly as the hub is wound.

The hub could also be created by varying the winding tension, since this changes the resin content. That is, to create the hub, the winding tension is relaxed linearly as the hub is wound allowing the fibers to soak more resin. However, the strength of the hub is not greatly improved over that of the pipe, since we are only increasing the resin content. Therefore, we recommend creating the taper hub by rotating the dispenser.

One of the major advantages of composites over traditional materials is the designer's ability to tailor the material properties to a specific application. This project is no exception; the winding angle is one of the material parameters we can vary to see the effect in the strength and stiffness of the joint.

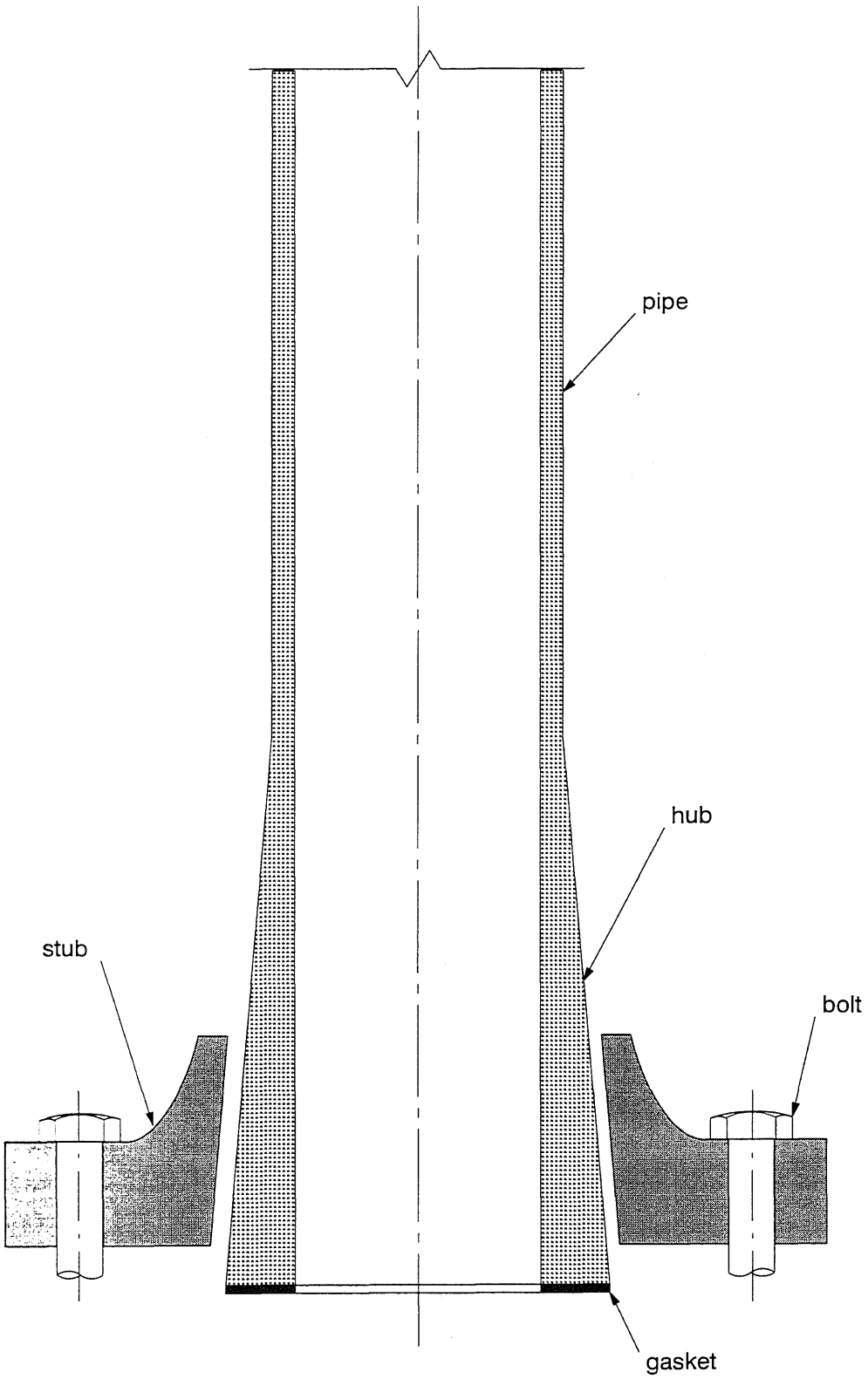

Figure 3.1: Components of Modified Stub Flange.

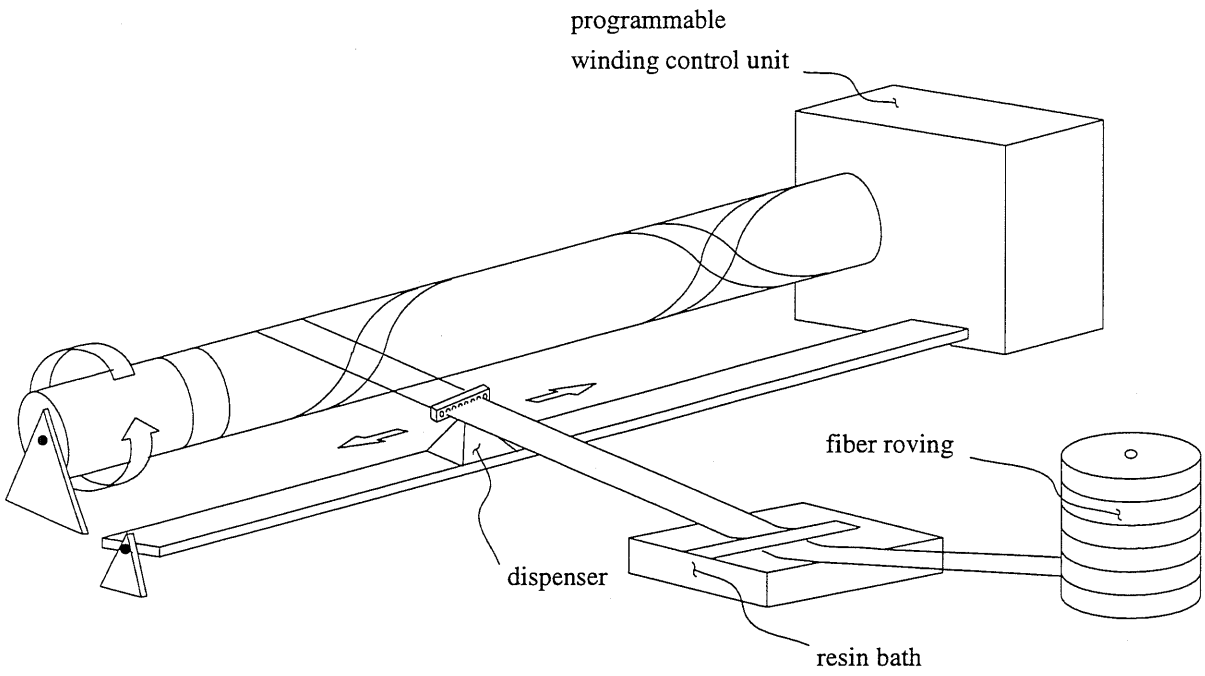

Figure 3.2: Filament Winding Process.

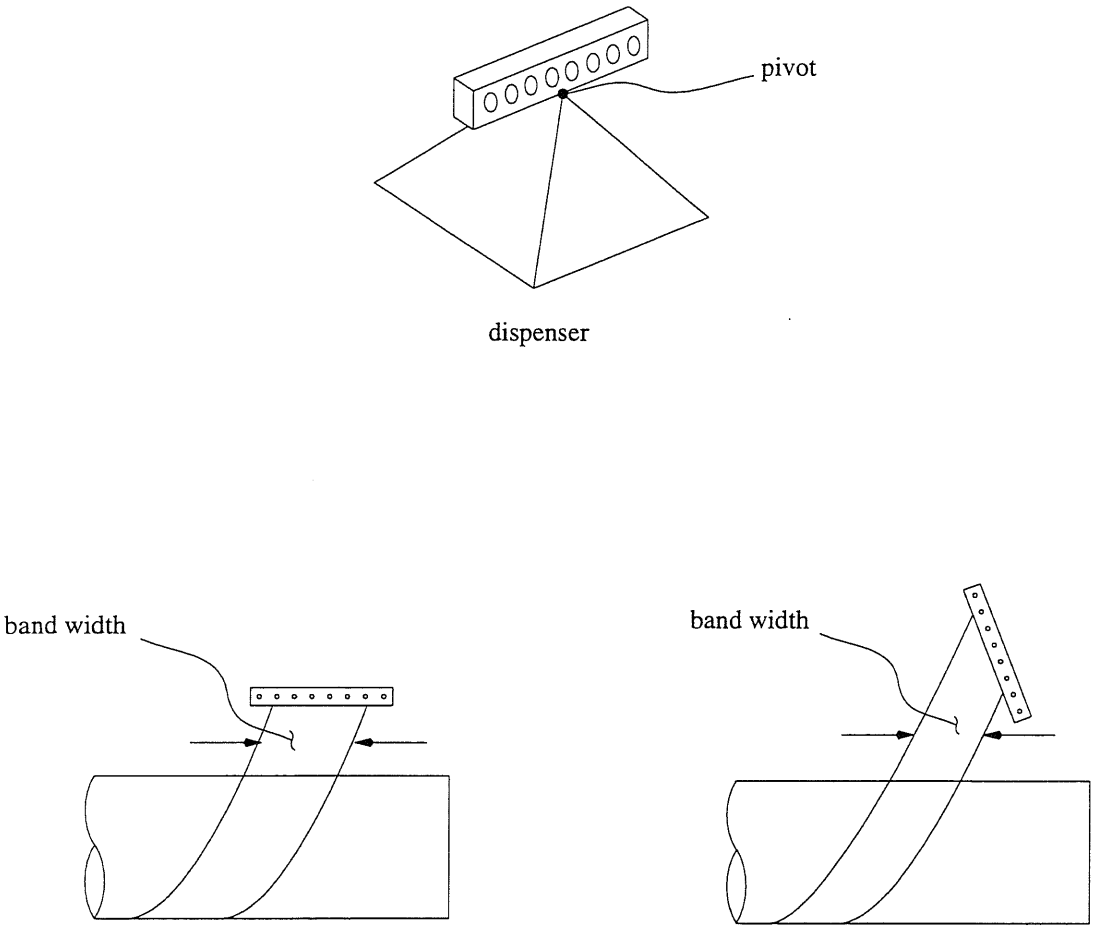

Figure 3.3: Modification to Filament Winding Machine.

Chapter 4

Design Philosophy of Joints

4.1 Introduction

Pipe joints are susceptible to two types of failures regardless of their material composition: material failure and leakage. The problem of leakage depends on the gasket and bolting rather than the joint material properties. However, some joint geometries are more susceptible to leakage than others. To safeguard against these two failures, pipe joint design must address three issues: (1) gasket design, (2) bolting design, and (3) flange design for the stub portion and the hub portion of the flange. We present the procedures involved in the analysis of all three problems in the next sections.

The loading conditions are based on the ASME BPV code section X, FRP flanged joint design specifications [5]. Requirements for materials, workmanship, performance and dimensions conform with ASTM D 4024 standard specification for machine made fiberglass (glass-fiber-reinforced thermosetting resin) flanges [7] and voluntary product standard PS 15-69 [42].

4.2 Gasket Design

Rubber gaskets are usually used to seal FRP joints in order to limit the bolt force required to conform the gasket to the mating FRP surfaces. Soft gaskets, such as those made from rubber, require a low unit compression to keep them leak tight. Rubber gasket specifications are covered in ASTM D 1330 standard [9]. Another reason for using a soft gasket is that if the gasket material is harder than the FRP material, disintegration of the mating surfaces can render the joint useless. The ASTM D 4024 standard does not cover guidelines for selecting a gasket for a specific

application, rather it refers the designer to the flange manufacturer's recommendation. However, PS 15-69 voluntary product standard [42] recommends a gasketing material with durometer shore A or shore A2 hardness of 40 to 70 degrees, 70 degrees being harder than 40 degrees. This standard, although originally intended for contact molded flanges, is widely used for the design of other types of FRP flanges. The durometer shore measure of hardness is based on a durometer reading; the details of this method can be found in ASTM D 2240 Rubber Properties – Durometer Hardness [8]. The Shore scale is arbitrary and covers a range of 10 to 100 degrees. There is no relation between this measure of hardness and engineering properties.

For design calculations we use the ASME code guidelines, which are based on two gasket constants, the m and y factors. The yield factor y is defined as the minimum gasket stress required to cause the gasket material to deform into the flange face irregularities. The m factor is defined as the ratio of minimum gasket stress needed to hold a seal under internal pressure to internal pressure. These factors are used to determine the bolt load to be applied for an effective seal. Also, the thickness of the gasket should be kept to a minimum to minimize the possibility of gasket blow out by internal pressure. Other general aspects of gasket design can be found in [24].

As the system is pressurized, the hydrostatic end force causes the hub to rotate, relieving some of the gasket pre-stress. At the point where the increasing internal pressure and the decreasing gasket pre-stress become equal, separation of the flange and gasket occurs and fluid penetrates. As the internal pressure continues to increase, the contact area recedes toward the outer diameter of the gasket. The purpose of the gasket is to maintain the joint leak tight by providing enough resiliency to ensure that the gasket pre-stress always exceeds the internal pressure. We will discuss this problem further in chapter 8.

The initial gasket pre-stress is provided by the pre-load in the bolts, this is commonly known as the seating condition, figure 4.1. In this state, the gasket deforms filling the irregularities on the flange face, insuring full contact over its entire surface. The internal pressure is then applied and the gasket pre-stress decreases. This is commonly known as the operating condition, figure 4.1. The ASME code specifies two distinct loading conditions for analysis based on the two gasket parameters y and m. These factors depend on the gasket material properties and its sealing performance. A list of values for these factors, which are obtained from a combination of industrial experience and experiments, is given in the ASME code for different gaskets.

We compute two bolt loads from vertical equilibrium in figure 4.1 for the two loading conditions as follows. For the seating condition the minimum required bolt load is

$$W_{m2} = H_G^s, \tag{4.1}$$

where H_G^s is the gasket seating load, i.e.,

$$H_G^s = g_1 \pi G y, \tag{4.2}$$

g_1 is the hub thickness at its large end, G is the location of the gasket stress resultant which we assume to be the mean diameter of the gasket contact face, i.e.,

$$G = B + g_1, \tag{4.3}$$

and B is the pipe inside diameter (here we assume that the entire width of the gasket is in contact). For the operating condition the minimum required bolt load is

$$W_{m1} = H_D + H_T + H_G^o, \tag{4.4}$$

where, H_D is the hydrostatic end load, i.e.,

$$H_D = \frac{\pi}{4} p B^2, \tag{4.5}$$

H_T is the fluid penetration load, i.e.,

$$H_T = \frac{\pi}{4} p (G^2 - B^2), \tag{4.6}$$

H_G^o is the gasket reaction for the operating condition, i.e.,

$$H_G^o = 2\pi b G m p, \tag{4.7}$$

p is the internal pressure, and b is the effective gasket width, defined in the ASME code as half the gasket width, i.e., $b = g_1/2$. That is, fluid penetration is assumed up to the middle of the gasket. Also, we assume that the diameter of the gasket stress resultant, G, remains unchanged after pressurization. The points at which the gasket resultants, G (for seating and operating conditions), are assumed to act and the effective gasket width, b, are not exact, but they are simple to calculate and are sufficiently accurate for most purposes. The 2 in equation (4.7) is an additional safety factor. Also, notice that in the analysis the gasket contact pressure is assumed uniform over the entire gasket contact surface, equations (4.2) and (4.7).

This formulation has received criticism over the years; the main complaint is that the computed bolt load is too low to keep the joint leak tight. However, the problem lies in the field operation. Bolt tightening at assembly is done one bolt at a time, which leads to elastic interac-

tion between bolts; i.e., after tightening the first bolt, tightening the rest of the bolts will affect the pre-loads in the previously tightened bolts, in fact bolt pre-load decreases. Even under controlled conditions in the laboratory, getting a uniform pre-load in all the bolts has proven to be difficult [11]. A uniform pre-load produces a nearly uniform compression on the gasket along the entire circumference of the joint. Bickford [11] states that bolt elastic interaction is one of the reasons why joints have always been overdesigned to function properly. The two most successful ways to get a uniform pre-load in all the bolts are: (1) apply the total torque in multiple equal increments and (2) simultaneous tightening of all bolts. As many as ten increments are needed to establish a uniform pre-load, in the field it is usually done in one increment. This is a serious problem. Many industries simultaneously tighten all bolts, e.g., heads in car engines. Bolting is covered in detail by Bickford [11]. In our investigation, as stated earlier, we will assume that the bolt load is transferred uniformly over the circumference of the gasket.

4.3 Bolt Design

The bolting is proportioned using the two loads computed in equations (4.1) and (4.3). The following criterion is used to determine the total minimum required bolt area to prevent leakage:

$$A_m = \max\left(\frac{W_{m1}}{S_b}, \frac{W_{m2}}{S_a}\right) \tag{4.8}$$

where S_a is the allowable bolt stress at ambient temperature and S_b is the allowable bolt stress at design temperature. These allowable bolt stresses can be found in the code for different materials [4]. Once the minimum required bolt area is known, the bolting system can be designed: bolt type, number of bolts, bolt circle C in figure 4.1 and bolt spacing.

When FRP piping meets already existing components (valves, pumps, etc.) in other materials, a traditional flanged joint will almost inevitably be used, with the FRP flanges being dimensioned to suit the metal flange to which they will be joined. Therefore, the number of bolts, bolt circle, and bolt spacing will be determined from the metallic flange standards. Consequently, once the number of bolts is known, bolting design entails choosing a type and size of bolt to give us the actual bolt area, A_b. Note the actual bolt area is computed from the root diameter of the thread or section of least diameter under stress; this is mandated by the ASME BPV code. The root diameter, D_{br}, for a bolt with an American Standard Unified 60° thread is [11]

$$D_{br} = \left(D_b - \frac{1.3}{N}\right), \tag{4.9}$$

where D_b is the nominal bolt diameter and N is the number of threads per inch. With this equation, we can compute the actual bolt area for a single bolt; then multiply this area by the number of bolts to get the total actual bolt area, A_b.

We initially apply W_{m1}, then as the pressure increases the bolt load begins to increase due to the hydrostatic end load and the fluid penetration load, see figure 4.1. To prevent leakage, the bolt load must be greater than the total minimum required bolt load,

$$W_{\min} = A_m S_a, \tag{4.10}$$

but to prevent bolt overstressing it should not exceed the maximum allowable bolt load,

$$W_{\max} = A_b S_a. \tag{4.11}$$

Therefore, the flange design bolt load, W, should be within this bolt load range, i.e.,

$$W_{\min} \leq W \leq W_{\max}. \tag{4.12}$$

To proportion metallic flanges, the ASME code assumes a design bolt load

$$W = \frac{W_{\min} + W_{\max}}{2}. \tag{4.13}$$

However, for the design calculations of the modified stub flange, we will use equation (4.11) because if the design calculations are done using the lower bolt load, the FRP portion of the modified stub flange could be significantly overstressed when the actual bolt load is applied. In metallic flanges this is not a significant problem because the metallic flanges may yield to relieve the stress concentrations, whereas the FRP portion of the modified stub flange can be adversely affected. In fact, the code makes the recommendation that where additional safety is needed against abuse, the flange may be designed using equation (4.11).

4.4 Flange Design

The flange geometry can be proportioned once the design bolt load is known. In this section and the next chapter, we cover the details and the rationale of the calculations. Figure 4.2 illustrates the loading and geometry for the exact and the simplified model used in the analysis of the modified stub flange. The model consists of four distinct axisymmetric structural components which are analyzed separately, following the development of the Taylor Forge Method used in metallic joint analysis [51] [52]. However, we modify the development for the composite component to account for orthotropic material properties using classical lamination theory.

This is the simplest way to analyze this structure due to the complexity of the boundary conditions. Numerically, however, the exact geometry and boundary conditions can be modeled using present day finite element analysis programs, such as ABAQUS, see chapter 8.

From here on, we deviate from the ASME code load calculations. The code recommends checking the stresses for the two distinct loading conditions aforementioned; however, the seating condition does not produce the critical stress in either the hub or the stub and obviously leakage is not a problem in the seating condition. Therefore, we continue the analysis using the operating condition loading, as shown in figure 4.1 except that W_{m2} is replaced by the actual bolt load W, which is defined by equation (4.11).

We break the analysis of the flange into two parts, the stub and pipe-hub. We model the stub as an isotropic annular plate with an inner ring stiffener, figure 4.2. In the pipe-hub part, we model the pipe as a cylindrical shell and the hub as a variable thickness cylindrical shell. The total solution can then be obtained by imposing the appropriate boundary and continuity conditions, as shown in figure 4.2.

4.4.1 Stub

To proportion the stub, we need the ring stiffener height, l, and the annular plate thickness, t, figure 4.2. These parameters can be determined from the bearing strength of the hub, i.e., the strength of the resin used in the construction of the pipe-hub portion, and the stub strength. Also, to reduce the number of unknown parameters, we assume that the ring stiffener thickness is half of the annular plate thickness. The reason we make this choice is that in traditional FRP flanges the hub thickness is specified as half of the flange thickness, see chapter 2. In the next paragraphs, we outline the methodology for determining these two parameters.

Ring Stiffener Height, l

We determine the ring dimension l from the compressive strength of the resin and the strength capacity of the stub material. We assume the bearing pressure distribution, q, from the stub onto the hub to be quadratic, see figure 4.3. The reason for this choice is that as the stub rotates, under the action of the bolt load, the top of the ring transfers almost no stress, leaving the lower portion of the contact surface to transmit most of the bearing stress, see chapter 8. Therefore, an approximate relation for the resultant force of q is

$$N_W \approx \frac{\pi}{3} q^{\max} D l. \tag{4.14}$$

This equation is computed by multiplying the pressure bearing surface area by the average bearing stress. D is the average diameter of the pressure bearing surface, i.e.,

$$D = B + 2g_1 - \frac{l(g_1 - g_0)}{\sqrt{h^2 + (g_1 - g_0)^2}}, \tag{4.15}$$

where g_0 is the pipe thickness and h is the hub length. Also, we can find N_W in terms of the bolt load from vertical equilibrium of the stub portion, see figure 4.3, the result is

$$N_W = W\left[\frac{\sqrt{h^2 + (g_1 - g_0)^2}}{g_1 - g_0}\right], \tag{4.16}$$

Dimension l must be large enough so that the maximum bearing stress, $q^{\max}$, is less than the compressive strength of the resin, σ_c^{resin},

$$q^{\max} < \sigma_c^{resin}. \tag{4.17}$$

That is, the pressure bearing surface πDl must be sufficient to prevent bearing failure.

Furthermore, the maximum stress in the ring should not exceed the allowable stress of the stub material; therefore, l should also be large enough to satisfy the following inequality:

$$\sigma_{\theta d}^r < S_{sa}, \tag{4.18}$$

where S_{sa} is the allowable stress of the stub material at ambient temperature and $\sigma_{\theta d}^r$ is the maximum circumferential stress in the ring, which we define in the next section.

Annular Plate Thickness, t

The annular plate thickness, t, is determined by computing the maximum stress in the stub and comparing it to the allowable stress. To determine the maximum stress in the stub, we analyze the stub as two distinct components, ring stiffener and annular plate, figure 4.2. The total solution can be obtained from the continuity conditions, namely M_{rd} in figure 4.2 must be continuous between the two parts. The maximum stress occurs at the ring plate interface in the annular plate.

The ring is modeled as a reinforcing ring. The formulation is analogous to shell analysis. The details can be found in [21]. The continuity condition results in the following equation:

$$M_{rd} = -\frac{4E\theta_d I_{hoop}}{D'^2}, \tag{4.19}$$

where E is the Young's modulus of elasticity, θ_d is the rotation of the ring caused by the axial moment M_{rd}, I_{hoop} is the moment of inertial of the ring in the hoop direction, i.e., $I_{hoop} = tl^3/24$, and $D' = D + t$.

The solution for the annular plate can be obtained by superimposing the solution for two distinct annular plate loadings (we are assuming linear isotropic elasticity), one with $\frac{W}{\pi C}$ acting alone and one with M_{rd} acting alone. The two solutions can be found in [45]. From these solutions, we get θ_d, which can then be substituted into equation (4.19) to get M_{rd}. This is done as follows:

$$\theta_d = \frac{D'}{2D_E(1+\nu)\left[1-(A/D')^2\right]}\left\{M_{rd}\left[1+\frac{(1+\nu)}{(1-\nu)}\left(\frac{A}{D'}\right)^2\right] - \frac{W}{4\pi}\left[\frac{(1+\nu)}{(1-\nu)}\left(\frac{A}{D'}\right)^2\ln\left(\frac{C}{D'}\right)^2+\left(\frac{C}{D'}\right)^2-1\right]\right\}, \tag{4.20}$$

where $D_E = \frac{Et^3}{12(1-\nu^2)}$, ν is Poisson's ratio and A is the outer diameter of the stub.

Solving for M_{rd} we get

$$M_{rd} = \frac{\frac{W}{4\pi}\left[\frac{1+\nu}{1-\nu}\left(\frac{A}{D'}\right)^2\ln\left(\frac{C}{D'}\right)^2+\left(\frac{C}{D'}\right)^2-1\right]}{\frac{D't^2}{l^3}\frac{(A^2/D'^2-1)}{(1-\nu)}+\left[1+\frac{1+\nu}{1-\nu}\left(\frac{A}{D'}\right)^2\right]}. \tag{4.21}$$

We now find the circumferential moment in the annular plate $M^p_{\theta d}$,

$$M^p_{\theta d} = \frac{-\theta_d D_E(1-\nu^2)}{D'} + \nu M_{rd}. \tag{4.22}$$

Substituting for θ_d we get

$$M^p_{\theta d} = \frac{(1-\nu)}{\left[(A/D')^2 - 1\right]}\left\{ - M_{rd}\left[1 + \frac{(1+\nu)}{(1-\nu)}\left(\frac{A}{D'}\right)^2\right] + \frac{W}{4\pi}\left[\frac{(1+\nu)}{(1-\nu)}\left(\frac{A}{D'}\right)^2 \ln\left(\frac{C}{D'}\right)^2 + \left(\frac{C}{D'}\right)^2 - 1\right]\right\} + \nu M_{rd}. \tag{4.23}$$

Also, we can obtain the maximum circumferential moment in the ring, $M^r_{\theta d}$,

$$M^r_{\theta d} = \frac{M_{rd} D'}{t}. \tag{4.24}$$

These quantities are in units of moment per unit length. We can now find the corresponding stresses at the ring annular plate interface. The axial stress is

$$\sigma_{rd} = \frac{6M_{rd}}{t^2}, \tag{4.25}$$

the circumferential stress in the annular plate is

$$\sigma^p_{\theta d} = \frac{6M^p_{\theta d}}{t^2}, \tag{4.26}$$

and the circumferential stress in the ring is

$$\sigma^r_{\theta d} = \frac{6M^r_{\theta d}}{l^2}. \tag{4.27}$$

These are the maximum stresses in the hub and the ring. Our choice of t and l should be such that the integrity of the stub and hub material is ensured. That is, t and l must be large enough so that inequalities (4.17), (4.18) and the following two inequalities are not violated.

$$\sigma_{rd} < S_{sa} \tag{4.28}$$

and

$$\sigma^p_{\theta d} < S_{sa}. \tag{4.29}$$

Therefore, to proportion the stub we first choose an h and g_1, then we carry out the calculations above for a particular l and t until all the above constraints are satisfied; then we conduct the analysis presented in the next section and next chapter. If all the constraints are satisfied, we have the final design, otherwise we choose different values for t, l, h, and g_1 and repeat the analysis until a satisfactory design is achieved.

4.4.2 Pipe-Hub

We obtain the analytical model for the pipe-hub component by making some basic assumptions. The end pressure load, H_D, is the stress resultant of the end pressure stress, σ_H (both quantities are proportional to the internal pressure, p). If we assume that the thickness of the hub is small compared to the radius, then the mid-surface line of the hub remains almost parallel to that for the pipe. This assumption greatly simplifies the analysis. The stub restrains the hub at the large end, especially if a metallic stub is used; therefore, we can assume that the radial deflection is negligible compared to the deflection undergone by the composite system. Henceforth, the deflection of the analytical model at the large end of the hub is neglected. Furthermore, following a procedure similar to the ASME code, we can reduce the bolt load and gasket reaction to an effective moment, M_W.

To find M_W, we need the vertical component of the resultant force of the ring pressure, q. We assume that the distribution of q is quadratic, this leads to a resultant force which acts at a diameter close to the bottom of the contact area, see figure 4.3. From vertical equilibrium, we can find the vertical component of N_W, i.e.,

$$H_W = W. \tag{4.30}$$

Also, the assumption that the radial deformation at the large end of the hub is zero implies that the radial component of N_W is balanced by forces caused by the internal pressure.

To reduce the loading at the large end of the hub to an equivalent moment, M_W, we sum the moments produced by each force about the center of the large end of the hub, figure 4.4.

$$M_W = \frac{H_T h_T + H_W h_W + H_D h_D}{\pi B}, \tag{4.31}$$

where H_T is defined in equation (4.6), H_W equation (4.30), H_D equation (4.5),

$$h_T = \frac{g_1}{4}, \tag{4.32}$$

$$h_W = \frac{g_1}{2}, \tag{4.33}$$

and

$$h_D = \frac{g_1 - g_0}{2}. \tag{4.34}$$

Notice that the effective moment, M_W, is an axial moment per unit circumferential length acting at the mid-surface of the large end of the hub, which for the simplified model is located at a radius of *B/2*, see figure 4.2. Substituting and rearranging the forces and moment arms, we get

$$M_W = \frac{p}{16B}\left[G^2 g_1 + B^2(g_1 - 2g_0)\right] + \frac{Wg_1}{2\pi B}. \tag{4.35}$$

We then perform a detailed analysis of the hub and the pipe using the methods described in chapter 5, thereby ensuring the integrity of the pipe and hub material.

4.5 Summary

In this chapter we presented the design philosophy for the gasket, the bolts and the flanging system. The design of the gasket and the bolts is similar to that for metallic systems. This entails finding a bolt load sufficient to keep the joint leak tight during the operating life of the joint, then choosing a sufficiently large bolt area to achieve this objective. The flange design bolt load is then computed using this bolt area. We also outlined a simplified analysis for the design of the proposed flanging system. That is, we presented a criterion for proportioning the stub and guidelines for computing the loading for the simplified pipe-hub model. The stress calculations for the pipe-hub model are presented in the next chapter.

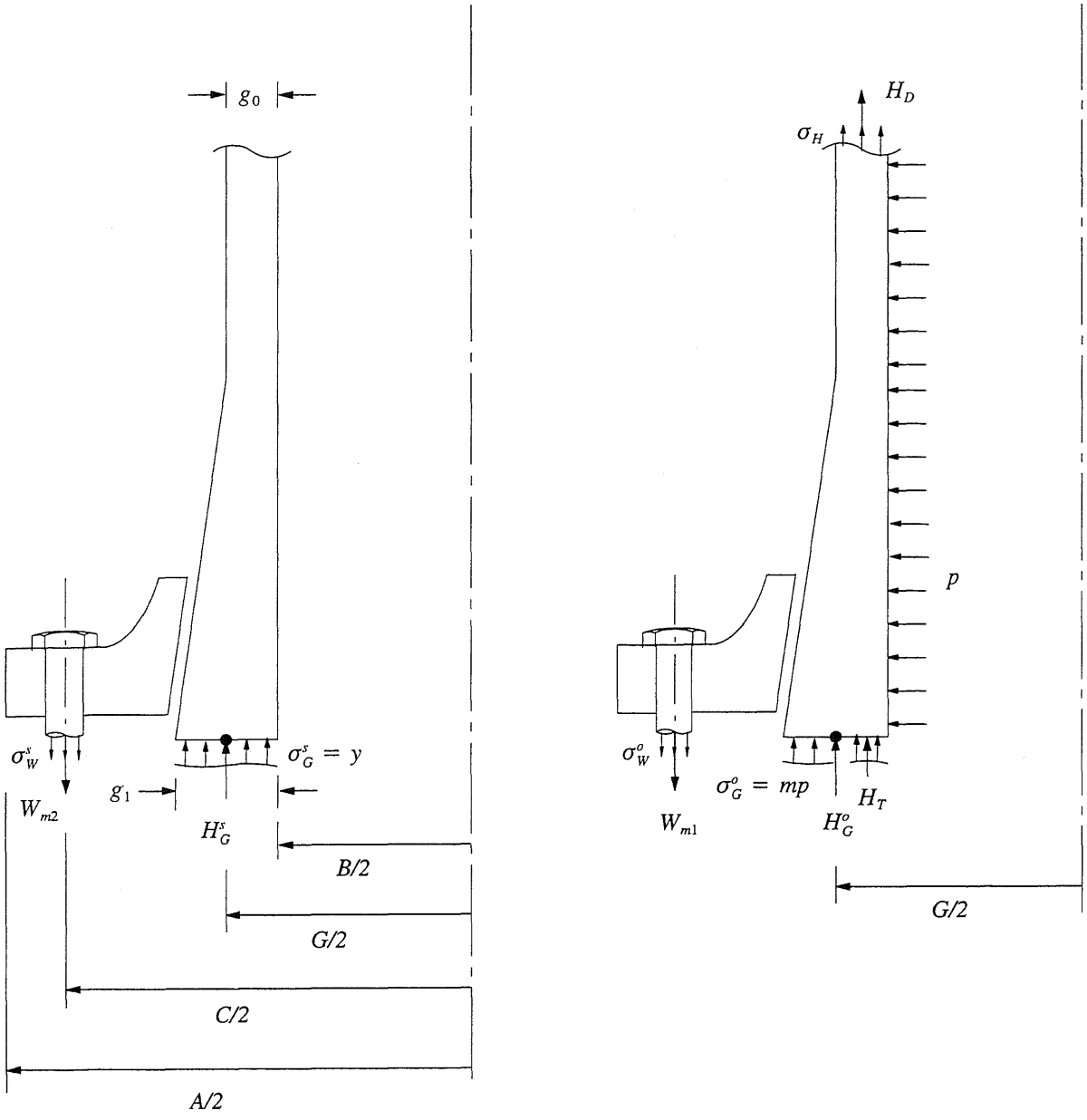

seating condition

operating condition

Figure 4.1: Seating and Operating Conditions.

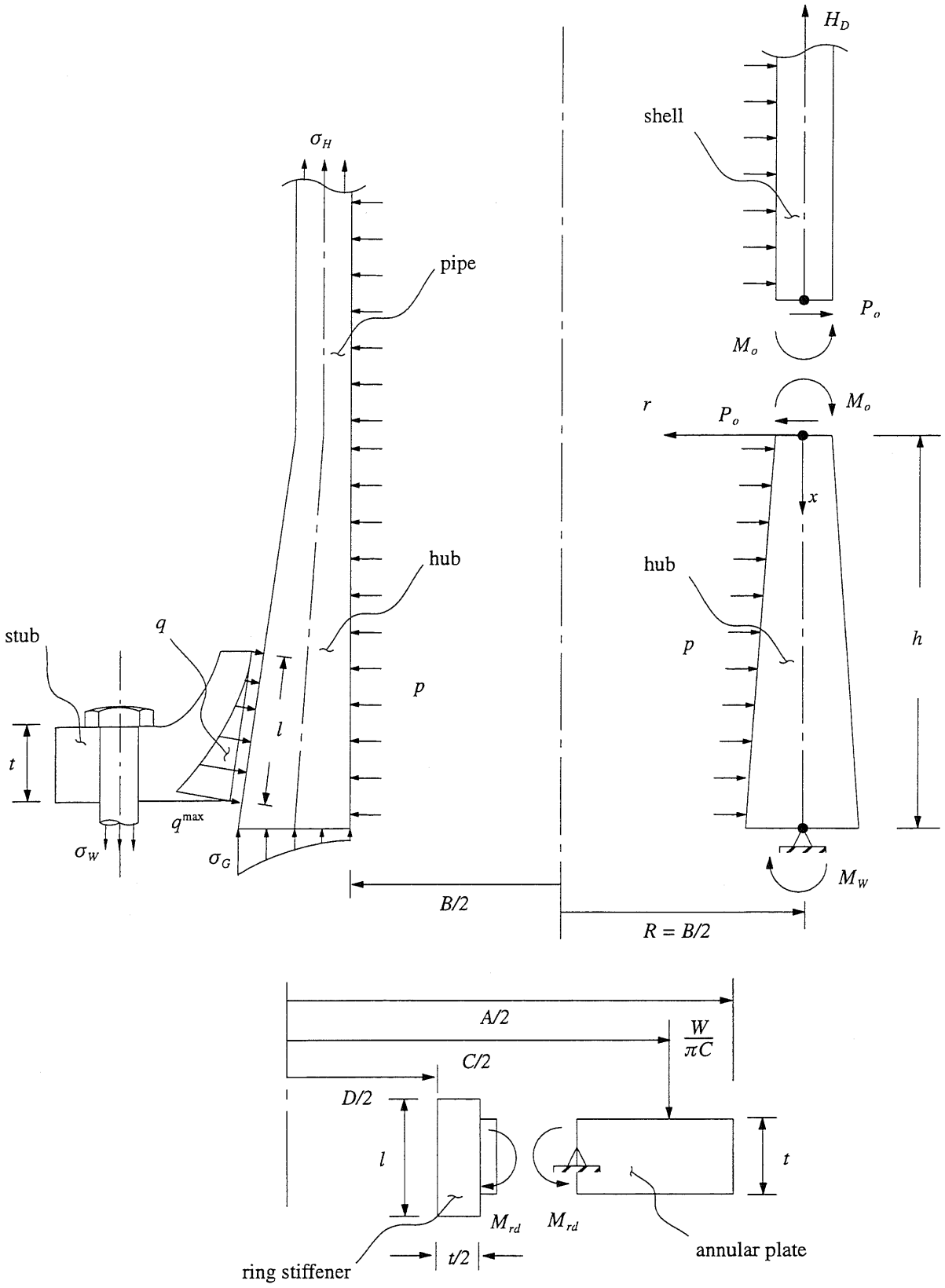

Figure 4.2: Exact and Model Flange Geometry and Loading.

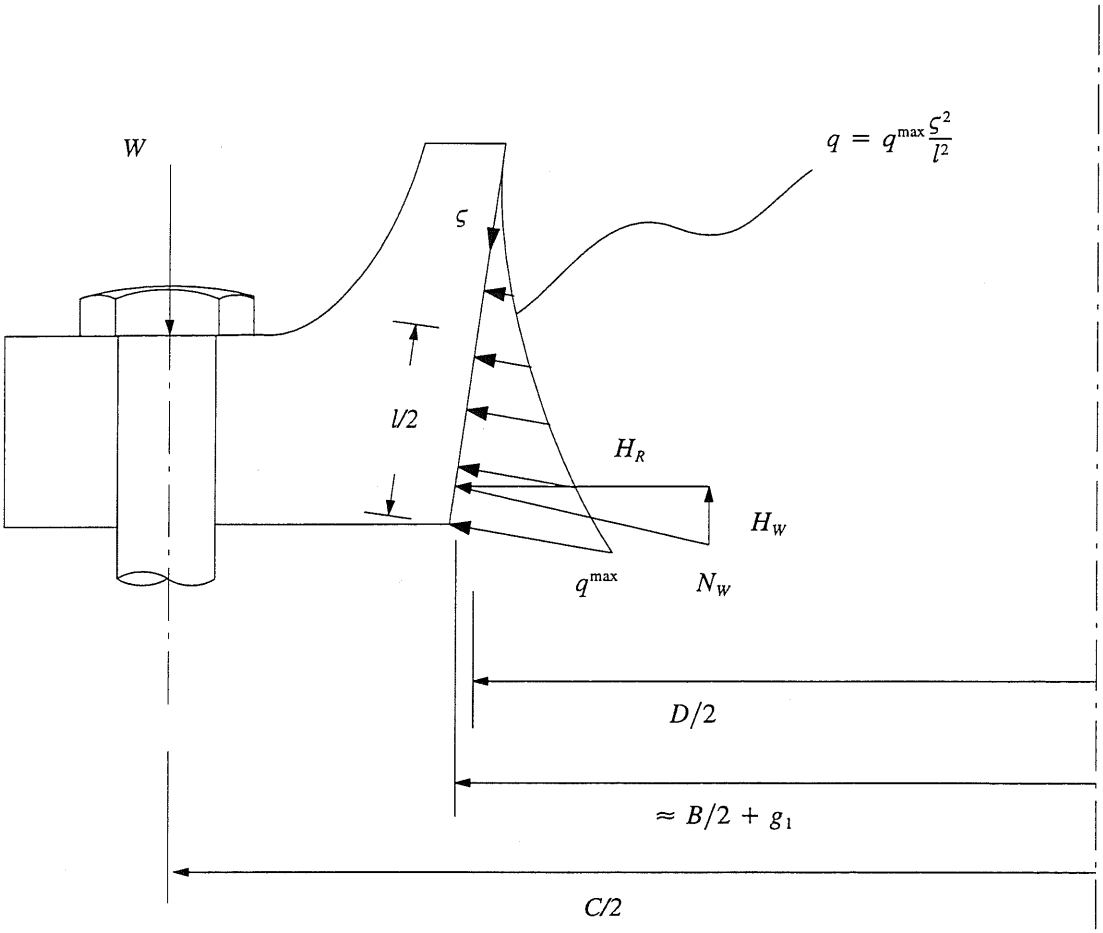

Figure 4.3: Stub Loading

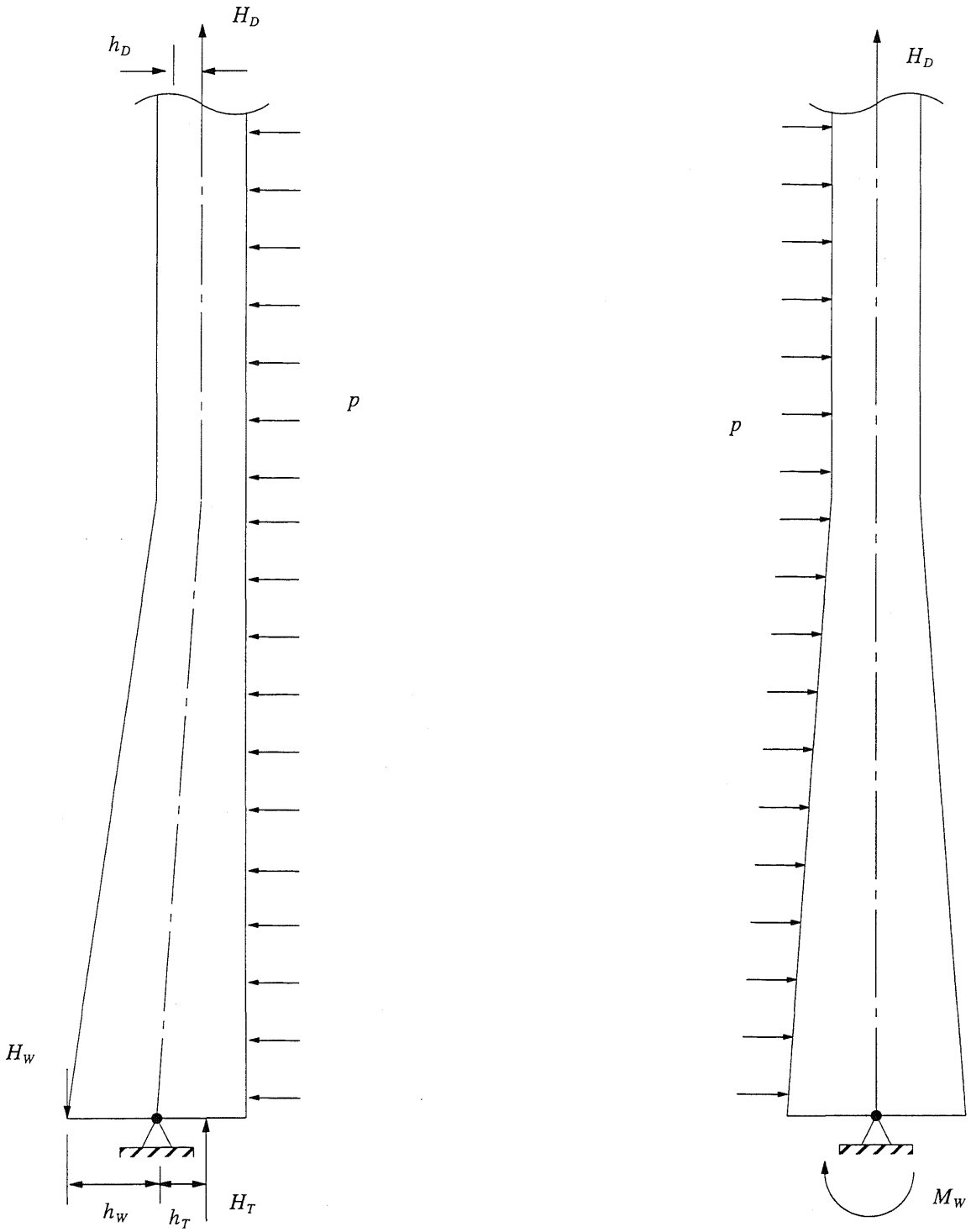

Figure 4.4: Pipe-Hub Loading

Chapter 5

Pipe-Hub Analytical Model

5.1 Introduction

The analytical model of the pipe-hub consists of two structural sections which are analyzed separately. The solutions for each of the two sections is obtained from classical laminated shell theory. The solution of the two sections can be combined to obtain the total solution for the pipe-hub system in terms of parameters that depend on the end conditions for each section. These parameters are computed by applying appropriate continuity and boundary conditions. We also compute the stresses from the laminated shell theory equations. The strength of the system is assumed to be determined by first ply failure. We determine first ply failure using the maximum work theory of Tsai-Hill, best known as the Tsai-Hill failure criterion. In this chapter we describe the procedure in detail.

5.2 The Uniform Thickness Shell

The cylindrical shell is modeled as an axisymmetric laminated shell. The equilibrium equations, kinematic assumptions, strain-displacement relations, and constitutive law can be reduced to a single equation. Details of the approach are given in appendices A, B, and C for a variable thickness cylindrical shell, which can easily be modified to suit the uniform thickness cylindrical shell. Also, the derivation for an isotropic uniform thickness cylindrical shell can be found in [50]; the procedure is identical for a laminated shell, with the exception of the calculation of the force and moment resultants in terms of laminated material properties. The final equation for the deflection in the shell $w^s(x)$, where x is the coordinate parallel to the axis of the shell, see figure 4.2, is

$$w^s_{,xxxx} + 4\beta^4 w^s = \left(\frac{A^*_{12}}{2A^*_{11}} - 1\right)\frac{p}{g_0^3 D^*_{11}}, \tag{5.1}$$

where

$$\beta^4 = \frac{1}{4R^2 g_0^2 D^*_{11} A^*_{11}}\left[A^*_{11}A^*_{22} - \left(A^*_{12}\right)^2\right]. \tag{5.2}$$

The superscript s denotes the cylindrical shell portion of the joint. Here $g_0 A^*_{ij}$ and $g_0^3 D^*_{ij}$ represent the stiffness of the laminated shell, and are defined in appendix B and repeated in figure 5.1. Equation (5.1) is written in terms of the material parameters, geometric parameters, loading, and radial displacement, and is the equation for a beam on an elastic foundation. Note that we assume the coupling matrix B_{ij} to be zero, which is the case in most practical structures with a number of laminae through the thickness (see chapter 6). This assumption allows us to use axisymmetry in the derivation of equation (5.1).

Equation (5.1) has the general solution [50]

$$w^s(x) = e^{\beta x}\left[C_5 \sin(\beta x) + C_6 \cos(\beta x)\right] + e^{-\beta x}\left[C_7 \sin(\beta x) + C_8 \cos(\beta x)\right] + \mu p, \tag{5.3}$$

where

$$\mu = -\frac{R^2}{2g_0}\left[\frac{2A^*_{11} - A^*_{12}}{A^*_{22}A^*_{11} - \left(A^*_{12}\right)^2}\right]. \tag{5.4}$$

The constants C_5, C_6, C_7, and C_8 are determined from the compatibility and boundary conditions. The slope, bending moment $M^s(x)$, and shear force $Q^s(x)$ in the shell are

$$w^s_{,x} = \beta e^{\beta x}\left\{C_5[\sin(\beta x) + \cos(\beta x)] + C_6[\cos(\beta x) - \sin(\beta x)]\right\} - \beta e^{-\beta x}\left\{C_7[\sin(\beta x) - \cos(\beta x)] + C_8[\sin(\beta x) + \cos(\beta x)]\right\}, \tag{5.5}$$

$$M^s(x) = -2g_0^3 D^*_{11}\beta^2\left\{e^{\beta x}\left[C_5 \cos(\beta x) - C_6 \sin(\beta x)\right] - e^{-\beta x}\left[C_7 \cos(\beta x) - C_8 \sin(\beta x)\right]\right\}, \tag{5.6}$$

and

$$Q^s(x) = -2g_0^3 D^*_{11}\beta^3\left\{e^{\beta x}\left[C_5(\cos(\beta x) - \sin(\beta x)) - C_6(\sin(\beta x) + \cos(\beta x))\right] + e^{-\beta x}\left[C_7(\sin(\beta x) + \cos(\beta x)) + C_8(\cos(\beta x) - \sin(\beta x))\right]\right\}. \tag{5.7}$$

5.3 The Variable Thickness Shell

The tapered hub is modeled as an axisymmetric laminated cylindrical shell of variable thickness. Again, the equilibrium equations, kinematic assumptions, strain-displacement relations, and constitutive law can be reduced to the single equation, as shown in appendices A, B, and C,

$$\left[D_{11}(x)w^h{}_{,xx}\right]_{,xx} + \left[A_{22}(x) - \frac{A_{12}^2(x)}{A_{22}(x)}\right]\frac{w^h}{R^2} = \left[\frac{A_{12}(x)}{2A_{11}(x)} - 1\right]p, \tag{5.8}$$

where the stiffness coefficients are now functions of position along the shell, and the superscript h denotes the hub. A similar equation is derived in [50] for an isotropic material.

To solve equation (5.8), we assume that the material properties are constant over the length of the hub (this may not be strictly correct in cases where the fiber winding angle must be varied to produce the variable thickness). However, using this assumption, we can transform equation (5.8) into an ordinary differential equation with coefficients that are simple polynomials of x. This equation can then be written in the form of a Bessel equation; see [50] or [52]. Hence, equation (5.8) becomes

$$\left(\psi^3 w^h{}_{,\psi\psi}\right)_{,\psi\psi} + \psi\rho^4 w^h = \left(\frac{A_{12}^*}{2A_{11}^*} - 1\right)\frac{ph^4}{\Delta\bar{g}^3 g_0^3 D_{11}^*}, \tag{5.9}$$

where

$$\psi = \frac{1}{\Delta\bar{g}}\left(1 + \Delta\bar{g}\frac{x}{h}\right), \tag{5.10}$$

$$\Delta\bar{g} = \frac{(g_1 - g_0)}{g_0}, \tag{5.11}$$

and

$$\rho^4 = \frac{h^4}{\Delta\bar{g}^2 g_0^2 R^2 D_{11}^*}\left[A_{22}^* - \frac{(A_{12}^*)^2}{A_{11}^*}\right]. \tag{5.12}$$

The stiffness coefficients $A_{ij}(x)$ and $D_{ij}(x)$ are written as $g(x)A_{ij}^*$ and $g^3(x)D_{ij}^*$, respectively, as shown in appendix B.

The homogeneous solution of equation (5.8) contains functions $k_i(\eta)$ defined in terms of Kelvin, or Thompson, functions [30] (see figure 5.2). The general solution of this equation is (see appendix D)

$$w^h(\eta) = \frac{2\rho}{\eta}\left[C_1k_1(\eta) + C_2k_2(\eta) + C_3k_3(\eta) + C_4k_4(\eta)\right] - \frac{4\rho^2 p^e}{\Delta\bar{g}\eta^2}, \tag{5.13}$$

where

$$\eta = 2\rho\sqrt{\psi}, \tag{5.14}$$

and

$$p^e = \frac{R^2 p}{2g_0}\left[\frac{2A_{11}^* - A_{12}^*}{A_{22}^*A_{11}^* - \left(A_{12}^*\right)^2}\right] = -\mu p. \tag{5.15}$$

As before, the constants C_1, C_2, C_3, and C_4 are determined from the compatibility and boundary conditions. The slope, bending moment $M^h(\eta)$, and shear force $Q^h(\eta)$ in the hub are then

$$w_{,x}^h(\eta) = \frac{4\rho^3}{h\eta^3}\left[C_1k_5(\eta) + C_2k_6(\eta) + C_3k_7(\eta) + C_4k_8(\eta)\right] + \frac{16\rho^4 p^e}{h\Delta\bar{g}\eta^4}, \tag{5.16}$$

$$M^h(\eta) = -\frac{g_0^3\Delta\bar{g}^3 D_{11}^*\eta}{8\rho h^2}\left[C_1k_9(\eta) + C_2k_{10}(\eta) + C_3k_{11}(\eta) + C_4k_{12}(\eta)\right] + \frac{2g_0^3\Delta\bar{g}^2 D_{11}^* p^e}{h^2}, \tag{5.17}$$

and

$$Q^h(\eta) = -\frac{g_0^3\Delta\bar{g}^3\rho^3 D_{11}^*}{h^3\eta}\left[C_1k_{13}(\eta) + C_2k_{14}(\eta) + C_3k_{15}(\eta) + C_4k_{16}(\eta)\right]. \tag{5.18}$$

5.4 Compatibility and Boundary Conditions

The solutions for $w^s(x)$ and $w^h(\eta)$ above are given in terms of eight constants of integration C_i, $i = 1, 8$. These constants are computed using the following eight compatibility and boundary conditions.

(i) At the gasket, the stub restrains the hub; therefore, we assume that the radial deflection in the hub at its large end is negligible compared to the deflection undergone by the rest composite system, i.e.,

$$w^h|_{x=h} = 0. \tag{5.19}$$

In addition, the moment at the gasket is the equivalent moment described in section 4.4.2, i.e.,

$$M^h|_{x=h} = M_W. \tag{5.20}$$

(ii) At the intersection of the hub and the shell, the displacements, rotations, bending moments, and shear forces are all continuous, i.e.,

$$w^h|_{x=0} = w^s|_{x=0}, \tag{5.21}$$

$$w^h_{,x}|_{x=0} = w^s_{,x}|_{x=0}, \tag{5.22}$$

$$M^h|_{x=0} = M^s|_{x=0}, \tag{5.23}$$

$$Q^h|_{x=0} = Q^s|_{x=0}. \tag{5.24}$$

(iii) At the far end of the shell, the moment and shear vanish, i.e.,

$$M^s|_{x\to-\infty} = 0, \tag{5.25}$$

$$Q^s|_{x\to-\infty} = 0. \tag{5.26}$$

Equations (5.25) and (5.26) imply that C_7 and C_8 are both zero. The remainder of the constants can be obtained by solving the following set of simultaneous equations for a given joint geometry:

$$k_1(\eta_1)C_1 + k_2(\eta_1)C_2 + k_3(\eta_1)C_3 + k_4(\eta_1)C_4 = \frac{2\rho p^e}{\Delta\bar{g}\eta_1}, \tag{5.27}$$

$$k_9(\eta_1)C_1 + k_{10}(\eta_1)C_2 + k_{11}(\eta_1)C_3 + k_{12}(\eta_1)C_4 = \frac{16\rho p^e}{\Delta\bar{g}\eta_1} - \frac{8\rho h^2 M_W}{g_0^3\Delta\bar{g}^3 D_{11}^*\eta_1}, \tag{5.28}$$

$$k_1(\eta_0)C_1 + k_2(\eta_0)C_2 + k_3(\eta_0)C_3 + k_4(\eta_0)C_4 - \frac{\eta_0}{2\rho}C_6 = 0, \tag{5.29}$$

$$k_5(\eta_0)C_1 + k_6(\eta_0)C_2 + k_7(\eta_0)C_3 + k_8(\eta_0)C_4 - \frac{\beta h\eta_0^3}{4\rho^3}C_5 - \frac{\beta h\eta_0^3}{4\rho^3}C_6 = -\frac{p^e\eta_0}{\rho}, \tag{5.30}$$

$$k_9(\eta_0)C_1 + k_{10}(\eta_0)C_2 + k_{11}(\eta_0)C_3 + k_{12}(\eta_0)C_4 - \frac{h^2\beta^2\eta_0^5}{4\rho^5}C_5 = \frac{4p^e\eta_0}{\rho}, \tag{5.31}$$

$$k_{13}(\eta_0)C_1 + k_{14}(\eta_0)C_2 + k_{15}(\eta_0)C_3 + k_{16}(\eta_0)C_4 - \frac{h^3\beta^3\eta_0^5}{8\rho^7}C_5 + \frac{h^3\beta^3\eta_0^5}{8\rho^7}C_6 = 0, \tag{5.32}$$

where

$$\eta_0 = 2\rho/\sqrt{\Delta\bar{g}} \tag{5.33}$$

and

$$\eta_1 = 2\rho / \sqrt{\frac{1 + \Delta\overline{g}}{\Delta\overline{g}}}. \tag{5.34}$$

The solution can easily be obtained using a computer program.

5.5 Stress Calculation

The aim of the analysis is to determine the stresses in each of the lamina forming the laminate. These stresses can be used to predict the load at which failure initiates, the ultimate load. In our study we assume this load to be the load at which the first laminae fails. To calculate the stresses, we make use of the equations found in appendix B. Once the stresses in each laminae are available, we can assess the ultimate load carrying capacity of the system using the Tsai-Hill failure criterion described in section 5.6.

We first consider the pipe. Stresses in any lamina (e.g., the k^{th}) can be obtained by using the following relations:

$$\sigma_{xs}^{(z)}(x) = \overline{Q}_{11}^{(z)}[u,_x^s(x) - zw,_{xx}^s(x)] - \overline{Q}_{12}^{(z)}\frac{w^s(x)}{R}, \tag{5.35}$$

$$\sigma_{\theta s}^{(z)}(x) = \overline{Q}_{12}^{(z)}[u,_x^s(x) - zw,_{xx}^s(x)] - \overline{Q}_{22}^{(z)}\frac{w^s(x)}{R}, \tag{5.36}$$

$$\tau_{x\theta s}^{(z)}(x) = \overline{Q}_{16}^{(z)}[u,_x^s(x) - zw,_{xx}^s(x)] - \overline{Q}_{26}^{(z)}\frac{w^s(x)}{R}, \tag{5.37}$$

where $\overline{Q}_{ij}^{(z)}$ are defined in appendix B, z takes the top and bottom values of each laminae $g_k^{'}$ shown in figure 5.1, i.e.,

$$g_k^{'} = \left(k - \frac{n}{2}\right)\frac{g_0}{n}. \tag{5.38}$$

The other unknowns in equations (5.35), (5.36) and (5.37) are

$$u,_x^s(x) = \frac{Rp}{2g_0A_{11}^*} + \frac{A_{12}^*}{A_{11}^*}\frac{w^s(x)}{R}, \tag{5.39}$$

$$w^s(x) = e^{\beta x}\left[C_5\sin(\beta x) + C_6\cos(\beta x)\right] + \mu p, \tag{5.40}$$

and

$$w,_{xx}^{s}(x) = 2\beta^2 e^{\beta x}\left[C_5\cos(\beta x) - C_6\sin(\beta x)\right]. \tag{5.41}$$

For laminate strength analysis, laminae stresses along the primary material laminae directions are preferred. These can now easily be obtained by using the transformation equations

$$\begin{Bmatrix}\sigma_1\\ \sigma_2\\ \tau_{12}\end{Bmatrix}^{(z)} = \begin{bmatrix} C^2 & S^2 & 2SC \\ S^2 & C^2 & -2SC \\ -SC & SC & C^2-S^2\end{bmatrix}\begin{Bmatrix}\sigma_x\\ \sigma_\theta\\ \tau_{x\theta}\end{Bmatrix}^{(z)}, \tag{5.42}$$

where $C = \cos\phi$, $S = \sin\phi$ and ϕ is the winding angle.

We now consider the hub. The lamina stresses in the hub can be determined from the following relations:

$$\sigma_{xh}^{(z)}(x) = \overline{Q}_{11}^{(z)}\left[u,_x^h(x) - zw,_{xx}^h(x)\right] - \overline{Q}_{12}^{(z)}\frac{w^h(x)}{R}, \tag{5.43}$$

$$\sigma_{\theta h}^{(z)}(x) = \overline{Q}_{12}^{(z)}\left[u,_x^h(x) - zw,_{xx}^h(x)\right] - \overline{Q}_{22}^{(z)}\frac{w^h(x)}{R}, \tag{5.44}$$

$$\tau_{x\theta h}^{(z)}(x) = \overline{Q}_{16}^{(z)}\left[u,_x^h(x) - zw,_{xx}^h(x)\right] - \overline{Q}_{26}^{(z)}\frac{w^h(x)}{R}, \tag{5.45}$$

where z takes the top and bottom values $g_k^*(x)$, which are functions of x, figure B.2, i.e.,

$$g_k{}^*(x) = \frac{g_0}{n}\left(k - \frac{n}{2}\right)\left(1 + \Delta\bar{g}\frac{x}{h}\right). \tag{5.46}$$

The other unknowns in equations (5.43), (5.44) and (5.45) are

$$u,_x{}^h(x) = \frac{Rp}{2g(x)A_{11}^*} + \frac{A_{12}^*}{A_{11}^*}\frac{w^h(x)}{R}, \tag{5.47}$$

$$w^h(\eta) = \frac{2\rho}{\eta}\left[C_1k_1(\eta) + C_2k_2(\eta) + C_3k_3(\eta) + C_4k_4(\eta)\right] - \frac{4\rho^2p^e}{\Delta\bar{g}\eta^2}, \tag{5.48}$$

and

$$w,_{xx}^h(\eta) = \frac{8\rho^5}{h^2\eta^5}\left[C_1k_9(\eta) + C_2k_{10}(\eta) + C_3k_{11}(\eta) + C_4k_{12}(\eta)\right] - \frac{128\rho^6p^e}{h^2\Delta\bar{g}\eta^6}. \tag{5.49}$$

We can use equation (5.42) to transform the stresses from laminate axis to the primary material lamina directions.

5.6 Failure Criterion

To find the strength capacity of the pipe-hub system, we use the Tsai-Hill criterion [33]. Ply failure initiates when the following inequality is violated:

$$\left(I_f\right)^2 < 1, \tag{5.50}$$

where I_f is the Tsai-Hill failure index. This is defined as follows:

$$I_f = \sqrt{\left[\frac{\sigma_{LL}^{(z)}}{\sigma_{LLU}}\right]^2 - \left[\frac{\sigma_{LL}^{(z)}}{\sigma_{LLU}}\right]\left[\frac{\sigma_{TT}^{(z)}}{\sigma_{LLU}}\right] + \left[\frac{\sigma_{TT}^{(z)}}{\sigma_{TTU}}\right]^2 + \left[\frac{\tau_{LT}^{(z)}}{\sigma_{LTU}}\right]^2}, \tag{5.51}$$

where σ_{LLU} is the longitudinal ultimate tensile strength, σ_{TTU} is the transverse ultimate tensile strength, and σ_{LTU} is the in-plane ultimate shear strength. When longitudinal or transverse stresses are compressive, the corresponding ultimate compressive strengths should be used. This failure criterion agrees well with experimental results [33] for some material systems, such as glass and epoxy.

5.7 Computer Implementation

We implemented the calculations presented in the last chapter and this chapter in a computer code. After computing the effective moment, M_W, for a specific geometry, the code computes displacements, stresses and the Tsai-Hill failure index, I_f. The Tsai-Hill failure index allows us to check for first ply failure at which point failure of the composite system is assumed. This tool helps us in the design of the system by allowing us to vary different material and geometric parameters quickly in order to obtain a satisfactory design.

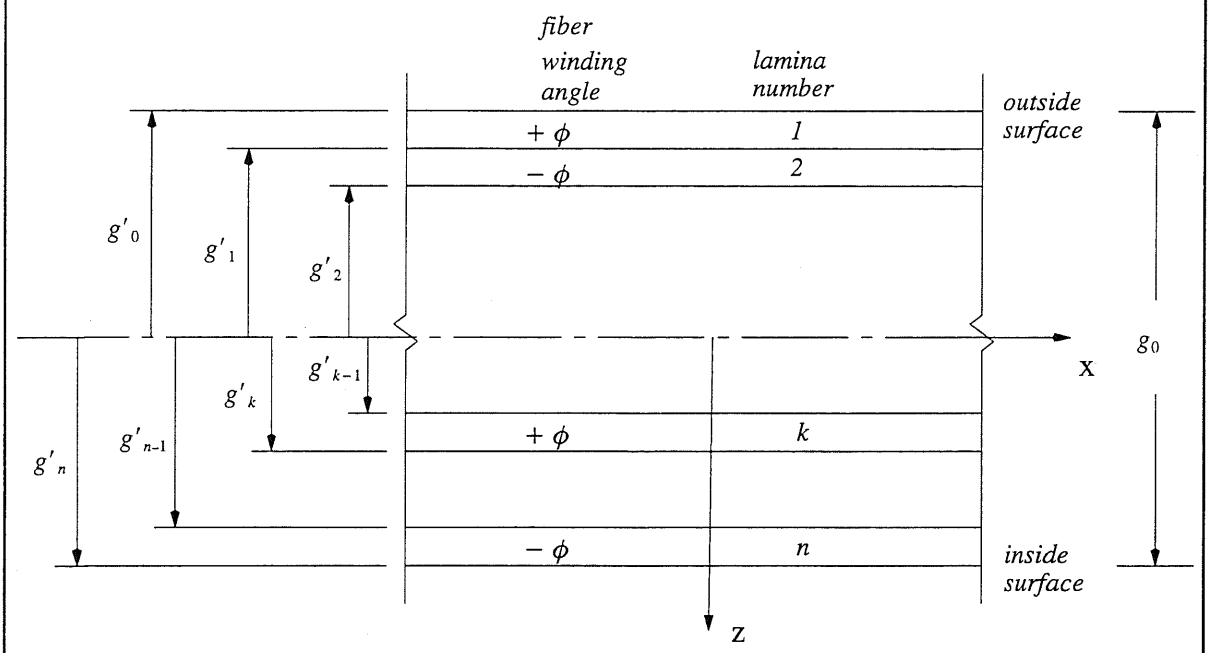

$$A_{ij} = g_0 A^*_{ij}$$

i,j take the values 1 and 2

$$D_{ij} = g_0^3 D^*_{ij}$$

$$A^*_{ij} = \frac{1}{n} \sum_{k=1}^{n} \overline{Q}^{(k)}_{ij}$$

$$D^*_{ij} = \frac{1}{3n} \sum_{k=1}^{n} \overline{Q}^{(k)}_{ij} \left(1 - 3k + 3k^2 + \frac{3n}{2} - 3nk + \frac{3n^2}{4} \right)$$

$\overline{Q}^{(k)}_{ij}$ = transformed reduced stiffness matrix

Figure 5.1: Computation of Stiffness Coefficients for a Laminated Shell.

$$k_1(\eta) = \text{ber}'(\eta)$$
$$k_2(\eta) = \text{bei}'(\eta)$$
$$k_3(\eta) = \text{ker}'(\eta)$$
$$k_4(\eta) = \text{kei}'(\eta)$$
$$k_5(\eta) = -\eta\text{bei}(\eta) - 2\text{ber}'(\eta)$$
$$k_6(\eta) = \eta\text{ber}(\eta) - 2\text{bei}'(\eta)$$
$$k_7(\eta) = -\eta\text{kei}(\eta) - 2\,\text{ker}'(\eta)$$
$$k_8(\eta) = \eta\,\text{ker}(\eta) - 2\text{kei}'(\eta)$$
$$k_9(\eta) = 4\eta\text{bei}(\eta) + 8\text{ber}'(\eta) - \eta^2\text{bei}'(\eta)$$
$$k_{10}(\eta) = -4\eta\text{ber}(\eta) + 8\text{bei}'(\eta) + \eta^2\text{ber}'(\eta)$$
$$k_{11}(\eta) = 4\eta\text{kei}(\eta) + 8\,\text{ker}'(\eta) - \eta^2\text{kei}'(\eta)$$
$$k_{12}(\eta) = -4\eta\,\text{ker}(\eta) + 8\text{kei}'(\eta) + \eta^2\,\text{ker}'(\eta)$$
$$k_{13}(\eta) = -\eta\text{ber}(\eta) + 2\text{bei}'(\eta)$$
$$k_{14}(\eta) = -\eta\text{bei}(\eta) - 2\text{ber}'(\eta)$$
$$k_{15}(\eta) = -\eta\,\text{ker}(\eta) + 2\text{kei}'(\eta)$$
$$k_{14}(\eta) = -\eta\text{kei}(\eta) - 2\,\text{ker}'(\eta)$$

where the prime denotes differentiation with respect to the argument of the function. The Kelvin functions are

$$\text{ber}(\eta) = \sum_{k=0}^{\infty} \frac{(-1)^k}{[(2k)!]^2}\left(\frac{\eta}{2}\right)^{4k}$$

$$\text{bei}(\eta) = \sum_{k=0}^{\infty} \frac{(-1)^k}{[(2k+1)!]^2}\left(\frac{\eta}{2}\right)^{4k+2}$$

$$\text{ker}(\eta) = -\left[\ln\left(\frac{\eta}{2}\right) + \gamma\right]\text{ber}(\eta) + \frac{\pi}{4}\text{bei}(\eta) + \sum_{k=0}^{\infty} \Phi(2k)\frac{(-1)^k}{[(2k)!]^2}\left(\frac{\eta}{2}\right)^{4k}$$

$$\text{kei}(\eta) = -\left[\ln\left(\frac{\eta}{2}\right) + \gamma\right]\text{bei}(\eta) - \frac{\pi}{4}\text{ber}(\eta) + \sum_{k=0}^{\infty} \Phi(2k+1)\frac{(-1)^k}{[(2k+1)!]^2}\left(\frac{\eta}{2}\right)^{4k+2}$$

where

$$\Phi(k) = \sum_{i=1}^{k} \frac{1}{i}$$

and Euler's constant is

$$\gamma = \lim_{k\to\infty}[\Phi(k) - \ln(k)] \approx 0.5772157$$

Figure 5.2: Kelvin Functions Used in the Solution.

Chapter 6

Verification of the Analytical Model

6.1 Introduction

We made a number of assumptions in the derivation of the analytical model described in chapters 4 and 5. In this chapter, we use the finite element method to validate some of these assumptions, using the specific problem shown in figure 6.1; the pipe thickness and the internal pressure are representative of a typical water line. The material properties for the composite system were extracted from [31] and [32], and are shown in table 6.1.

In the formulation of the analytical model we assumed that the deformation of the composite system is axisymmetric. However, depending on the stacking sequence of the plies composing the laminate, this assumption may or may not be valid. In the next section we will present results that validate the axisymmetric assumption for practical lay-ups. Also, we check the stub formulas derived in section 4.4.1 and the pipe-hub formulas derived in chapter 5 using the commercial finite element package ABAQUS. We check the results using three dimensional shell and axisymmetric shell elements. This check shows the close agreement between the simplified formulation and the ABAQUS results. Furthermore, we conduct a thorough investigation of the stresses in the composite system for a specific laminate lay-up.

6.2 Axisymmetric Assumption

Geometrically axisymmetric laminated systems and their isotropic counterparts may respond differently when subjected to identical loading conditions. For instance, a single ply filament wound cylinder subjected to internal pressure will tend to twist as it expands, whereas an

isotropic cylinder only expands under internal pressure. This is a consequence of the coupling between stretching and shear inherent to laminated materials. As the number of plies in the filament wound cylinder increases, the twisting mode becomes increasingly small and expansion is the primary deformation mode of the system.

To illustrate this phenomenon, we conducted finite element analyses of the cylindrical system depicted in figure 6.1 (a) for three different ply lay-ups using an eight node three dimensional shell element (S8R5) in ABAQUS. The first case is a single ply system wound at an angle of $+ 54.7°$ to the axial direction of the cylindrical system (see figure B.1 for a definition of coordinate systems). The other two cases are a two ply $\pm 54.7°$ and a 32 ply $[\pm 54.7°]_{16}$ system. The laminate thickness is the same in all three cases. The circumferential displacements are plotted in figure 6.2 and the axial displacements are plotted in figure 6.3 for all three cases. From this result, it is clear that the axisymmetric assumption is not valid for the single ply case. However, the circumferential displacement is negligible when the second ply is wound in the opposite direction to the first ply; this indicates that the axisymmetric assumption holds for multi-ply lay-ups. Figure 6.4 shows the twisting behavior of the single ply case as the system is pressurized, producing large circumferential displacements as it unwinds. As the system twists, a further expansion due to the unwinding is observed, see figure 6.3. This expansion is completely eliminated for the two ply system.

The twisting can be attributed to the coupling stiffnesses, B_{ij} $(i, j = 1, 2, 6)$ [33]. These stiffnesses are zero for laminated systems that are symmetric in both geometry and material properties about the middle surface. For angle-ply systems, such as filament wound components, the coupling stiffnesses go to zero as the number of layers increases. In fact, for angle-ply lay-up laminates all but the *16* and *26* components of B_{ij} are zero. The *16* and *26* components of B_{ij} are inversely proportional to the number of layers in the laminate, n, and proportional to the winding angle, ϕ, i.e.,

$$B_{16} = - \overline{Q}_{16} \frac{g^2}{2n} \tag{6.1}$$

and

$$B_{26} = - \overline{Q}_{26} \frac{g^2}{2n}, \tag{6.2}$$

where $\overline{Q}_{ij}$ are defined in Appendix B and g is the laminate thickness. We plot the variations of B_{16} and B_{26} with respect to n and ϕ for a glass/polyester angle-ply laminate in figure 6.5. These

plots clearly shows that as the number of plies increases, the coupling stiffnesses vanish. Notice that the only practical variation in ϕ is between 0° and 90°.

The results presented in this section clearly show that we are justified in using an axisymmetric formulation for the composite pipe-hub component of the modified stub flanged joint, provided the lay-up of the system contains more than two plies, which is the case for most practical piping applications.

6.3 Verification of the Stub Model Analysis Using the Finite Element Method

In this section we verify the simplified analytical formulation used to determined the maximum stresses in the stub, which was presented in section 4.4.1. These stresses are used to determine the annular plate thickness, *t,* and ring stiffener height, *l.* We checked this simplified analysis using finite element analysis for the specific geometry and loading depicted in figure 6.1 (b). Our particular choice of geometry and loading is arbitrary and is presented here for illustration purposes only. For the finite element solution, we model the stub with 37 axisymmetric shell elements (SAX2) in ABAQUS using different thickness for the two sections, ring stiffener and annular plate. Also, we use the material properties for a typical steel, i.e., Young's modulus of 29,000,000 *psi* and Poisson's ratio of 0.3. In both analyses, we compute the moments and corresponding maximum stresses at the ring annular plate interface. The results are presented in table 6.2; the error is less than two percent in all cases.

6.4 Verification of the Pipe-Hub Model Analysis Using the Finite Element Method

To check the validity of the analysis presented in chapter 5, we compare the results of our analytical model with those obtained from finite element analysis. For these analyses, we used the geometry and loading shown in figure 6.1 (a), and the material and strength properties given in table 6.1. A computer program was written that computes displacements, moments, stresses and the Tsai-Hill failure index using our simplified method. For the finite element analysis, we used a three node axisymmetric shell element (SAX2). We first consider a 72-laminae cross-ply laminate, $[0°/90°]_{36}$. Plots of the distribution of displacements and moments computed using the two methods are shown in figures 6.6 and 6.7. Clearly, the agreement between the two solution methods is excellent.

To verify the results for different winding angles and hub slopes, we used a one element strip mesh as shown in figure 6.8. In the finite element model, we use a four node reduced integration three dimensional shell element (S4R5), which has 5 degrees-of-freedom per node. This was necessary because the ABAQUS axisymmetric elements do not allow us to consider

arbitrary winding angles. Again, we use the geometry and loading depicted in figure 6.1 (a), and the material and strength properties given in table 6.1.

6.4.1 Analysis for Various Winding Angles

First, we vary the winding angle for a 72-laminae angle-ply laminate, $[\pm \phi]_{36}$. Plots of the distribution of displacements and moments computed using our simplified analytical method and finite element analysis are shown in figures 6.9 and 6.10. Again, the agreement between the two solution methods is excellent. Furthermore, in tables 6.3 and 6.4 we list a comparison of the maximum displacements and moments for the $[\pm \phi]_{36}$ lay-up. Note that the error is less than 2% in all cases.

Figure 6.9 shows that as the winding angle decreases (i.e., becomes closer to being parallel to the axial direction), the stiffness of the pipe-hub diminishes until an angle of approximately 15°, and then begins to increase as the angle reaches 0°. It would seem intuitive that the stiffness would continue to diminish until the fibers are parallel to the axial direction. At this point, the radial deformation is essentially controlled by the stiffness of the resin because all the fibers are oriented in the axial direction leaving the matrix to carry the entire circumferential stress. The reversal in the axial deformation at the lower winding angles is due to the hydrostatic end load H_D (see figure 4.4). At the lower winding angles, the fibers are almost parallel to the axial direction and carry most of the hydrostatic end load H_D. Therefore, the fibers are prestressed; consequently, catenary effects cause some of the transverse load, in this case the radial internal pressure, to be carried by axial stress in the fibers rather than by circumferential stress in the resin alone. When the hydrostatic end load is not included in the analysis, the system continues to expand as the winding angle reaches 0°, consistent with intuition. Therefore, the hydrostatic end load H_D appears to provide additional stiffness to the pipe-hub at the lower winding angles.

Of practical importance are the higher winding angles, from both a manufacturing and a strength stand point. The shallow winding angles are difficult to wind because of fiber slippage when placed on the mandrel (in particular for a cylindrical structure, such as a pipe).

Furthermore, most filament wound pipes are wound at $\pm$ 54.7° to produce equal circumferential and axial stresses. This result was derived from netting analysis [47]. In this method, the fibers are assumed to carry the entire load. For pressurized angle-ply systems, such as pressurized filament wound pipes, the ratio of circumferential to axial stress is equal to $\tan^2(\phi)$; the ratio of the applied circumferential to axial stress from membrane analysis is 2:1. Therefore,

netting analysis predicts an optimum winding angle of 54.7°, i.e., the laminate is equally stressed in both the axial and circumferential directions. This is the winding angle we use for the remainder of our study.

6.4.2 Variation of Large End of the Hub

We also vary the large end of the hub, g_1, which is proportional to the hub slope $(g_1 - g_0)/h$. Plots of the distribution of displacements and moments computed using our simplified analytical model and finite element analysis are depicted in figures 6.11 and 6.12. The comparison of maximum displacements and moments is listed in tables 6.5 and 6.6. Notice the increase in moment near the pipe-hub interface as g_1 increases; this is due to the fact that the discontinuity between the pipe and the hub becomes increasingly severe as the hub slope increases.

6.4.3 Laminate Stresses

We plot the distribution of stresses and Tsai-Hill failure index for a $[\pm\ 54.7°]_{36}$ lay-up along the entire length of the pipe-hub system in figures 6.13 through 6.16. The kink in the distribution of stresses at the pipe-hub interface is due to the discontinuity in the gradient of the stresses across the interface. This can easily be checked by taking the derivative of the stress equations for both the pipe and the hub, and showing that the difference in these derivatives does not vanish. For example, this can be done for the axial stress as follows:

$$\sigma_{xh,x}|_{x=0} - \sigma_{xs,x}|_{x=0} = \frac{\overline{Q}_{11} Rp\Delta\overline{g}}{2A^*_{11} g_1 h}, \tag{6.3}$$

which is a non-zero constant. To compute the Tsai-Hill failure index, we use the ultimate strength capacity for the glass/polyester composite listed in table 6.1. The Tsai-Hill failure index is defined in equation (5.51).

The variation of stresses and Tsai-Hill failure index through the laminate thickness is obtained by calculating the stress variation in all the laminae. The results are plotted in figures 6.17 through 6.20 for a $[\pm\ 54.7°]_{36}$ lay-up. In general, the variation of stress through the laminate thickness is not linear since the stiffness of each laminae, $\overline{Q}_{ij}$, can vary from one lamina to the next one. Stresses may be discontinuous at the interface of two laminae, and the stress gradient in two adjoining laminae may also differ. The ABAQUS results capture this behavior for all stresses and Tsai-Hill failure index, however, our model only captures the behavior for

shear stresses, figure 6.20. Still, the agreement between the two solution methods is good. The reason for the discrepancy in our model is that in the axisymmetric formulation, the in-plane shearing strain is set to zero ($\gamma_{x\theta}^{(z)} = 0$), see appendix A. Clearly, for an angle-ply laminate composed of more that two plies there is in-plane shearing at the interface of two adjoining lamina, which is the reason for the stepped stress distribution in the finite element results. However, this in-plane shear stress at the interface of two adjoining lamina is small.

The linearity of the in-plane normal stresses can be proven by expanding the stress equations (5.42). For example, this can be done for the pipe axial stress as follows:

$$\begin{aligned}\sigma_{1s}^{(z)} = {} & [u,_x{}^s(x) - zw,_{xx}^s(x)]\Big[Q_{11}\big(C^6 + S^4C^2 + 2S^2C^4\big) + Q_{12}\big(S^6 + S^2C^4 + 2S^4C^2\big)\Big] \\ & - \frac{w^s(x)}{R}\Big[Q_{11}\big(S^2C^4 + 2S^4C^2\big) - Q_{12}\big(-C^6 + S^4C^2 - 2S^2C^4\big) + Q_{66}4S^4C^2\Big],\end{aligned} \tag{6.4}$$

where $C = \cos(\phi)$, $S = \sin(\phi)$ and the other quantities are defined in chapter 5 and appendix B. This stress is continuous through the laminate thickness because the stiffnesses Q_{ij} are equal for all the lamina through the thickness and the sines and cosines are raised to even powers (notice that $\sin^m(\phi) = \sin^m(-\phi)$ and $\cos^m(\phi) = \cos^m(-\phi)$, when m is even). This means that for an angle-ply laminate, constructed from equal material and thickness lamina, the in-plane normal stresses in our formulation vary linearly through the thickness. This is due to z, equations (5.35), (5.36), (5.43) and (5.44).

6.5 Summary

The axisymmetric assumption used in the analytical model of the composite system, although not strictly correct, is sufficiently accurate for most practical applications. Specifically, for lay-ups composed of more than two plies since the circumferential displacements are practically negligible. The results presented in this chapter clearly validate the mathematical formulation presented in chapters 4 and 5.

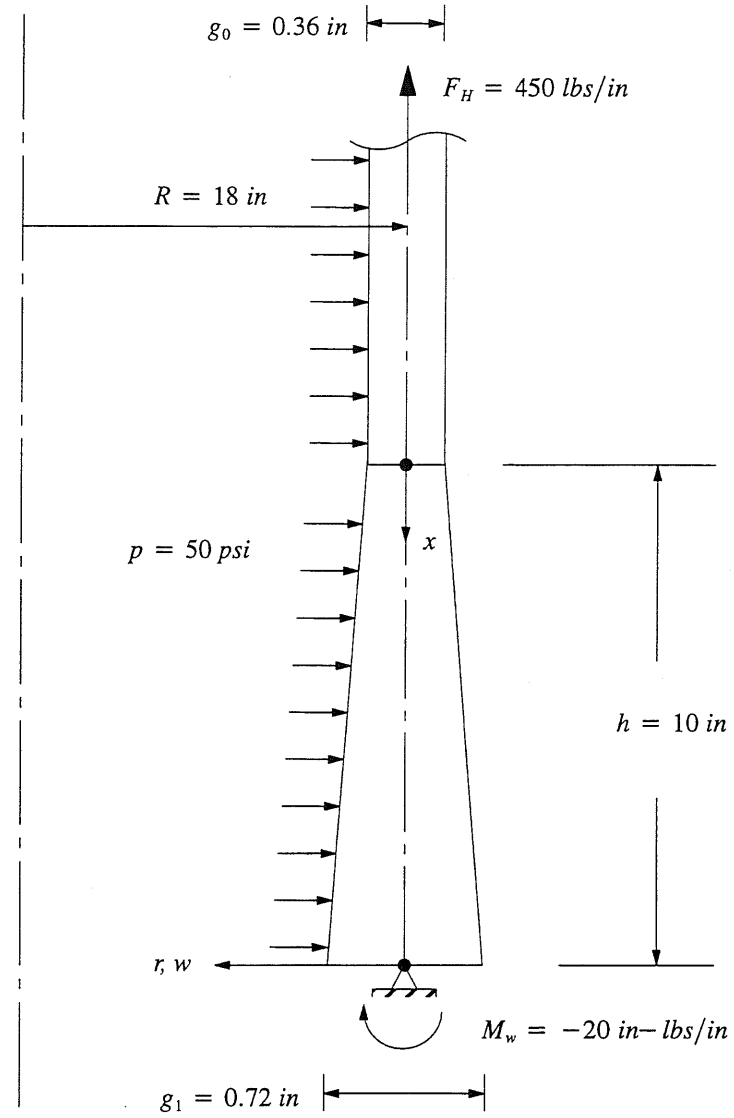

Figure 6.1: Description for the Verification Problems, Lay-Up $[\pm\phi]_{n/2}$.

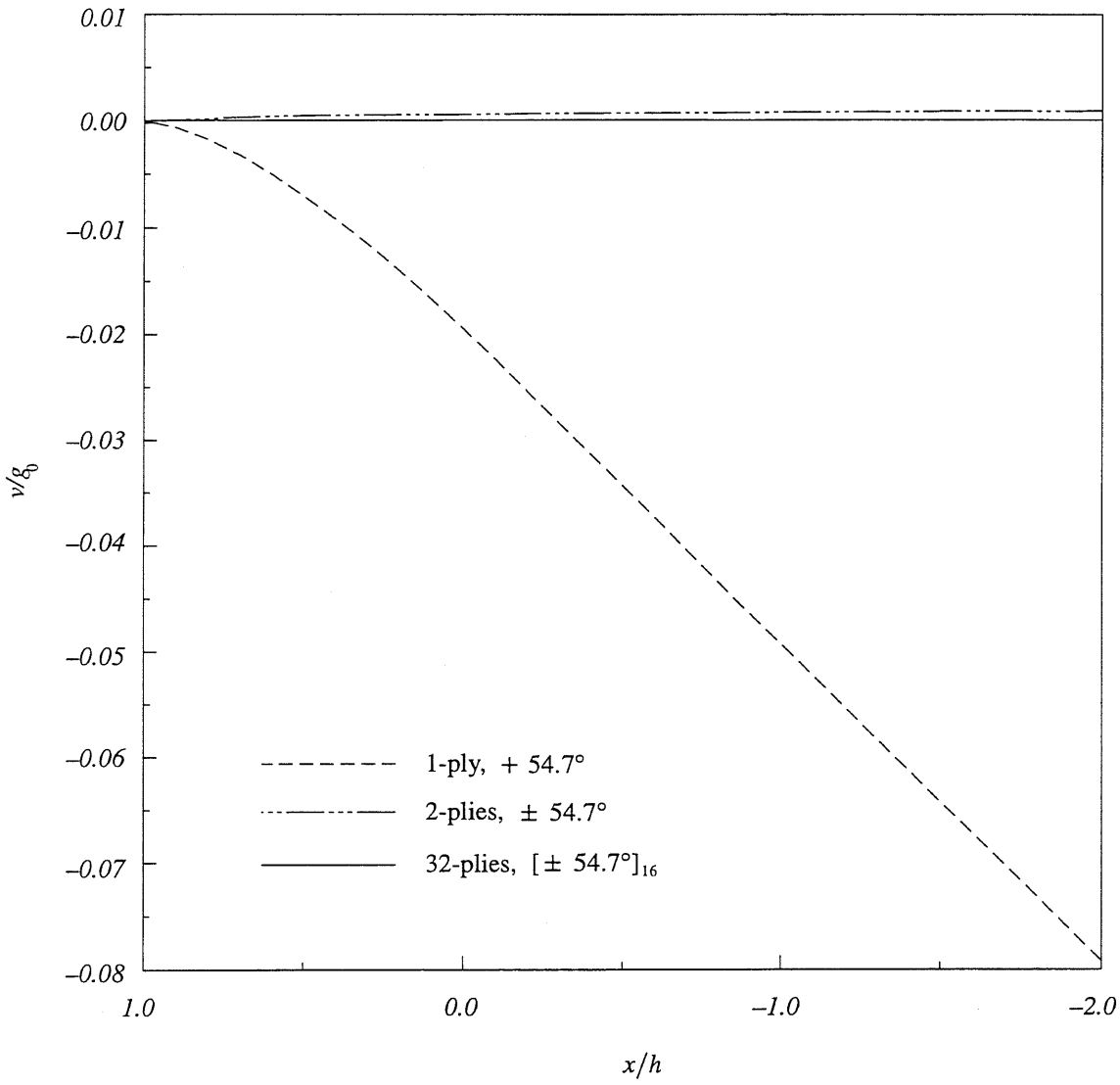

Figure 6.2: Distribution of Circumferential Displacements, ABAQUS (S8R5).

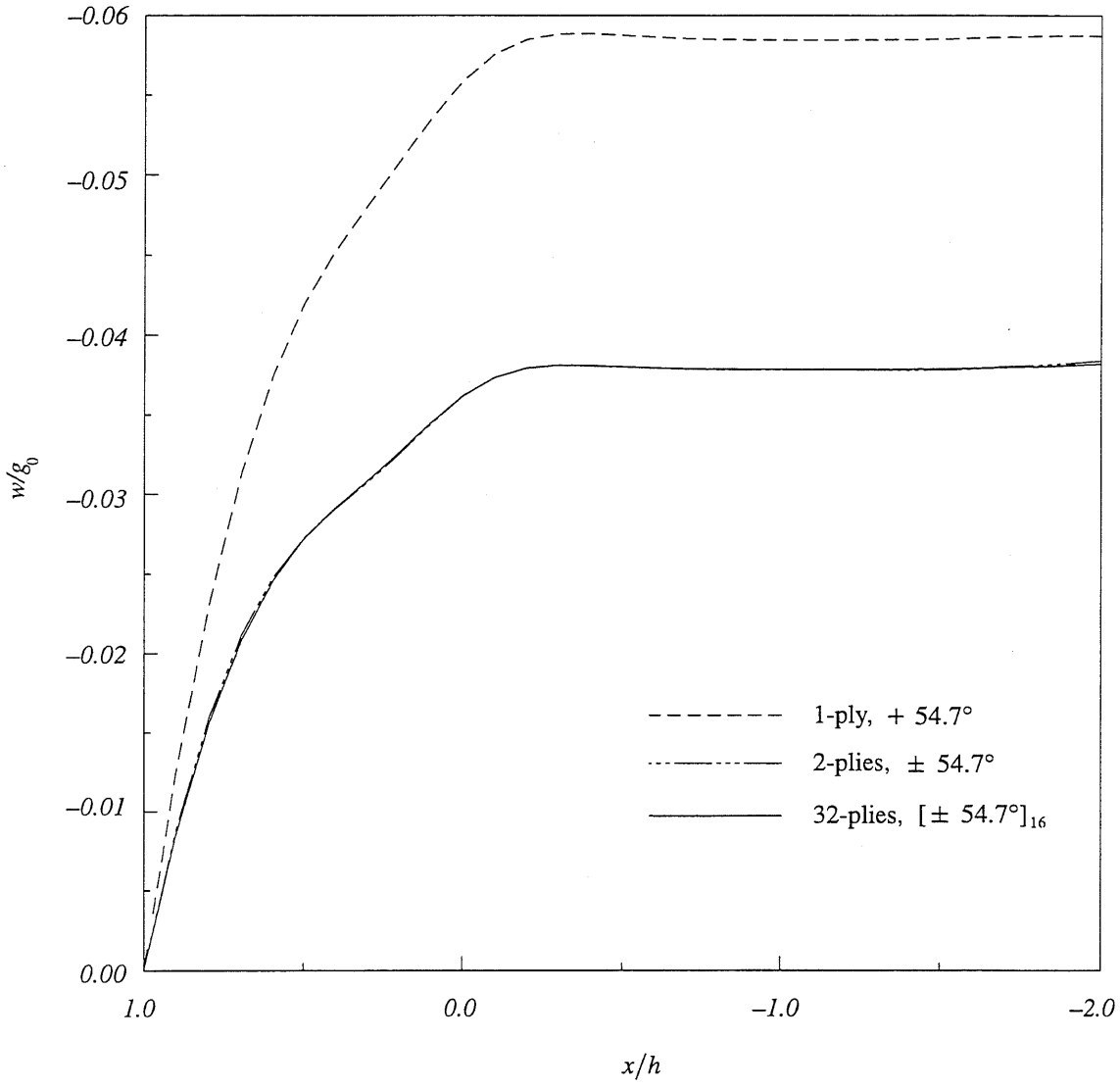

Figure 6.3: Distribution of Axial Displacements, ABAQUS (S8R5).

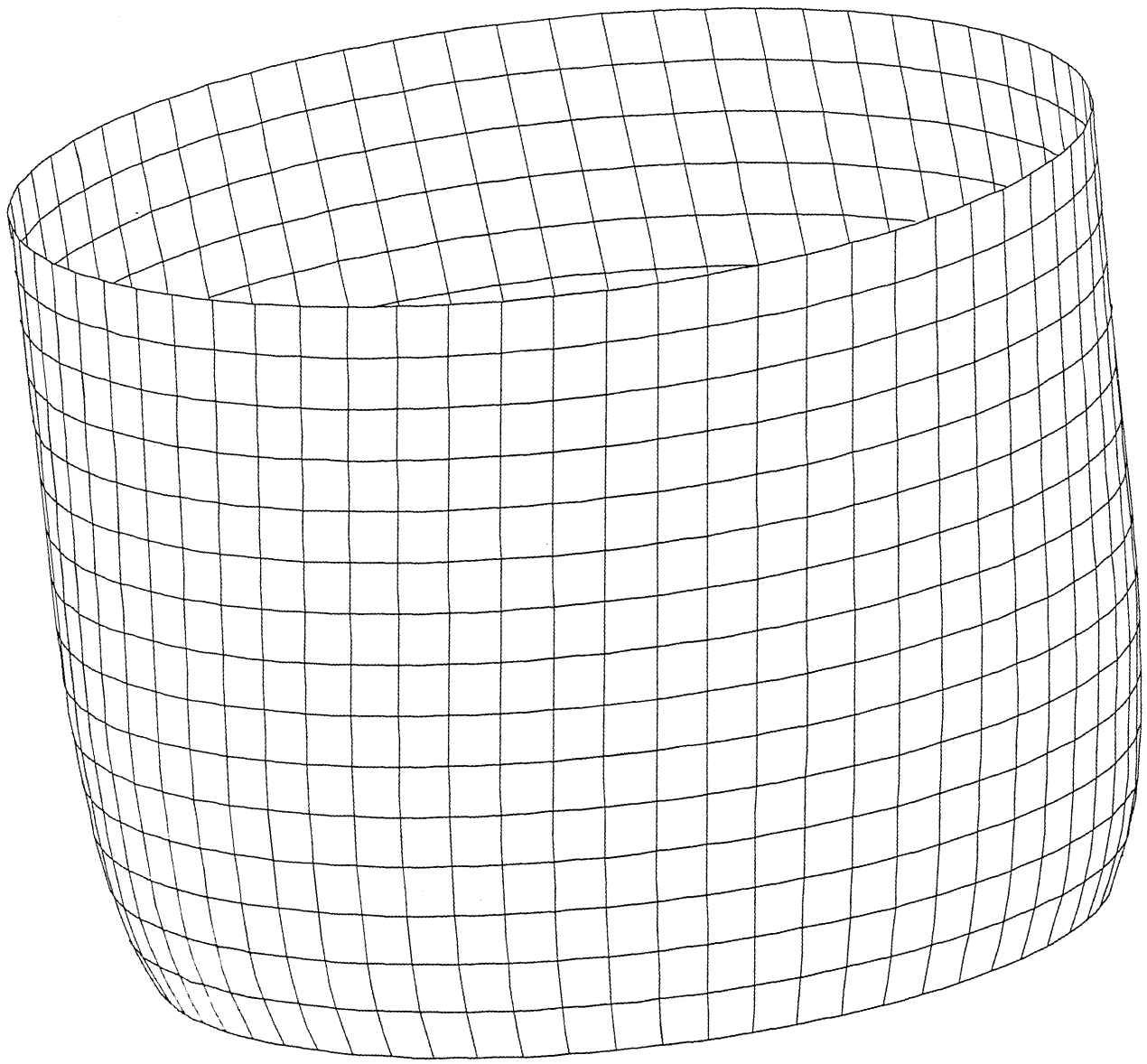

Figure 6.4: Twisting of a Laminated Cylinder, 1-Ply + 54.7°.

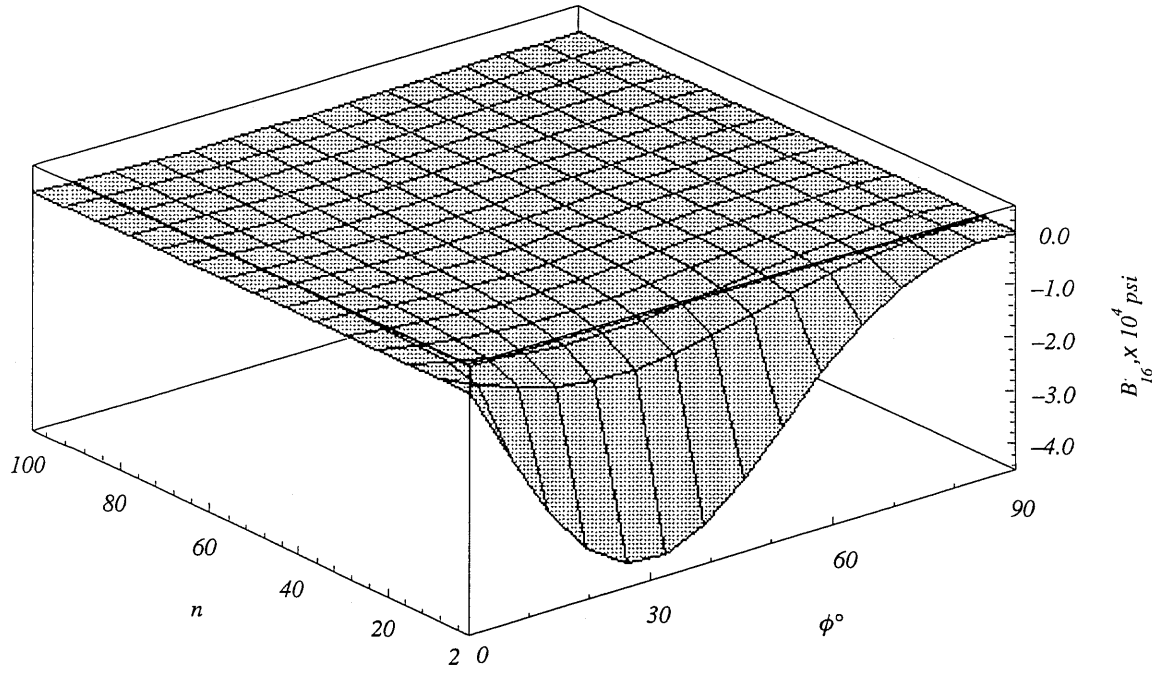

B_{16}

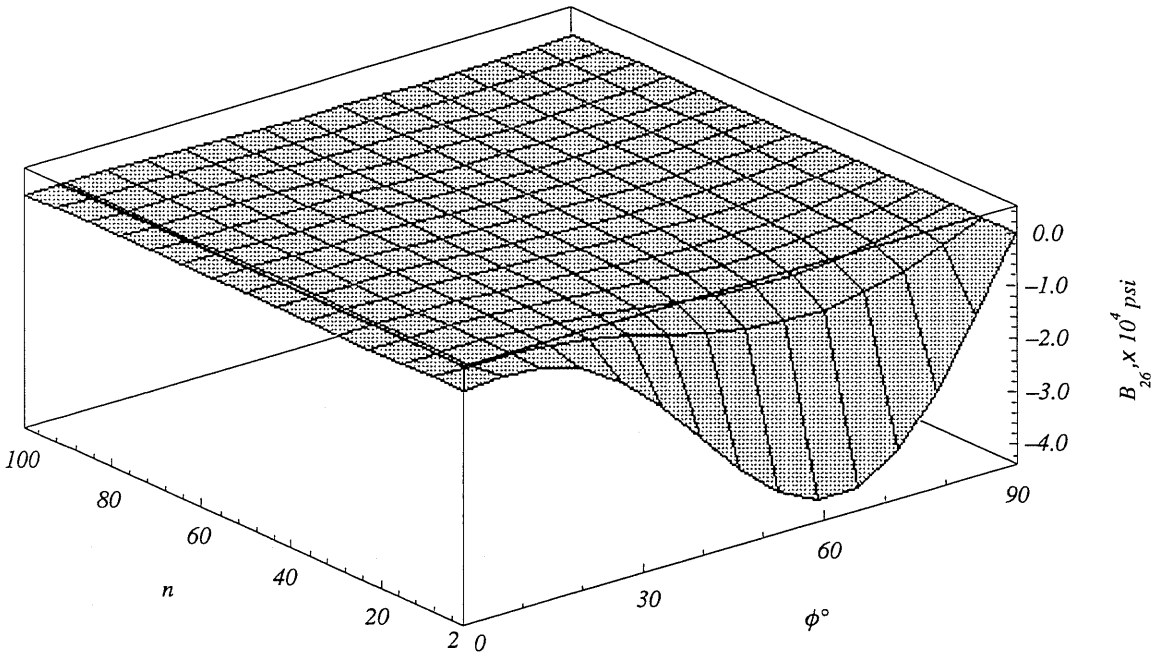

B_{26}

Figure 6.5: Coupling Stiffnesses B_{16} and B_{26} for a Glass/Polyester Angle-Ply Laminate.

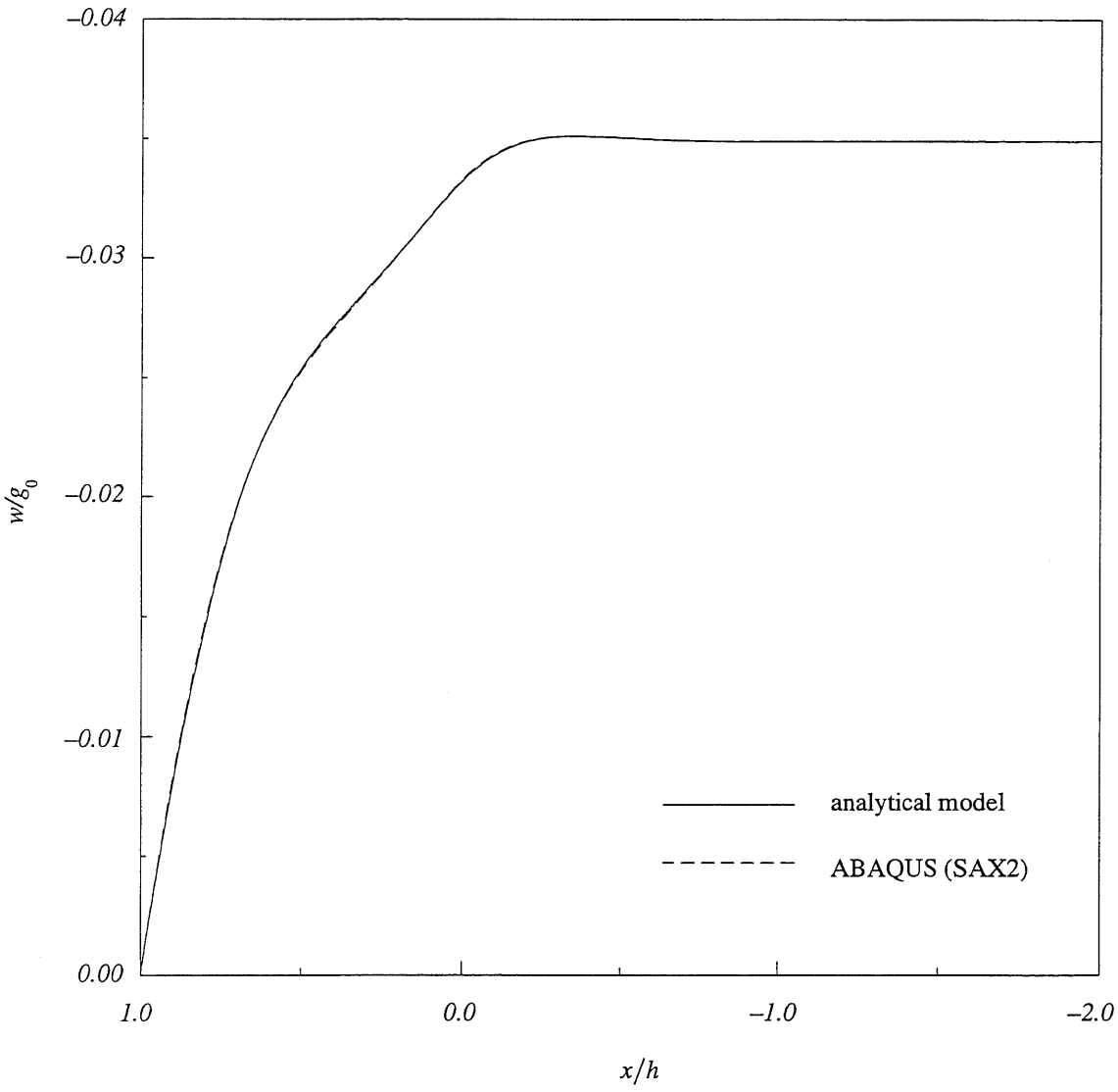

Figure 6.6: Distribution of Radial Displacements, Lay-Up $[0°/90°]_{36}$.

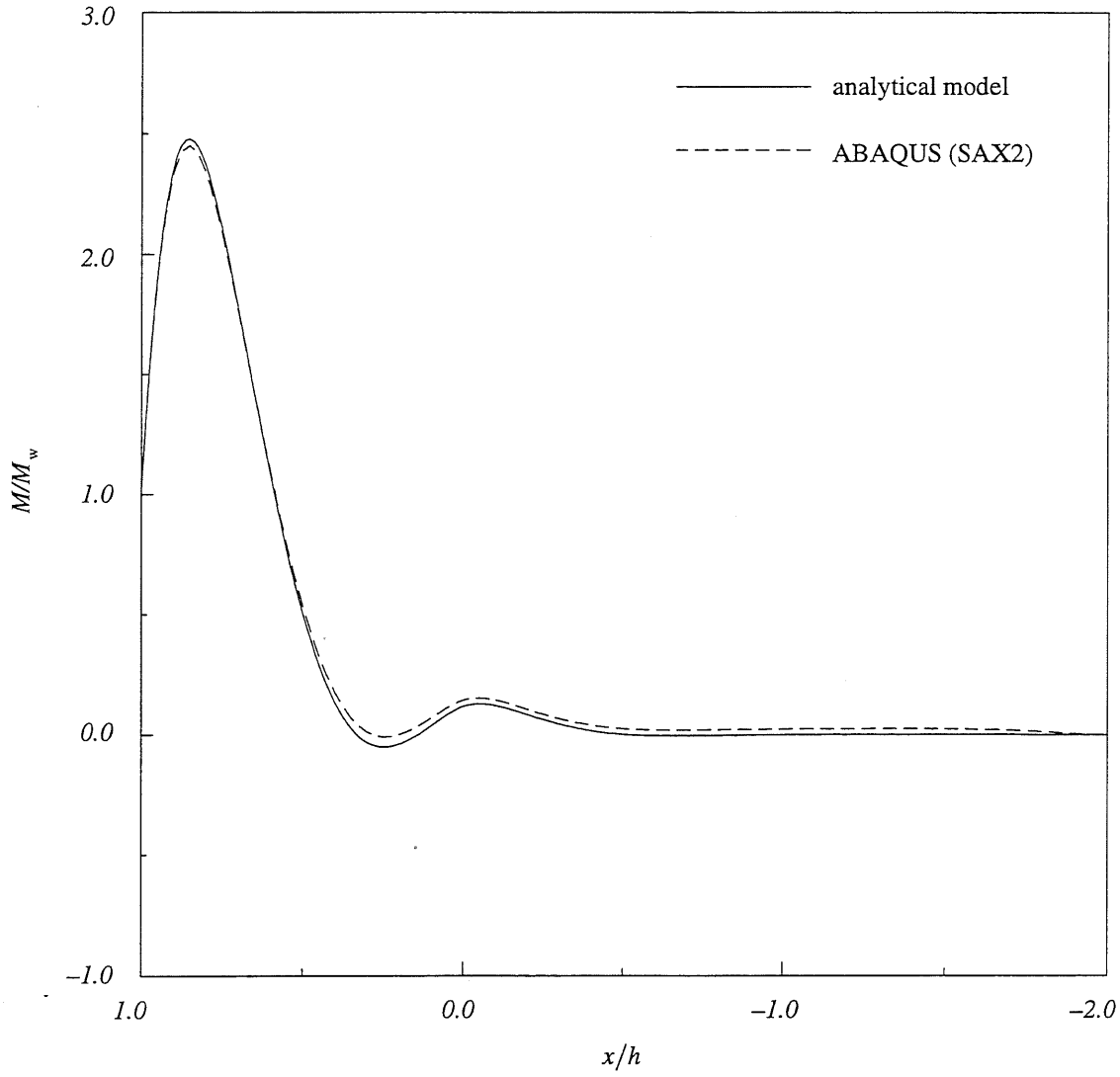

Figure 6.7: Distribution of Axial Moments, Lay-Up $[0°/90°]_{36}$.

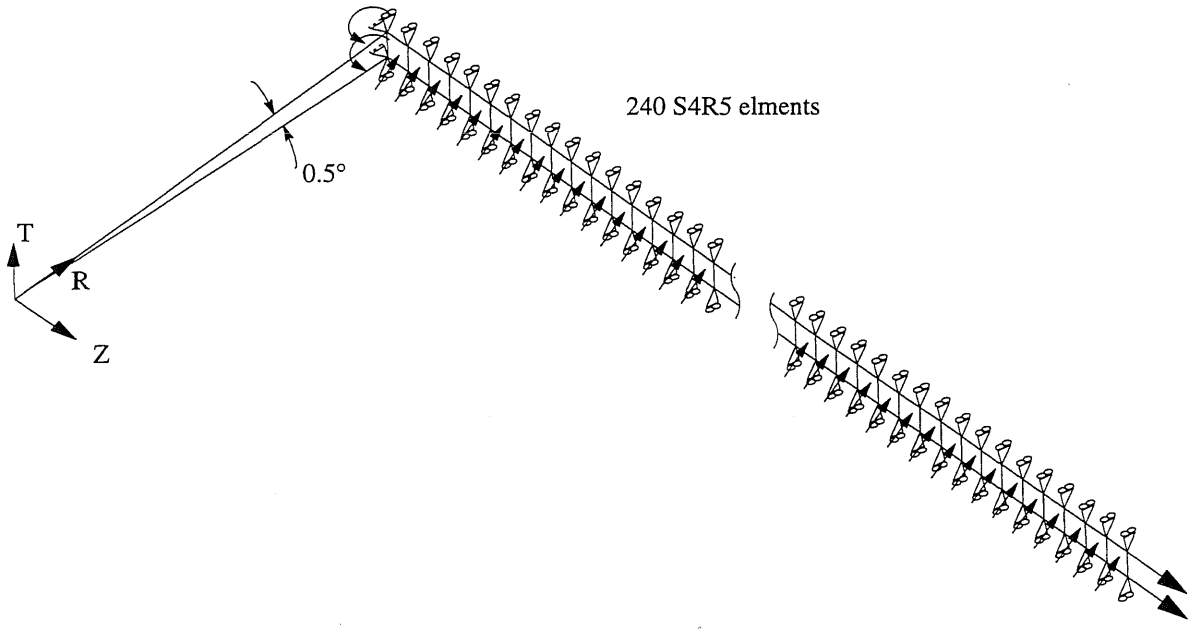

Figure 6.8: Finite Element Mesh for the Verification Problem.

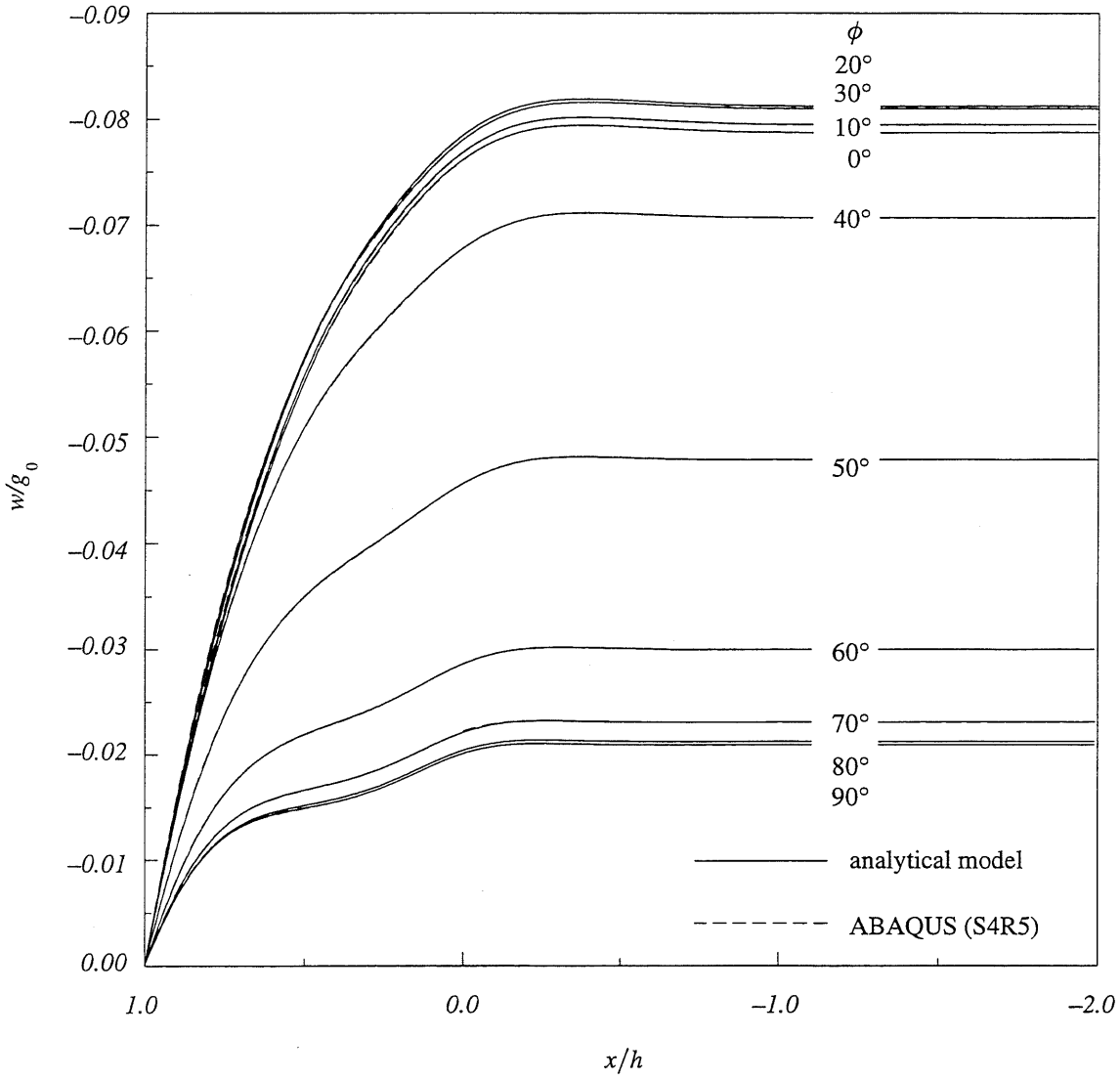

Figure 6.9: Distribution of Radial Displacements, Lay-Up $[\pm\ \phi]_{36}$.

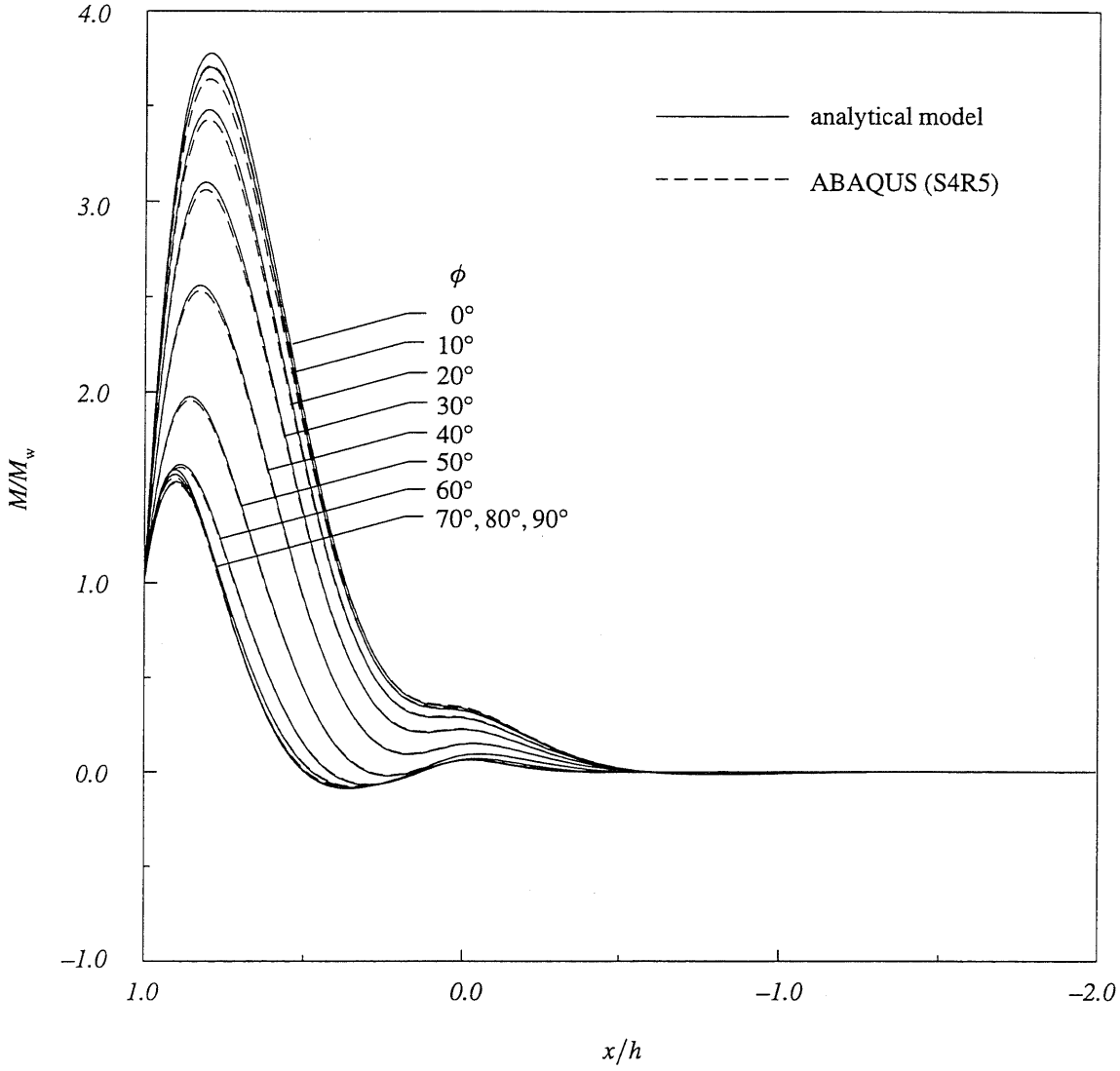

Figure 6.10: Distribution of Axial Moments, Lay-Up $[\pm \phi]_{36}$.

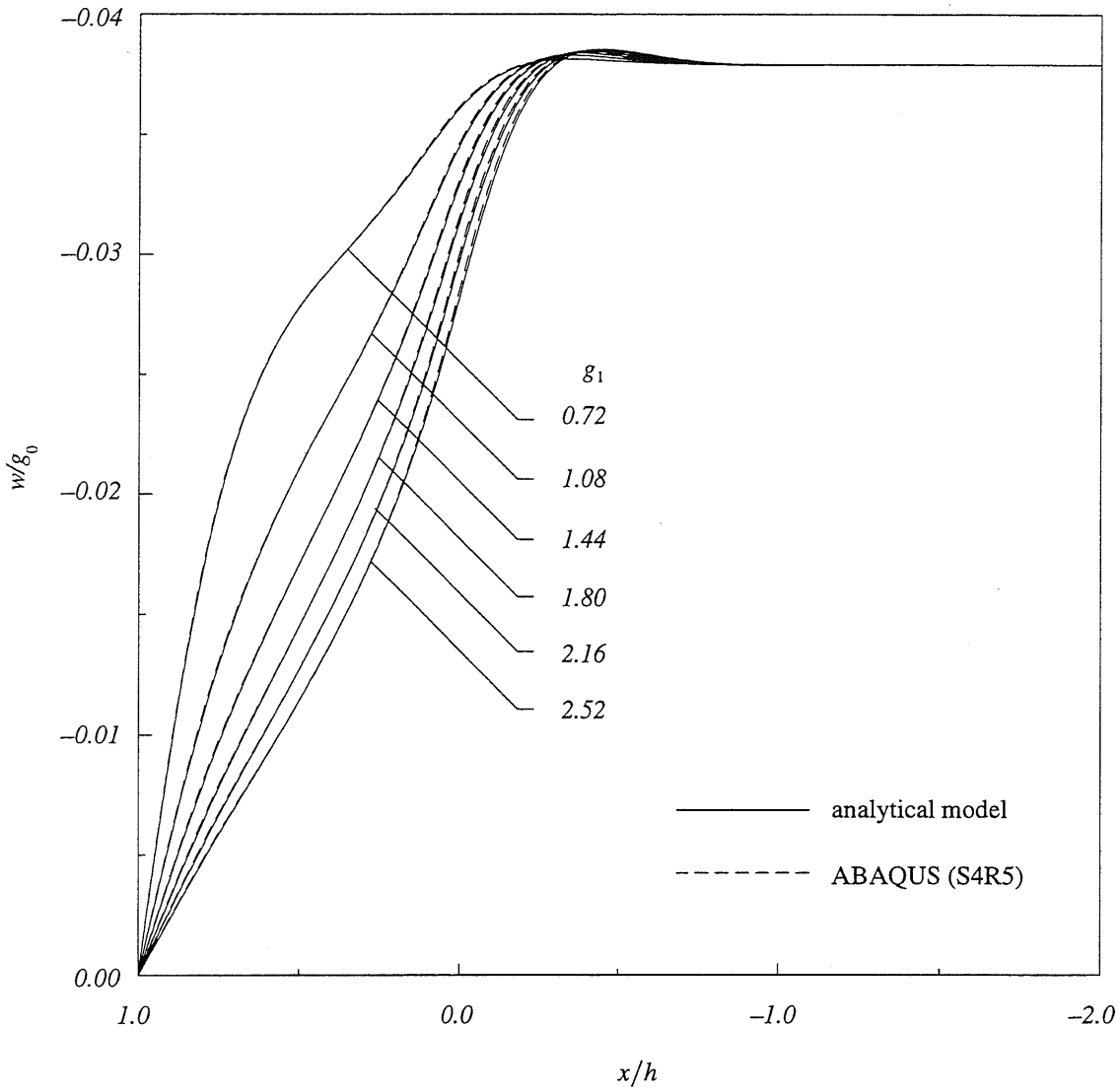

Figure 6.11: Distribution of Radial Displacements for Different g_1, Lay-Up $[\pm 54.7°]_{36}$.

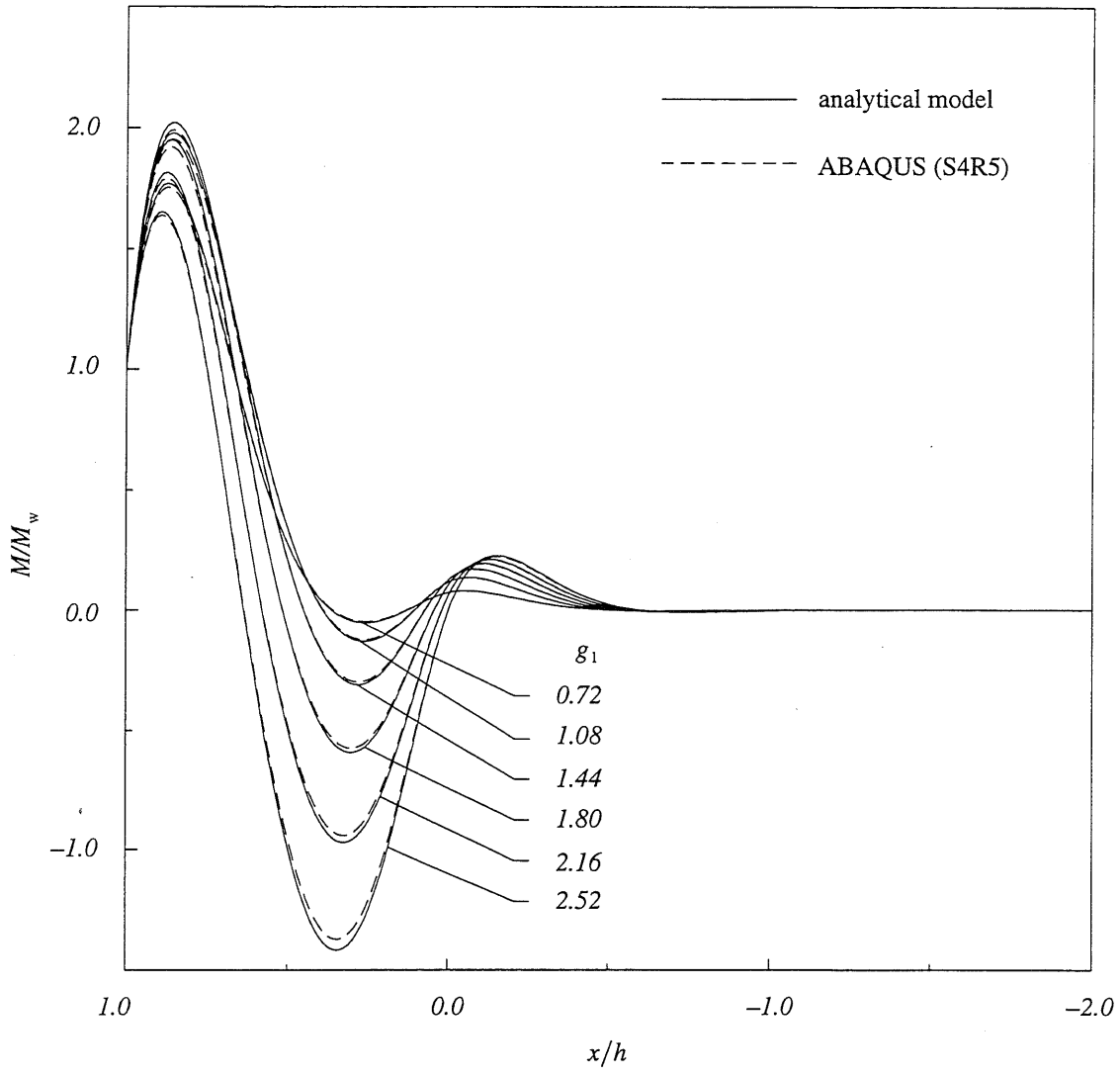

Figure 6.12: Distribution of Axial Moments for Different g_1, Lay-Up $[\pm\ 54.7°]_{36}$.

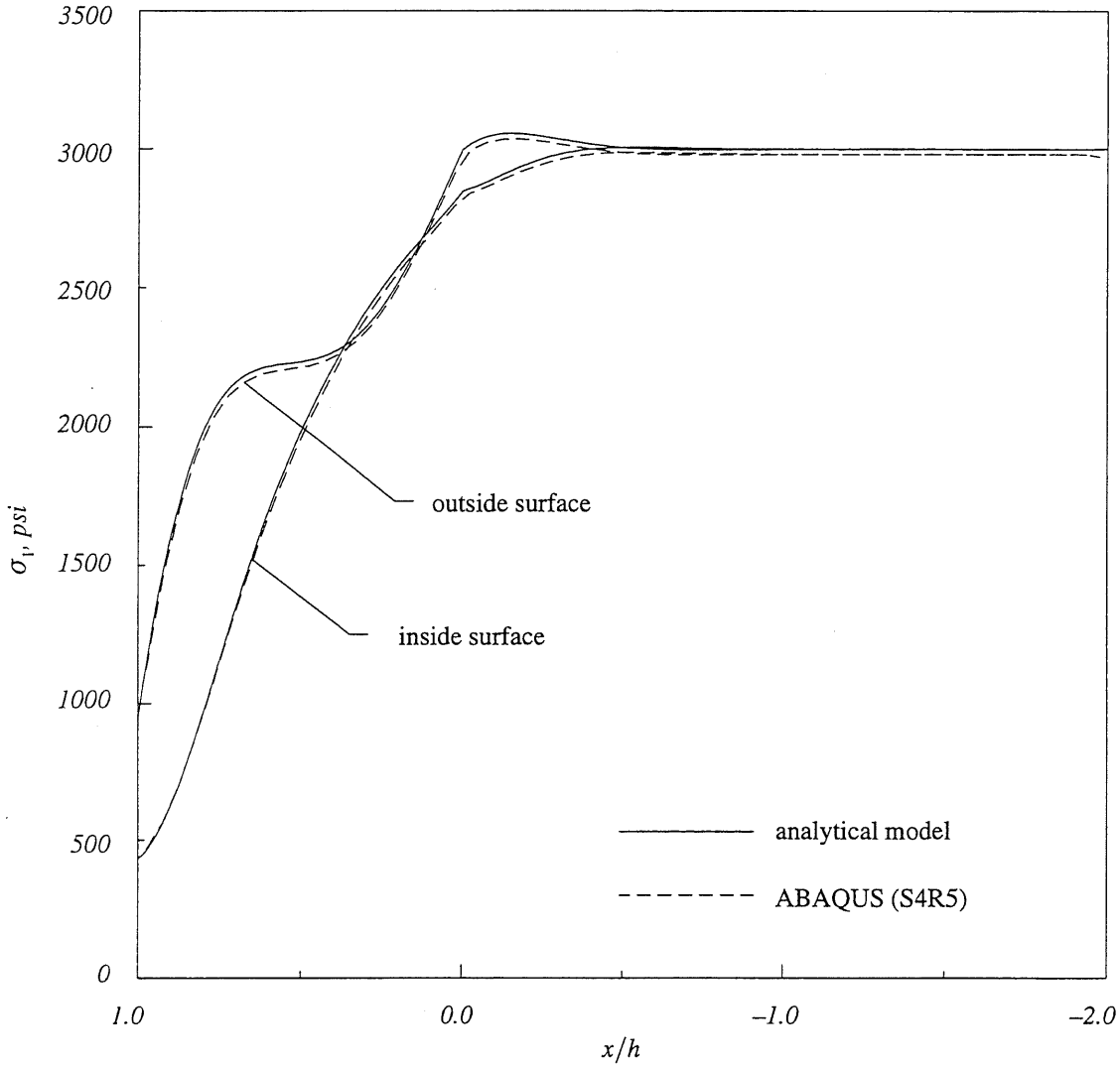

Figure 6.13: Distribution of Axial Stresses, Lay-Up $[\pm\ 54.7°]_{36}$.

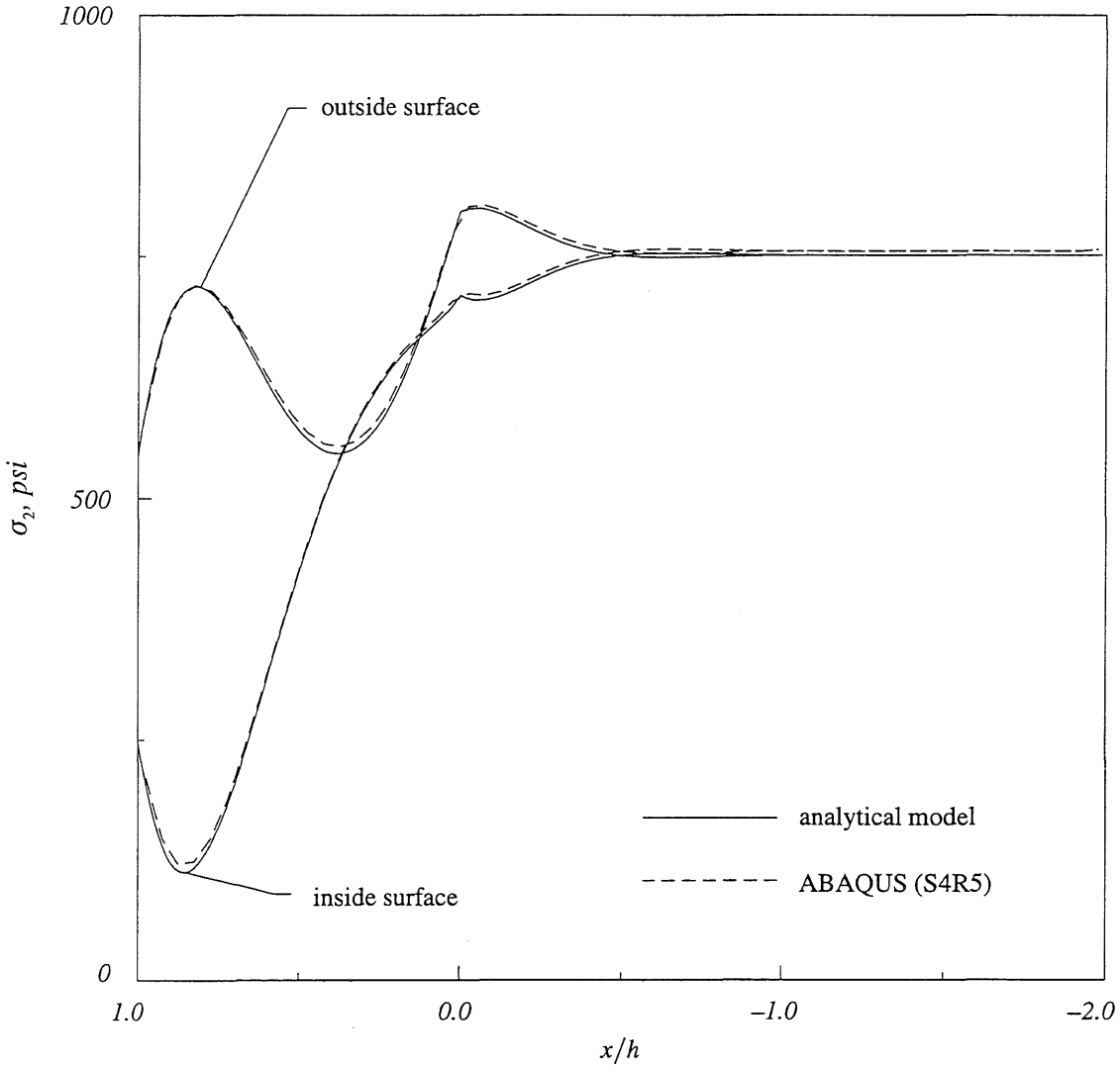

Figure 6.14: Distribution of Circumferential Stresses, Lay-Up $[\pm\ 54.7°]_{36}$.

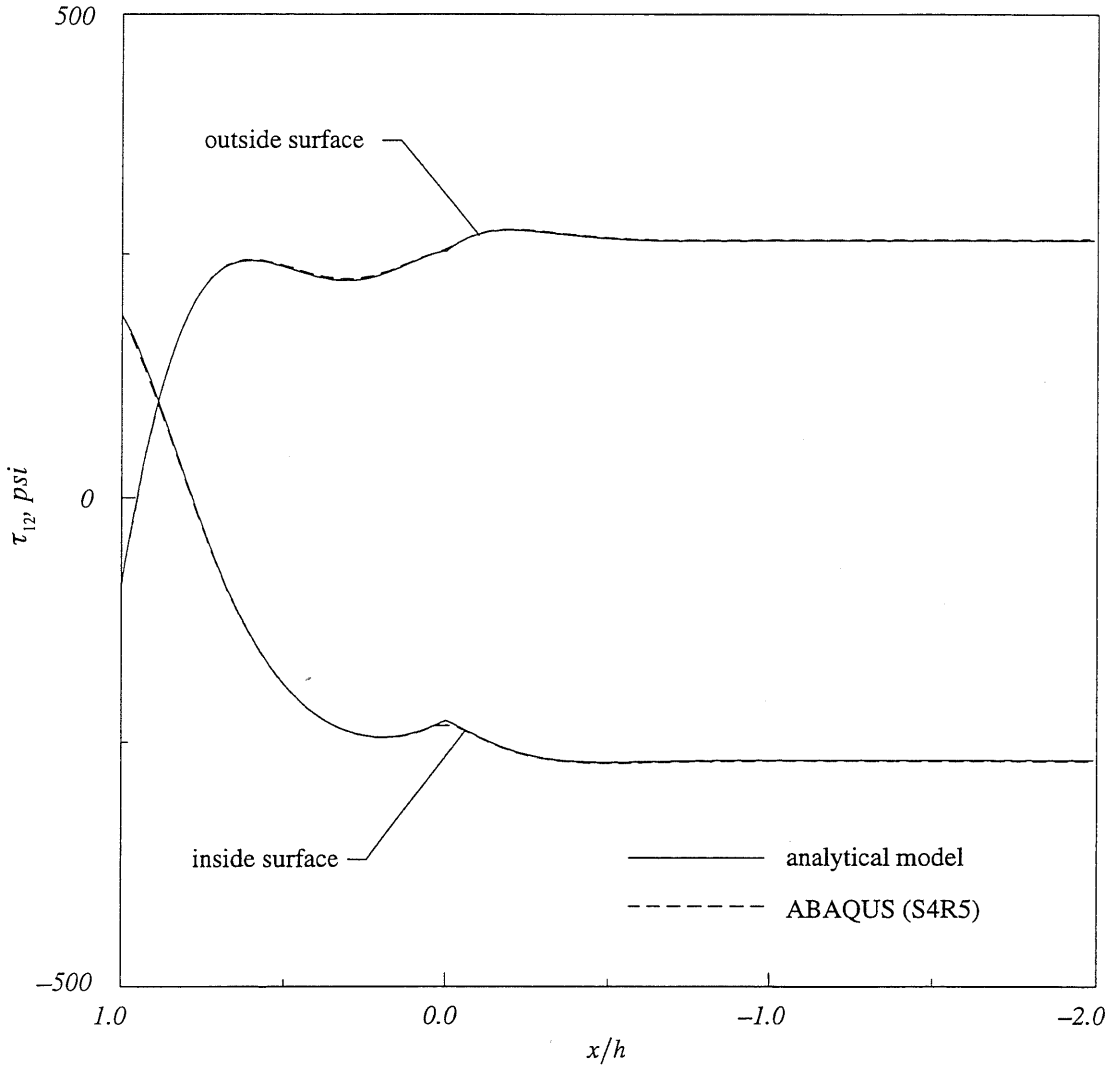

Figure 6.15: Distribution of Shear Stresses, Lay-Up $[\pm\ 54.7°]_{36}$.

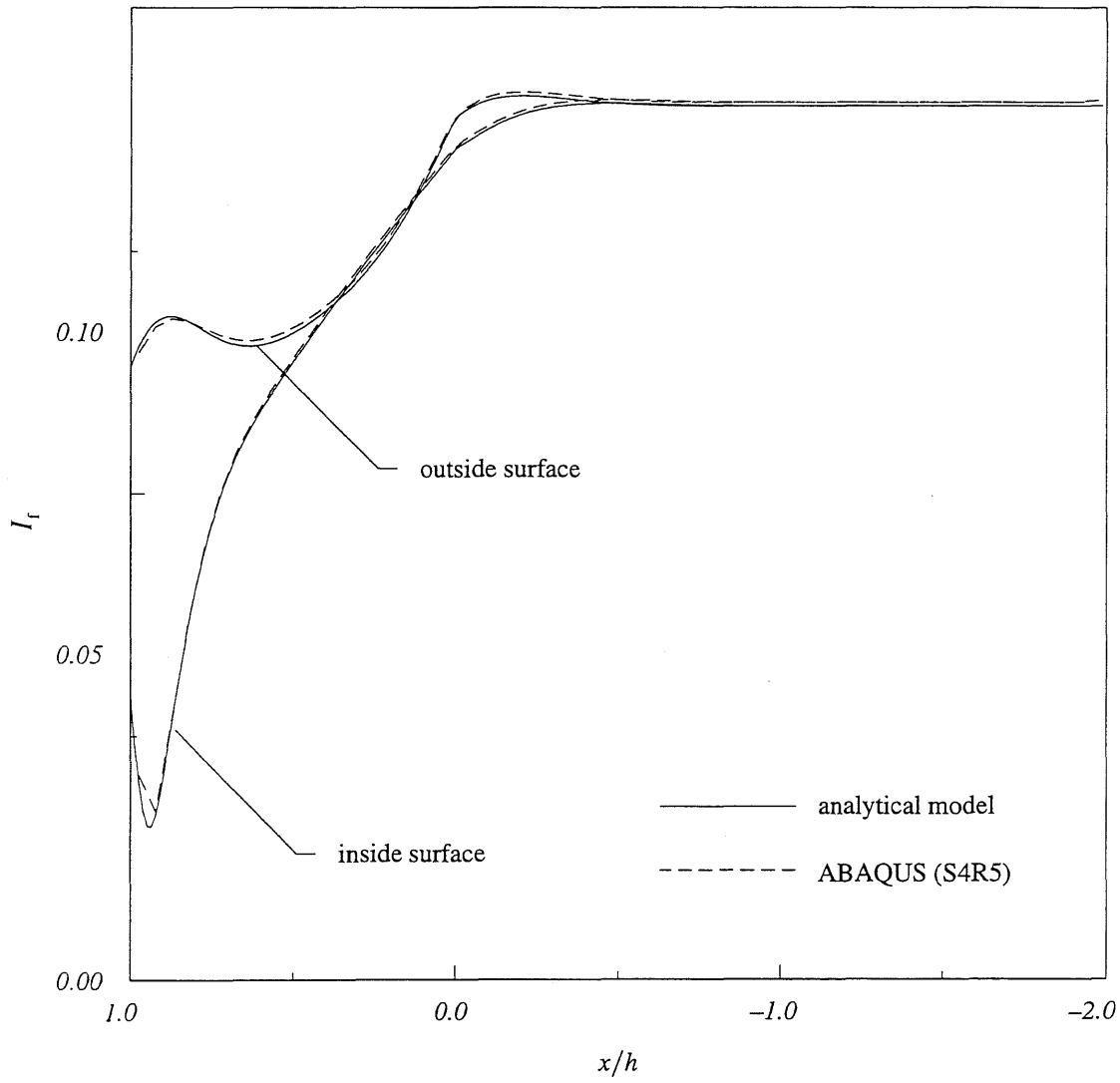

Figure 6.16: Distribution of Tsai-Hill Failure Index, Lay-Up $[\pm\ 54.7°]_{36}$.

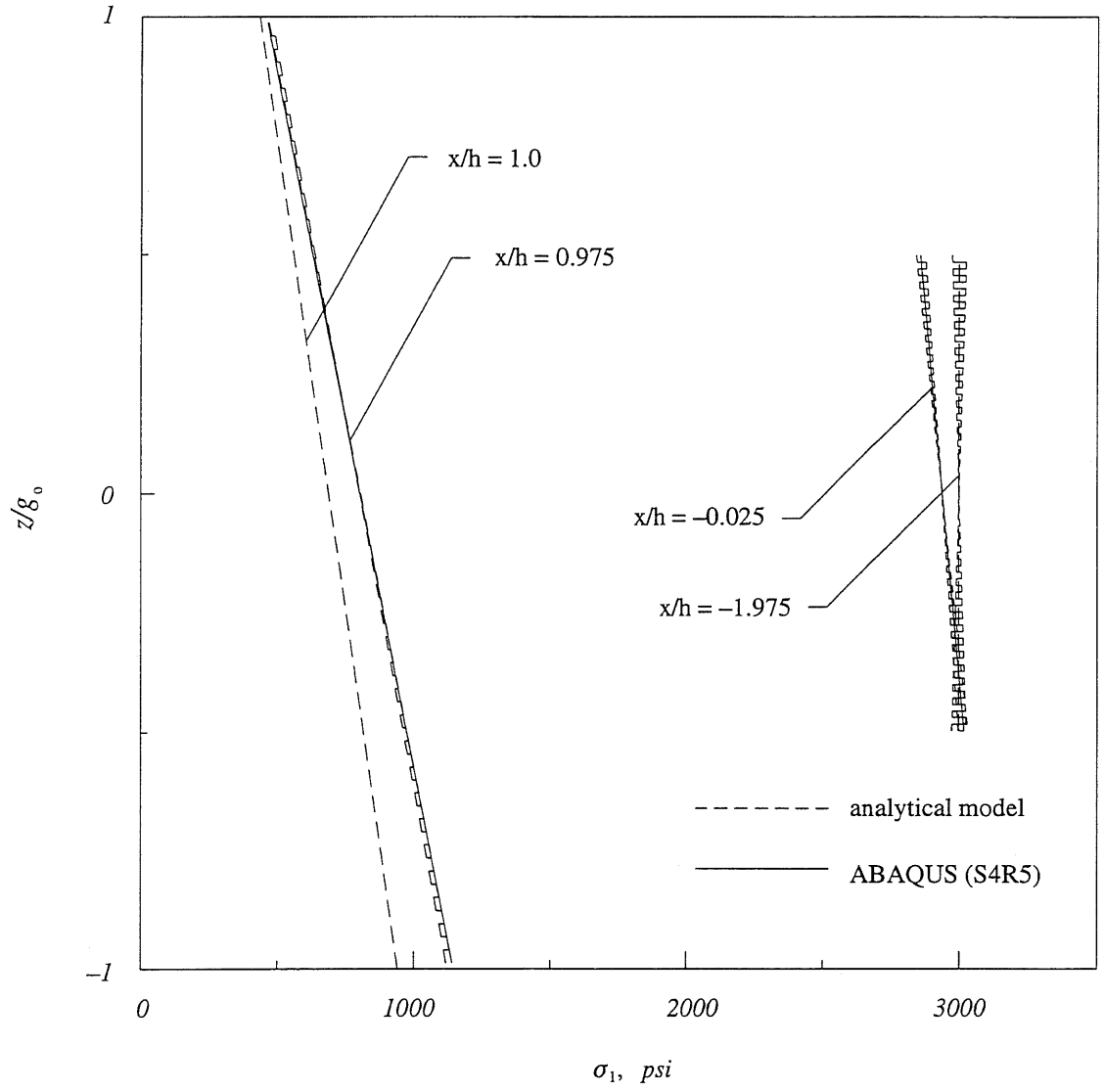

Figure 6.17: Axial Stresses Through the Thickness, Lay-Up $[\pm 54.7°]_{36}$.

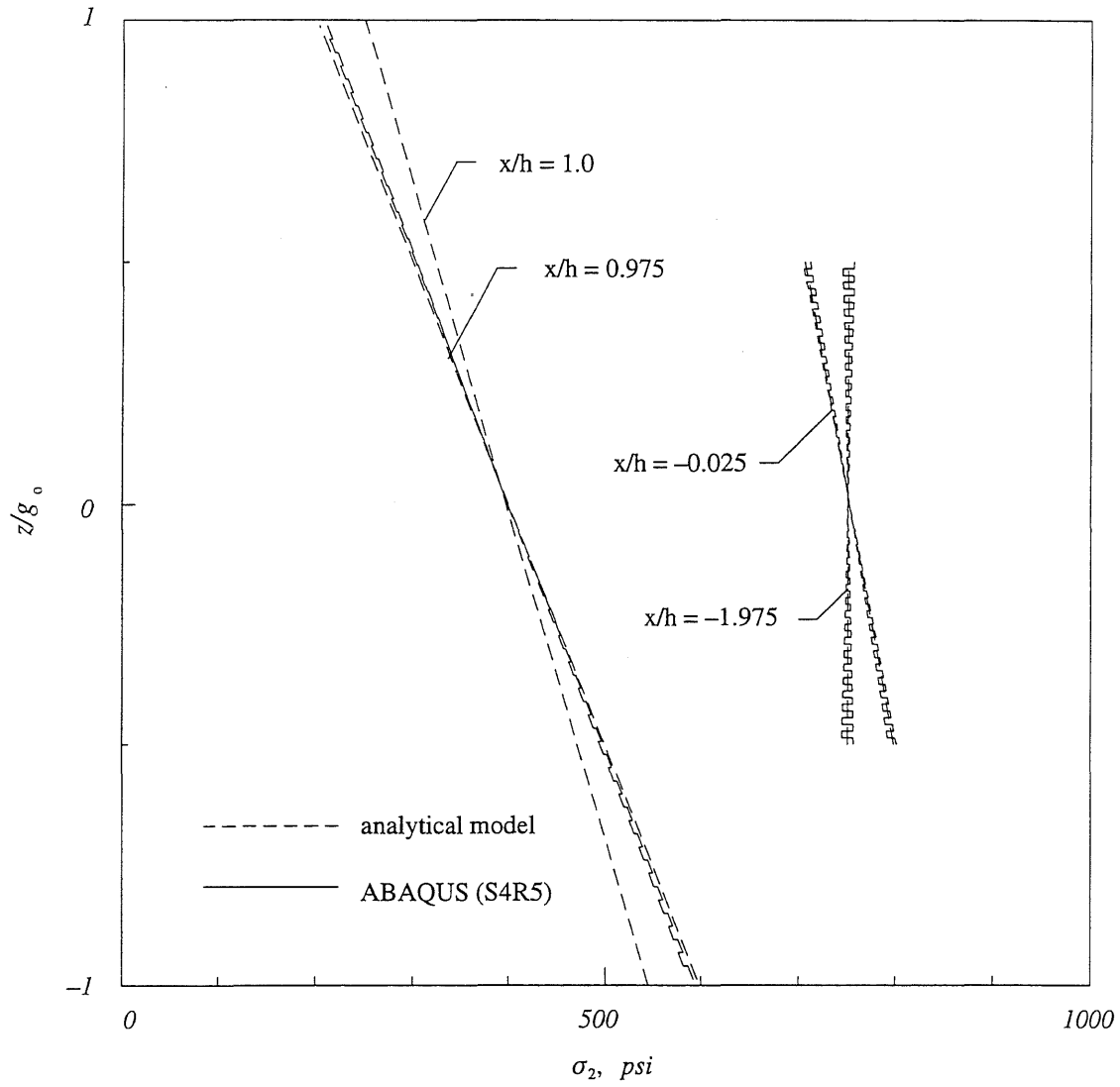

Figure 6.18: Circumferential Stresses Through the Thickness, Lay-Up $[\pm\ 54.7°]_{36}$.

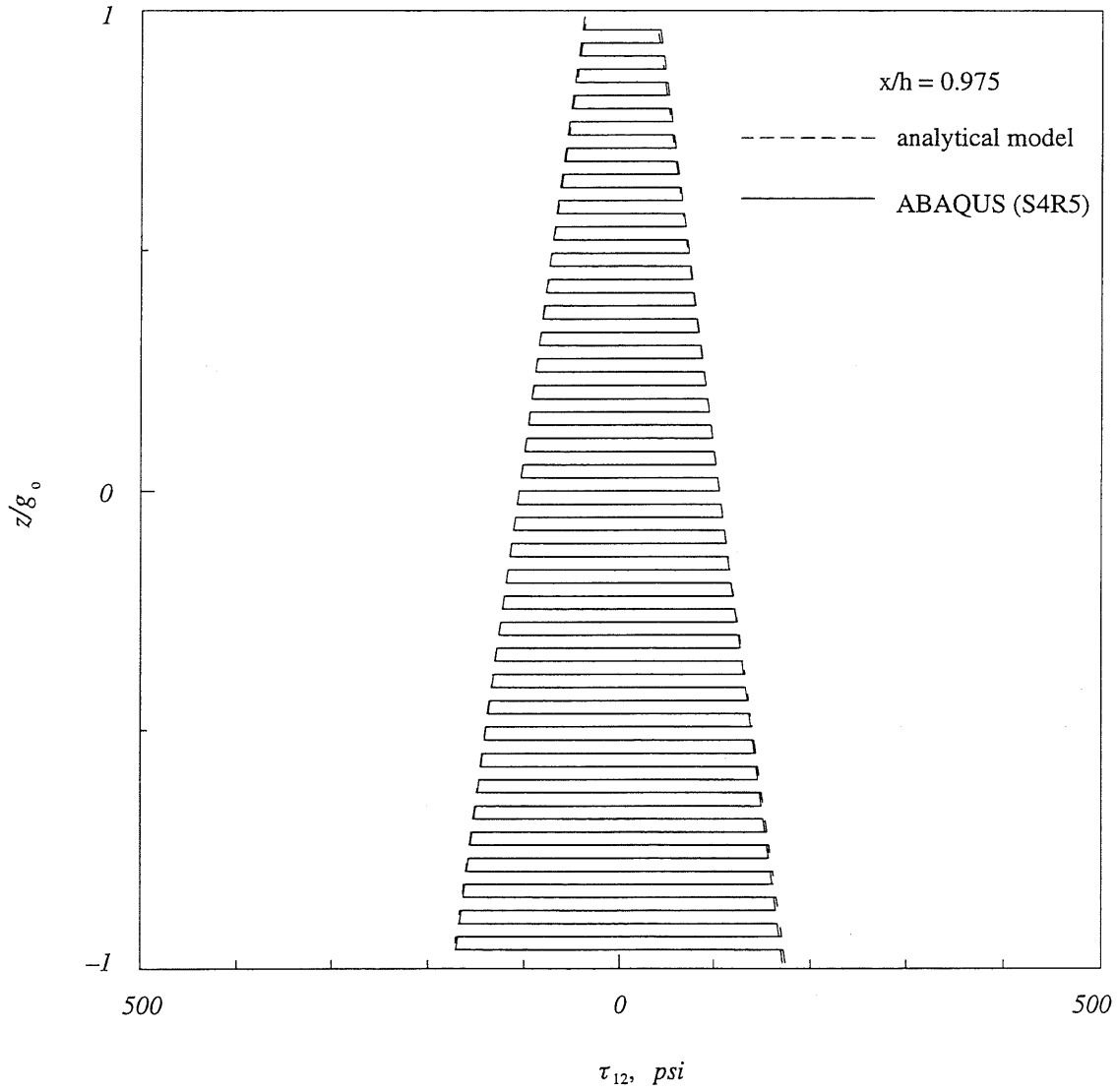

Figure 6.19: Shear Stresses Through the Thickness, Lay-Up $[\pm 54.7°]_{36}$.

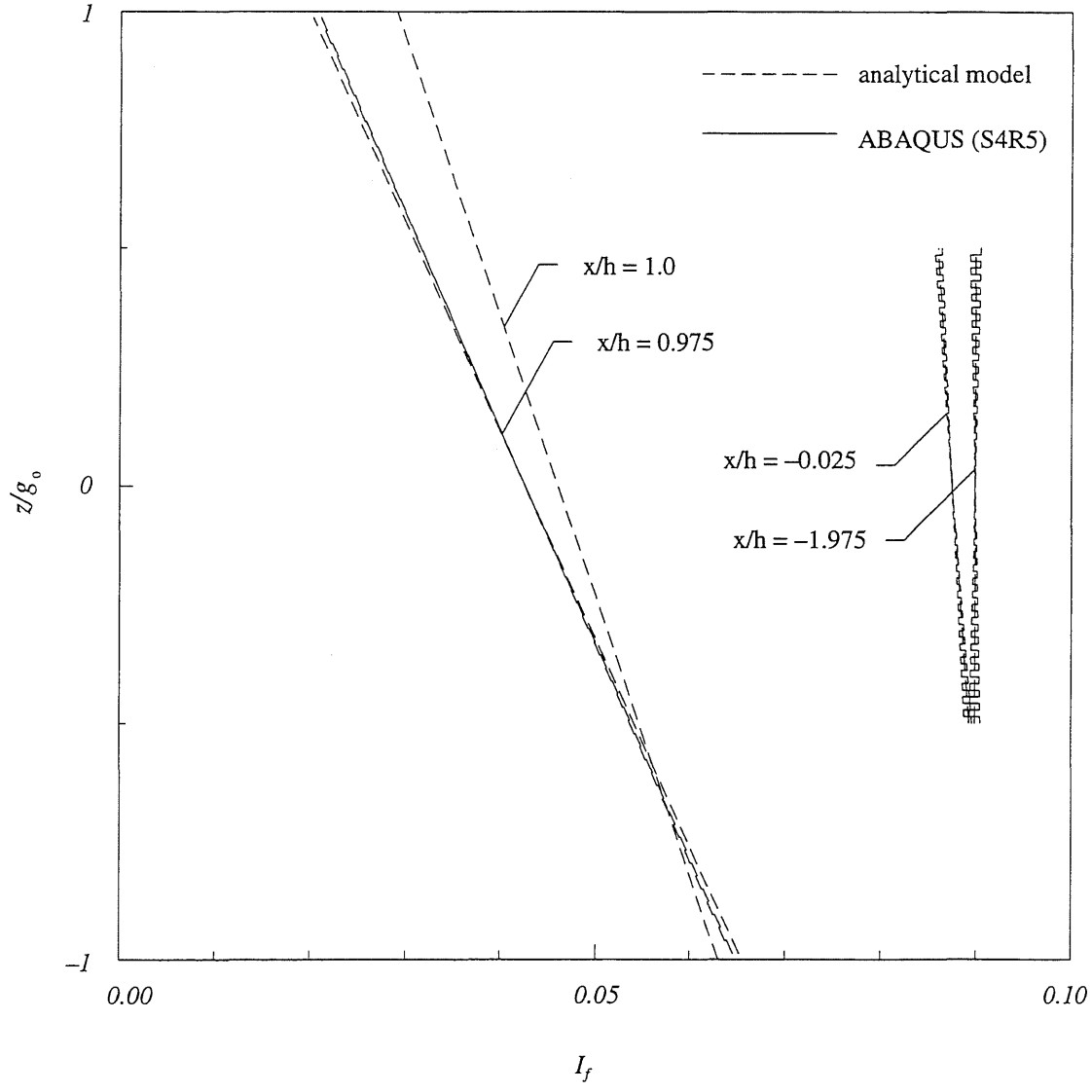

Figure 6.20: Tsai-Hill Failure Index Through the Thickness, Lay-Up $[\pm 54.7°]_{36}$.

Elastic Properties		
	GPa	10^6 *psi*
Longitudinal Modulus, E_{LL}	35.41	5.136
Transverse Modulus, E_{TT}	10.50	1.522
In-plane Shear Modulus, G_{LT}	3.03	0.439
Major Poisson's Ration, ν_{LT}	0.281	
Minor Poisson's Ration, ν_{TT}	0.350	
Strength Properties		
	MPa	10^3 *psi*
Longitudinal Tension, σ_{LLU}	820.0	118.93
Longitudinal Compression, σ^c_{LLU}	610.0	88.47
Transverse Tension, σ_{TTU}	75.0	10.88
Transverse Compression, σ^c_{TTU}	133.0	19.29
In-plane Shear, τ_{LTU}	34.5	5.00

Table 6.1: Unidirectional Strength and Stiffness Properties of Glass/Polyester Composite for a Fiber Volume Fraction of 0.46 [31].

Stub Analysis Results		
	ABAQUS	$\frac{ABAQUS}{model}$
M_{rd}, *in-lbs/in*	1027	1.011
σ_{rd}, *psi*	2736	1.011
$M^{p}_{\theta d}$, *in-lbs/in*	3499	0.982
$\sigma^{p}_{\theta d}$, *psi*	9331	0.982
$M^{r}_{\theta d}$, *in-lbs/in*	25836	0.991
$\sigma^{r}_{\theta d}$, *psi*	17224	0.991

Table 6.2: Analytical Model and ABAQUS Results for the Stub.

Winding Angle, ϕ	*ABAQUS* w_{max} (*in*)	$\frac{w_{max}\ (ABAQUS)}{w_{max}\ (model)}$
0°	–0.02858	1.00
10°	–0.02885	1.00
20°	–0.02947	1.00
30°	–0.02936	1.00
40°	–0.02560	1.00
50°	–0.01732	1.00
60°	–0.01086	1.00
70°	–0.00835	1.00
80°	–0.00769	1.00
90°	–0.00757	1.00

Table 6.3: List of ABAQUS and Analytical Model Maximum Displacements, Lay-Up $[\pm \phi]_{36}$.

Winding Angle, ϕ	*ABAQUS* $M_{x\max}$ ($in\text{-}lbs/in$)	$\frac{M_{x\max}\,(ABAQUS)}{M_{x\max}\,(model)}$
0°	–74.24	0.983
10°	–72.81	0.983
20°	–68.53	0.985
30°	–61.19	0.987
40°	–50.68	0.989
50°	–39.19	0.991
60°	–32.12	0.990
70°	–30.44	0.994
80°	–31.03	0.989
90°	–31.49	0.989

Table 6.4: List of ABAQUS and Analytical Model Maximum Axial Moments, Lay-Up $[\pm\,\phi]_{36}$.

Hub Large End Width, g_1	*ABAQUS* w_{max} (*in*)	$\frac{w_{max}\ (ABAQUS)}{w_{max}\ (model)}$
0.72	–0.01373	1.000
1.08	–0.01378	1.000
1.44	–0.01382	1.000
1.80	–0.01384	1.000
2.16	–0.01386	1.000
2.52	–0.01387	1.000

Table 6.5: List of ABAQUS and Analytical Model Maximum Displacements for Different g_1, Lay-Up $[\pm\ 54.7°]_{36}$.

Hub Large End Width, g_1	$ABAQUS\ M_{x\max}$ ($in\text{-}lbs/in$)	$\frac{M_{x\max}\ (ABAQUS)}{M_{x\max}\ (model)}$
0.72	–35.09	0.991
1.08	–39.06	0.988
1.44	–39.82	0.986
1.80	–38.44	0.985
2.16	–35.85	0.987
2.52	–32.78	0.991

Table 6.6: List of ABAQUS and Analytical Model Maximum Axial Moments for Different g_1, Lay-Up $[\pm\ 54.7°]_{36}$.

Chapter 7

Design Examples

7.1 Introduction

Economic competition forces the engineer to strive constructively for the lowest unit cost over the service life of the structure. This can be accomplished by developing an optimum design. In this investigation, we are not going to study the optimization of the proposed joint using mathematical optimization techniques because of the large number of variables involved. Rather, we will use a parametric sensitivity approach to obtain a satisfactory, not an optimum, design. That is, we vary a number of geometric and material parameters until we achieve a combination which produces stresses in the system within the allowable limits with reasonable economy of materials.

In this chapter, we carry out strength analysis calculations for the design of two modified stub flanges for two piping service conditions, different pipe sizes and operating pressures (both at ambient temperature). In one case, we will proportion the joint for a 36 inch diameter water line under 50 psi internal pressure, *case I*. The second case is an 18 inch diameter water line subjected to 100 psi internal pressure, *case II*.

7.2 Outline of the Design Process

In designing the modified stub flange for a specific application, we follow the calculations presented in chapters 4 and 5. That is, given the internal pressure, operating temperature, pipe inside diameter and thickness, we can proportion bolting and modified stub flange geometry by carrying out the following steps:

(i) Select the gasket, material and thickness:

- *Material*: as we explained in chapter 4, rubber is used in sealing FRP joints because a harder material can damage the hub contact surface. Therefore, we are limited to one type of gasket material, which can be made of different hardnesses. The ASME BPV code [4] lists gasket parameters for two types of rubber gaskets, see table 7.1.
- *Thickness*: the gasket thickness should be kept as small as possible to reduce the possibility of gasket blowout. The pressure acts on the inner edge of the gasket, tending to push it out from between the flanges.

(ii) Compute the bolt loads for both the seating and the operating conditions using equations (4.1), (4.3) and table 7.1. Then, find the minimum required bolt area, equations (4.8).

(iii) Design the bolting system, i.e., choose a bolt type (material), bolt size and compute the design bolt load. From the bolt size, find the actual bolt area, A_b, then compute the design bolt load using equation (4.11). Note that the number of bolts to be employed and the diameter of the bolt circle (bolt spacing) are determined from the metallic flange standards for the pressure temperature ratings specified.

- Choose a bolt type based on service conditions.
- Determine bolt size sufficient to satisfy minimum required bolt area.

(iv) With the design bolt load, after selecting a material system for the flanging components, we can proportion the stub and pipe-hub.

- Choose a material for the stub based on service conditions, usually the same material as for the bolts, but lower strength.
- Choose a material and laminae lay-up for the pipe-hub with suitable chemical resistance to the service environment.
- The guidelines for proportioning the stub are outlined in section 4.4.1. Use the standards found in references [2] and [3] to proportion the outside diameter of the stub and the bolt ring diameter.
- To proportion the pipe-hub, we follow the guidelines in section 4.4.2 and chapter 5.

These four basic steps are shown in figure 7.1. Design iterations for different *l, t, h,* and g_1 can be performed quickly using the computer code described in section 5.7. By using this iterative procedure, a satisfactory design is obtained. We demonstrate the procedure in the next section.

7.3 Design Examples

To demonstrate the design process we use a sample calculation sheet such as the one used for metallic flanges [5]. The design sheets for design *case I* and *case II* are depicted in figures 7.2 and 7.4 respectively. This is a very effective way of presenting the design conditions, geometry and calculations. On the left column we specify the problem conditions and on the right hand side of the sheet the design calculations. Hence, it is easy to follow the design philosophy. That is, once we have determined the design conditions, for a specific choice of material system, we carry out the design calculations for a specific l, t, h, and g_1. If the stresses in the stub are below the allowable limit and the constraint on I_f is not violated, we have the final design; otherwise we repeat the calculations with a different l, t, h, and g_1 until the inequalities are satisfied. We can also vary the winding angle to find the strongest material system for the given loading. However, as stated in chapter 6, we will focus on a winding angle of 54.7° because this is used to wind most filament wound pipes. Furthermore, a different material system with superior properties can be used to satisfy the inequalities, probably at a higher cost. Depending on the application, combinations of all these strength enhancing procedures can be used to arrive at a satisfactory design.

The design conditions for the two cases are the same except for the design internal pressure and the geometry. The material properties for the composite system were presented in chapter 6. The properties for the bolting, the stub and the gasket were extracted from the ASME BPV code Section VIII [4]. In both cases, the material lay-up for the composite system is chosen arbitrarily, and is typical of similar systems reported in the literature [32].

The pipe thickness is computed from the membrane hoop stress equation, $g_0 = pB/2\sigma_a$, for an allowable stress σ_a, which is usually taken to be 2500 psi [27]. From this equation, we get a pipe thickness of 0.36 inches in both cases. Further details on pipe design are covered in ASTM D 2996 Standard Specification for Filament Wound Fiberglass (Glass-Fiber-Reinforced Thermosetting-Resin) Pipe [10].

Although PS 15-69 voluntary product standard [42] recommends a gasketing material with durometer hardness of 40 to 70 degrees for FRP joints, we use a gasket with durometer hardness of 75 degrees [12]. The reason for using this gasket material is that we were unable to find material properties for gaskets of lower hardness in the literature. The material properties will be used in the next chapter to conduct a detailed finite element analysis of the joint.

The geometry of the joint, except for l, t, h, and g_1, were extracted from the standards found in references [2] and [3]. There are other practical restrictions on the dimensions of the

stub and hub [1], e.g., dimension R must be large enough to fit the wrench when tightening the bolts. Therefore, in some cases it may be impractical to use a stub with a ring; in these cases, a uniformed thickness plate can be used for the stub.

On the right column, we begin the analysis with an arbitrary h and g_1, then we compute the required bolt load to maintain the joint leak tight under both seating and operating conditions. One of these two loads governs the bolting design. With the required bolt load known, we choose the bolting system, which we use to compute the actual bolt area used in the assembly of the joint. From this actual bolt area, we compute the design bolt load. This design bolt load is then used to proportion the stub and the pipe-hub components.

Notice that we have chosen an annular ring thickness, t, equal to the ring stiffener height, l, in both designs. We made this choice because it may be more economical to machine the stub out of a flat plate than to custom fabricate it (with a longer ring stiffener height that the annular plate thickness in order to save some weight), since the savings in weight achieved by using a thinner annular plate thickness does not compensate the extra expense in fabricating the stub using the computed values. However, for cases where the computed ring stiffener height is much larger than the annular plate thickness, the designer is justified in using different values for the two dimensions.

With the design bolt load known, we can find the effective end moment, which we use in the pipe-hub analysis calculations. Once we know the stresses, we can check for first ply failure using the Tsai-Hill failure criterion. We iterate for h and g_1 until the failure index inequality is satisfied.

In figures 7.3 and 7.5 we plot the inner and outer ply Tsai-Hill failure index along the entire length of the pipe-hub system for design *case I* and *case II* respectively. The uppermost points in the plots represent the failure envelope, i.e., the most severely stressed plies are on the inner surface first, then on the outer surface and finally both inner and outer plies are equally stressed. These plots show that the factor of safety for the pipes is about ten and that for the hubs is around five, *case I* is 5.35 and *case II* is 5.25. The ASME code requires a factor of safety of five for filament wound vessels with uncut filaments [5]. Also, for comparison purposes, we show the results of the analytical and finite element models, which agree well.

7.4 Summary

In this chapter we have demonstrated the simplicity of the design process. The design sample calculation sheet can be programmed in a spreadsheet shielding the designer from the

mathematics of the formulation. The designer simply needs to choose a material system for the different joint components and vary l, t, h, and g_1 until a satisfactory design is achieved. The material lay-up for the FRP portion of the joint and the pipe thickness are obtained from the pipe design. We make the recommendation that a factor of safety of at least five be used in the design of the modified stub joint when there is uncertainty in the material properties; however, for cases where the material properties are known to a high degree of certainty, a lower factor of safety may be used. In the next chapter we conduct a detailed finite element analysis for the design *case I*.

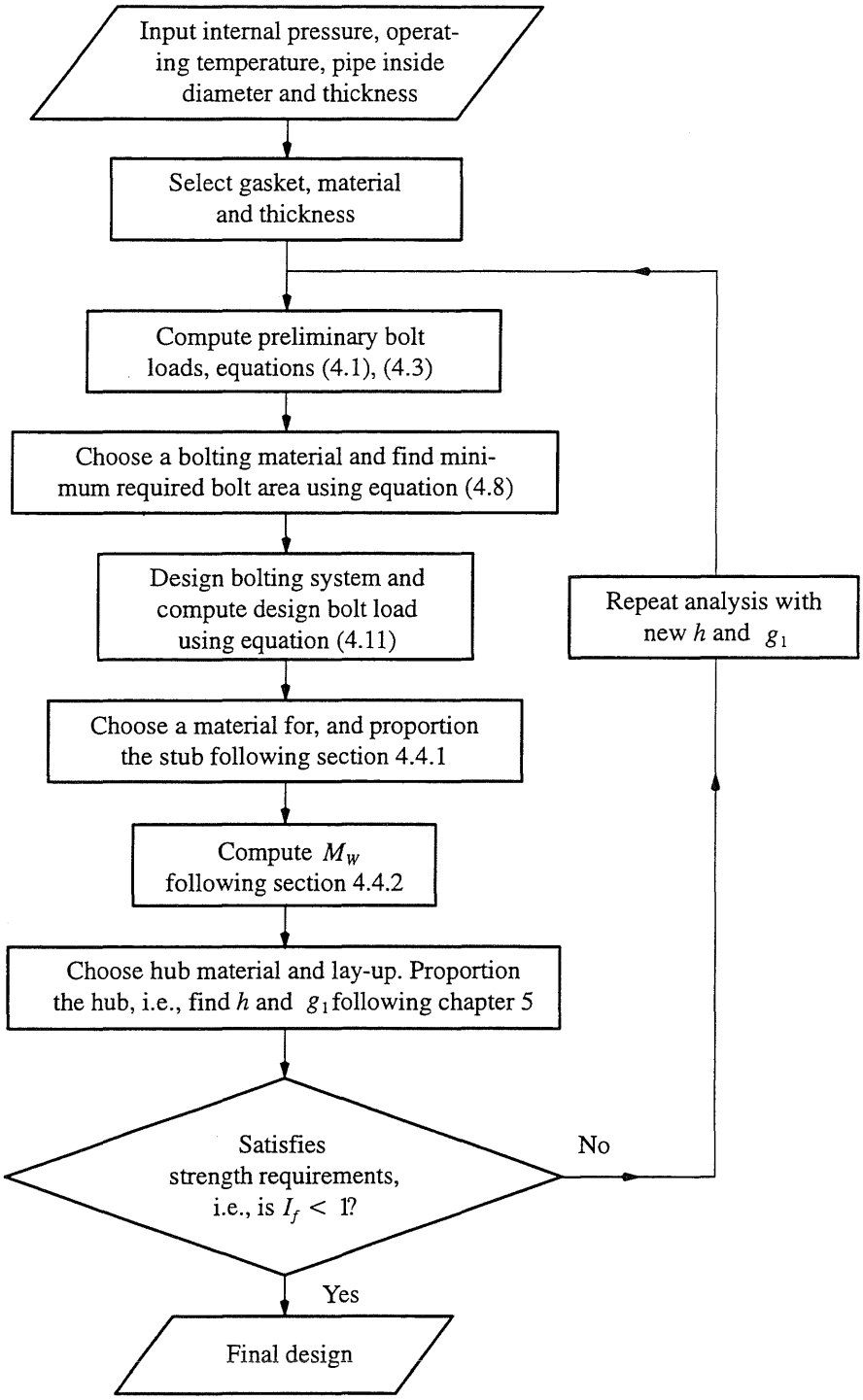

Figure 7.1: Design Sequence.

DESIGN CONDITIONS	
design pressure, p	50 *psi*
design temperature	150 °*F*
flanging material	
pipe-hub, $[\pm 54.7°]_4$ Glass/Polyester [32]	
E_{LL}	5.136×10^6 *psi*
E_{TT}	1.522×10^6 *psi*
G_{LT}	0.439×10^6 *psi*
ν_{LT}	0.281
ν_{TT}	0.35
σ_{1U}	118.93×10^3 *psi*
$\sigma^c{}_{1U}$	88.47×10^3 *psi*
σ_{2U}	10.88×10^3 *psi*
$\sigma^c{}_{2U}$	19.29×10^3 *psi*
τ_{12U}	5.00×10^3 *psi*
σ_c^{resin}	19.29×10^3 *psi*
stub, steel, SA-105 [4]	
allowable stresses: design temp., S_{sb}	17500 *psi*
allowable stresses: atm. temp., S_{sa}	17500 *psi*
bolting, steel, SA-320 Gr. L7M, [4]	
allowable stresses: design temp., S_b	20000 *psi*
allowable stresses: atm. temp., S_a	20000 *psi*
gasket, Neoprene, 75 durometer, [4]	
m	1.0
y	200.0 *psi*
thickness	1/8 *in.*

Geometry

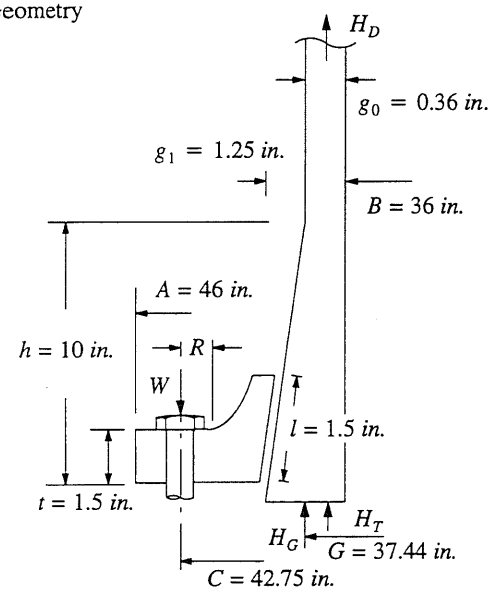

32 – 7/16'' ϕ bolts, 16 threads/in [11]

DESIGN CALCULATIONS	
choose a g_1	1.25 *in*
choose an h	10 *in*
compute design bolt load	
$W_{m1} = \pi p G^2/4 + 2\pi b G m p$	61803 *lbs*
$W_{m2} = g_1 \pi G y$	29256 *lbs*
$A_m = \max(W_{m1}/S_b, W_{m2}/S_a)$	3.09 in^2
A_b	3.19 in^2 32 – 7/16" ϕ bolts
$W = S_a A_b$	63800 *lbs*
proportion the stub	
$N_W = W\left(\sqrt{h^2 + (g_1 - g_0)^2}\right)/(g_1 - g_0)$	719687 *lbs*
$l_m = 3N_W/(\sigma_c^{resin} \pi D)$	0.89 *in.*
$M_{rd} = \dfrac{\frac{W}{4\pi}\left[\frac{1+\nu}{1-\nu}\left(\frac{A}{D'}\right)^2 \ln\left(\frac{C}{D'}\right)^2 + \left(\frac{C}{D'}\right)^2 - 1\right]}{\frac{D't^2}{l^3}\frac{\left(A^2/D'^2 - 1\right)}{(1-\nu)} + \left[1 + \frac{1+\nu}{1-\nu}\left(\frac{A}{D'}\right)^2\right]}$	212 *in-lbs/in*
$M^p_{\theta d} = -\theta_d D_E (1 - \nu^2)/D' + \nu M_{rd}$	5475 *in-lbs/in*
$M^r_{\theta d} = M_{rd} D'/t$	5412 *in-lbs/in*
$\sigma_{rd} = 6M_{rd}/t^2$	564 *psi.*
$\sigma^p_{\theta d} = 6M^p_{\theta d}/t^2$	14600 *psi.*
$\sigma^r_{\theta d} = 6M^r_{\theta d}/l^2$	14431 *psi.*
choose l so that $l < l_m$ & $\sigma^r_{\theta d} < S_{sa}$	1.5 *in.*
choose t so that $\sigma_{rd} < S_{sa}$ & $\sigma^p_{\theta d} < S_{sa}$	1.5 *in.*
proportion the pipe-hub	
$H_T = \pi p (G^2 - B^2)/4$	3596 *lbs*
$H_W = W$	63800 *lbs*
$H_D = \pi p B^2/4$	50894 *lbs*
$h_T = g_1/4$	0.3125 *in.*
$h_W = g_1/2$	0.625 *in.*
$h_D = (g_1 - g_0)/4$	0.445 *in.*
$M_W = (H_T h_T + H_W h_W + H_D h_D)/\pi B$	563 *in-lbs/in*
I_f	0.186
If $I_f < 1$ *use* g_1 *and* h	**OK**
else choose new g_1 *and* h	

Job: 36 inch diameter flange example, *Case I*

Designed by: Hector Estrada

Date: April, 30 1997

Figure 7.2: Modified Stub Flange Sample Calculation Sheet, *Case I.*

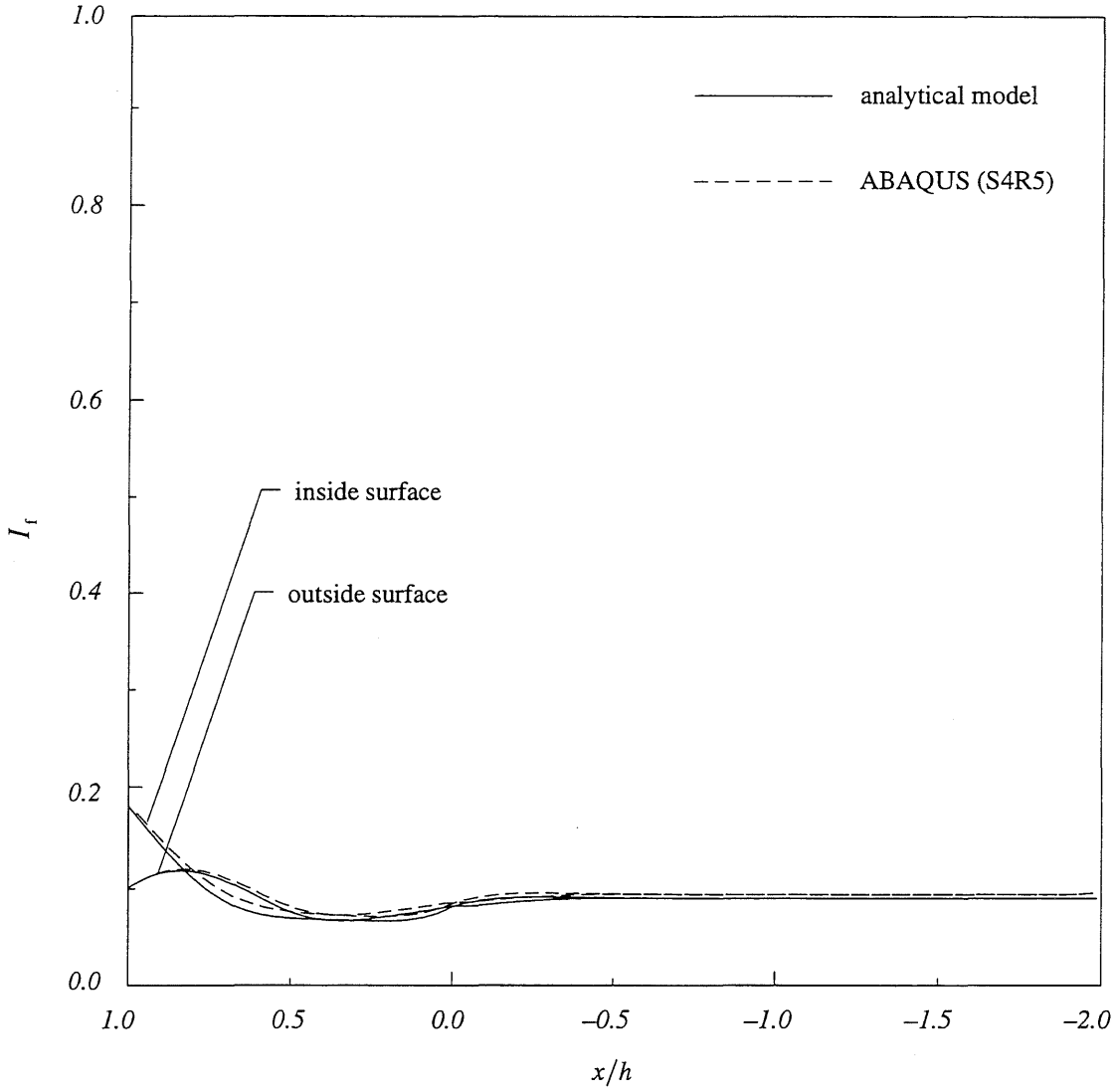

Figure 7.3: Distribution of Tsai-Hill Failure Index (operating condition), *Case I.*

DESIGN CONDITIONS		DESIGN CALCULATIONS	
design pressure, p	100 *psi*	choose a g_1	1.44 *in*
design temperature	150 °*F*	choose an h	10 *in*
flanging material		compute design bolt load	
pipe-hub, $[\pm\ 54.7°]_4$ Glass/Polyester [32]		$W_{m1} = \pi pG^2/4 + 2\pi bGmp$	38476 *lbs*
E_{LL}	5.136×10^6 *psi*	$W_{m2} = g_1\pi Gy$	17589 *lbs*
E_{TT}	1.522×10^6 *psi*	$A_m = \max(W_{m1}/S_b, W_{m2}/S_a)$	1.93 in^2
G_{LT}	0.439×10^6 *psi*	A_b	2.01 in^2 16 – 1/2" ϕ bolts
ν_{LT}	0.281	$W = S_a A_b$	40200 *lbs*
ν_{TT}	0.35	proportion the stub	
σ_{1U}	118.93×10^3 *psi*	$N_W = W\left(\sqrt{h^2 + (g_1 - g_0)^2}\right)/(g_1 - g_0)$	374387 *lbs*
$\sigma^c{}_{1U}$	88.47×10^3 *psi*	$l_m = 3N_W/(\sigma_c^{resin}\pi D)$	0.86 *in.*
σ_{2U}	10.88×10^3 *psi*	$M_{rd} = \dfrac{\frac{W}{4\pi}\left[\frac{1+\nu}{1-\nu}\left(\frac{A}{D'}\right)^2 \ln\left(\frac{C}{D'}\right)^2 + \left(\frac{C}{D'}\right)^2 - 1\right]}{\frac{D't^2}{l^3}\frac{\left(A^2/D'^2-1\right)}{(1-\nu)} + \left[1 + \frac{1+\nu}{1-\nu}\left(\frac{A}{D'}\right)^2\right]}$	129 *in-lbs/in*
$\sigma^c{}_{2U}$	19.29×10^3 *psi*		
τ_{12U}	5.00×10^3 *psi*		
σ_c^{resin}	19.29×10^3 *psi*		
stub, steel, SA-105 [4]		$M^p_{\theta d} = -\theta_d D_E(1 - \nu^2)/D' + \nu M_{rd}$	2731 *in-lbs/in*
allowable stresses: design temp., S_{sb}	17500 *psi*	$M^r_{\theta d} = M_{rd}D'/t$	2692 *in-lbs/in*
allowable stresses: atm. temp., S_{sa}	17500 *psi*	$\sigma_{rd} = 6M_{rd}/t^2$	778 *psi.*
bolting, steel, SA-320 Gr. L7M, [4]		$\sigma^p_{\theta d} = 6M^p_{\theta d}/t^2$	16387 *psi.*
allowable stresses: design temp., S_b	20000 *psi*	$\sigma^r_{\theta d} = 6M^r_{\theta d}/l^2$	16154 *psi.*
allowable stresses: atm. temp., S_a	20000 *psi*	choose l so that $l < l_m$ & $\sigma^r_{\theta d} < S_{sa}$	1.0 *in.*
gasket, Neoprene, 75 durometer, [4]		choose t so that $\sigma_{rd} < S_{sa}$ & $\sigma^p_{\theta d} < S_{sa}$	1.0 *in.*
m	1.0	proportion the pipe-hub	
y	200.0 *psi*	$H_T = \pi p(G^2 - B^2)/4$	4234 *lbs*
thickness	1/8 *in.*	$H_W = W$	40200 *lbs*
Geometry		$H_D = \pi pB^2/4$	25447 *lbs*
		$h_T = g_1/4$	0.36 *in.*
		$h_W = g_1/2$	0.72 *in.*
		$h_D = (g_1 - g_0)/4$	0.54 *in.*
		$M_W = (H_T h_T + H_W h_W + H_D h_D)/\pi B$	782 *in-lbs/in*
		I_f	0.190
		If $I_f < 1$ *use* g_1 *and* h *else choose new* g_1 *and* h	**OK**
		Job: 18 inch diameter flange example, *Case II*	
		Designed by: Hector Estrada	
		Date: April, 30 1997	

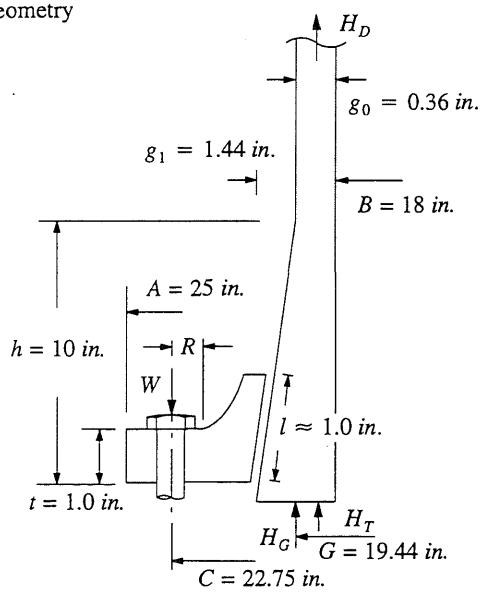

16 – 1/2'' ϕ bolts, 13 threads/in [11]

Figure 7.4: Modified Stub Flange Sample Calculation Sheet, *Case II.*

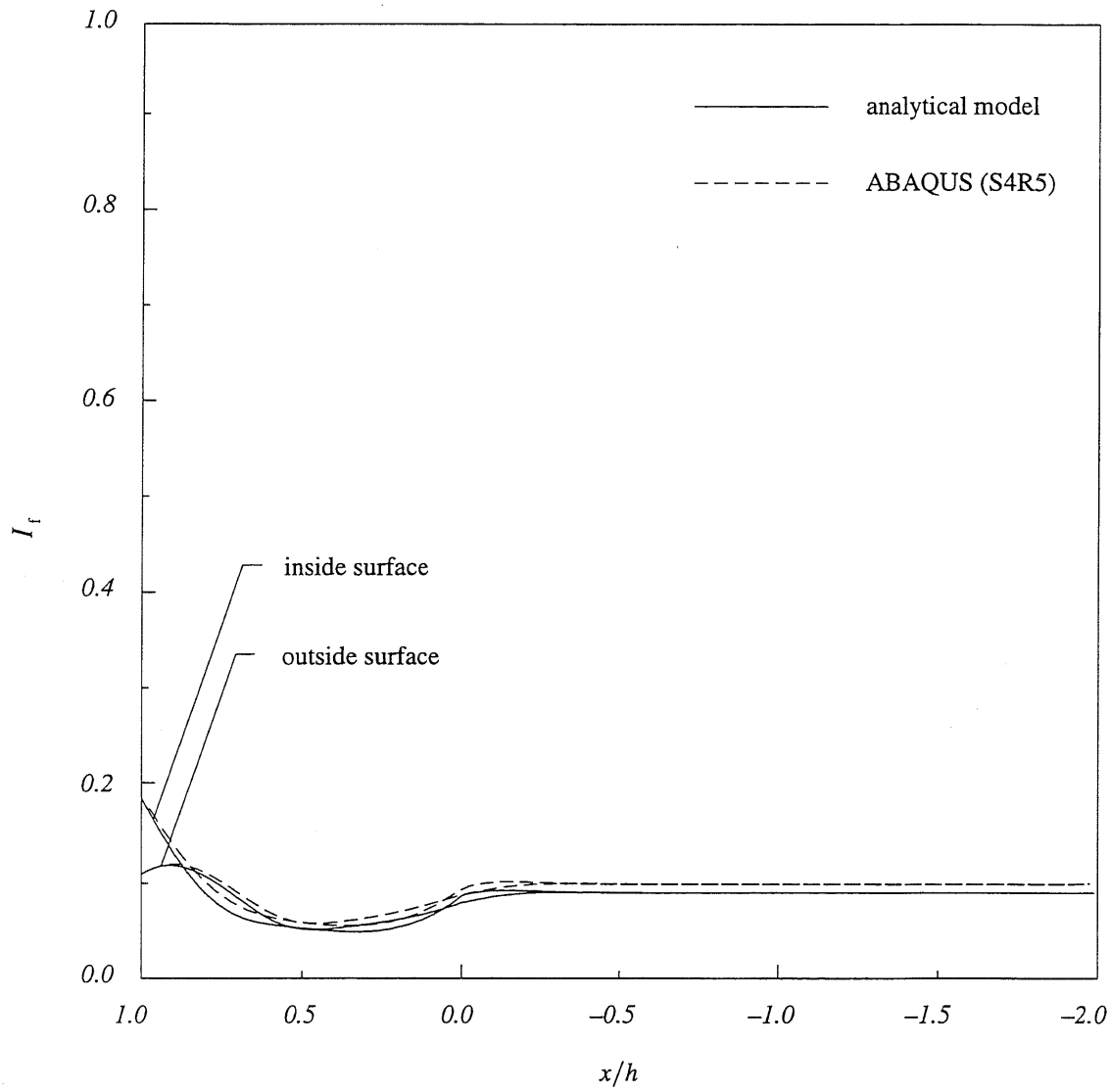

Figure 7.5: Distribution of Tsai-Hill Failure Index (operating condition), *Case II.*

Gasket Material	Gasket Factor *m*	Min. Design Seating Stress *y*, psi
Below 75A Shore Durometer	0.5	0
75A or Higher Shore Durometer	1.0	200

Table 7.1: Gasket Parameters for Elastomers [4].

Chapter 8

Detailed Finite Element Analysis of the Composite Joint

8.1 Introduction

The analyses presented in this chapter are an attempt to validate the design method presented in the earlier chapters, since we do not perform experimental testing of the proposed joint. Finite element analysis cannot duplicate experimental testing exactly, but can provide useful insight into the overall behavior and performance of the joint.

We perform three dimensional and axisymmetric finite element analyses of the modified stub flanged joint for design case I discussed in chapter 7. The primary emphasis will be on assessing the strength of the flange and the leak tightness of the gasket. The bolt interaction will not be considered; therefore, we assume a constant bolt load over the history of the analyses.

First, we describe the evolution of leakage over the loading history of the joint and give a description of the gasket used in the analyses. We then discuss the detailed finite element analyses: we describe the three dimensional analysis, and then we discuss the analysis for the axisymmetric model. In the three dimensional model, we make use of the cyclic symmetry of the system and only consider a 1/64 segment portion of the total circumference of the joint, see figure 8.1. Since ABAQUS does not support pressure penetration in three dimensional contact analysis, we also conduct an axisymmetric analysis to properly model joint leakage. The dimensions for the joint were derived in chapter 7 and are repeated in figure 8.2. We raised the stub 1/16" above the gasket-hub interface to prevent the mating flanges from coming into contact when the system is loaded, see figure 8.2.

8.2 Leakage Development Description

A sequence of load steps is shown in figure 8.3 with their respective contact areas. The flange rotates as the internal pressure increases causing loss of contact between the gasket and the flange. The rotation is caused by the bolt load, the hydrostatic end load and by the fluid penetrating the space where the contact is lost. In the first step, only the bolt load is applied. In this case, the reacting gasket pressure is greater closest to the bolt and decreases away from the bolt. In the radial direction the contact pressure is largest near the bolt and decreases toward the inside of the pipe; in the circumferential direction the pressure is greatest close to the bolt and decreases toward the point between two bolts. The circumferential variation can only be captured in a three dimensional analysis. However, as we will see later, for closely spaced bolts the pressure distribution on the gasket is almost uniform in the circumferential direction. The stub diffuses the bolt load uniformly onto the hub and the bolt load is transferred almost uniformly to the gasket. Therefore, the pressure distribution in the hoop direction is dictated by the number of bolts (closely spaced bolts provide a uniform gasket stress), which is usually determined from practical limitations since the mechanic needs to be able to tighten the bolts. The bolt spacing (usually two to three bolt diameters) is therefore dictated by the size of the wrench used to tighten the bolts. So, an axisymmetric analysis can be used to study the leakage problem rather than using a more time consuming three dimensional analysis. In the second step, the loss of contact area has allowed fluid to penetrate. This process continues until the contact area reduces to zero, at this point leakage occurs.

8.3 Gasket Description

The gasket material constants given in the ASME BPV code, table 7.1, are not related to engineering material constants such as Young's modulus and Poisson's ratio; however, to conduct a detailed finite element analysis of leakage, we need the material behavior of the gasket. Furthermore, rubber is a nearly incompressible material (Poisson's ratio almost equal to 0.5) and its constitutive behavior is nonlinear. Therefore, to properly model the material behavior of rubber we need a complete stress-strain response. In this study, we use a synthetic rubber (Neoprene) gasket, 75 shore durometer hardness. The material properties were extracted from reference [12]. The data is reported in a load-deflection diagram, which was obtained from a gasket compression test using an X-Y continuous recorder; consequently, we had to digitize several points along the plot, which are listed in table 8.1.

The gasket is a standard 1/8 inch 2"–150# size, 2-3/8 inch inside – 3-3/16 inch outside diameter, which gives a total surface area of 5.54 inches. Therefore, from the load and the total surface area we compute the nominal stress, table 8.1. Also, from the deflection and the gasket thickness (one eight of an inch) we can compute the nominal strain, table 8.1. With the nominal

stress and nominal strain, we can calibrate a hyperelastic material model in ABAQUS, as shown in figure 8.4.

ABAQUS uses a strain energy functional, rather than Young's modulus and Poisson's ratio, to relate stresses to stains in hyperelastic material models. ABAQUS has a number of hyperelastic material models, we chose a second degree Mooney-Rivlin material model. Given a set of experimental test data, the calibration of the hyperelastic material model can be done by ABAQUS, which uses a least squares fit. We refer the reader to the ABAQUS documentation [29] for further details on the procedure.

In the analysis of a hyperelastic material, ABAQUS requires the use of hybrid elements in the mesh of the hyperelastic material because of the incompressibility of the material. Therefore, the gasket is meshed with eight node reduced integration hybrid axisymmetric continuum elements (CAX8RH) in the axisymmetric model and twenty node reduced integration hybrid continuum elements (C3D20RH) in the three dimensional model.

8.4 Joint Loading

The initial gasket pre-stress is provided by the pre-load in the bolts (the seating condition). In this state, the gasket deforms filling the irregularities on the flange face, insuring full contact over its entire surface. We decided in chapter four not to consider this loading condition because the load required to seat a rubber gasket is small. The internal pressure is then applied and the gasket pre-stress decreases and the bolt load increases (the operating condition). The pressure penetration described in section 8.2 causes an additional decrease in gasket pre-stress and increase in bolt load; but as the flanging system deforms, some relaxation of the bolt pre-load occurs. The final load carried by the bolts depends on this bolt-flange interaction, which in turn depends on the stiffness of the flanging system and the extent of the fluid penetration. Furthermore, the fluid penetration is also a function of the flange stiffness. The bolt load relaxation is due to compatibility of the system deformation, i.e., the deformation in the bolts and the flange have to be compatible. This is a complex interaction and we do not consider it here. Therefore, the real evolution of the loading will not be captured. We will study the long term behavior of the joint; therefore, we assume that the bolt load remains constant over the history of the loading. The justification for this is that in practice the mechanic will usually retighten the bolts to maintain the required load to prevent leakage. Other issues of load relaxation will not be considered, such as creep of the resin in the composite and other long term relaxation problems.

8.5 Finite Element Models

8.5.1 Three Dimensional Finite Element Model

We used PATRAN to create the finite element mesh depicted in figure 8.5, and ABAQUS to perform the analysis. The mesh for this analysis represents a 5.625° segment of the flange. Second order brick elements with reduced integration are employed throughout the mesh of the flanging system and gasket, see figure 8.5. The contact between the bottom of the hub and the gasket and that between the hub and the stub are modeled using contact pairs. Contact is modeled by the interaction of contact surfaces defined by grouping specific element faces in the contacting regions. This contact formulation uses a master-slave concept to enforce the contact constraint. Since the gasket is not rigidly attached to the hub (it can be blown out by the internal pressure in cases where soft gaskets are used and flange faces are very smooth), we allow relative sliding between the gasket and hub contact surfaces. Small relative sliding is also allowed between the hub and stub contact surfaces. We use a standard Coulomb friction model in the contact formulation to control the sliding. We assume a coefficient of static friction of 0.8, a very rough surface, in the gasket-hub contact interaction and a value of 0.2, a much smoother surface, in the hub-stub contact interaction. These choices are made arbitrarily because of the lack of data.

The material properties used in the analysis were introduced in the last chapter for the flanging system and in section 8.3 for the gasket. ABAQUS also supports laminated materials for three dimensional analysis. In the composite portion of the system, we have eight layers through the pipe thickness, which we model with four elements through the thickness, two layers per element. The material properties are specified via the full three dimensional constitutive relations, in this case transversely isotropic.

The loading is depicted in figure 8.6; it consists of the hydrostatic end load, internal pressure, and bolt load. The hydrostatic end load is smeared over the top surface of the pipe. The bolt load is taken as 1/64 of the total bolt load and is smeared uniformly over a small area representing the area over which the bolt head would transfer the load, the shaded area in figure 8.7. Notice that in the real case, when the flange rotates, the bolt head pressure would not be uniform over this area; it would be greater on the portion of the area closest to the inside of the pipe. Pressure penetration is not applied to this model because the three dimensional contact formulation does not support this type of loading.

As we described earlier, we are only modeling a 1/64 segment of the total flange. Therefore, we have to add boundary conditions to make the model behave as if the whole component were being modeled. Symmetry boundary conditions are applied to the symmetry plane of the gasket, i.e., the axial displacement at the middle of the gasket is zero, see figure 8.6. The planes

through angles $0°$ and $5.625°$ are also symmetric planes and are constrained appropriately, i.e., the circumferential deformation is zero, see figure 8.7.

8.5.2 Axisymmetric Finite Element Model

In this section, we study the development of leakage in the modified stub flange joint using the pressure penetration option in contact finite elements using ABAQUS. The contact stress distribution on the gasket is studied using slide line elements and pressure is allowed to penetrate as contact is lost.

Again, we used PATRAN to create the finite element mesh depicted in figure 8.8. Second order reduced integration axisymmetric elements are used throughout the mesh of the flanging system and gasket. The contact between the hub and the stub is again modeled using a contact pair. Contact between the gasket and the flange face is modeled using axisymmetric slide line elements (ISL22A) on the gasket and a *slideline* which is attached to the hub face. This contact formulation uses a master-slave concept to enforce the contact constraint. A slide line is a group of nodes associated with the master surface. The surface on which the slide line elements are placed is the slave surface. The nodes of the slide line elements are constrained not to penetrate into the master surface. To model the sliding, in both contact cases, we use the same friction formulation as in the three dimensional case.

The material properties for the gasket are described in section 8.3. The material properties for the composite system are the same as those used in the three dimensional case and can be found in chapter 7. However, the lay-up for the axisymmetric case is $[0°/90°]_4$. This was necessary because the ABAQUS axisymmetric elements do not allow us to consider arbitrary winding angles. Also, none of the axisymmetric elements support laminated material models; therefore, we use one element for every layer, eight elements through the thickness of the pipe. We use a transversely isotropic constitutive law and specify the elasticity constants via the orthotropic material model in ABAQUS.

The stub material is inhomogeneous because of the presence of the bolt holes, the shaded area in figure 8.8. This is handled by smearing the material properties used in the bolt hole area of the mesh, i.e., using material properties corresponding to a weaker material in the bolt hole area. Guidelines for determining effective material properties for perforated plates can be found in the ASME code Sections VIII [4]. For the model presented here, the effective material properties are calculated using an elasticity moduli reduction factor. This factor is simply $1 - AH/AA$, where AH is the total volume of the bolt holes and AA the volume swept by the bolt diameter along the entire circumference of the flange, along the bolt circle diameter. Hence, the reduction factor is 0.88. The effective in-plane moduli of elasticity are obtained by multiply-

ing the reduction factor by the flange modulus. The in-plane Poisson's ratio is left unchanged. The modulus in the hoop direction should be very small and the hoop Poisson's ratio should be zero. The effective shear modulus is computed from its respective modulus of elasticity and Poisson's ratio. Hence, the material properties for the bolt hole area are $E_r = E_z = 25,588\ ksi$, $E_\theta = 0.025\ ksi$, $\nu_{rz} = 0.3$, $\nu_{z\theta} = \nu_{r\theta} = 0$, $G_{rz} = 9,842\ ksi$, and $G_{r\theta} = G_{z\theta} = 0.012\ ksi$. These elasticity moduli are specified via the orthotropic material model in ABAQUS for the bolt hole part of the mesh.

The loading is depicted in figure 8.8. The internal pressure loading is broken down into three loads: (i) the internal pressure, which acts on the inside surface of the vessel, (ii) the hydrostatic end load, which is the membrane stress in the pipe, due to the internal pressure, and (iii) the penetrating pressure as the contact between the flange face and the gasket is lost. The total bolt load is smeared over the upper bolt hole surface as a normal pressure, as shown in figure 8.8. The fluid penetration described in section 8.2 can easily be simulated in ABAQUS, but is only supported for axisymmetric analysis. This fluid pressure can penetrate into the mating surface interface until some area on the surfaces is reached where the contact pressure between the abutting surfaces exceeds the fluid pressure, cutting off further penetration. The pressure penetration load starts from the inside of the pipe, left side in figure 8.8, and penetrates between the surfaces continuously from this side.

In an axisymmetric analysis, the formulation of the element takes care of the boundary conditions in the circumferential direction. Therefore, the only boundary conditions we have to specify in this model are symmetry boundary conditions on the symmetry plane of the gasket, i.e., the axial displacement in the middle of the gasket is zero, see figure 8.8.

8.6 Results and Discussion of the Analyses

We analyzed both models using non-linear large displacement analyses. The nonlinearities in the problem are due to the contact conditions and the gasket material behavior. The three dimensional model, although only about five times larger (in terms of degrees of freedom) than the axisymmetric model, required 26 times more CPU time to run; both problems were solved in 24 load increments. A true comparison, however, cannot be made because in the axisymmetric model pressure penetration was also included but not in the three dimensional analysis.

8.6.1 Three Dimensional Finite Element Results

Figure 8.9 shows the deformed configuration of the model predicted by the analysis; figure 8.10 shows a close up of the deformation in the neighborhood of the gasket. The magnification factor in both figures is ten. These figures clearly show that over a quarter of the contact

between the gasket and the flange is lost. However, as we will see later the pressure on the portion of the gasket that remains in contact is greater that the minimum required to keep the joint leak tight. The separation between the hub and the stub is caused by the magnification of the displacement and is not actual deformation in the system, as we can see in figure 8.11. There is however loss of contact at the top of the stub; this will be clearer when we look at the contact pressure. In figure 8.11, we can see that the stub slid down, because the element lines in the hub and stub do not match after deformation.

Figure 8.12 shows the gasket contact pressure computed for the three dimensional analysis. Most of the surface is unloaded, except for the outer most patch of elements, a quarter of the surface. Therefore, the assumption we made in chapter four about the extent of the fluid penetration is violated for this particular problem; however the pressure over this quarter of the gasket is higher than the minimum required to maintain leak tightness of the fluid, i.e., the contact pressure is greater than $p^*m = 50\ psi$, the pressure times the leak tightness factor. Also, we can clearly see that the contact pressure in the circumferential direction is not uniform, as described earlier; this pressure is higher on the side where the bolt load is applied. However, the difference is relatively small and we can assume this distribution to be uniform in the circumferential direction, which then allows us to analyze the system using an axisymmetric analysis.

Figure 8.13 depicts the normal contact pressure distribution on the hub at the interface between the hub and the stub predicted by the three dimensional analysis. The stub rotates and most of the contact surface is unloaded. However, the bearing strength of the composite is not exceeded, i.e., the pressure at every point is less than 20,000 *psi*. In the circumferential direction, the contact pressure is uniform for most of the surface, except at the ends. From this plot, the reason for the non-uniform gasket stress is apparent. That is, the bolt load is not transferred uniformly over the entire stub-hub interface, but again is higher where the bolt load is applied; however most of the contact pressure remains uniform over the contact surface between the stub and the hub in the circumferential direction. The bolt load causes localize stress concentration on the side of the bolt and does not appear to affect the gasket contact pressure distribution significantly.

Figures 8.14 through 8.17 depict fringe plots of the von Mises, radial, circumferential and axial stress distributions, respectively. Notice that the von Mises stress is only relevant for the stub and gasket portions of the joint, since the material in the pipe-hub component is orthotropic. Also, in tables 8.2 to 8.4, we list the maximum and minimum (algebraic) values of all stress components and the von Mises stress for the three distinct joint components (pipe-hub, stub, and gasket). In figure 8.18, we give the location of these values. Stress concentrations localized around the bolt hole area govern most maximum and minimum values in the stub. In

fact, the allowable stress is exceeded in this localized portion. The reason for this stress concentration is due to the presence of the bolt hole and is caused mostly by the circumferential stress. However, the yield stress of the stub material, steel, is not exceeded.

To asses the strength capacity of the composite material, we had used the Tsai-Hill failure criteria in the previous chapters; however, since this is not directly applicable to three dimensional stress states, we use a maximum stress failure criteria in this chapter. The stresses in the pipe-hub component are in principal material directions. Therefore, using the strengths listed in table 6.1, chapter six, we can check if stresses in the composite system exceed any of these strengths. From table 8.2 we can see that none of the maximum or minimum stresses exceed the strength capacity of the composite material.

8.6.2 Axisymmetric Finite Element Results

Figure 8.19 shows the deformed configuration of the model predicted by the axisymmetric analysis in the neighborhood of the gasket. The magnification factor is ten. This figure, again, show that over a quarter of the contact between the gasket and the flange is lost, consistent with the three dimensional analysis. Again, the axisymmetric analysis predicts the pressure on the portion of the gasket that remains in contact to be greater that the minimum required to keep the joint leak tight. The separation between the hub and the stub is again caused by the magnification of the displacement and is not actual deformation in the system, as we can see in figure 8.20; again, the stub sliding down the hub is apparent.

Figure 8.21 depicts the gasket contact stress for the operating condition. The ASME code minimum gasket pressure to maintained a leak tight joint, mp is also shown in figure 8.22 and it falls below the average ABAQUS computed pressure. Also, in our gasket design formulation, we assumed that loss of contact, hence pressure penetration, occurs up to the middle of the gasket; however, the resulting penetration from the ABAQUS results is about 75% into the gasket. But, the surface pressure is relatively large so that leakage would not be a problem. The gasket contact pressure for the axisymmetric case is about one third of that for the three dimensional case; this is due to the fact that we are allowing pressure to penetrate the space where contact is lost in the axisymmetric case and therefore some of the bolt load is balanced by the pressure acting on the contact face of the hub. Therefore, the leakage results from the three dimensional case should be used with caution.

Figures 8.22 depicts a fringe plot of the von Mises stress distribution. Again, this stress is only relevant for the stub and gasket portions of the joint, since the material in the pipe-hub component is orthotropic. Notice that the stress concentrations localized around the bolt area are not as severe as those in the full three dimensional case. However, the maximum von Mises

stress, which occurs at the top of the inside of the flange, is slightly over the allowable stress given by the ASME code; however, this stress is less than the yield stress of the stub material.

8.7 Conclusions

The method described here can be used to study leakage behavior and to validate the code formulation for other gasket materials and joint configurations. The ASME method, although not theoretically exact, is sufficiently accurate for all practical purposes, and is far more simple to implement than the finite element formulation presented here. However, for critical applications, the formulation presented here can provide greater insight into the behavior of the particular joint configuration. In critical design cases where a more rigorous solution to the flange is needed, the axisymmetric model can produce a satisfactory solution at a much lower cost than the three dimensional model. However, it does not capture the stress concentrations in the bolt hole area. The leakage behavior, though, is captured more accurately in the axisymmetric case than in the three dimensional case because of the option to allow pressure to penetrate the space where contact is lost; this however is not supported in three dimensional analysis in ABAQUS at present. Also, the limitation on the winding angle for the axisymmetric case must be considered when using this method. This model can also be modified to study the bolt-stub interaction behavior.

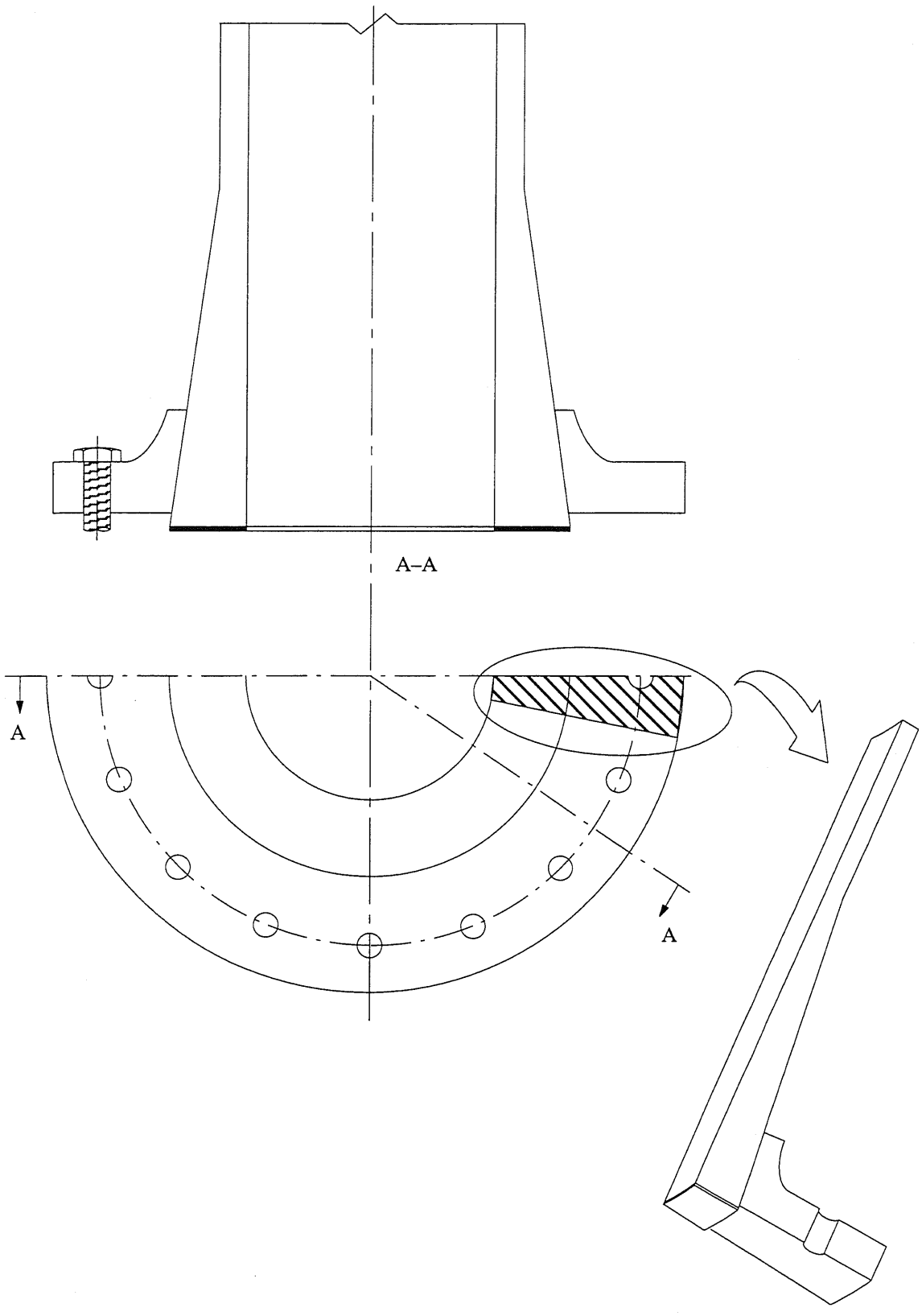

Figure 8.1: Schematic of the Modified Stub Flanged joint.

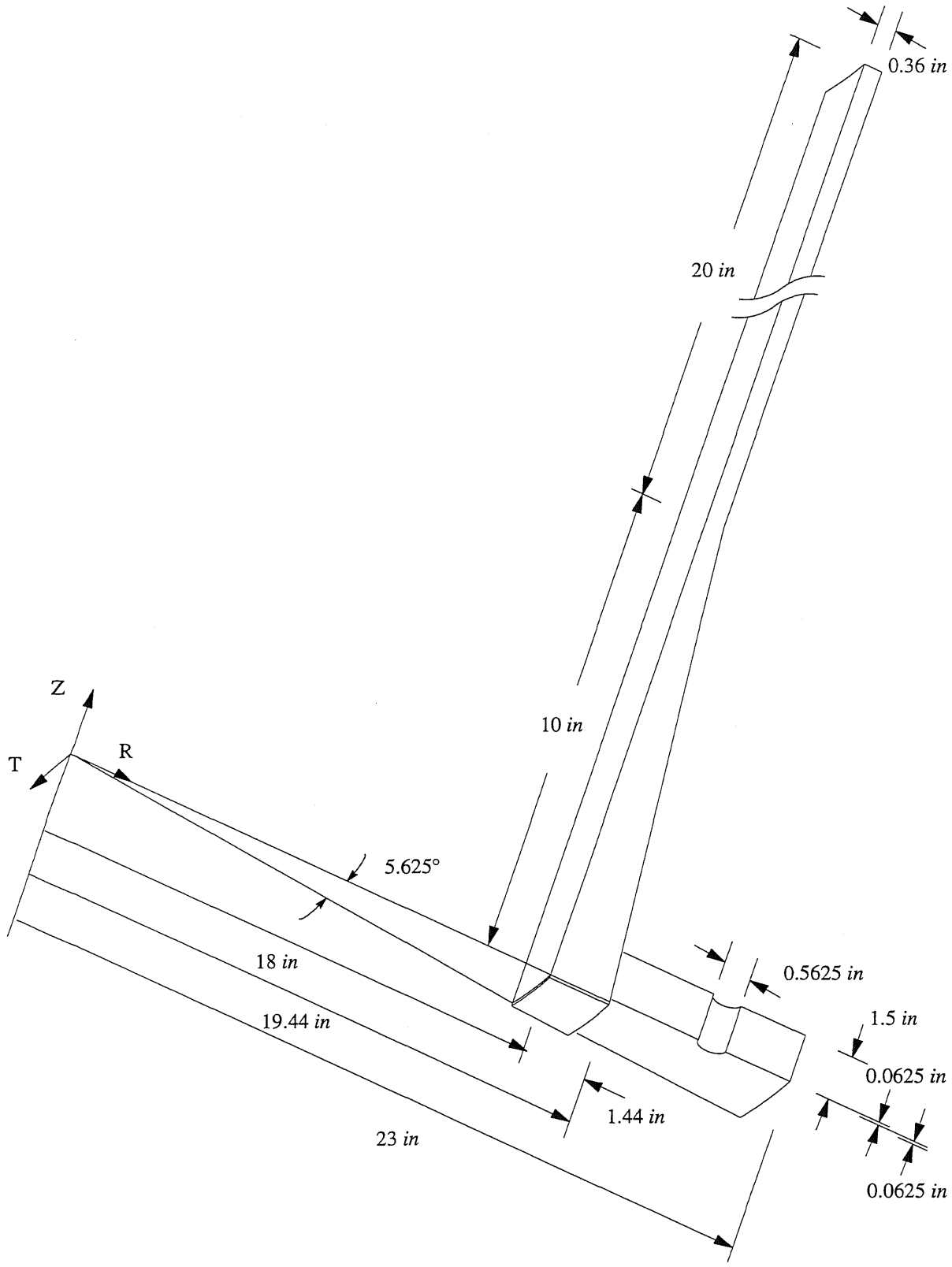

Figure 8.2: 5.625° Segment 3-D Model of the Modified Stub Flange.

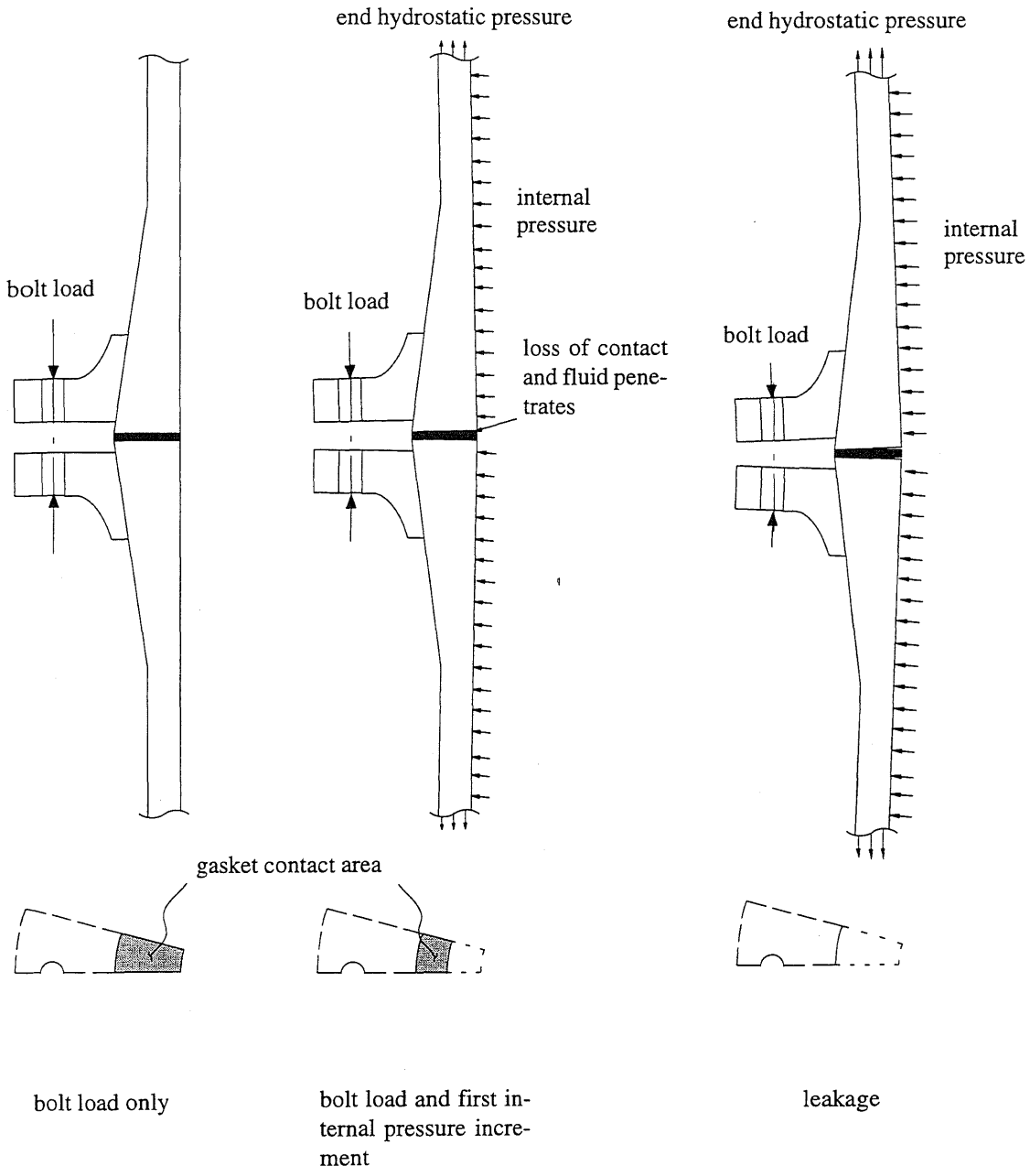

Figure 8.3: Contact Area at Three Load Increments.

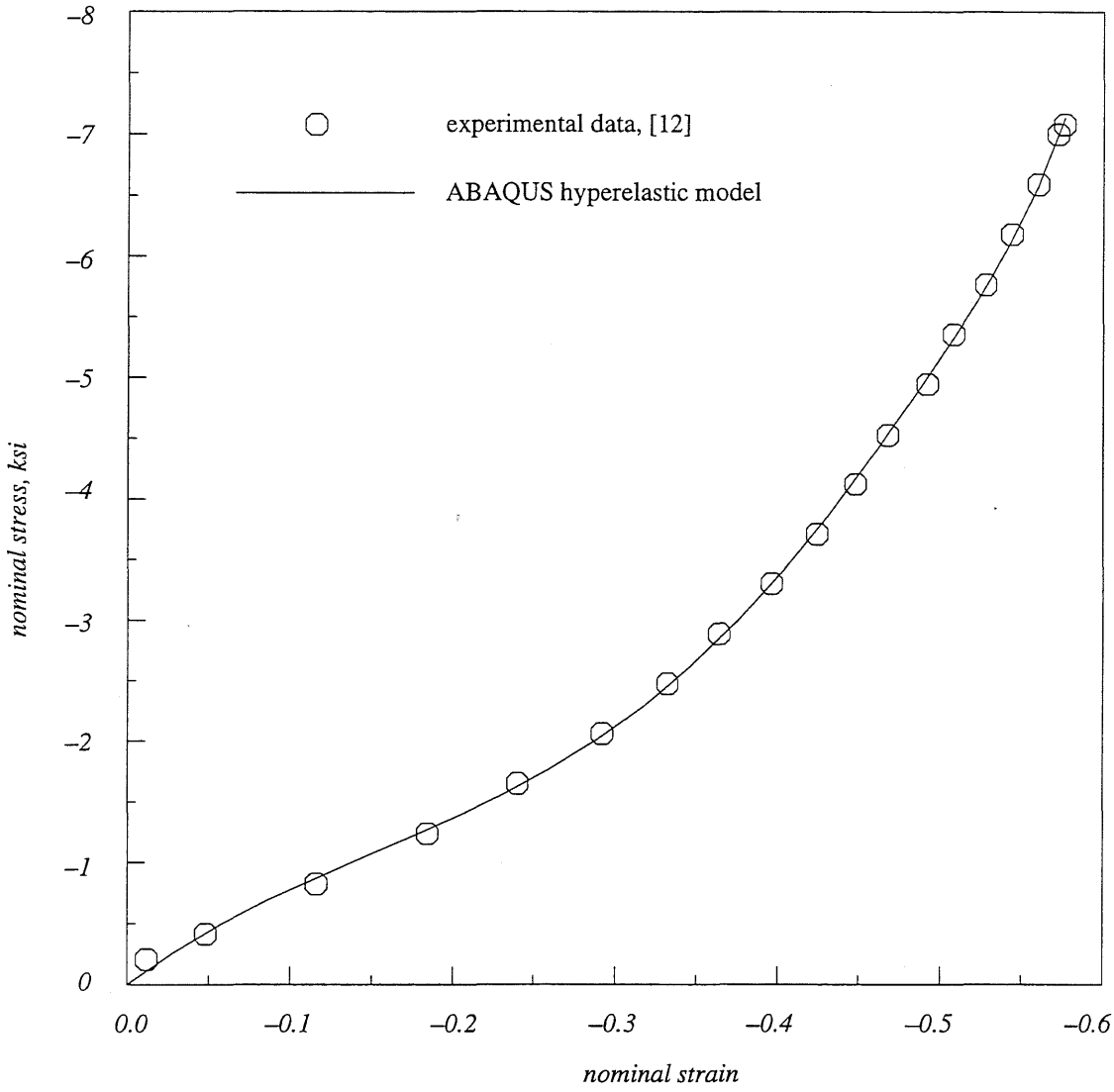

Figure 8.4: Gasket Stress-Strain Diagram.

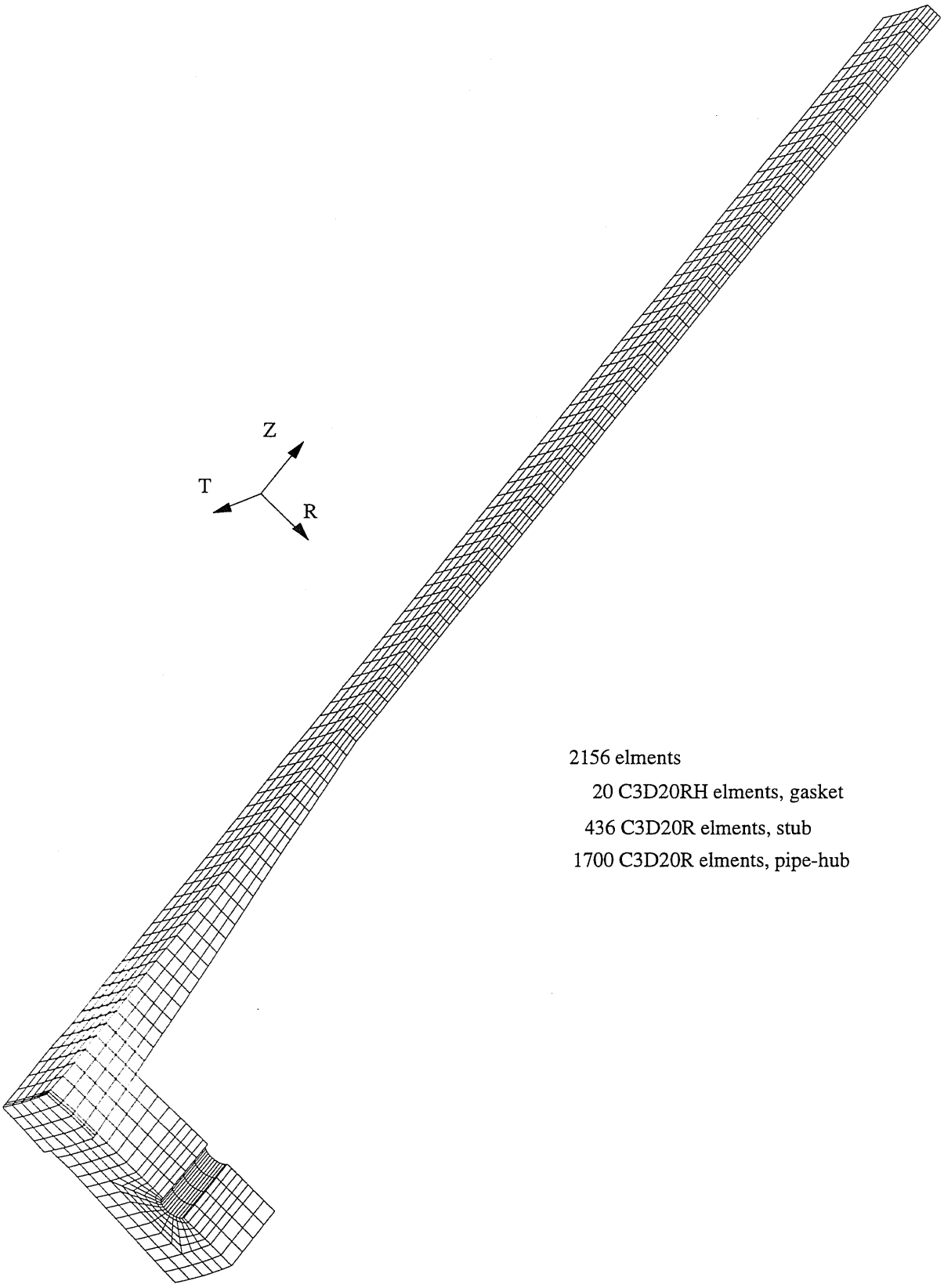

Figure 8.5: 3-D Finite Element Mesh Entire Model.

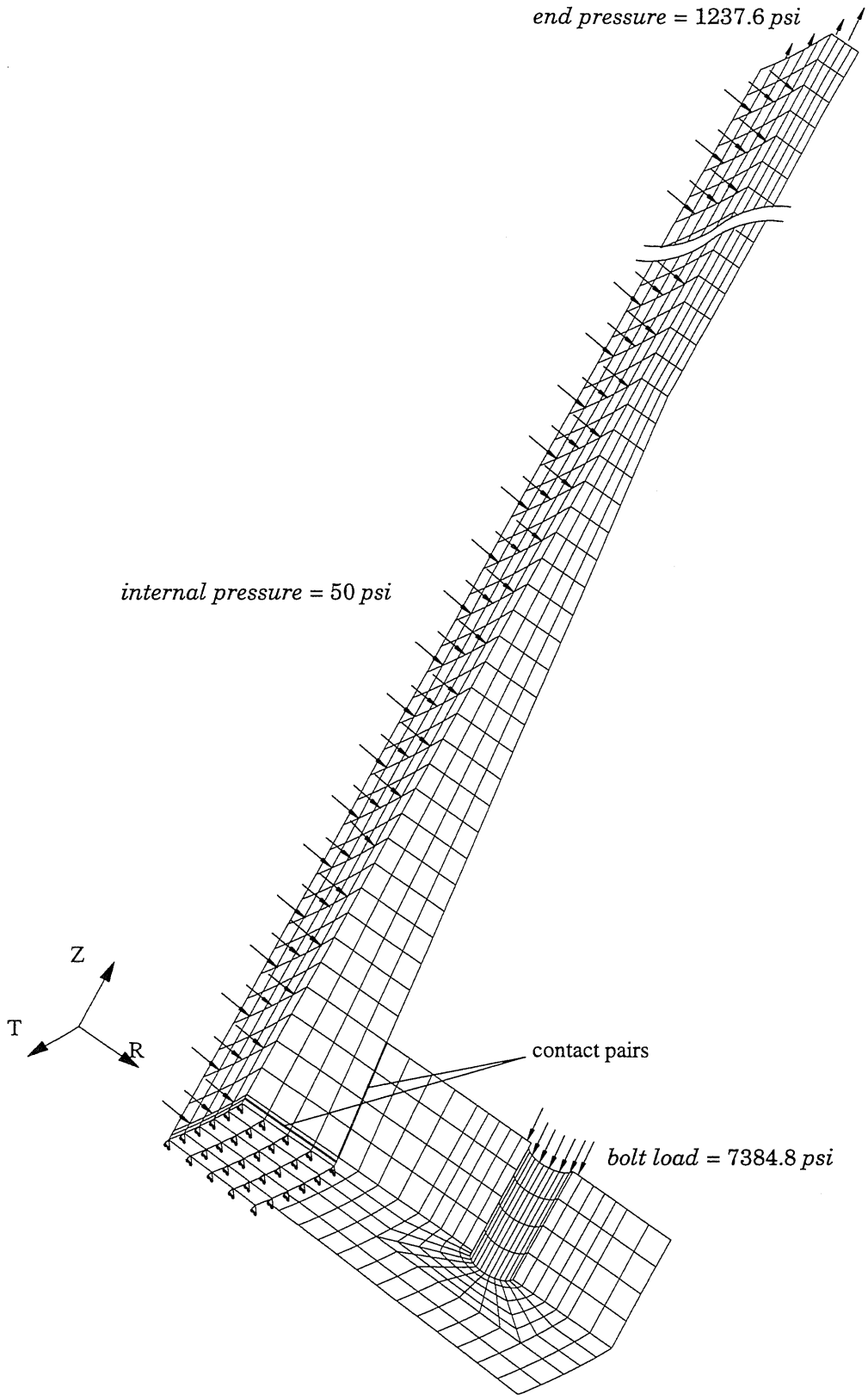

Figure 8.6: 3-D Finite Element Model Loads and Boundary Conditions.

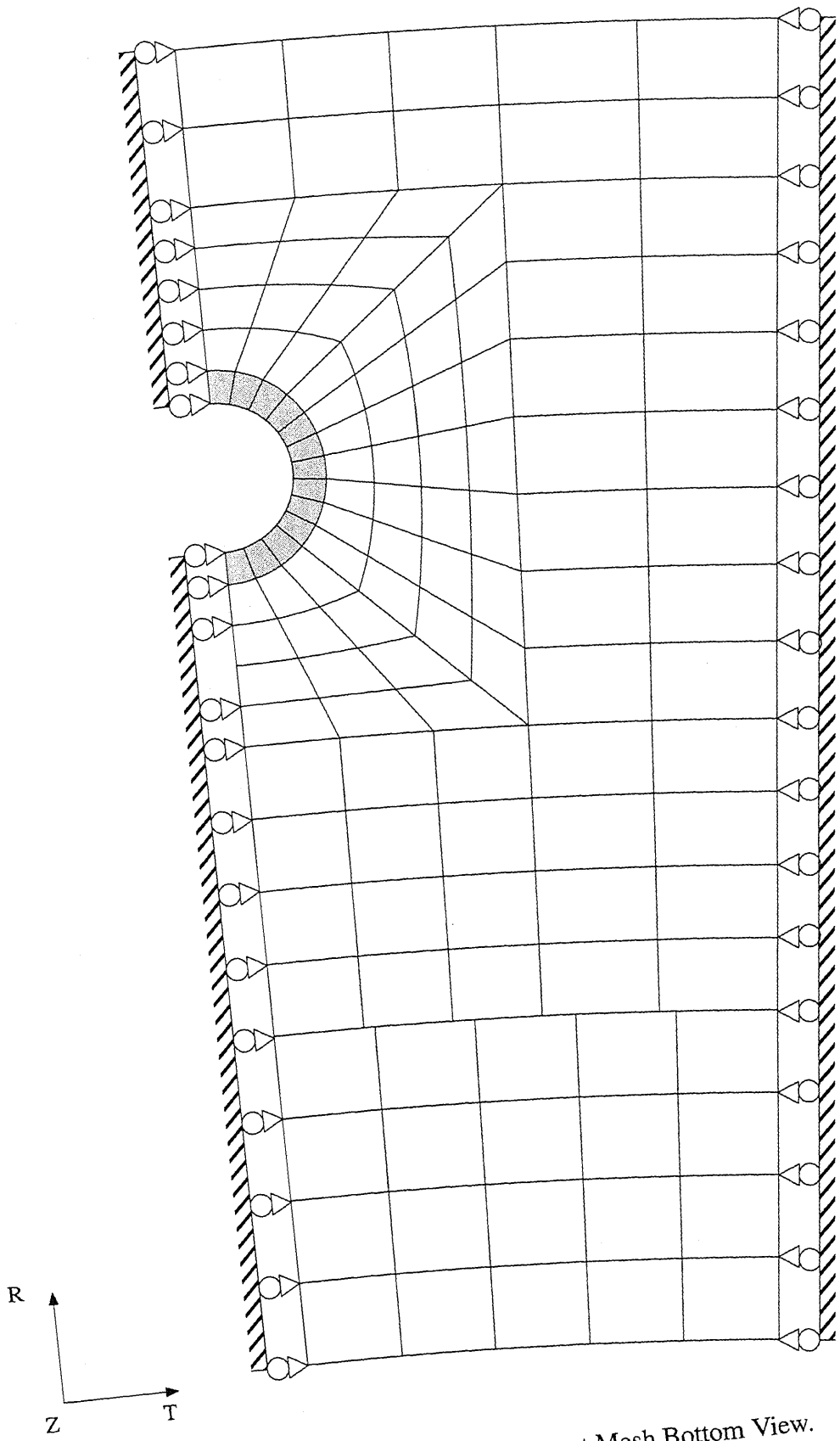

Figure 8.7: 3-D Finite Element Mesh Bottom View.

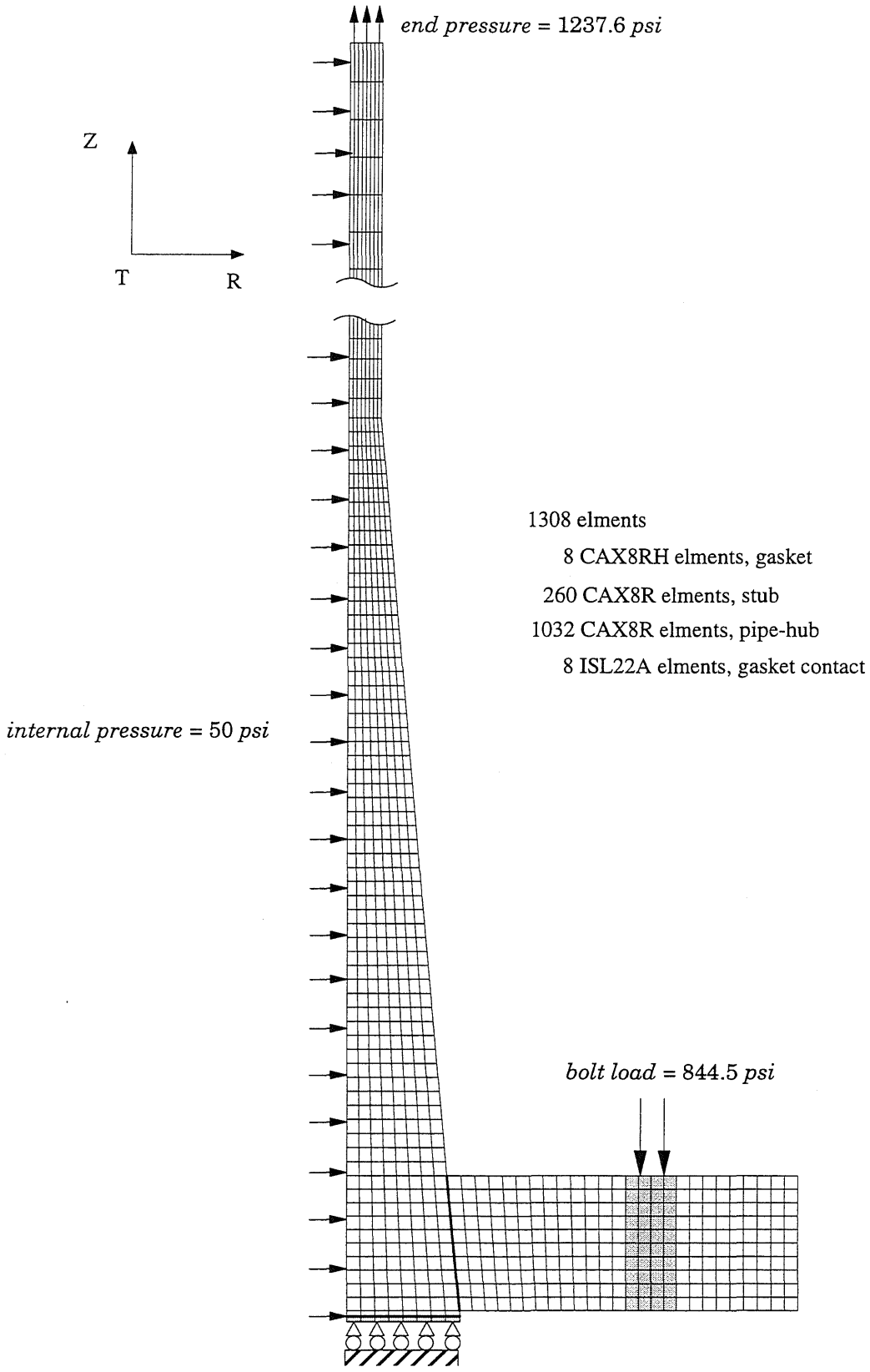

Figure 8.8: Axisymmetric Finite Element Mesh.

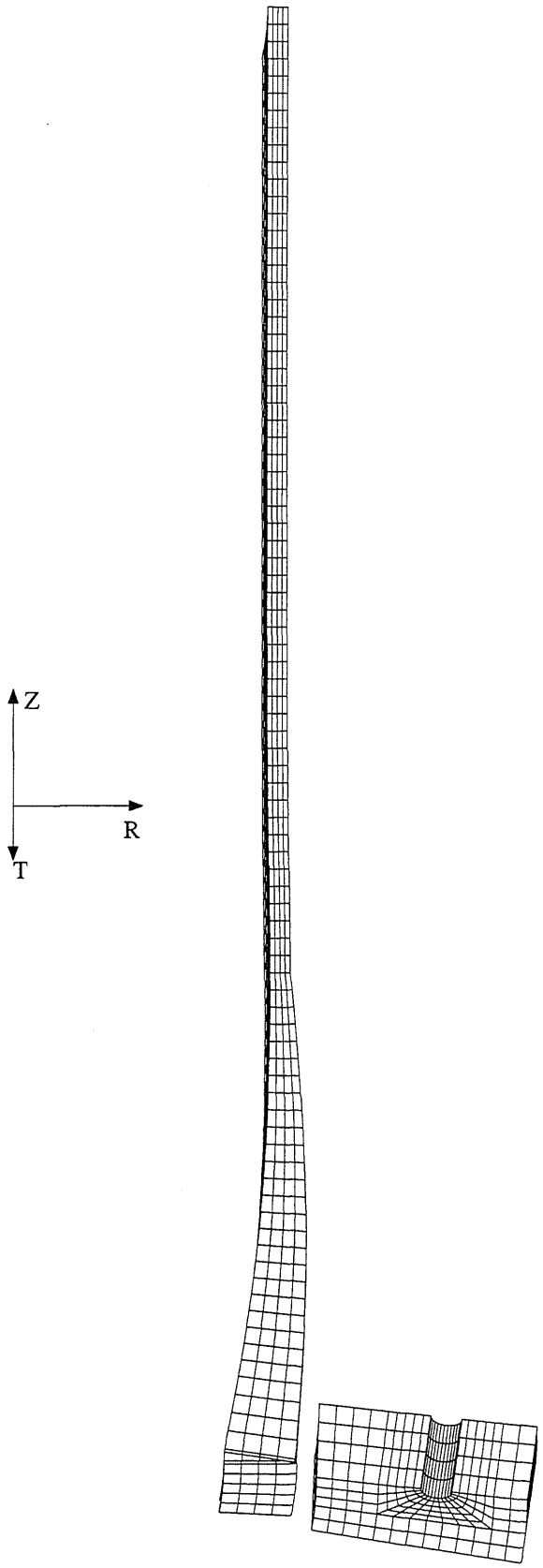

Figure 8.9: 3-D Model Deformed Shape, Magnification 10.

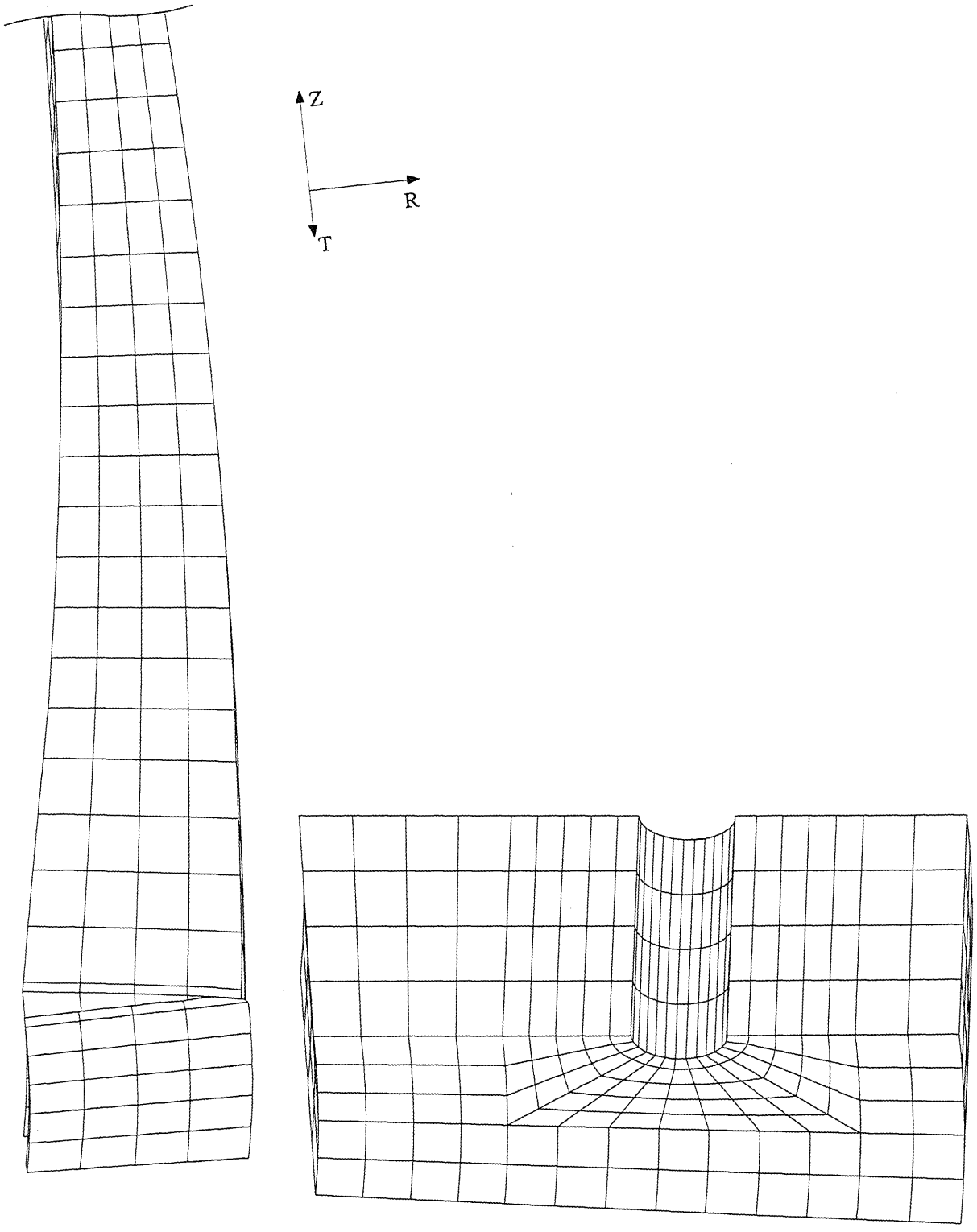

Figure 8.10: 3-D Gasket and Stub Model Deformed Shape, Magnification 10.

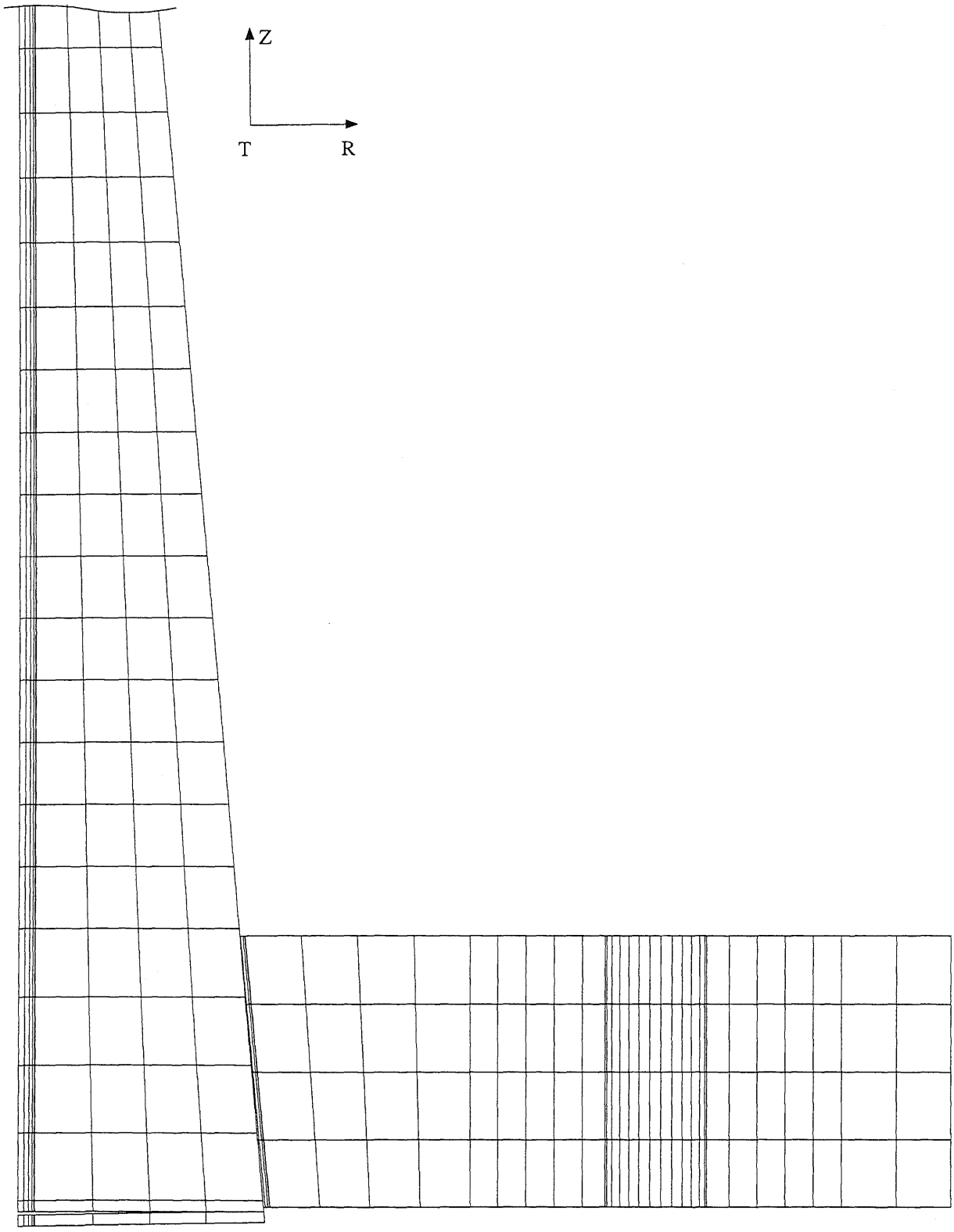

Figure 8.11: 3-D Gasket and Stub Model Deformed Shape, Magnification 1.

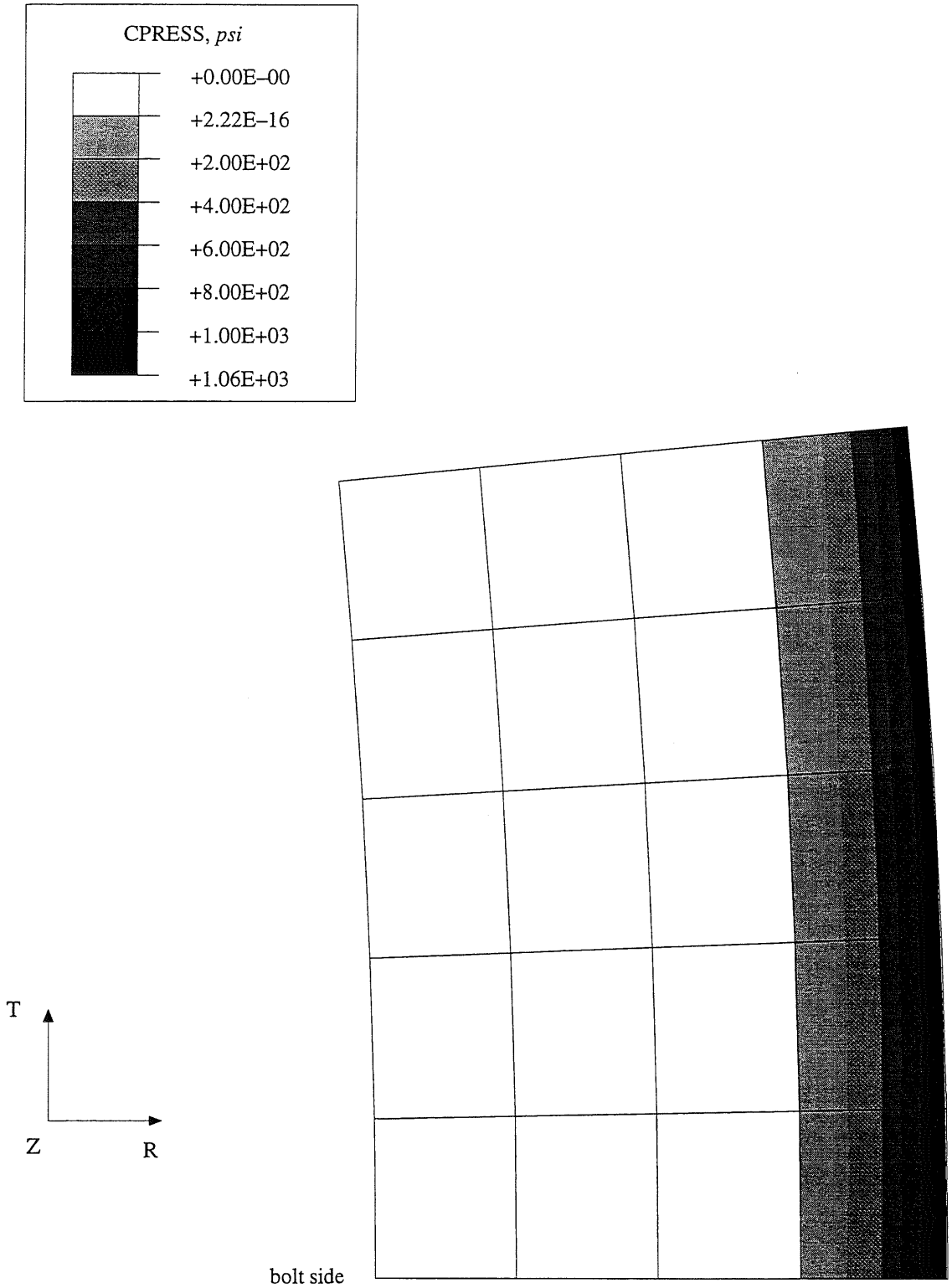

Figure 8.12: Gasket Contact Pressure Distribution.

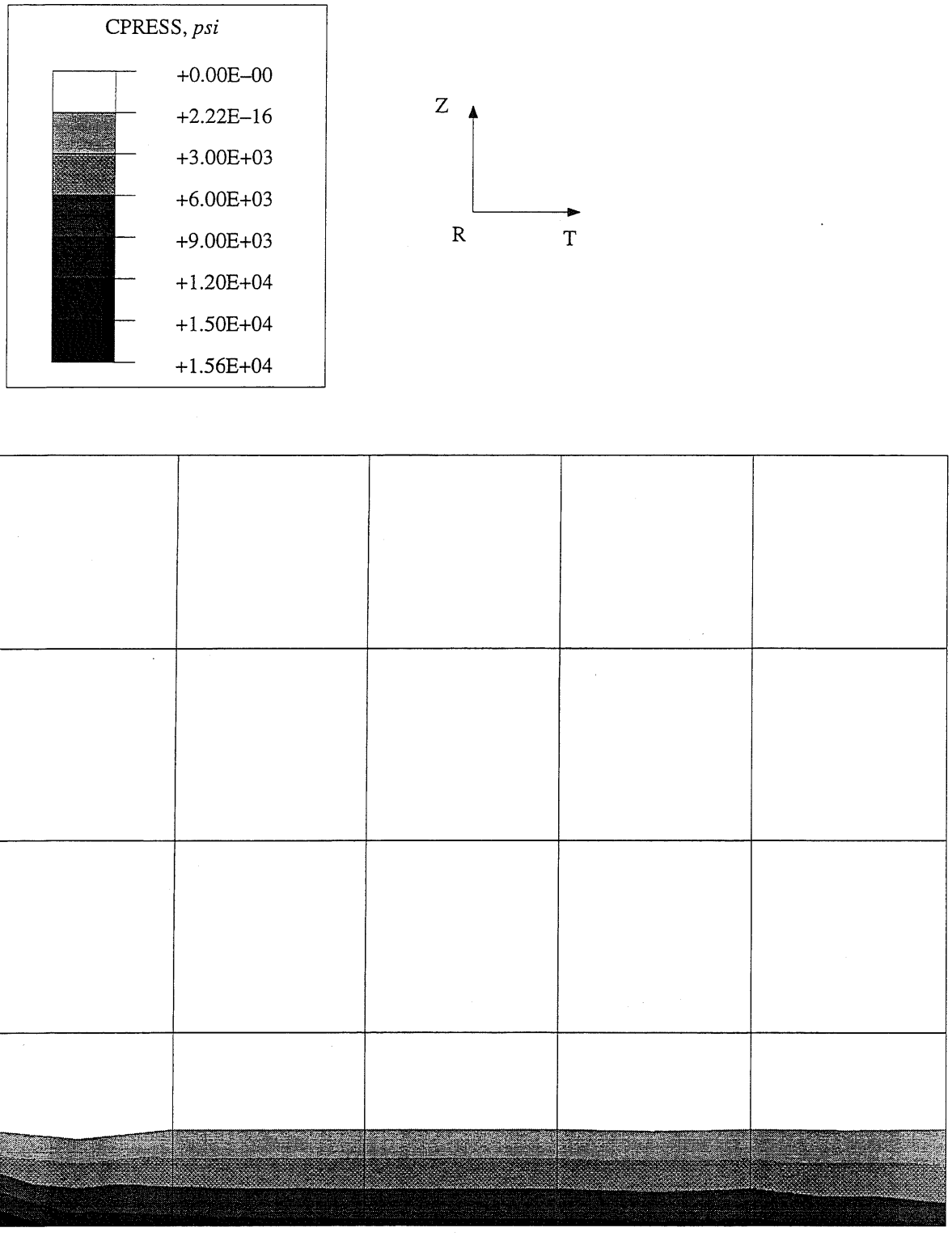

Figure 8.13: Hub Contact Surface Pressure Distribution.

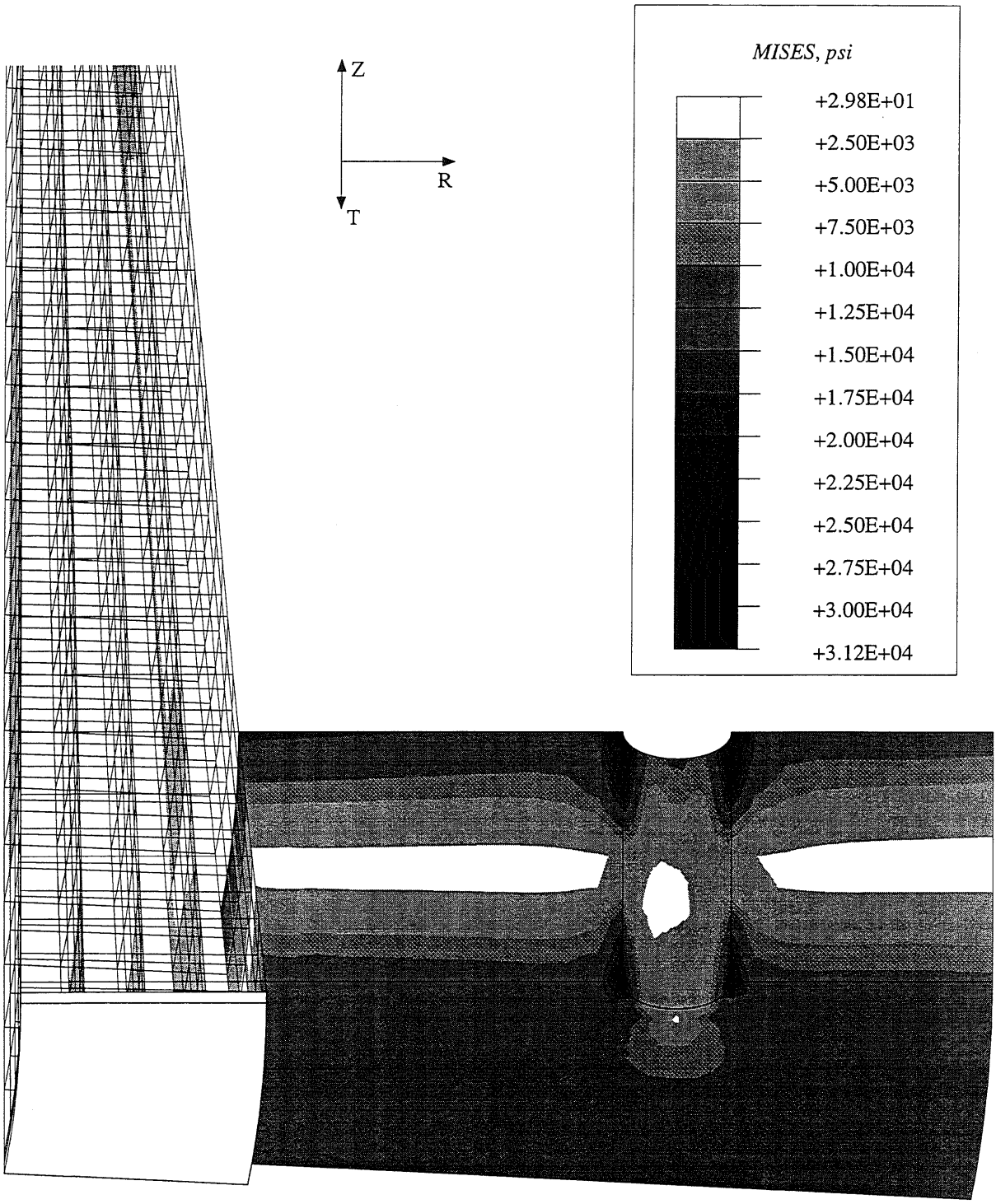

Figure 8.14: 3-D Distribution of von Mises Stresses.

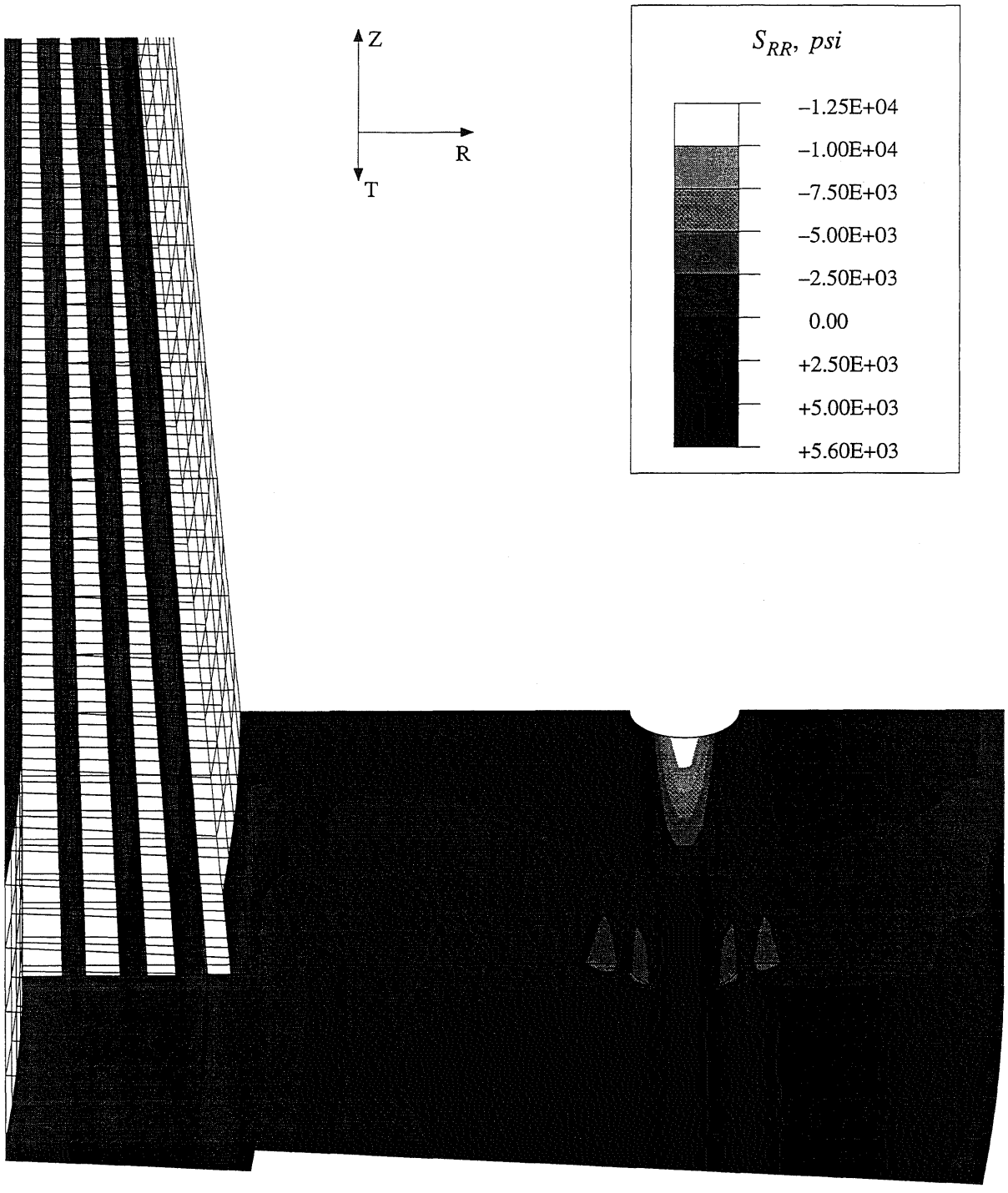

Figure 8.15: 3-D Distribution of Radial Stresses.

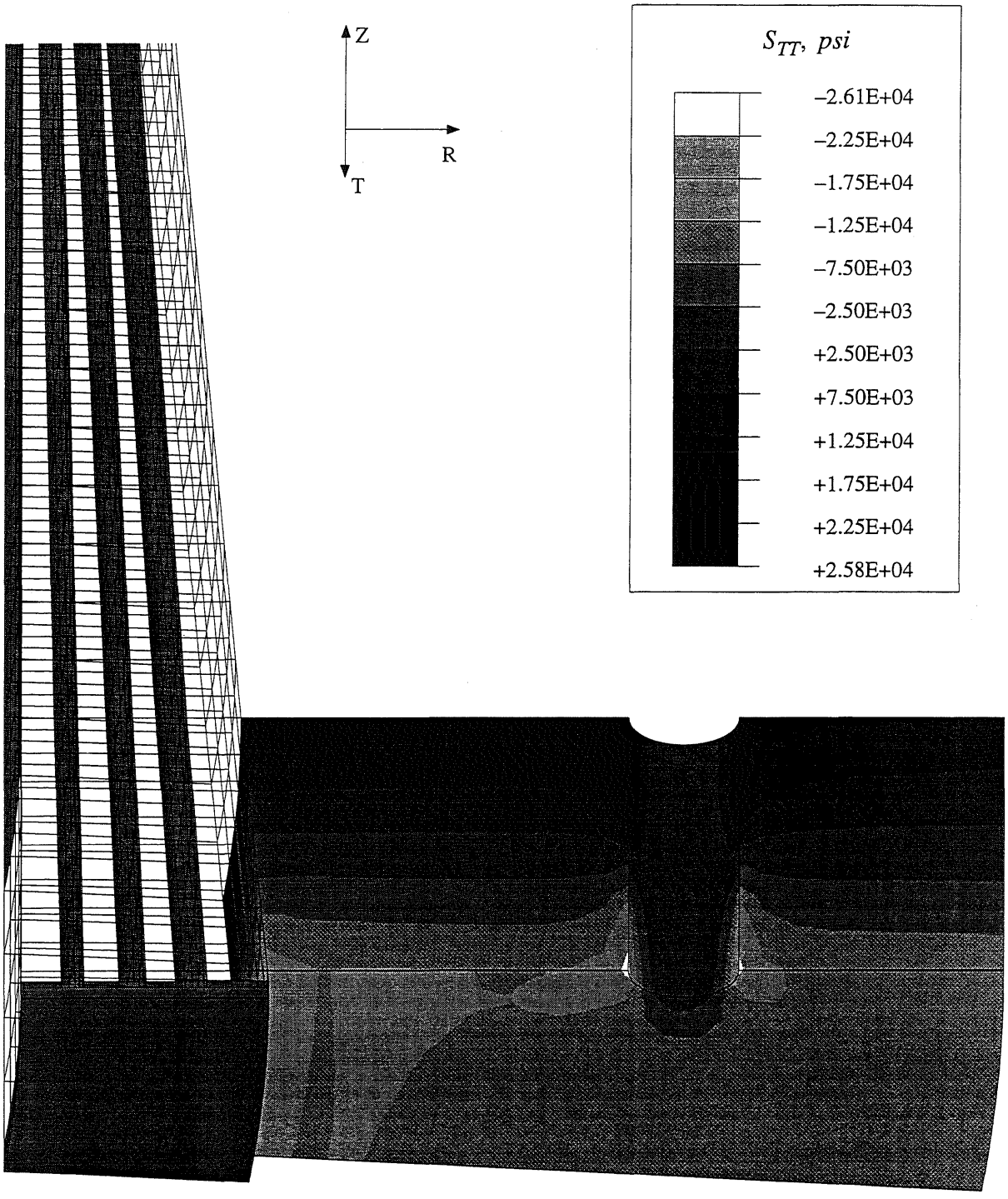

Figure 8.16: 3-D Distribution of Circumferential Stresses.

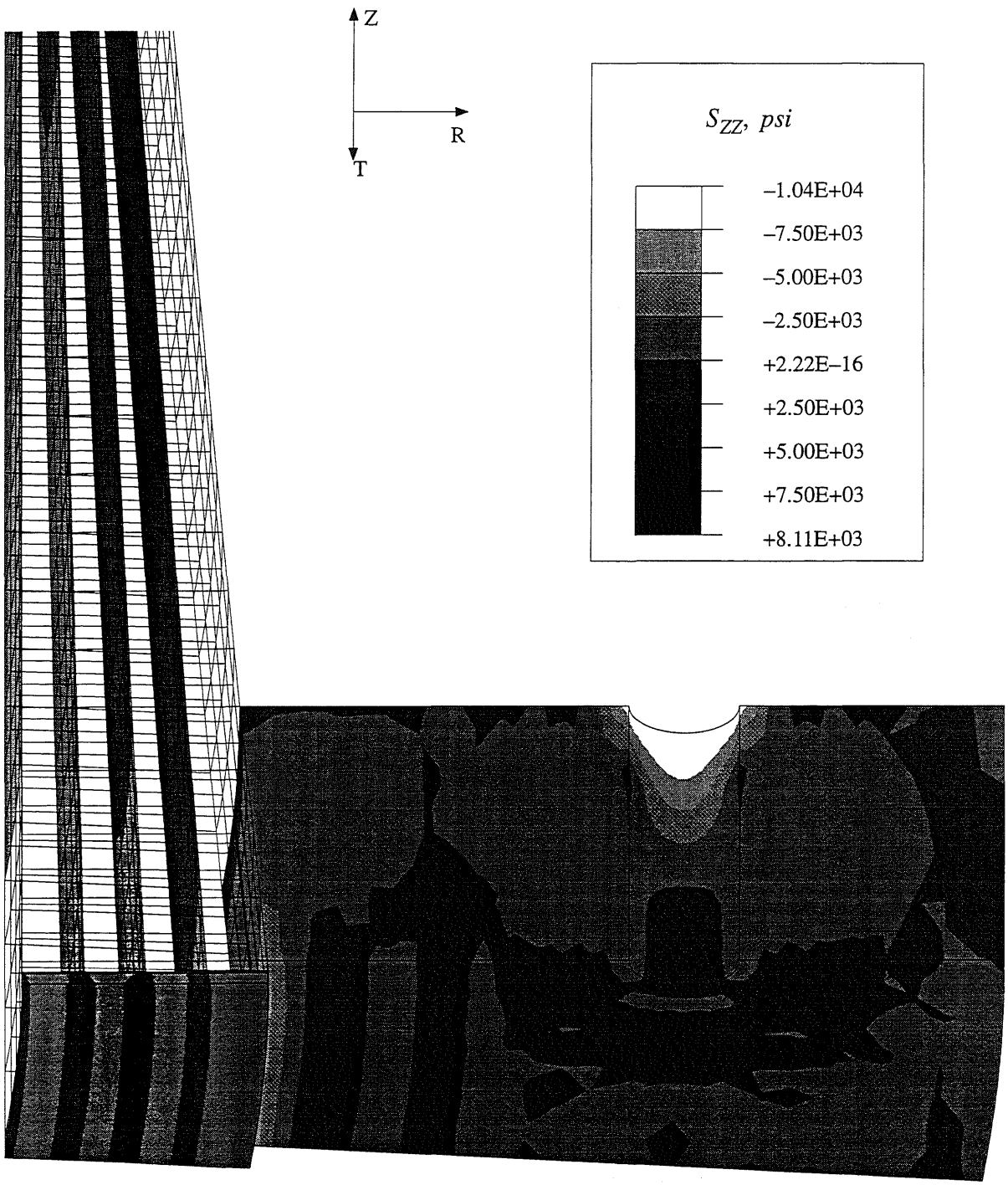

Figure 8.17: 3-D Distribution of Axial Stresses.

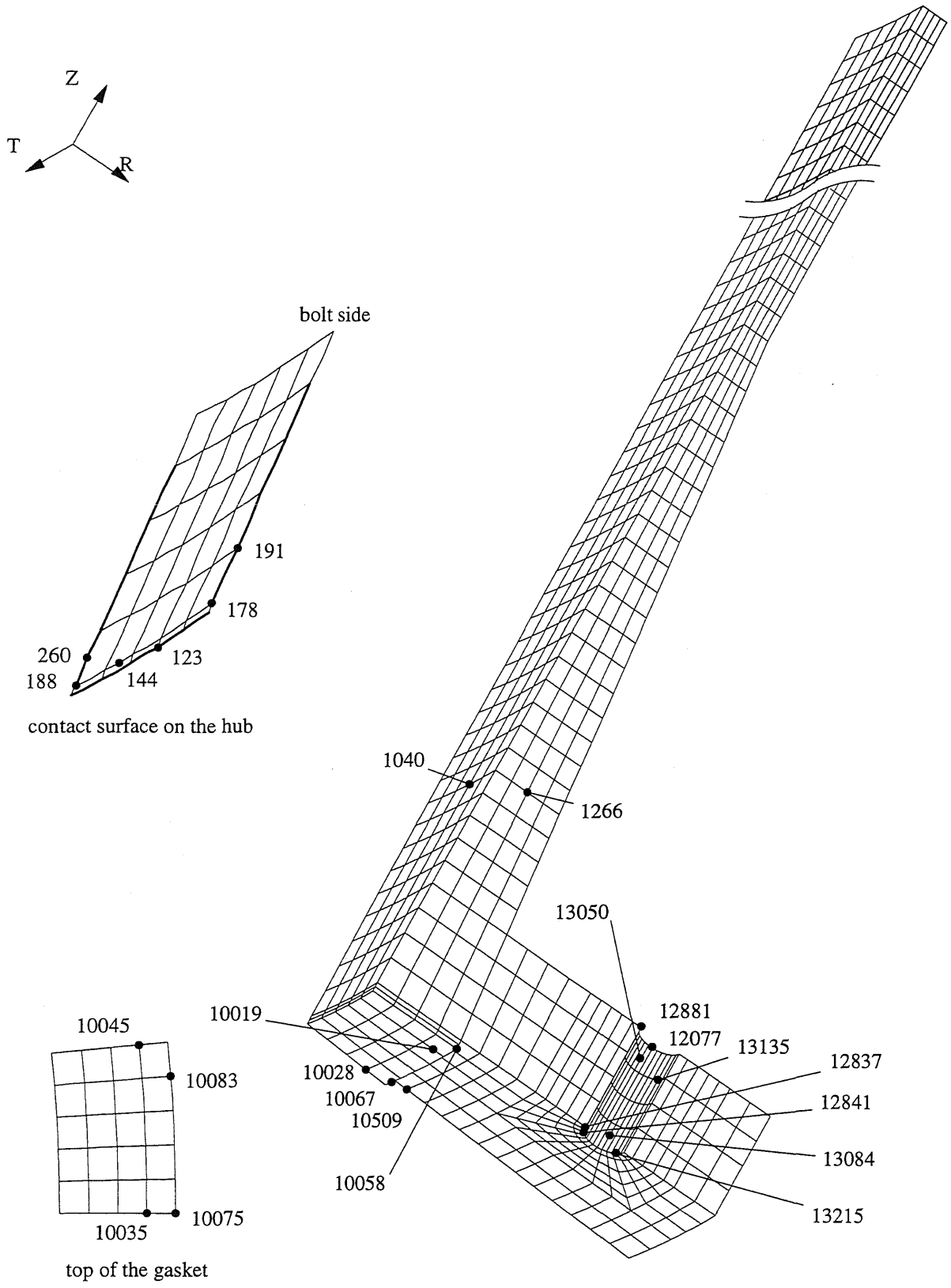

Figure 8.18: Location of the Stresses Reported in Table 8.2 though 8.4.

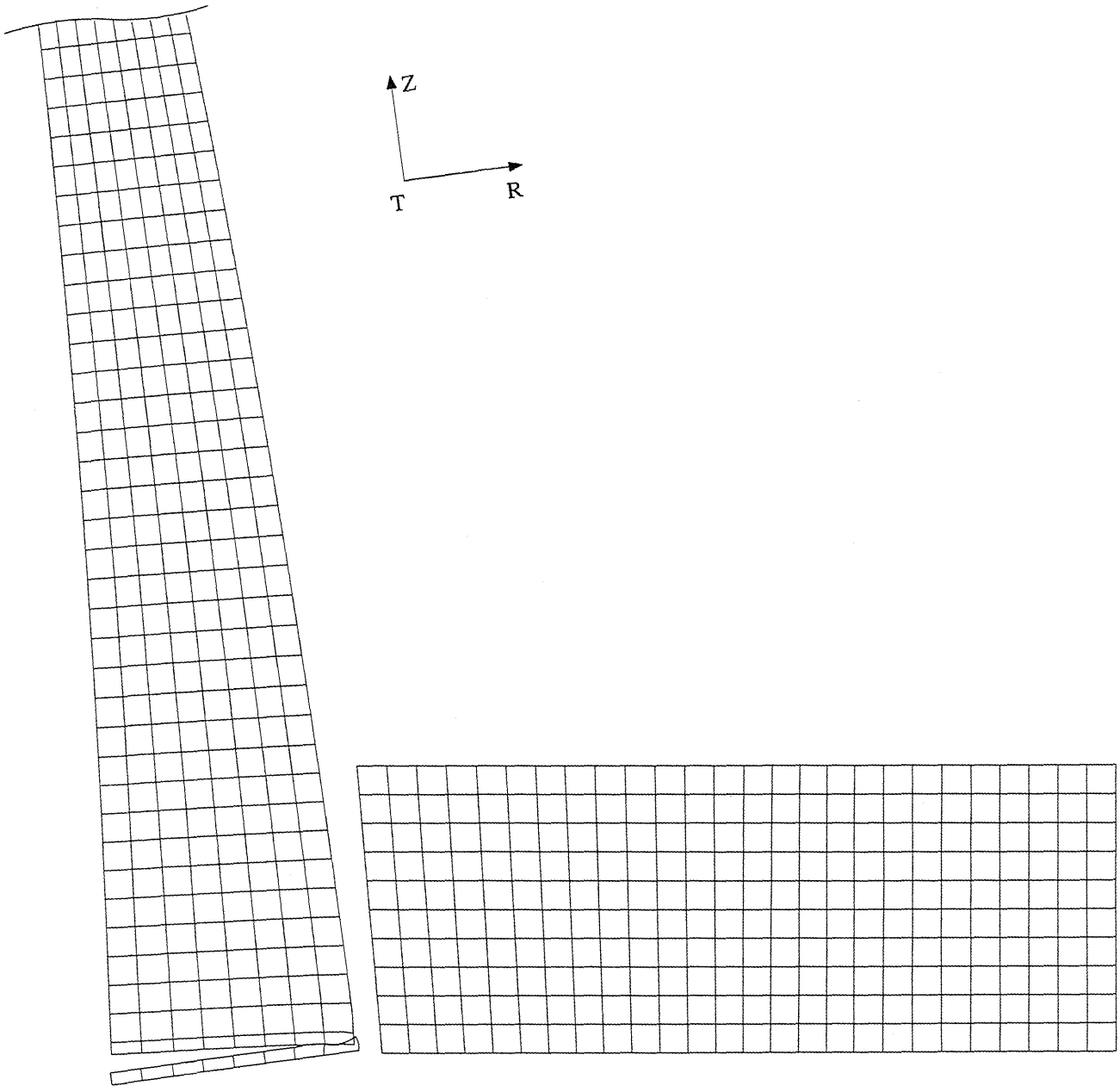

Figure 8.19: Axisymmetric Gasket and Stub Model Deformed Shape, Magnification 10.

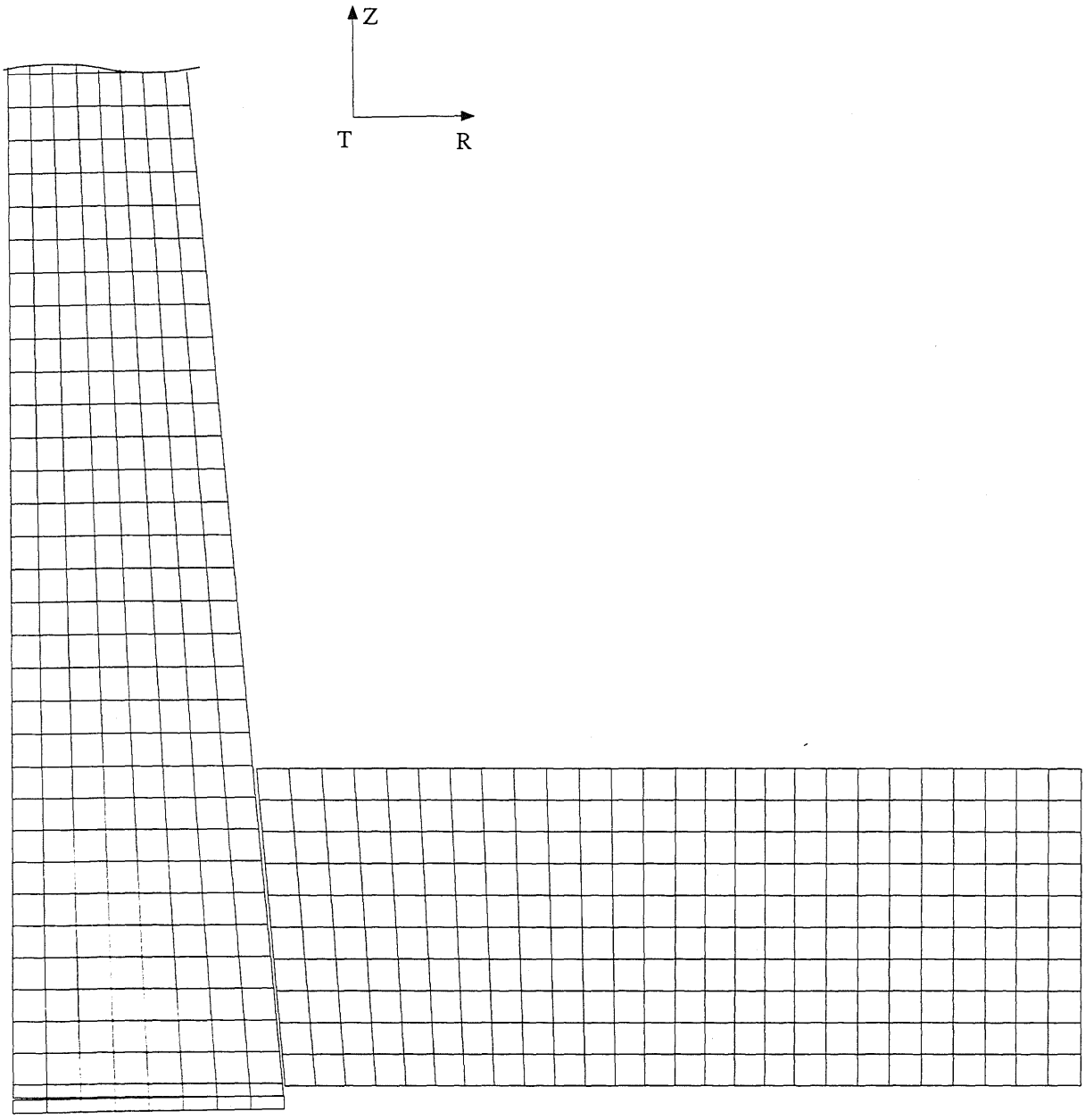

Figure 8.20: Axisymmetric Gasket and Stub Model Deformed Shape, Magnification 1.

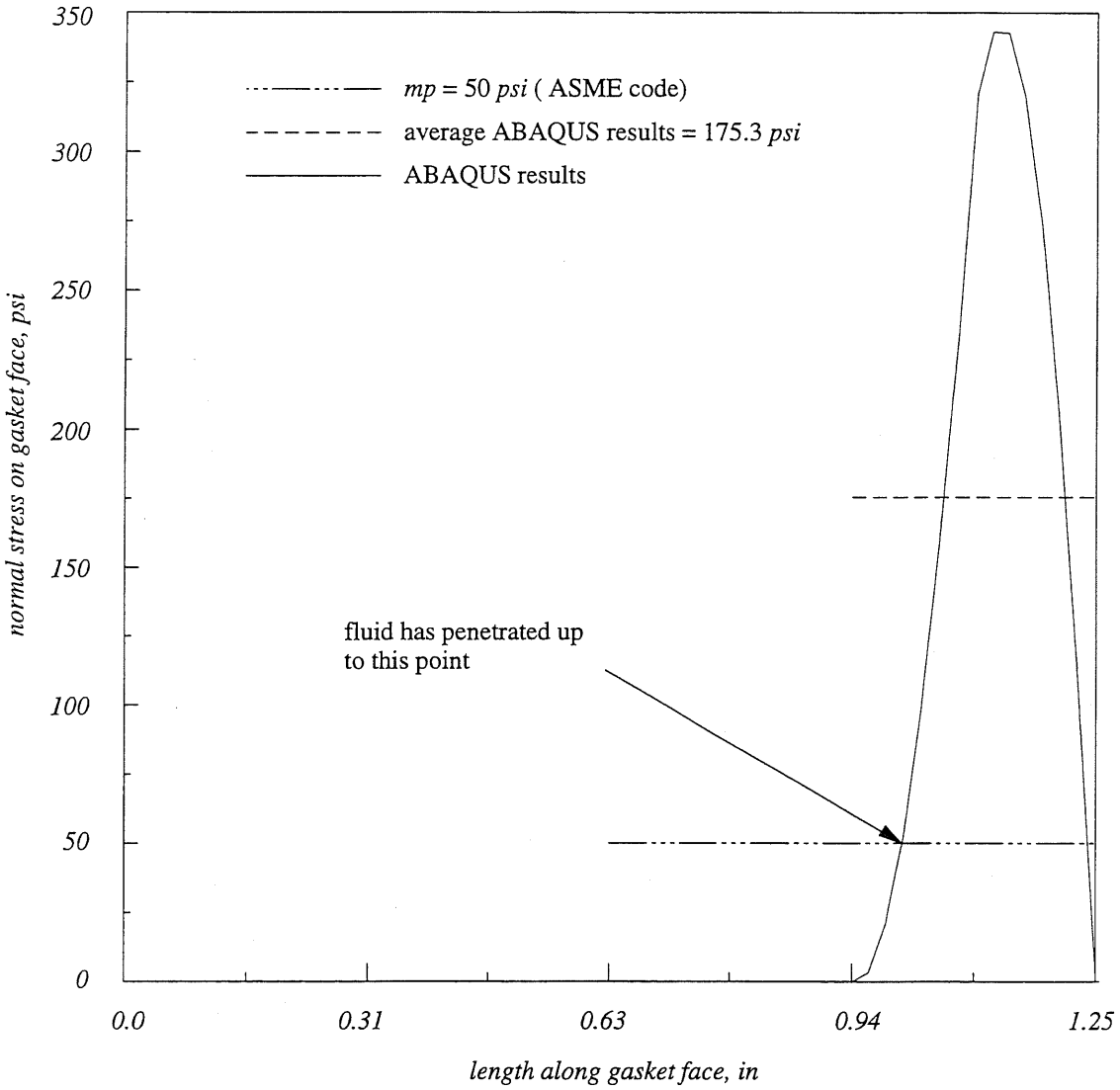

Figure 8.21: Gasket Contact Stress, Axisymmetric case.

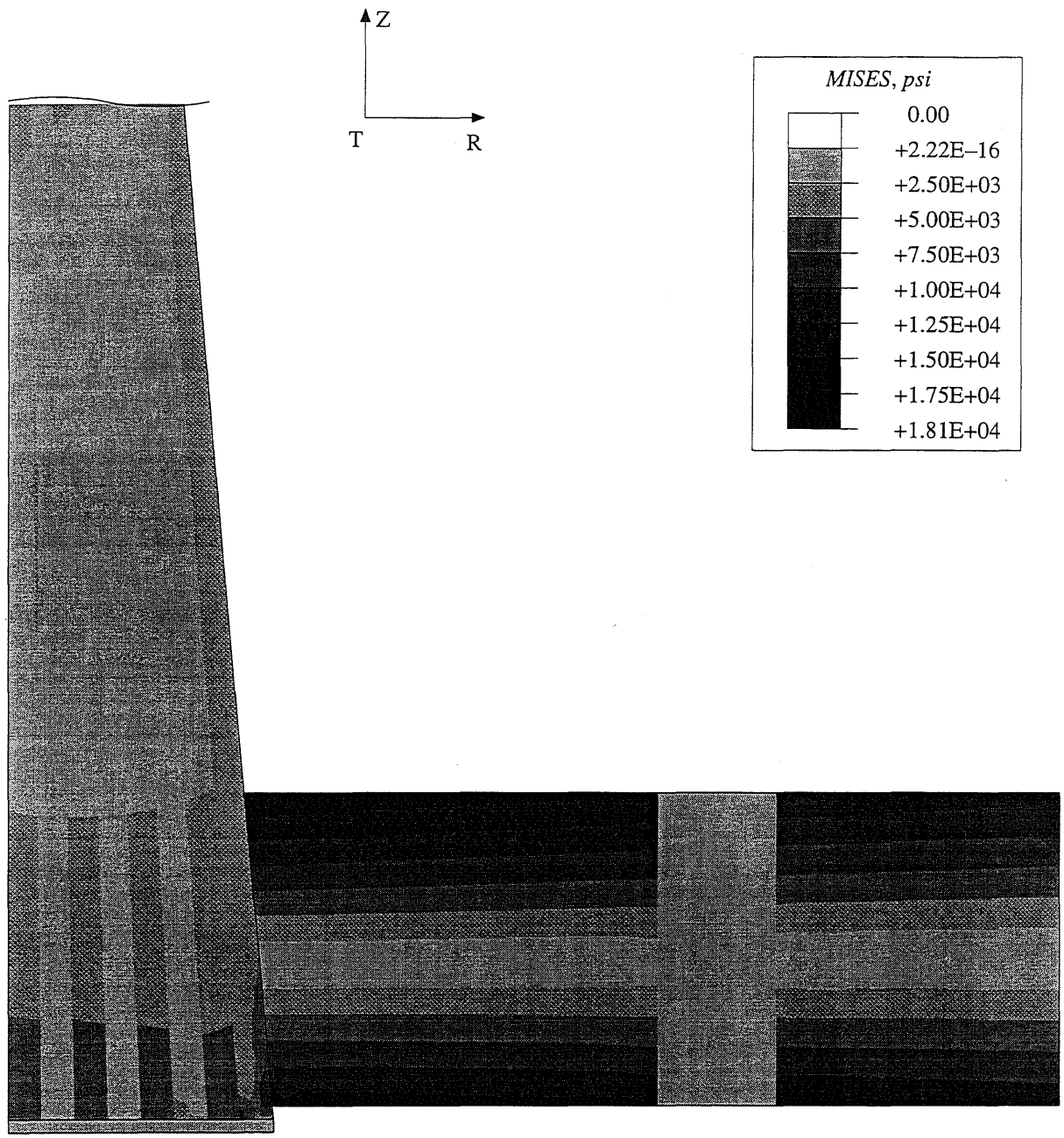

Figure 8.22: Distribution of von Mises Stresses in the Axisymmetric Model.

Load, lbs	Deformation, inches	Nominal Stress, psi	Nominal Stress, MPa	Nominal Strain
–1140	–0.0020	–205.8	–1.42	–0.012
–2280	–0.0060	–411.7	–2.84	–0.048
–4560	–0.0145	–823.4	–5.68	–0.116
–6840	–0.0230	–1235.1	–8.51	–0.184
–9120	–0.0300	–1646.9	–11.35	–0.240
–11400	–0.0365	–2058.6	–14.19	–0.292
–13680	–0.0415	–2470.3	–17.03	–0.332
–15960	–0.0455	–2882.0	–19.87	–0.364
–18240	–0.0495	–3293.8	–22.71	–0.396
–20520	–0.0530	–3705.5	–25.55	–0.424
–22800	–0.0560	–4117.2	–28.39	–0.448
–25080	–0.0585	–4528.9	–31.22	–0.468
–27360	–0.0615	–4940.7	–34.06	–0.492
–29640	–0.0635	–5352.4	–36.90	–0.508
–31920	–0.0660	–5764.1	–39.74	–0.528
–34200	–0.0680	–6175.6	–42.58	–0.544
–36480	–0.0700	–6587.6	–45.42	–0.560
–38760	–0.0715	–6999.3	–48.26	–0.572
–39200	–0.0720	–7078.7	–48.80	–0.576

Table 8.1: 1/8" Synthetic Rubber (Neoprene) Gasket, 75 Shore Durometer Hardness [12].

	Maximum		Minimum	
stresses	value, *psi*	location, node	value, *psi*	location, node
S_{RR}	2405.0	188	–7595.0	130
S_{TT}	8464.0	1266	–10498.0	1512
S_{ZZ}	8115.0	260	–3289.0	742
S_{RT}	912.2	1040	–1237.0	144
S_{RZ}	1284.0	191	–679.6	144
S_{TZ}	3760.0	178	1789.0	123

Table 8.2: Range of Stresses in the 3-D Pipe-Hub Component.

	Maximum		Minimum	
stresses	value, *psi*	location, node	value, *psi*	location, node
S_{RR}	5604.0	13084	–12508.0	13077
S_{TT}	25806.0	12881	–26198.0	12837
S_{ZZ}	2303.0	10509	–10429.0	13077
S_{RT}	6724.0	13215	–6881.0	12841
S_{RZ}	1651.0	13050	–5260.0	10457
S_{TZ}	2193.0	13135	–530.9	13077
MISES	31245.0	12881	——	——

Table 8.3: Range of Stresses in the 3-D Stub Component.

	Maximum		Minimum	
stresses	value, *psi*	location, node	value, *psi*	location, node
S_{RR}	7.9	10045	–532.1	10075
S_{TT}	65.4	10019	–807.4	10058
S_{ZZ}	61.7	10019	–982.6	10075
S_{RT}	41.7	10067	–4.2	10028
S_{RZ}	29.0	10035	–298.7	10075
S_{TZ}	3.7	10045	–31.5	10083
MISES	648.9	10075	——	——

Table 8.4: Range of Stresses in the 3-D Gasket Component.

Chapter 9

Conclusions and Future Work

9.1 Conclusions

An innovative joining technique for filament wound pipes has been developed. This pipe joint was fashioned to address some of the problems reported in the literature. Since we have not yet manufactured and tested the joint, we cannot definitively comment as to its success in alleviating the problems faced by current FRP pipe designers. All of the problems with the current FRP pipe joining techniques are probably not completely eliminated, but the discontinuity, pull-back, bearing failure, and faulty construction problems are addressed by our design. This joint can be used to connect piping systems to pumps, valves or pre-existing flanged metallic piping systems.

We also described a possible manufacturing procedure using current filament winding equipment with minor alterations. The possible alteration to current equipment consists of mounting the dispenser on a pivot mechanism so as to allow the dispenser to rotate. This joint may be used for piping systems where one end is flanged and the other is such that the ring can be slipped on, since the hub is manufactured at the same time as the pipe. A two piece ring can be used in cases where both ends are flanged, or a butt-and-strap joint can be used to connect two pipe-hub sections together. This two piece ring could be assembled in the same way as the connecting rod in the crankshaft of an engine.

We also presented a design philosophy for the modified stub flanged joint, gasket, bolts and flanging system. The design of the gasket and the bolts is similar to that for metallic systems. This entails finding a bolt load sufficient to keep the joint leak tight during the operating life

of the joint, then choosing a sufficiently large bolt area to achieve this objective. The flange design bolt load is then computed using this bolt area. With this bolt load, we can proportion the two components of the modified stub flanged joint, pipe-hub and stub components. Also, we have validated the design calculations with finite element analysis. Our approach is well suited to design calculations, since many geometric and material parameters can be varied quickly and easily in order to find a satisfactory design.

We also used detailed finite element analysis of a specific geometry to demonstrate that our simple calculations can produce safe designs. There are some stress concentrations that are not captured by our design equations and we have made allowances for them in the factors of safety we recommend in the design calculations. In the detailed finite element modeling, we demonstrated that an axisymmetric analysis (which is much more cost effective than a full 3-D analysis, in terms of generating the model and running the analysis) can be used in analyzing critical designs. The leakage behavior of the modified stub flange was also studied using contact elements. The results showed that the gasket design guidelines do provide sufficient load to keep the joint leak tight.

9.2 Recommendations for Future Work

Further analytical investigation of FRP joints would concentrate on the assumptions of perfect bond between layers and the cylindrical variable thickness shell. Shear deformation is not accounted for in the stress analysis of the pipe and hub. Studies of other composite systems warrant consideration of shear deformation in the analysis of these models. Therefore, we will revisit and expand the model formulation to include shear deformation. Also, the tapered end is modeled as a variable thickness cylindrical shell in the current study, whereas a variable thickness conical shell is more appropriate.

Although the results of the analytical model compare well with finite element analysis, they must be verified experimentally. The experimental investigation would focus on the feasibility of the proposed manufacturing technique, verification of the design criteria, and identification of suitable material systems from which to manufacture the joint. Furthermore, a number of filament winding procedures are now available such as helical winding and robotic winding. The feasibility of these different winding techniques for the manufacturing of the modified stub flanged joint should be studied.

A detailed investigation of temperature and hygrothermal effects needs to be conducted. The system may be exposed to moisture and severe temperature when in operation or during the curing process.

In order to conduct detailed finite element analysis of leakage, we need reliable gasket material properties; therefore, experimental and numerical investigations of gasket material properties are required. Also, present gasket investigation is limited to metallic joint applications. Our focus would be on gasketing materials best suited to FRP joints, such as rubber. Specifically, we would concentrate our investigation on the application of finite element analysis to obtain gasket design parameters, such as the gasket leak tightness ratio m and the gasket yield factor y. Furthermore, we would conduct correlations of experimental data with the gasket factors presented in the ASME BPV code.

The interaction between the composite system and the stub should also be studied further considering different stub systems, systems with and without a ring stiffener. Also, the sliding of the stub down the hub should be studied carefully and recommendations for the offset between the bottom of the hub and the stub should be derived, i.e., specify a tolerance so that the mating flanges do not come into contact. Further issues of design should be studied, such as bolt size and applied torque.

Appendix A

Axisymmetric Variable Thickness Cylindrical Shell

A.1 Introduction

A shell is a structural system with its mid-surface defined, in general, by a curved surface, i.e., dimensions in the plane of the structural system are much larger than the perpendicular dimension, its thickness. In this appendix, we concentrate on a shell generated by a general line when revolved about an axis, a *surface of revolution*; in particular, the shell generated by a straight line parallel to the axis of revolution, a *cylindrical shell*. The thickness need not be uniform over the entire surface; in the case presented in this appendix, the thickness varies uniformly in the axial direction (see figure A.1) and is uniform in the circumferential direction. The deformation in shells is measured with respect to a coordinate system on their mid-surface, see figure A.2.

If the loading is such that it causes the cylindrical shell to deform into another surface of revolution, then an a*xisymmetric analysis* can be used. That is, because of axial symmetry, there is no circumferential displacement or change in any quantity in the circumferential direction (i.e., $\frac{\partial(\,)}{\partial\theta} = 0$). Therefore, for an axisymmetric cylindrical shell, some of the stress resultants reduce to zero, the non-zero resultants are shown on figure A.3.

This appendix is organized as follows. In section A.2, we present the definition of the stress resultants. The equations of equilibrium for a differential element are presented in section A.3. The relevant kinematic equations are presented in section A.4.

A.2 Definition of Stress Resultants

Figure A.4 shows the tractions acting on a differential element shown shaded in figure A.2. However, it is more convenient to work with a simpler but equivalent system of forces and moments acting on the shell cross-section. These resultant forces and moments, at a distance x from the origin, are defined as follows. The resultant forces are obtained by integrating the corresponding tractions through the shell thickness, e.g., the axial stress resultant is

$$N_x R d\theta = \int_{-g(x)/2}^{g(x)/2} \sigma_x^{(z)}(R - z) dz d\theta, \tag{A.1}$$

where $\sigma_x^{(z)}$ is the average axial stress in a fiber located at a distance z from the neutral axis. Now solving for the stress resultant we get

$$N_x = \int_{-g(x)/2}^{g(x)/2} \sigma_x^{(z)}\left(1 - \frac{z}{R}\right) dz. \tag{A.2}$$

A further assumption made in thin shell theory is that the shell radius R is much larger than the distance z, i.e., $\frac{z}{R} << 1$. This assumption allows us to reduce the equation above to

$$N_x = \int_{-g(x)/2}^{g(x)/2} \sigma_x^{(z)} dz. \tag{A.3}$$

Similarly, the resultant moments are obtained by integration through the thickness of the corresponding stresses acting on a fiber at a distance z from the mid-plane surface times the moment arm about the mid-surface. Therefore, the relevant stress resultants are

$$\left\{N_x,\ N_\theta,\ Q_x,\ M_x,\ M_\theta\right\} = \int_{-g(x)/2}^{g(x)/2} \left\{\sigma_x^{(z)},\ \sigma_\theta^{(z)},\ \tau_{xz}^{(z)},\ z\sigma_x^{(z)},\ z\sigma_\theta^{(z)}\right\} dz. \tag{A.4}$$

Note that the limits of integration are functions of x, since we are integrating at a distance x from the origin. Also, these stress resultants are forces and moments per unit circumferential length.

A.3 Axisymmetric Equilibrium Equations

The stress resultants shown in figure A.3 are for the axisymmetric case and can be computed using equation (A.4) and appendix B. From force and moment balance, we obtain three equilibrium equations in four unknowns N_x, N_θ, Q_x, and M_x :

$$\sum F_x = 0 \quad \Rightarrow \quad N_{x,x} + X = 0, \tag{A.5}$$

$$\sum F_z = 0 \quad \Rightarrow \quad Q_{x,x} + \frac{N_\theta}{R} + Z = 0, \tag{A.6}$$

$$\sum M_\theta = 0 \quad \Rightarrow \quad M_{x,x} - Q_x = 0. \tag{A.7}$$

The comma in the subscript denotes partial differentiation. The other three equations of equilibrium are identically satisfied.

A reduction in the number of equations is possible from three [(A.5), (A.6), and (A.7)] to two [(A.6) and (A.7)], i.e., integrating equation (A.5) we get

$$N_x = -\int X dx + C = \overline{N}_x, \tag{A.8}$$

where $\overline{N}_x$ is the equivalent resultant end pressure, as shown in figure A.1.

Therefore, we are left with two equations (A.6) and (A.7) in three unknowns Q_x, N_θ, and M_x. We need to consider the displacement relations, or kinematics.

A.4 Kinematics

In this formulation we will assume small displacements and linear strains. Other assumptions include; straight fibers normal to the midplane before deformation remain straight and normal to the midplane after deformation (Love's first approximation, i.e., out-of-plane shear strains are zero, $\gamma_{z\theta}^{(z)} = \gamma_{zx}^{(z)} = 0$ – the superscript *(z)* denotes that these values are for a fiber at a distance z from the neutral axis), and inextensible (i.e., normal strain is zero, $\epsilon_z^{(z)} = 0$), see figure A.5. In shell theory the normal out-of-plane stress is small compared to the in-plane normal stresses, $\sigma_z^{(z)} \approx 0$; this is a contradiction, but it does not affect the end result.

We need the deformation of a fiber located a distance z away from the midplane. To aid us in deriving the strain equations in terms of displacements, we use figure A.5. For this derivation we use engineering strain, i.e., $\epsilon = \frac{\Delta L}{L}$. Therefore, the axial strain $\epsilon_x^{(z)}$, defined by the change in length of the side dx, is

$$\epsilon_x^{(z)} = \frac{u^{(z)} + u_{,x}^{(z)} dx - u^{(z)}}{dx} = u_{,x}^{(z)}, \tag{A.9}$$

and the circumferential strain $\epsilon_\theta^{(z)}$, defined by the change in length of the $Rd\theta$ side (in the plane perpendicular to the page in figure A.5) is

$$\epsilon_\theta^{(z)} = \frac{[(R - z) - w^{(z)}]d\theta - (R - z)d\theta}{(R - z)d\theta} = -\frac{w^{(z)}}{R}, \tag{A.10}$$

where the negative sign arises because a displacement w in the positive z direction leads to a negative or compressive strain. Due to axial symmetry, there is no in-plane shearing strain in the differential element, i.e., $\gamma_{x\theta}^{(z)} = 0$. Also, since we assume small deformations, the rotations of the differential element dx at points A and B are approximately equal, i.e., $\Omega_A \approx \Omega_B$. We assume these rotations to be equal to Ω, the rotation of the side dx, which is given by

$$\Omega = \frac{w + w_{,x}dx - w}{dx} = w_{,x}. \tag{A.11}$$

We can now find the fiber displacements in terms of the midplane displacements. The radial displacement is the same for any point through the thickness because of the last assumption made in the beginning of this section, i.e.,

$$w^{(z)} = w, \tag{A.12}$$

and due to axial symmetry, there is no circumferential displacement. The fiber axial displacement is a function of the midplane axial displacement and the axial rotation

$$u^{(z)} = u - zw_{,x}. \tag{A.13}$$

Note, the midplane displacements vary in the axial direction, therefore, they are functions of x.

Substituting equations (A.12) and (A.13) into equations (A.9) and (A.10), we get the desired strain displacement relations

$$\left.\begin{aligned} \epsilon_x^{(z)} &= u_{,x}(x) - zw_{,xx}(x), \\ \epsilon_\theta^{(z)} &= -\frac{w(x)}{R}, \\ \gamma_{x\theta}^{(z)} &= 0. \end{aligned}\right\} \tag{A.14}$$

Here, we have introduced three more equations, but also five more unknowns, therefore we need the relation between stresses and strains, the constitutive law, appendix B.

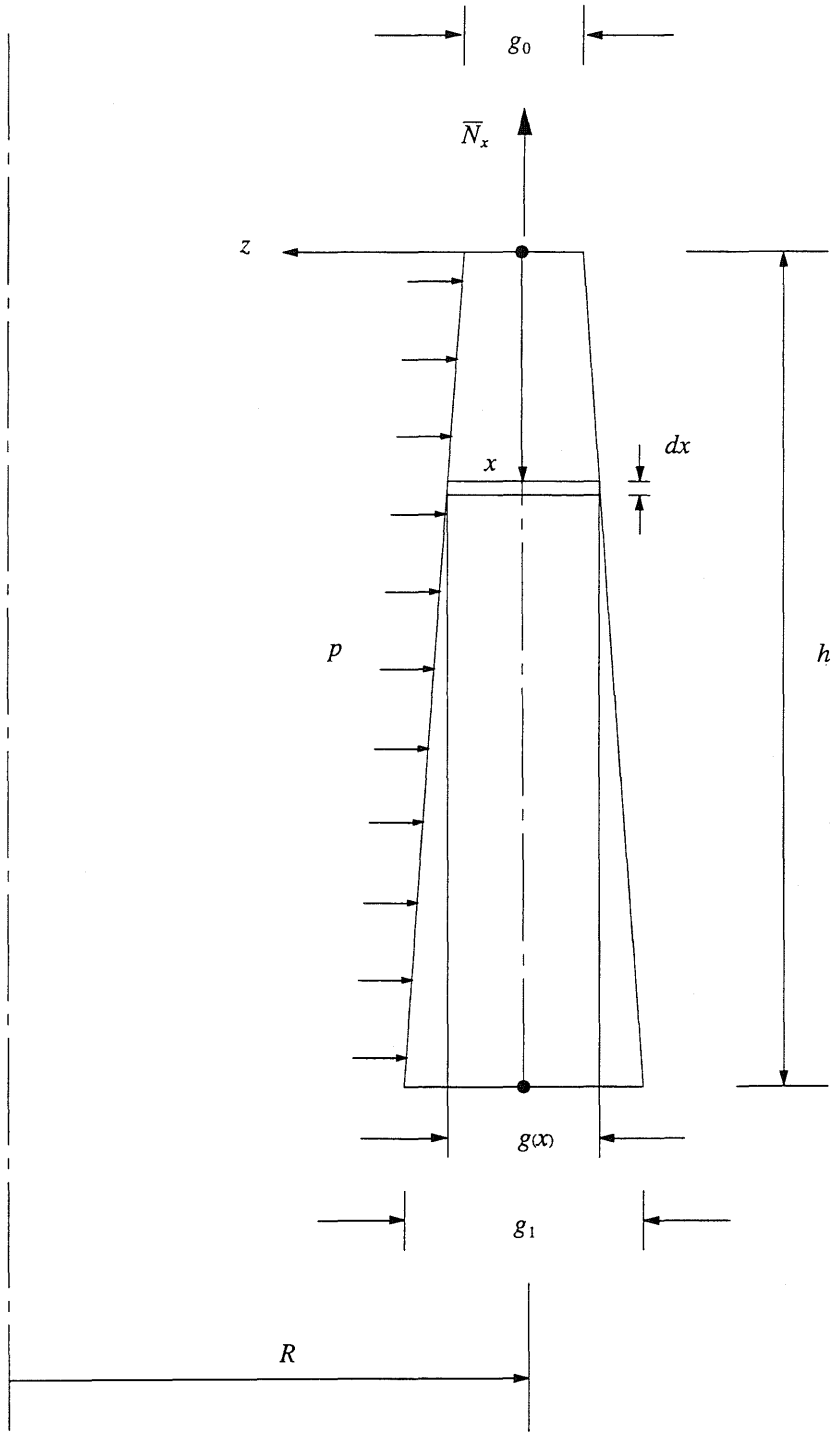

Figure A.1: Shell Geometry and Loading

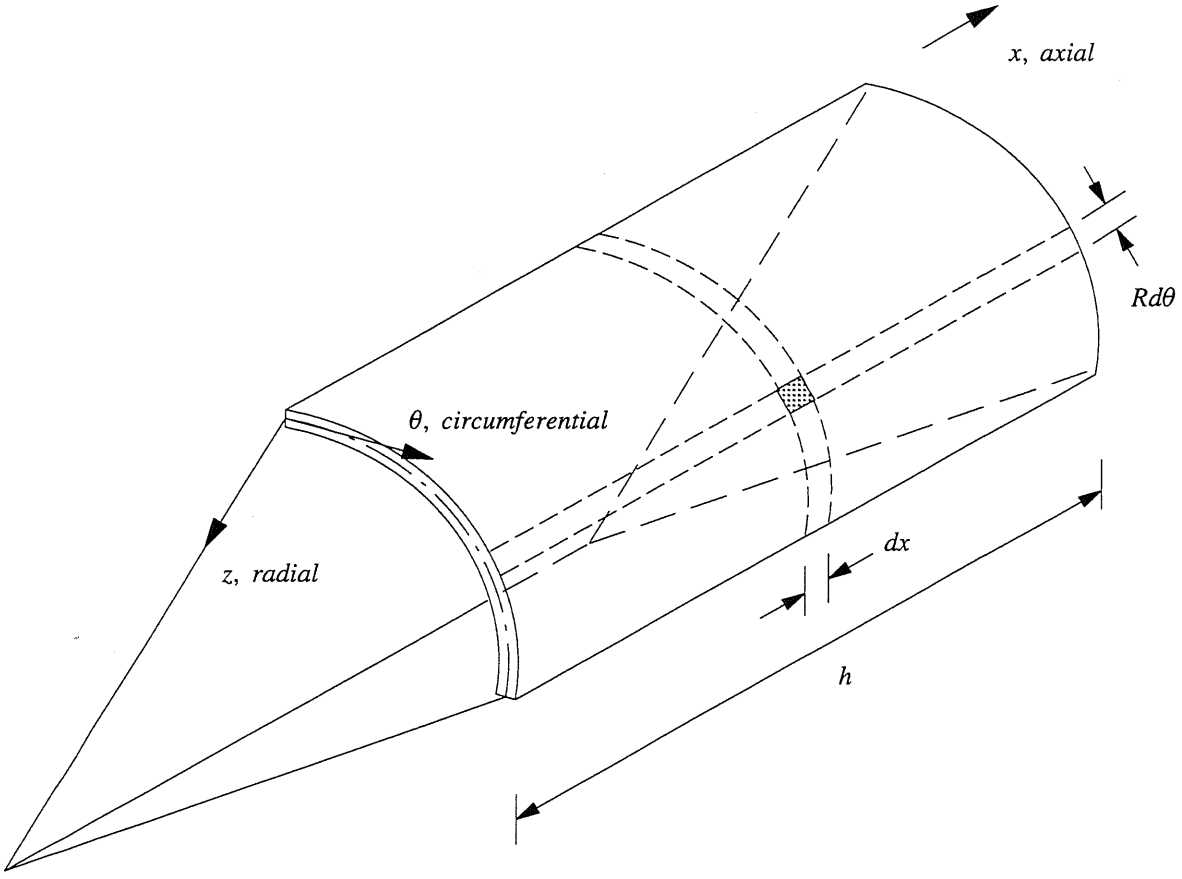

Figure A.2: Cylindrical Shell

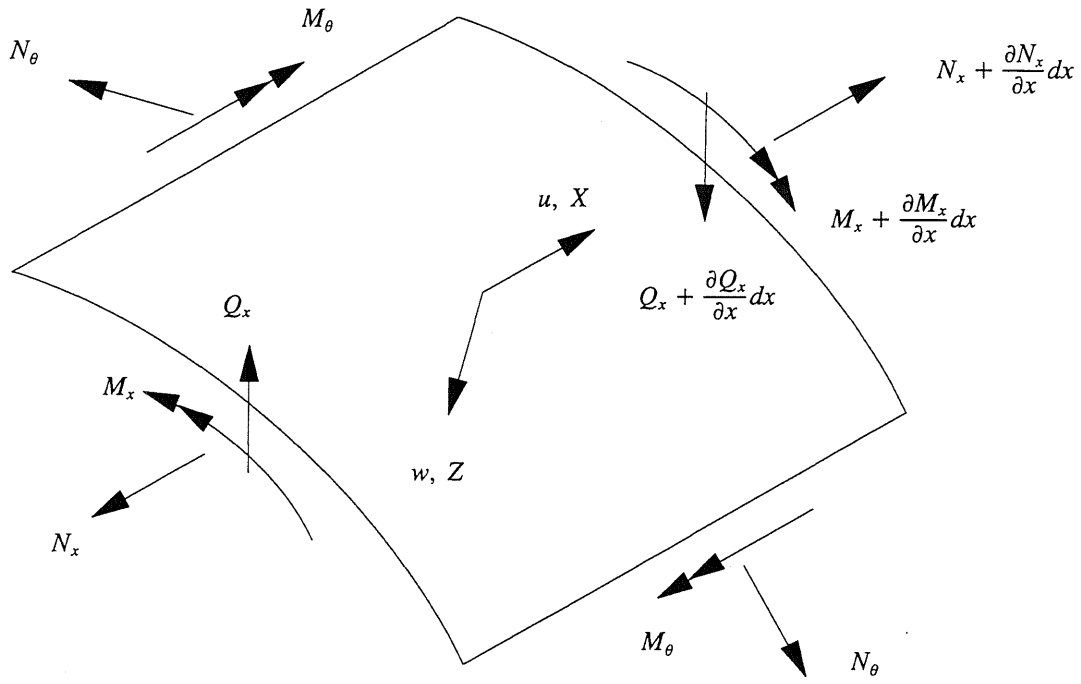

Figure A.3: Stress Resultant Equilibrium and Midplane Displacements.

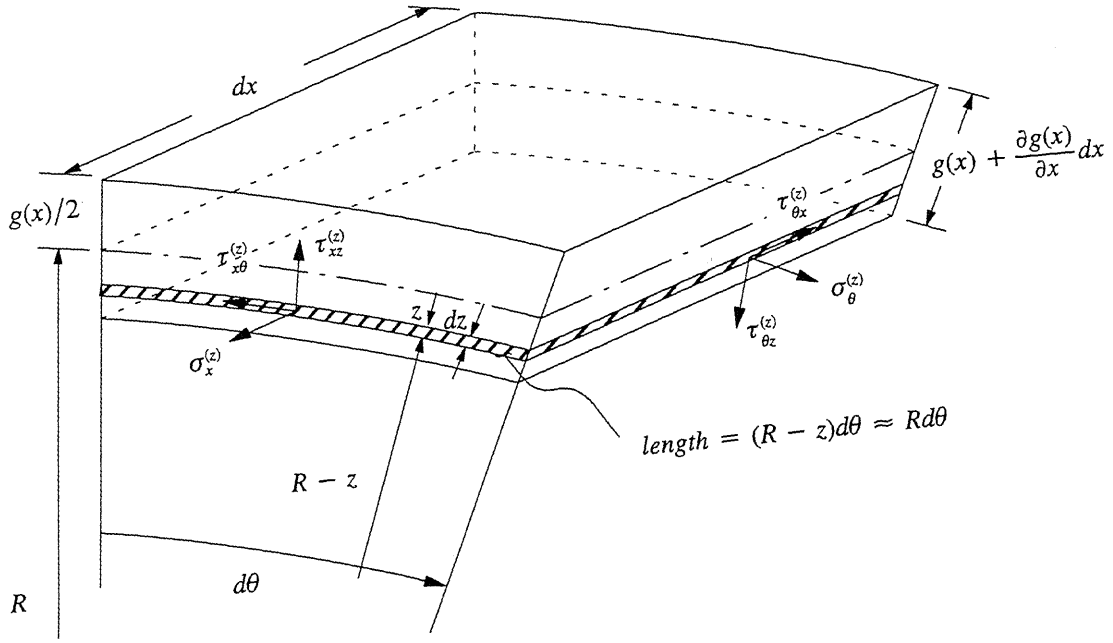

Figure A.4: Shell Stresses.

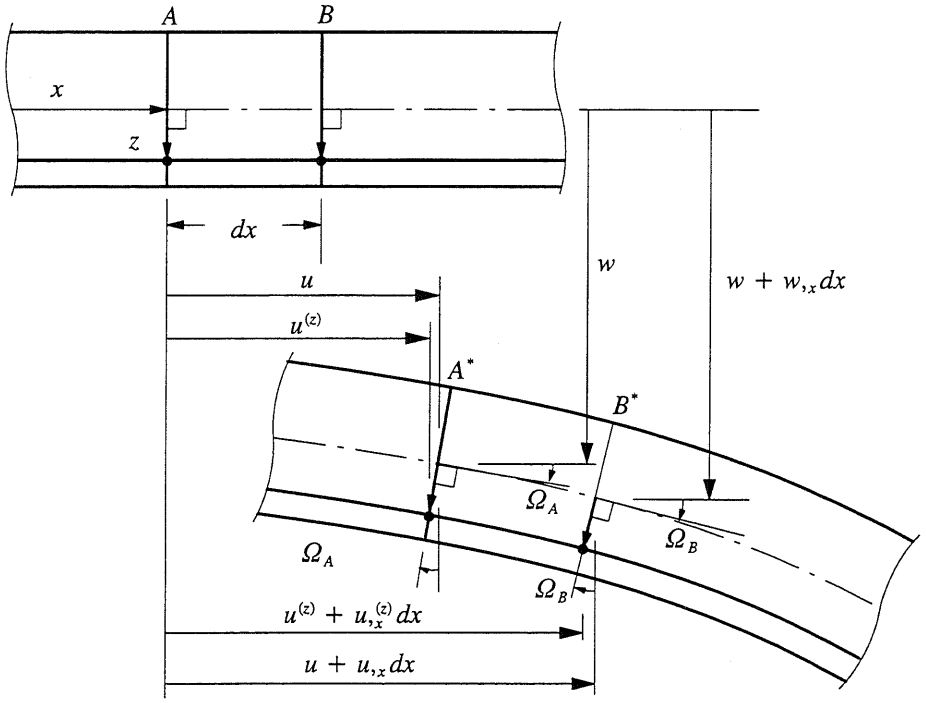

Figure A.5: Axially Symmetric Deformation of a Cylindrical Shell.

Appendix B

Review of Lamination Theory

B.1 Introduction

Lamination Theory is part of the theory of Mechanics of Composite Materials. A composite material, or commonly known as a *composite* in the literature, is defined as a combination of chemically distinct materials on the macroscale bonded together by a distinct interface to produce a material system with enhanced material properties. One example well known to Civil Engineers is *reinforced concrete;* steel reinforcing bars are embedded in the concrete paste to improve its tensile strength. This type of composite, however, is not analyzed using lamination theory. Lamination theory is used in the analysis of fiber reinforced matrix materials which are manufactured in layers, *laminae*, each lamina consisting of parallel fibers embedded in a matrix. Laminae can be stacked in a specified sequence of orientation to form a laminate. The sequence of orientation can be chosen to meet design strength and stiffness demands. Lamination theory can be summarized as the development of equations that relate generalized strains to generalized forces through the constitutive law. In this appendix, we review the fundamentals of lamination theory needed in our study.

At the micro-level a composite is a complex system consisting of fibers and matrix combined to form a monolithic system. The material system is simplified by assuming that the fiber and matrix properties can be combined into an effective transversely isotropic material layer.

In this appendix, we make use of the derivations presented in appendix A to aid us in the derivation of lamination theory. We now state other assumptions made:

(i) Each lamina acts as a homogeneous transversely isotropic linear elastic system.

(ii) The laminae in a laminate are perfectly bonded together.

(iii) Each layer is of linear varying thickness. Each lamina has equal thickness at the large end ($g_1 = nt_1$) and at the small end ($g_0 = nt_0$) and varies linearly along the axial direction.

(iv) All the assumptions made in appendix A hold.

The following section describes the derivation of lamination theory.

B.2 Stress-Strain Relations for Plane Stress in a Transversely Isotropic Material

The constitutive relations for a transversely isotropic material in plane stress in contracted notation are as follows:

$$\begin{Bmatrix} \sigma_1 \\ \sigma_2 \\ \tau_{12} \end{Bmatrix}^{(z)} = \begin{bmatrix} Q_{11} & Q_{12} & 0 \\ Q_{12} & Q_{22} & 0 \\ 0 & 0 & Q_{66} \end{bmatrix} \begin{Bmatrix} \epsilon_1 \\ \epsilon_2 \\ \gamma_{12} \end{Bmatrix}^{(z)}. \tag{B.1}$$

We can write the above equation in matrix form as

$$\{\sigma\}^{(z)} = [Q]\{\epsilon\}^{(z)}, \tag{B.2}$$

where the constitutive matrix components are

$$\left.\begin{aligned} Q_{11} &= \frac{E_1}{1 - \nu_{12}\nu_{21}}, \\ Q_{12} &= \frac{\nu_{12}E_2}{1 - \nu_{12}\nu_{21}} = \frac{\nu_{21}E_1}{1 - \nu_{12}\nu_{21}} \quad \Rightarrow \quad \frac{\nu_{12}}{E_1} = \frac{\nu_{21}}{E_2}, \\ Q_{22} &= \frac{E_2}{1 - \nu_{12}\nu_{21}}, \\ Q_{66} &= G_{12}. \end{aligned}\right\} \tag{B.3}$$

In these equations, E_1 is Young's modulus in the laminae fiber direction, E_2 is Young's modulus transverse to the laminae fiber direction, G_{12} is the laminae in-plane shear modulus, ν_{12} is the major Poisson's ratio, and ν_{21} is the minor Poisson's ratio (see Jones [33] for the computation of these quantities from the properties of each constituent).

In figure B.1 *(a)* we show the global coordinate system, laminate coordinates (x, θ, z), and the local coordinate system, laminae coordinates ($1, 2, 3$). The in-plane laminae coordinates

run parallel and perpendicular to the fiber orientation and make an angle ϕ with the laminate coordinates, see figure B.1 *(b)*. The stresses can be transformed from laminae coordinates to laminate coordinates using the tensoral transformation laws. The final result is

$$\begin{Bmatrix} \sigma_x \\ \sigma_\theta \\ \tau_{x\theta} \end{Bmatrix}^{(z)} = \begin{bmatrix} C^2 & S^2 & -2SC \\ S^2 & C^2 & 2SC \\ SC & -SC & C^2-S^2 \end{bmatrix} \begin{Bmatrix} \sigma_1 \\ \sigma_2 \\ \tau_{12} \end{Bmatrix}^{(z)}, \tag{B.4}$$

where $C = \cos\phi$ and $S = \sin\phi$. Again, we can write the above equation in matrix form,

$$\{\bar{\sigma}\}^{(z)} = [T]^{-1}\{\sigma\}^{(z)}. \tag{B.5}$$

Similarly, the strains can be transformed from laminae coordinates to laminate coordinates

$$\begin{Bmatrix} \epsilon_x \\ \epsilon_\theta \\ \gamma_{x\theta}/2 \end{Bmatrix}^{(z)} = \begin{bmatrix} C^2 & S^2 & -2SC \\ S^2 & C^2 & 2SC \\ SC & -SC & C^2-S^2 \end{bmatrix} \begin{Bmatrix} \epsilon_1 \\ \epsilon_2 \\ \gamma_{12}/2 \end{Bmatrix}^{(z)},$$

or in matrix form,

$$\left\{\bar{\epsilon}'\right\}^{(z)} = [T]^{-1}\left\{\epsilon'\right\}^{(z)}. \tag{B.6}$$

We now introduce the following relations (this is due to the fundamental difference between engineering and tensorial definitions of strain):

$$\begin{Bmatrix} \epsilon_x \\ \epsilon_\theta \\ \gamma_{x\theta} \end{Bmatrix}^{(z)} = \begin{bmatrix} 1 & 0 & 0 \\ 0 & 1 & 0 \\ 0 & 0 & 2 \end{bmatrix} \begin{Bmatrix} \epsilon_x \\ \epsilon_\theta \\ \gamma_{x\theta}/2 \end{Bmatrix}^{(z)} \quad \Rightarrow \quad \{\bar{\epsilon}\}^{(z)} = [R]\left\{\bar{\epsilon}'\right\}^{(z)} \tag{B.7}$$

and

$$\begin{Bmatrix} \epsilon_1 \\ \epsilon_2 \\ \gamma_{12} \end{Bmatrix}^{(z)} = \begin{bmatrix} 1 & 0 & 0 \\ 0 & 1 & 0 \\ 0 & 0 & 2 \end{bmatrix} \begin{Bmatrix} \epsilon_1 \\ \epsilon_2 \\ \gamma_{12}/2 \end{Bmatrix}^{(z)} \quad \Rightarrow \quad \{\epsilon\}^{(z)} = [R]\left\{\epsilon'\right\}^{(z)}. \tag{B.8}$$

The constitutive relations in laminate coordinates can be derived as follows:

$$
\begin{aligned}
\{\overline{\sigma}\}^{(z)} &= [T]^{-1}\{\sigma\}^{(z)} \\
&= [T]^{-1}[Q]\{\epsilon\}^{(z)} \\
&= [T]^{-1}[Q][R]\left\{\epsilon'\right\}^{(z)} \\
&= [T]^{-1}[Q][R][T]\left\{\overline{\epsilon}'\right\}^{(z)} \\
&= [T]^{-1}[Q][R][T][R]^{-1}\{\overline{\epsilon}\}^{(z)} \\
&= [T]^{-1}[Q][T]^{-T}\{\overline{\epsilon}\}^{(z)} \qquad \Rightarrow \quad [T]^{-T} = [R][T][R]^{-1} \\
&= \left[\overline{Q}\right]\{\overline{\epsilon}\}^{(z)} \qquad \Rightarrow \quad \left[\overline{Q}\right] = [T]^{-1}[Q][T]^{-T}.
\end{aligned}
$$

Finally, in component form, the constitutive relations in laminate coordinates are

$$
\begin{Bmatrix} \sigma_x \\ \sigma_\theta \\ \tau_{x\theta} \end{Bmatrix}^{(z)} = \begin{bmatrix} \overline{Q}_{11} & \overline{Q}_{12} & \overline{Q}_{16} \\ \overline{Q}_{12} & \overline{Q}_{22} & \overline{Q}_{26} \\ \overline{Q}_{16} & \overline{Q}_{26} & \overline{Q}_{66} \end{bmatrix} \begin{Bmatrix} \epsilon_x \\ \epsilon_\theta \\ \gamma_{x\theta} \end{Bmatrix}^{(z)}, \tag{B.9}
$$

where

$$
\left.
\begin{aligned}
\overline{Q}_{11} &= Q_{11}C^4 + 2(Q_{12} + 2Q_{66})S^2C^2 + Q_{22}S^4, \\
\overline{Q}_{12} &= (Q_{11} + Q_{22} - 4Q_{66})S^2C^2 + Q_{12}(S^4 + C^4), \\
\overline{Q}_{22} &= Q_{11}S^4 + 2(Q_{12} + 2Q_{66})S^2C^2 + Q_{22}C^4, \\
\overline{Q}_{16} &= (Q_{11} - Q_{12} - 2Q_{66})SC^3 + (Q_{12} - Q_{22} + 2Q_{66})S^3C, \\
\overline{Q}_{26} &= (Q_{11} - Q_{12} - 2Q_{66})S^3C + (Q_{12} - Q_{22} + 2Q_{66})SC^3, \\
\overline{Q}_{66} &= (Q_{11} + Q_{22} - 2Q_{12} - 2Q_{66})S^2C^2 + Q_{66}(S^4 + C^4).
\end{aligned}
\right\} \tag{B.10}
$$

Now, substituting equations (A.14) into equations (B.9) we get:

$$
\sigma_x^{(z)} = \overline{Q}_{11}^{(z)}(u_{,x} - zw_{,xx}) + \overline{Q}_{12}^{(z)}\left(\frac{-w}{R}\right), \tag{B.11}
$$

$$
\sigma_\theta^{(z)} = \overline{Q}_{12}^{(z)}(u_{,x} - zw_{,xx}) + \overline{Q}_{22}^{(z)}\left(\frac{-w}{R}\right), \tag{B.12}
$$

$$
\tau_{x\theta}^{(z)} = \overline{Q}_{16}^{(z)}(u_{,x} - zw_{,xx}) + \overline{Q}_{26}^{(z)}\left(\frac{-w}{R}\right). \tag{B.13}
$$

As we explained in appendix A, we integrate the stresses through the thickness to get the stress resultants. After substituting the stresses, equations (B.11), (B.12), and (B.13), into equations (A.4) and integrating, we can arrange equations (A.4) in matrix form as

$$\begin{Bmatrix} N_x \\ N_\theta \end{Bmatrix} = \begin{bmatrix} A_{11}(x) & A_{12}(x) \\ A_{12}(x) & A_{22}(x) \end{bmatrix} \begin{Bmatrix} u_{,x} \\ -\frac{w}{R} \end{Bmatrix} + \begin{bmatrix} B_{11}(x) & B_{12}(x) \\ B_{12}(x) & B_{22}(x) \end{bmatrix} \begin{Bmatrix} -w_{,xx} \\ 0 \end{Bmatrix}, \tag{B.14}$$

and

$$\begin{Bmatrix} M_x \\ M_\theta \end{Bmatrix} = \begin{bmatrix} B_{11}(x) & B_{12}(x) \\ B_{12}(x) & B_{22}(x) \end{bmatrix} \begin{Bmatrix} u_{,x} \\ -\frac{w}{R} \end{Bmatrix} + \begin{bmatrix} D_{11}(x) & D_{12}(x) \\ D_{12}(x) & D_{22}(x) \end{bmatrix} \begin{Bmatrix} -w_{,xx} \\ 0 \end{Bmatrix}, \tag{B.15}$$

where

$$A_{ij}(x) = \sum_{k=1}^{n} \overline{Q}_{ij}^{k} \left(g_k^*(x) - g_{k-1}^*(x) \right), \tag{B.16}$$

$$B_{ij}(x) = \frac{1}{2} \sum_{k=1}^{n} \overline{Q}_{ij}^{k} \left(g_k^{*2}(x) - g_{k-1}^{*2}(x) \right), \tag{B.17}$$

and

$$D_{ij}(x) = \frac{1}{3} \sum_{k=1}^{n} \overline{Q}_{ij}^{k} \left(g_k^{*3}(x) - g_{k-1}^{*3}(x) \right). \tag{B.18}$$

Note that i, j take the values 1 and 2.

For symmetric laminated shells $B_{ij}(x) = 0$. Also, laminated shells composed of angle-ply and cross-ply lay-ups with large number of laminae (entailing 4 lamina or more as explained in Jones [33] and illustrated in chapter 6), behave as symmetric laminates, i.e., $B_{ij}(x) \simeq 0$.

From figure B.2, one can easily find expressions for the distance from the middle-surface to the top and bottom of lamina k. These are

$$g_k^*(x) = \left(k - \frac{n}{2} \right) t(x) \tag{B.19}$$

and

$$g_{k-1}^*(x) = \left(k - \frac{n}{2} - 1 \right) t(x), \tag{B.20}$$

respectively, where

$$t(x) = \frac{g_0}{n} \left(1 + \Delta \overline{g} \frac{x}{h} \right). \tag{B.21}$$

Hence, $A_{ij}(x)$ and $D_{ij}(x)$ can be rewritten as

$$A_{ij}(x) = g(x)A^*_{ij} \tag{B.22}$$

and

$$D_{ij}(x) = g^3(x)D^*_{ij}, \tag{B.23}$$

where

$$A^*_{ij} = \frac{1}{n}\sum_{k=1}^{n} \overline{Q}^k_{ij}, \tag{B.24}$$

$$D^*_{ij} = \frac{1}{3n^3}\sum_{k=1}^{n} \overline{Q}^k_{ij}\left(1 - 3k + 3k^2 + \frac{3}{2}n - 3kn + \frac{3}{4}n^2\right), \tag{B.25}$$

$$g(x) = g_0\left(1 + \Delta\overline{g}\frac{x}{h}\right), \tag{B.26}$$

and

$$\Delta\overline{g} = \frac{g_1 - g_0}{g_0}. \tag{B.27}$$

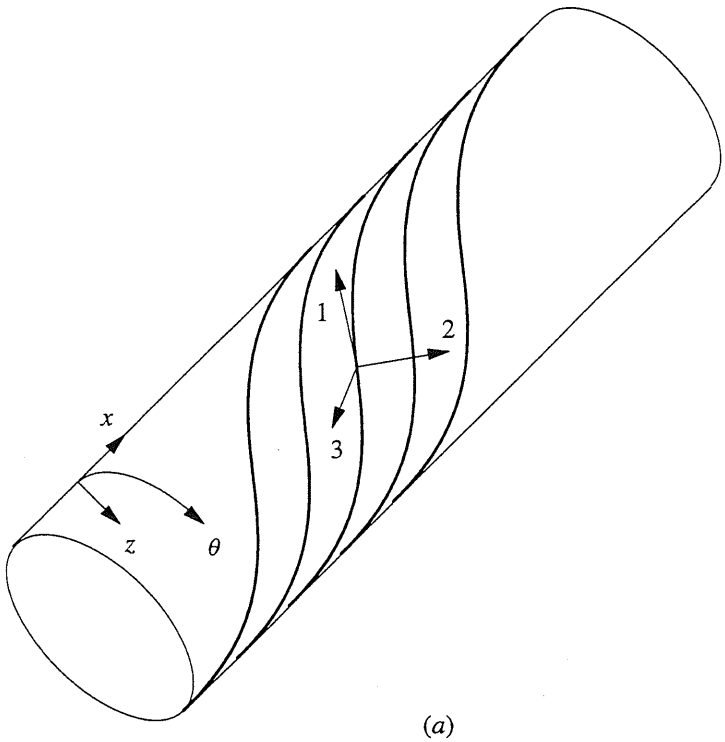

(*a*)

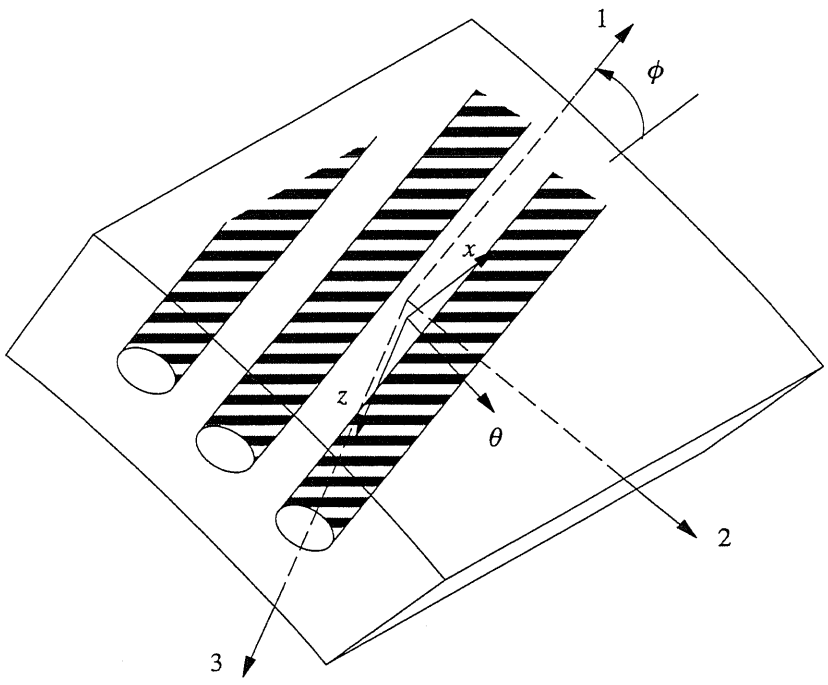

(*b*)

Figure B.1 Coordinate System Definitions.

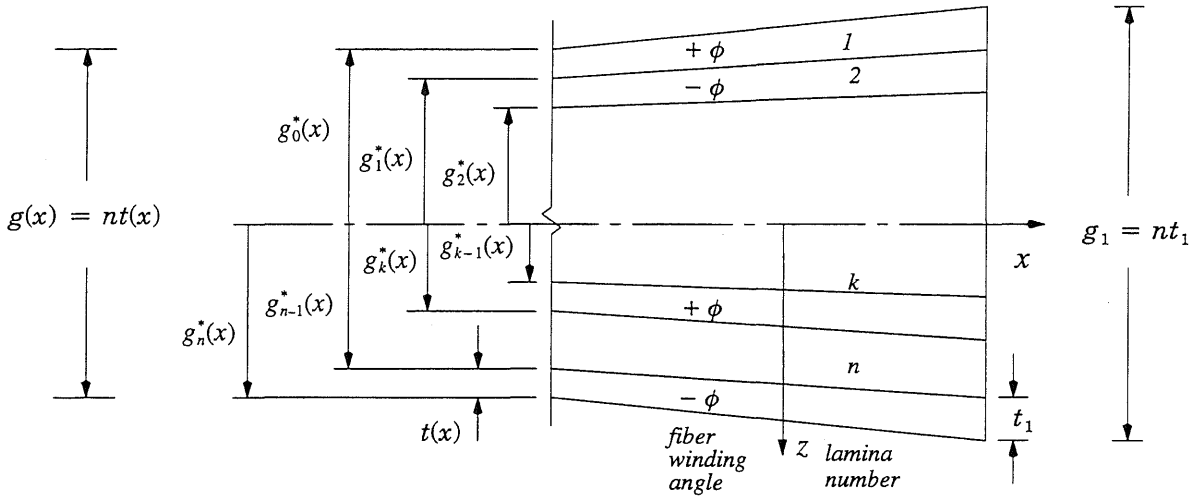

Figure B.2 Geometry of Layered Tapered Laminate.

Appendix C

Derivation of the Tapered Beam on an Elastic Foundation Equation

The equilibrium equations, kinematic assumptions, strain-displacement relations, and constitutive law presented in appendices A and B can be reduced to a single equation. This equation is known as the tapered beam on an elastic foundation equation in shell theory.

From equilibrium, differentiating equation (A.7) with respect to x once and solving the result for $Q_{x,x}$,

$$Q_{x,x} = M_{x,xx}. \tag{C.1}$$

Now substituting this result into equation (A.6),

$$M_{x,xx} + \frac{N_\theta}{R} + Z = 0. \tag{C.2}$$

Furthermore, from equations (B.14) and (B.15) (and assuming $B_{ij}(x) = 0$, as explained in appendix B), N_x, N_θ, and M_x can be defined in terms of the displacements and stiffness coefficients as follows:

$$N_x = g(x)A^*_{11}u_{,x} - g(x)A^*_{12}\frac{w}{R}, \tag{C.3}$$

$$N_\theta = g(x)A^*_{12}u_{,x} - g(x)A^*_{22}\frac{w}{R}, \tag{C.4}$$

and

$$M_x = -g^3(x)D_{11}^* w_{,xx}. \tag{C.5}$$

Now, substitute N_θ and M_x into equation (C.2),

$$\left(-g^3(x)D_{11}^* w_{,xx}\right)_{,xx} + g(x)A_{12}^* \frac{u_{,x}}{R} - g(x)A_{22}^* \frac{w}{R^2} + Z = 0. \tag{C.6}$$

The only unknowns in equation (C.6) are w and $u_{,x}$, but we only have one equation. Note, however, that we can get an expression for $u_{,x}$ in terms of known quantities and w. This can be done by substituting into equation (C.3) the value for N_x from equation (A.8). The result is

$$u_{,x} = \frac{\overline{N}_x}{g(x)A_{11}^*} + \frac{g(x)A_{12}^*}{g(x)A_{11}^*}\frac{w}{R}. \tag{C.7}$$

Now substitute this result into equation (C.6) to get

$$\left(g^3(x)w_{,xx}\right)_{,xx} + g(x)\frac{h^4}{D_{11}^*}\left(A_{22}^* - \frac{A_{12}^{*2}}{A_{11}^*}\right)\frac{w}{R^2} = \frac{h^4}{D_{11}^*}\left(Z + \frac{A_{12}^*}{A_{11}^*}\frac{\overline{N}_x}{R}\right). \tag{C.8}$$

Note that the term $\frac{A_{12}^*}{A_{11}^*}\frac{\overline{N}_x}{R}$ is due to the Poisson effect, caused by radial deformation. If the shell is not restrained in the axial direction, this term is zero.

If we look at the pressurized condition, $Z = p$, $\overline{N}_x$ is the axial membrane stress due to the internal pressure, p. Note $\overline{N}_x$ is a function of x, since $\overline{N}_x = \sigma_x^{membrane} g(x)$, but we can assume that the variation is small and hence $\overline{N}_x$ is constant. Therefore, the membrane stress resultant is

$$\overline{N}_x = \frac{R}{2}p. \tag{C.9}$$

Substituting this result into (C.8) we get

$$\left(g^3(x)w_{,xx}\right)_{,xx} + g(x)\frac{h^4}{D_{11}^*}\left(A_{22}^* - \frac{A_{12}^{*2}}{A_{11}^*}\right)\frac{w}{R^2} = -\frac{h^4}{D_{11}^*}\left(1 - \frac{A_{12}^*}{2A_{11}^*}\right)p. \tag{C.10}$$

We now transform equation (C.10) into a more manageable form. First, we let $\Delta\bar{g}\psi = (1 + \Delta\bar{g}x/h)$, which implies that $g(\psi) = g_0\Delta\bar{g}\psi$. Then substitute these two quantities into equation (C.10), the result is the tapered beam on an elastic foundation equation, i.e.,

$$\left(\psi^3 w_{,\psi\psi}\right)_{,\psi\psi} + \psi\rho^4 w = \left(\frac{A_{12}^*}{2A_{11}^*} - 1\right)\frac{ph^4}{\Delta\bar{g}^3 g_0^3 D_{11}^*}, \tag{C.11}$$

where

$$\rho^4 = \frac{h^4}{\Delta \bar{g}^2 g_0^2 R^2 D_{11}^*}\left[A_{22}^* - \frac{\left(A_{12}^*\right)^2}{A_{11}^*}\right]. \tag{C.12}$$

Appendix D

Solution to the Tapered Beam on an Elastic Foundation Equation

The solution to equation (C.11) is done in two parts, the particular and homogeneous parts. Here we present the two solutions and the total solution, including the slope, bending moment, and shear force.

D.1 Particular Solution

We choose a solution of the following form

$$w_P = -\frac{Const}{\psi}. \tag{D.1}$$

Differentiating w_P and substituting it into the tapered beam on elastic foundation equation and solving for *Const*, we get

$$Const = \frac{p^e}{\Delta \bar{g}}, \tag{D.2}$$

where

$$p^e = \frac{R^2 p}{2g_0}\left[\frac{2A_{11}^* - A_{12}^*}{A_{22}^* A_{11}^* - \left(A_{12}^*\right)^2}\right]. \tag{D.3}$$

Therefore, the particular solution, w_P, is

$$w_P = \frac{p^e}{\Delta \bar{g} \psi}. \tag{D.4}$$

D.2 Homogeneous Solution

Setting the left-hand side of equation (C.11) to zero, we get the homogeneous equation

$$\left(\psi^3 w_{H,\psi\psi}\right)_{,\psi\psi} + \psi \rho^4 w_H = 0. \tag{D.5}$$

The solution of equation (D.5) can be reduced to the solution of two second order ordinary differential equations, as shown in reference [50] pages 488 – 490. These second order ordinary differential equations are

$$\psi w_{H,\psi\psi} + 2 w_{H,\psi} \pm i\rho^2 w_H = 0, \tag{D.6}$$

where $i = \sqrt{-1}$. These equations can be transformed into Bessel equations by introducing the new variables $H = 2\rho\sqrt{i\psi}$ and $\zeta = w_H \sqrt{\psi}$. After some algebraic manipulation we get

$$H^2 \zeta_{,HH} + H\zeta_{,H} + \left(\pm H^2 - 1\right)\zeta = 0. \tag{D.7}$$

Taking the (+) sign, the resulting equation is a complex Bessel equation of the first order. Its standard solution is of the form

$$\zeta^{(+)} = C_1^* J_1(H) + C_2^* Y_1(H), \tag{D.8}$$

where $J_1(H)$ is a first order Bessel function of the first kind and $Y_1(H)$ is a first order Bessel function of the second kind. Taking the (–) sign and substitute $H^* = iH$ into equation (D.7), we get

$$H^{*2}\zeta_{,H^*H^*} + H^*\zeta_{,H^*} + \left(H^{*2} - 1\right)\zeta = 0, \tag{D.9}$$

which is also a first order complex Bessel equation. And its standard solution is similar to (D.8), i.e.,

$$\zeta^{(-)} = C_3^* J_1(H^*) + C_4^* Y_1(H^*). \tag{D.10}$$

The form of each solution (D.8) and (D.10) is complex, which we know has no physical meaning. But, the real parts and complex conjugate of the complex parts can be linearly combined to make up each solution, which is real.

We now rearrange equation (D.8) into its real and complex parts. We can greatly simplify the analysis by making the following observation, $J_1(x) = -J'_0(x)$ where the prime, i.e., $(\cdot)'$, denotes the derivative of the function with respect to its argument. We also let $\eta = 2\rho\sqrt{\psi}$, which means that $H = \sqrt{i}\eta$. Then

$$J_0\left(\sqrt{i}\eta\right) = ber(\eta) - i\,bei(\eta), \tag{D.11}$$

and $ber(x)$ and $bei(x)$ are known as Kelvin, or Thompson, functions [30] (see chapter 5 for the definitions of all of these functions). Differentiating equation (D.11) we get

$$J'_0\left(\sqrt{i}\eta\right) = \frac{1}{\sqrt{i}}\{ber'(\eta) - ibei'(\eta)\}. \tag{D.12}$$

When dealing with complex variables, it is customary to take a second solution of the form $K_1(x) = -\pi/2\left[J_1(ix) + iY_1(ix)\right]$, i.e., a linear combination of the two solutions for the real case. Again to simplify the algebra, we make the following observation, $K_1(x) = -K'_0(x)$, where

$$K_0\left(\sqrt{i}\eta\right) = ker(\eta) + ikei(\eta), \tag{D.13}$$

where $ker\,(x)$ and $kei(x)$ are also Kelvin, or Thompson, functions [30] (see the chapter 5 for the definitions of all of these functions). Differentiating (D.13), we get

$$K'_0\left(\sqrt{i}\eta\right) = \frac{1}{\sqrt{i}}\{ker'(\eta) + ikei'(\eta)\}. \tag{D.14}$$

Therefore, equation (D.8) becomes

$$\zeta^{(+)} = -\frac{C_1^*}{\sqrt{i}}[ber'(\eta) - ibei'(\eta)] - \frac{C_2^*}{\sqrt{i}}[ker'(\eta) + ikei'(\eta)]. \tag{D.15}$$

We now consider equation (D.10). For this case $H^* = i\sqrt{i}\eta$ and following the same steps as above, we get

$$J'_0\left(i\sqrt{i}\eta\right) = \frac{1}{\sqrt{i}}\{ber'(\eta) + ibei'(\eta)\} \tag{D.16}$$

and

$$\begin{aligned} K'_0\left(i\sqrt{i}\eta\right) &= \frac{1}{\sqrt{i}}\{ker'(i\eta) + ikei'(i\eta)\} \\ &= \frac{1}{\sqrt{i}}\{-iker'(\eta) + i\pi bei'(\eta) - kei'(\eta) - \pi ber'(\eta)\}. \end{aligned} \tag{D.17}$$

Therefore, equation (D.10) becomes

$$\zeta^{(-)} = -\frac{C_3^*}{\sqrt{i}}[bei'(\eta) - iber'(\eta)] - \frac{C_4^*}{\sqrt{i}}[-iker'(\eta) - kei'(\eta) + i\pi bei'(\eta) - \pi ber'(\eta)]. \tag{D.18}$$

Combining the solution to both problems, equations (D.15) and (D.18), the resulting function satisfies the homogeneous equation, (D.5), i.e.,

$$\zeta = \left[-\frac{C_1^*}{\sqrt{i}} + i\frac{C_3^*}{\sqrt{i}} + \pi\frac{C_4^*}{\sqrt{i}}\right]ber'(\eta) + \left[i\frac{C_1^*}{\sqrt{i}} - \frac{C_3^*}{\sqrt{i}} - i\pi\frac{C_4^*}{\sqrt{i}}\right]bei'(\eta) + \left[-\frac{C_2^*}{\sqrt{i}} + i\frac{C_4^*}{\sqrt{i}}\right]ker'(\eta) + \left[-i\frac{C_2^*}{\sqrt{i}} + \frac{C_4^*}{\sqrt{i}}\right]kei'(\eta). \tag{D.19}$$

Since the coefficients of the derivatives are complex and arbitrary, we can replace them with arbitrary real coefficients, i.e.,

$$\zeta = C_1 ber'(\eta) + C_2 bei'(\eta) + C_3 ker'(\eta) + C_4 kei'(\eta). \tag{D.20}$$

Now substituting equation (D.20) back into $\zeta = w_H\sqrt{\psi}$, we get

$$w_H = \frac{2\rho}{\eta}\left[C_1 ber'(\eta) + C_2 bei'(\eta) + C_3 ker'(\eta) + C_4 kei'(\eta)\right]. \tag{D.21}$$

D.3 Total Solution

Combining the particular and homogeneous solutions we get the total solution,

$$w(\eta) = \frac{2\rho}{\eta}\left[C_1 k_1(\eta) + C_2 k_2(\eta) + C_3 k_3(\eta) + C_4 k_4(\eta)\right] - \frac{4\rho^2 p^e}{\Delta\bar{g}\eta^2}. \tag{D.22}$$

We have redefined the Kelvin function as $k_i(\eta)$, which are listed in chapter 5. The constants C_1, C_2, C_3, and C_4 are determined from the boundary conditions. The slope, bending moment $M(\eta)$, and shear force $Q(\eta)$ are then

$$\frac{dw}{dx} = \frac{4\rho^3}{h\eta^3}\left[C_1 k_5(\eta) + C_2 k_6(\eta) + C_3 k_7(\eta) + C_4 k_8(\eta)\right] + \frac{16\rho^4 p^e}{h\Delta\bar{g}\eta^4}, \tag{D.23}$$

$$M(\eta) = -D_{11}(x)\frac{d^2w}{dx^2} = -\frac{g_0^3\Delta\bar{g}^3 D_{11}^*\eta}{8\rho h^2}\left[C_1 k_9(\eta) + C_2 k_{10}(\eta) + C_3 k_{11}(\eta) + C_4 k_{12}(\eta)\right] + \frac{2g_0^3\Delta\bar{g}^2 D_{11}^* p^e}{h^2}, \tag{D.24}$$

and

$$Q_x(\eta) = \frac{dM_x(x)}{dx}$$

$$= -\frac{g_0^3 D_{11}^* \Delta \bar{g}^3 \rho \eta}{4h^3}\left[C_1 k_{13}(\eta) + C_2 k_{14}(\eta) + C_3 k_{15}(\eta) + C_4 k_{16}(\eta)\right]. \tag{D.25}$$

References

[1] Anonymous, 1979. *Modern Flanges Design*, Taylor Forge Inc., Engineering Department Bulletin No. 502, Chicago.

[2] ASME/ANSI Standard B16.5. Pipe Flanges and Flanged Fittings, New York.

[3] ASME/ANSI Standard B16.1. Cast Iron Pipe Flanges and Flanged Fittings, New York.

[4] ASME Boiler and Pressure Vessel Code, Sections VIII, Division 1, Pressure Vessels. The American Society of Mechanical Engineers, New York.

[5] ASME Boiler and Pressure Vessel Code, Sections X, Fiberglass Reinforced Plastic Pressure Vessels. The American Society of Mechanical Engineers, New York.

[6] ASTM Standard Specification D5421 for Contact Molded Fiberglass (Glass Fiber Reinforced Thermosetting Resin) Flanges, 1995.

[7] ASTM Standard Specification D4024 for Machine Made Fiberglass (Glass Fiber Reinforced Thermosetting Resin) Flanges, 1995.

[8] ASTM Standard Specification D2440 for Rubber Properties – Durometer Hardness, 1995.

[9] ASTM Standard Specification D1330 for Rubber Sheet Gaskets, 1995.

[10] ASTM Standard Specification D2996 Filament-Wound Fiberglass (Glass-Fiber-Reinforced Thermosetting-Resin) Pipe, 1995.

[11] J. H. Bickford, 1995. *An Introduction to the Design and Behavior of Bolted Joints.* 3rd edition, Marcel Dekker, Inc.

[12] A. E. Blach, 1983. *Bolted Flanged Connections with Full Face Gaskets.* Ph.D. Thesis, Ecole Polytechnique, Montreal.

[13] A. E. Blach, A. Bazergui, and R. Baldur, 1986. Full Face Gasketed Bolted Flange Connections, *Welding Research Council*, Bulletin 314, May 1986.

[14] A. E. Blach and S. V. Hoa, 1987. Bolted Flange Connections for Glass Fiber Reinforced Plastic Pipes and Pressure Vessels. *Proceedings 11th International Conference on Fluid Sealing, Cannes, France,* pp. 642–661.

[15] A. E. Blach and S. V. Hoa, 1988. The Effects of Pull-Back on Stresses in FRP Flanges. *Experimental Techniques,* Vol. 12, pp. 12–16.

[16] A. E. Blach, 1988. FRP Bolted Flanged Connections Problems in Design, Fabrication and Use. *Analytical and Testing Methodologies for Design with Advanced Materials*, G. C. Sih, J. T. Pindera, and S. V. Hoa (editors), Elsevier Science, pp. 349–358.

[17] A. E. Blach and L. Sun, 1990. Fiber Reinforced Plastic Bolted Flanged Connections. Proceedings, *2nd International Symposium on Fluid Sealing,* La Baule, France, September, 1990, pp. 445–457.

[18] A. E. Blach, 1996. Fiber Reinforced Plastic Bolted Flanged Connections. *Proceedings of the 8th International Conference on Pressure Vessel Technology,* Vol. 2, Design and Analysis, Montreal, Canada, July, 1996, pp. 301–306.

[19] J. Bustillos and L. Craigie, 1990. Finite Element Analysis in Reinforced plastic Process Equipment Design. *Managing Corrosion with Plastics*, Volume IX, Published by National Association of Corrosion Engineers, paper 2.

[20] N. P. Cheremisinoff and P. N. Cheremisinoff, 1978. *Fiberglass-Reinforced Plastic Deskbook.* Ann Arbor Science Publishers, Inc.

[21] R. D. Cook and W. C. Young, 1985. *Advanced Mechanics of Materials*, Macmillan Publishing Company.

[22] D. Cratchley and N. J. Clifford, October 29, 1971. Four Glass Reinforced Thermosetting Resins for Pipeline Applications. *Design with Composite Materials*, Institution of Mechanical Engineers.

[23] R. D. Currie, 1993. Glass Reinforced Polyester Pipe Engineering and Usage, 1973 to 1993. *C459/024 IMechE*, pp 107–116.

[24] D. E. Czernic, 1996. *Gaskets Design, Selection, and Testing*. McGraw-Hill.

[25] H. Estrada and I. D. Parsons, 1996. A GRP Pipe Joint for Filament Wound Pipes: Strength Analysis and Design. *Pressure Vessels and Piping Design, Analysis, and Severe Accidents*, ASME, PVP–Vol. 331, pp. 13–19.

[26] D. E. Fiddes and J. Lazarou, 1972. Press Moulded Flanges for GRP pipe Systems. *Composites*, November 1972, pp. 254–258.

[27] T. E. Graham, 1989. FRP Flange for Process Pipe and Tanks. In *Managing Corrosion with Plastics,* Tenth Biennial Symposium, November 6–9, 1989, San Antonio TX.

[28] E. W. Godwin, F. L. Matthews and P. F. Kilty, 1986. The Design of Bolted Flange Joints in GRP. *Plastics and Rubber Processing and Applications*, Vol. 6, pp. 161–167.

[29] Hibbitt, Karlsson & Sorensen, Inc., ABAQUS 5.5 user's manual.

[30] F. B. Hildebrand, 1962. *Advance Calculus for Engineers*, Prentice-Hall, Inc.

[31] S. V. Hoa, 1991. *Analysis for Design of Fiber Reinforced Plastic Vessels and Piping*, Technomic Publishing Co., Inc.

[32] S. V. Hoa, 1982. Strain Analysis of Dual Laminated Cylindrical Fiber Glass Reinforced Plastic Vessels. *Journal of Reinforced Plastics and Composites*, Vol. 1, No. 3, pp. 242–253.

[33] R. M. Jones, 1975. *Mechanics of Composite Materials*, Hemisphere Publishing Corp.

[34] G. F. Leon, 1989. Design of Plastic Piping and Fittings – a PVRC Program. *Advances in Bolted Joint Technology*, Hsu, K. H., Bickford, J. H., Gwaltney, R. G., and Leon, G. F. (editors), pp. 81–86, ASME PVP vol. 158.

[35] G. F. Leon, G. E. O. Widera, and C. Ziu, 1993. Comparison of International Standards for (Polymer) Plastic Piping Design. *Codes and Standards in a Global Environment*, pp. 55–63, ASME PVP vol. 259.

[36] G. F. Leon, D. K. Chew, G. E. O. Widera, and W. E. Short, II, 1995. Comparison of International Design Rules for Plastic Bolted Flange Connections. *Current Topics in Computational Mechanics*, pp. 189–203, ASME PVP vol. 305.

[37] J. H. Mallinson, 1988. *Corrosion-Resistant Plastic Composites in Chemical Plant Design*, Marcel Dekker, Inc., New York.

[38] F. L. Matthews, D. M. Foulkes, E. W. Godwin and P. F. Kilty, 1984. The Strength of Bolted Flanged Joints in GRP Pipes. *Proceedings of the 14th Reinforced Plastics Congress*, The British Plastics Federation, pp. 143–149.

[39] J. L. McLarty, 1985. Design Details of Integral Flanges for the Ends of Very Large Composite Fiber Structures. *Composite Structures 3, Proceedings of the Third International Conference,* Elsevier Applied Science, pp. 189–203.

[40] A. Muscati and J. A. Blomfield, 1977. Full Scale Burst Tests on GRP Pipes. *Designing with Fiber Reinforced Materials*, Institution of Mechanical Engineers, pp. 7–10.

[41] A. Muscati and J. A. Blomfield, 1981. A Comparison of The Failure Pressure as Predicted by Finite Element Stress Analysis with Results of Full Scale Burst Tests on GRP Flanges. *Composite Structures, Proceedings of the First International Conference,* Elsevier Applied Science, pp. 690–703.

[42] National Bureau of Standards Voluntary Product Standard, PS15–69, Custom Contact-Molded Reinforced Polyester, Chemical-Resistant Process Equipment. A copy of this product can be found in appendix B of reference [20].

[43] D. N. Paliwal, N. Malhotra, and K. M. Gupta, 1996. Design of Loose Type Orthotropic Flange. *International Journal of Pressure Vessel and Piping*, v 65, pp. 127–135.

[44] PDA Engineering, PATRAN 2.5 User's Manual.

[45] R. J. Roark and W. C. Young, 1975. *Formulas for Stress and Strain*, 5 th ed., McGraw-Hill Book Company, New York.

[46] J. A. Rolston, 1984. When and How to Select Plastics. *31st Biennial Report on Materials of Constructions*, *Chemical Engineering*, October 29, 1984, pp. 70–75.

[47] D. V. Rosato and C. S. Grove, 1964. *Filament Winding*, Wiley, New York.

[48] L. Sun, 1995. *Bolted Flanged Connections Made of Fiber Reinforced Plastic Materials.* Ph.D. Dissertation, Concordia University, Montreal.

[49] R. C. Talbot, 1984. Using Fiberglass-Reinforced Plastics. *31st Biennial Report on Materials of Constructions*, *Chemical Engineering*, October 29, 1984, pp. 76–82.

[50] S. P. Timoshenko and S. Woinowsky-Krieger, 1959. *Theory of Plates and Shells*, McGraw–Hill.

[51] E. O. Waters, D. B. Wesstrom, D. B. Rossheim and F. S. Williams, 1937. Formulas for Stresses in Bolted Flanged Connections. *Transactions of the ASME*, Vol. 59, pp. 161–169.

[52] E. O. Waters, D. B. Wesstrom, D. B. Rossheim and F. S. Williams, 1949. Development of General Formulas for Bolted Flanges. *Taylor Forge & Pipe Works.*